CFD OPTIMIZATION STUDY OF HIGH-EFFICIENCY JET EJECTORS

A Dissertation

by

SOMSAK WATANAWANAVET

Submitted to the Office of Graduate Studies of
Texas A&M University
in partial fulfillment of the requirements for the degree of

DOCTOR OF PHILOSOPHY

May 2008

Major Subject: Chemical Engineering

CFD OPTIMIZATION STUDY OF HIGH-EFFICIENCY JET EJECTORS

A Dissertation

by

SOMSAK WATANAWANAVET

Submitted to the Office of Graduate Studies of
Texas A&M University
in partial fulfillment of the requirements for the degree of

DOCTOR OF PHILOSOPHY

Approved by:

Chair of Committee,	Mark T. Holtzapple
Committee Members,	Charles J. Glover
	Othon K. Rediniotis
	Richard R. Davison
Head of Department,	Michael Pishko

May 2008

Major Subject: Chemical Engineering

ABSTRACT

CFD Optimization Study of High-Efficiency Jet Ejectors. (May 2008)

Somsak Watanawanavet, B.S., Chulalongkorn University;

M.S., Texas A&M University

Chair of Advisory Committee: Dr. Mark T. Holtzapple

Research was performed to optimize the high-efficiency jet ejector geometry by varying motive velocities from Mach 0.50 to 3.25, and mass flow ratio from 0.02 to 100.0. The high-efficiency jet ejector was simulated by Fluent Computational Fluid Dynamics (CFD) software. A conventional finite-volume scheme was utilized to solve two-dimensional transport equations with the standard k-ε turbulence model. In the optimization study of the constant-area jet ejectors, all parameters were expressed in dimensionless terms. The objective of the study was to investigate the optimal length, throat diameter, and optimal nozzle diameter at any operating conditions. Also, the optimum compression ratio and efficiency were calculated.

By comparing simulation results to an experiment, CFD modeling has shown high-quality results. The overall deviation was 8.19%, thus confirming the reliability of the modeling results.

The results from the optimization study indicate that the jet ejector efficiency improves significantly compared to a conventional jet-ejector design. In cases with a subsonic motive velocity, the efficiency of the jet ejector is greater than 90%. A high compression ratio can be achieved with greater motive velocity and mass flow ratio. The

ejector performance between the optimal jet ejectors and conventional jet ejectors provided by Graham Corporation was compared. The results show that substituting a single optimal jet ejector for a single conventional ejector reduces the motive stream consumption by about 10% to 30%, which could decrease operating costs tremendously.

Dimensionless group analysis reveals that the research results are valid for any fluid, operating pressure and geometric scale for a given motive-stream Mach number and momentum ratio. The explanation of how to implement the optimization results and selecting the best operating conditions to minimize the motive stream consumption was included at the end of the dissertation.

DEDICATION

To my parents, for their encouragement both physically and mentally

ACKNOWLEDGEMENTS

I would like to thank the chair of my committee, Dr. Mark T. Holtzapple, for his intellect, time, and guidance. Because of these characteristics, I thoroughly enjoyed doing the research under his advisory.

I am very grateful to my committee member, Dr. Charles J. Glover, for his wonderful ideas and dedication. His idea for deriving the newly defined efficiency equation was applied.

I am very appreciative to my committee members, Dr. Othon Rediniotis and Dr. Richard R. Davison, for their sincere commentary and contributions during the research process.

I am very grateful to Mr. David Carrabba of Gooseneck Trailer for facilitating space and a compressor to perform an experiment, also, financially supporting all expenses in building and testing the optimal jet ejectors.

I would like to thank the Graham Corporation for supplying a jet ejector used in the testing process.

I want to thank the Shell Company for financially supporting the project.

I am very thankful for Ganesh Mohan and my research group members. They provided a great contribution in proving the dimensionless group analysis and came up with a wonderful result.

Lastly, I would like to especially thank Lakkana Kittiratanawiwat. Her support helped me overcome the difficulties of this dissertation.

TABLE OF CONTENTS

		Page
ABSTRACT…….		iii
DEDICATION…….		v
ACKNOWLEDGEMENTS……..		vi
TABLE OF CONTENTS……..		vii
LIST OF FIGURES……..		ix
LIST OF TABLES……		xv
CHAPTER		
I	INTRODUCTION…….....	1
II	LITERATURE REVIEW……..	4
	Design and Optimization……..	4
	Operating and Maintenance……..	12
	Internal Flow Field…….……	14
	Shock Wave……..	15
	Multi-Stage Jet Ejector System……..…	18
III	THEORY……..	22
	Conventional Jet Ejector……...	22
	Computational Fluid Dynamics……	25
	Dimensionless Forms of Fluid Transport Equations……	46
	Compressible Flow……...	52
IV	MODEL VERIFICATION……...	59
	Introduction……...	59
	Methodology…….	60
	Results and Discussion…….	71
	Conclusion……	80

CHAPTER		Page
V	CONSTANT-PRESSURE VS. CONSTANT-AREA JET EJECTOR OPTIMIZATION…..……..……	81
	Introduction……...	81
	Methodology…….	82
	Results and Discussion…….	86
	Conclusion……	96
VI	CONSTANT-AREA JET EJECTOR OPTIMIZATION….	97
	Introduction……...	97
	Methodology…….	98
	Results and Discussion…….	99
	Example……	108
	Conclusion……	113
VII	NOZZLE OPTIMIZATION…….	114
	Introduction……...	114
	Methodology…….	114
	Results and Discussion…….	118
	Conclusion……	134
VIII	DIMENSIONLESS ANALYSIS……..	135
	Introduction……...	135
	Methodology…….	136
	Results and Discussion…….	142
	Example……	160
	Conclusion……	168
IX	EXPERIMENT COMPARISON BETWEEN OPTIMUM AND CONVENTIONAL JET EJECTOR…….……	169
	Introduction……...	169
	Methodology…….	170
	Results and Discussion…….	178
	Conclusion……	197

CHAPTER Page

X APPLYING A HIGH-EFFICIENCY JET EJECTOR IN A VAPOR-COMPRESSION DESALINATION SYSTEM.... 199

Introduction……... 199
Methodology……. 199
Optimum Jet Ejector Implemented in a Vapor-Compression Desalination System…… 205
Results and Discussion……. 215
Conclusion…… 226

XI SUMMARY AND CONCLUSIONS…… 227

Future Research……. 228

LITERATURE CITED..…….. 229

APPENDIX A MATHEMATICAL DERIVATION OF AN EFFICIENCY EQUATION…… 232

APPENDIX B RESULTS OF MODEL ACCURACY EXPERIMENT… 247

APPENDIX C FLUID PROPERTIES OF OPTIMIZATION CASES…... 253

APPENDIX D SALT WATER PROPERTIES AND THE DETAIL DATA OF THE DESALINATION CASE STUDY…….. 258

APPENDIX E THE PROCEDURE TO CALCULATE THE INLET MOTIVE-STREAM PRESSURE…….. 266

APPENDIX F RESULT OF EXTRA STUDY IN CONVERGENT NOZZLE…… 269

APPENDIX G ADDITIONAL RESULTS ON EXPERIMENT COMPARISON BETWEEN OPTIMUM AND CONVENTIONAL JET EJECTOR……... 272

VITA……..… 282

LIST OF FIGURES

FIGURE		Page
1	Jet ejector type ……..……	5
2	Symbols in jet ejector……	6
3	Entrainment ratio as a function of molecular weight……	10
4	Entrainment ratio as a linear function of temperature for air and steam…….....	11
5	Flow variable profile inside the throat section, A) velocity, B) pressure, C) temperature ……..	15
6	Iso-Mach contours for various ejector throat area ratios…..	17
7	Variation in stream pressure and velocity as a function of location along the ejector..…….....	18
8	Conventional jet ejector design…….	24
9	Overview of the computational solution procedure……..	26
10	Control volume used to illustrate discretisation of a scalar transport equation……..	28
11	Variation of a variable ϕ between *x=0 and x=L*……..	31
12	One-dimensional control volume …….	31
13	Procedure of the segregated solver……	36
14	Procedure of the coupled solver……	38
15	Experimental apparatus for measuring the nozzle efficiency……..……..	60
16	Experimental apparatus of jet ejector with no pinch valve closing…….……..	65

FIGURE Page

17 A schematic representation of pinch valve closings during the jet ejector experiment. The 6-in (0.1524-m) tube was closed inch-by-inch (5 in = 0.127 m, 4 in = 0.1016 m, 3 in = 0.0762 m) to create back pressure in the system.……. 66

18 Grid size of an entire computational domain …… 67

19 Various stages of model development. A) The first model, B) the second model, and C) the final model.…… 68

20 The experiment result comparing with the CFD result with various motive velocities. (A) 563 m/s, (B) 528 m/s, (C) 490 m/s, (D) 449 m/s, and (E) 411 m/s……...… 77

21 Base-case design …….. 83

22 Symbols in jet ejector (A) constant-pressure (B) constant-area ……..……. 84

23 Optimization procedure ……..…….. 85

24 Compression ratio of optimal constant-pressure and constant-area jet ejectors with various motive velocities. Mach numbers: (A) 0.50, (B) 1.00, (C) 1.50, (D) 2.00, and (E) 2.50……...……...… 87

25 Efficiency of constant-pressure and constant-area jet ejectors with various motive velocities. Mach numbers: (A) 0.50, (B) 1.00, (C) 1.50, (D) 2.00, and (E) 2.50……... 89

26 Optimal geometry of constant-area jet ejector (A) throat length, and (B) throat diameter ……... 95

27 Optimization methodology ……...…… 99

28 Jet ejector geometry in high-efficiency jet ejector ...……..... 100

FIGURE Page

29 Optimized constant-area jet ejector. (A) Optimal throat diameter ratio D_T/D_P, (B) optimal throat length ratio L_T/D_P, (C) compression ratio P_o/P_p, and (D) efficiency ……..…….. 106

30 Relationship between compression ratio and mass flow ratio for each motive velocity ……..……...…… 110

31 Graph for step 3…….…… 110

32 Required mass flow ratio for each motive velocity to achieve 1.10 compression ratio……..… 111

33 Relationship between efficiency and mass flow ratio for each motive velocity ……. 111

34 Efficiency of each motive velocity at compression ratio 1.10……..…….. 112

35 Nozzle configurations investigated. (A) Two stage (B) Annular (C) Two-tube circular array (D) Three -tube circular array (E) Four-tube circular array (F) Six-tube circular array (G) Eight-tube circular array……..…...…..... 116

36 Definition of *l* in the annular nozzle design ……..……. 117

37 Definition of *l* in the multiple-tube circular array nozzle design ……..……... 117

38 CFD simulation results for different nozzle diameter ratios at 170 m/s. A) Compression ratio B) Efficiency…. 119

39 CFD simulation results for different nozzle diameter ratios at 340 m/s. A) Compression ratio B) Efficiency… 120

40 CFD simulation results for different nozzle diameter ratios at 510 m/s. A) Compression ratio B) Efficiency.... 121

41 CFD simulation results for different nozzle diameter ratios at 680 m/s. A) Compression ratio B) Efficiency.... 122

FIGURE Page

42 CFD simulation results for different nozzle diameter ratios at 850 m/s. A) Compression ratio B) Efficiency….. 123

43 CFD simulation results for different nozzle diameter ratios at 1020 m/s. A) Compression ratio B) Efficiency..... 124

44 CFD simulation results for different nozzle diameter ratios at 1104 m/s. A) Compression ratio B) Efficiency..... 125

45 CFD simulation results for different nozzle diameter ratios at 1104 m/s at mass flow rate below 1. A) Compression ratio B) Efficiency…….....…... 126

46 Optimal axial position for four-tube circular array…… 133

47 Flow parameters ……..…….…. 138

48 Procedure for the dimensionless group analysis …….…. 139

49 Momentum ratio deviation for a given C_p and motive velocity at various outlet pressure P_o. (A) 0.01 atm (B) 0.03 atm (C) 0.06 atm (D) 0.1 atm (E) 0.3 atm (F) 5 atm, and (G) 10 atm……...….. 149

50 C_{pm} deviation for a given C_p and motive velocity at various outlet pressure P_o. (A) 0.01 atm (B) 0.03 atm (C) 0.06 atm (D) 0.1 atm (E) 0.3 atm (F) 5 atm, and (G) 10 atm..…..... 153

51 Interpolation of various parameters for the example problem. (A) C_p, (B) optimum throat diameter ratio, (C) optimum throat length ratio, (D) C_{pm}, and (E) Momentum ratio……...…... 166

52 Experimental apparatus …….…….……... 171

53 Experimental procedure ……...…..… 173

54 Measurement positions in pipe …….……. 175

55 Velocity profile in pipe…… …….……. 177

FIGURE Page

56 Compression ratio for a given mass flow ratio for optimal and conventional jet ejector at motive velocities (A) 390 m/s, (B) 370 m/s, (C) 320 m/s, and (D) 298 m/s..... 179

57 Efficiency for a given mass flow ratio for optimal and conventional jet ejector at motive velocities (A) 390 m/s, (B) 370 m/s, (C) 320 m/s, and (D) 298 m/s.... 181

58 Enlarged view of the low-compression-ratio region of Figure 5 (A) 390 m/s, (B) 370 m/s, (C) 320 m/s, and (D) 298 m/s……..….... 183

59 Efficiency for a given motive velocity for optimal and conventional jet ejector at various compression ratios (A) 1.10, (B) 1.20, (C) 1.30, and (D) 1.40……...…... 189

60 Compression ratio of optimal jet ejector compared to CFD model at motive velocities (A) 390 m/s, (B) 370 m/s, (C) 320 m/s, and (D) 298 m/s.……...… 191

61 Efficiency of optimal jet ejector compared to CFD model at motive velocities (A) 390 m/s, (B) 370 m/s, (C) 320 m/s, and (D) 298 m/s ……..…… 193

62 The graph presenting the relationship between compression ratio and mass flow ratio of each motive velocity…..... 201

63 Graph according to Step 3……...….. 202

64 The graph presents the required mass flow ratio of each motive velocity to achieve 1.10 compression ratio…..... 202

65 Graph presenting the relationship between efficiency and mass flow ratio of each motive velocity...……..... 203

66 The graph presenting the efficiency of each motive velocity at 1.10 compression ratio ……...…..….... 203

67 A jet ejector implemented in a two-stage thermocompression still with multi-effect evaporator.……..……...… 207

FIGURE Page

68 A single latent heat exchanger ……..…….....…. 208

69 The flow diagram of the first few heat exchangers …….. 210

70 Mass flow and pressure of the first two effects …....….. 214

LIST OF TABLES

TABLE		Page
1	Summary of literature results about the optimization of the jet ejector…….	12
2	Capacities and operating ranges of a multistage jet ejector..	19
3	Sub-atmospheric pressure regions…….	20
4	Comparison of CPU time consuming of each turbulence model…….	43
5	Data obtained at the inlet and outlet of the nozzle …..…….	61
6	Boundary condition specification of the CFD models ..…...	69
7	Summarize parameter specification in CFD analysis……	70
8	Data obtained at the outlet of the jet ejector for various pinch valve closings ……...…..	72
9	Static pressures for various pinch valve closings ..……..	73
10	Simulation result of the model stability (A) coarse-grid model (B) fine-grid model …...……...……	75
11	The percentage deviation between the experiment and CFD analysis for each motive stream velocity and pinch valve position……..……	79
12	Summary of the optimal geometries for the constant-area and constant-pressure jet ejectors ……..	93
13	Jet ejector dimension according to points in Figure 28 …...	100
14	The optimization study result ……..…….	102
15	Results according to Step 1……...	109
16	Summary of the mass flow ratio and efficiency for each motive velocity at 1.10 compression ratio ……	112

TABLE		Page
17	Optimal single-nozzle diameter …….……..	118
18	Improved jet ejector compression ratio for circular array nozzle design …….....	128
19	Improved compression ratio (%) of four-tube circular array compared to optimal single-nozzle design …….	129
20	The optimum constant-area jet ejector geometry with a four-tube circular array …….	130
21	Geometric parameters in dimensionless term ...……...……	137
22	Fluid variables in dimensionless formation ……...…..	138
23	Experimental conditions of each approach ...……	139
24	Experimental conditions of the further investigation ……..	140
25	Result of maintaining constant motive-stream Mach number (1.197) and C_p (31.99)…….……..	144
26	Result of maintaining constant motive-stream velocity (407 m/s) and C_p (31.99)…….……...……..	145
27	Result of further investigation ……..	146
28	Evaluation of dimensionless groups using high-pressure steam as the motive fluid; Mach number = 1.197…….	147
29	Evaluation of dimensionless groups using compressed air as the motive fluid; Mach number = 1.197……..	148
30	Dimensionless group of the optimal constant-area jet ejector geometry at 1-atm operating pressure from Chapter VI …….……..	157
31	Summarize ejector geometries of both optimum and manufacture design ……...…	170
32	Summarize the position of each point in the pipe ……...…..	174

TABLE Page

33	Summary of the mass flow ratios for both designs at various compression ratios ……	187
34	Reduction in motive stream usage ..……..	188
35	Results comparing between experimental results and CFD modeling at various motive velocities (A) 390 m/s, (B) 370 m/s, (C) 320 m/s, and (D) 298 m/s.……..	195
36	Results according to Step 1……	200
37	Summary of the mass flow ratio and efficiency for each motive velocity at 1.10 compression ratio ……..…..	204
38	Information for the enthalpy balance …….……..	211
39	The results of the vapor-compression desalination system implemented an optimum jet ejector …….....	216
40	Q_{seawater} of each temperature interval ……	224
41	The results of different amounts of steam from the first latent heat exchanger ……	225

CHAPTER I

INTRODUCTION

Jet ejectors are the simplest devices among all compressors and vacuum pumps. They do not contain any moving parts, lubricants or seals; therefore, they are highly reliable devices with low capital and maintenance costs. Furthermore, most jet ejectors use steam or compressed air as the motive fluid, which are easily found in chemical plants. Due to their simplicity and high reliability, they are widely used in chemical industrial processes; however, jet ejectors have a low efficiency. The major consideration of this study is to optimize jet ejector efficiency at each operating condition. Consequently, the motive stream consumption and operating cost is minimized.

Many factors affect jet ejector performance, including the fluid molecular weight, feed temperature, mixing tube length, nozzle position, throat dimension, motive velocity, Reynolds number, pressure ratio, and specific heat ratio (DeFrate and Hoerl (1959); and Kim et al. (1999)).

Previous research by Riffat and Omer (2001) and Da-Wen and Eames (1995) studied the effect of nozzle position on jet ejector performance on both designs; constant-pressure and constant-area. They found that it greatly affects jet ejector performance, as it determines the distance over which the motive and propelled stream are completely mixed. ESDU (1986) suggested that the nozzle should be placed between 0.5 and 1.0 throat

---

This dissertation follows the style of the *AIChE Journal*.

diameters before the entrance of the throat section. Holton (1951) studied the effect of molecular weight, whereas Holton and Schultz (1951) studied the effect of fluid temperature.

A number of researchers investigated the effect of jet ejector geometry on jet ejector performance. For example, Kroll (1947) investigated the effect of convergence, divergence, length, and diameter of the throat section, nozzle position, induced fluid entrance, and motive velocity. Croft and Lilley (1976) investigated the optimum length and diameter of the throat section, nozzle position, and angle of divergence.

A few literature researchers have studied the effect of nozzle diameter on jet ejector performance, which is also investigated here. In addition, this study also investigates the optimum constant-area jet ejector geometry (length and diameter of the throat section, nozzle diameter, and nozzle position) for each operating condition (motive-stream Mach number and mass flow ratio). The mass flow ratio varies from 0.02 to 100.0 kg motive/kg propelled. The motive velocity at the nozzle exit varies from Mach 0.39 to 5.34. The back pressure of the ejector is maintained constant at 101.3 kPa. Steam is used as a working fluid.

In this research, computational fluid dynamic (CFD) software, Fluent, was employed to optimize the jet ejector designs. CFD software has been proved by a number of researchers (Riffat and Everitt, 1999; Hoggarth, 1970; Riffat et al., 1996; Thalpallitea et al., 1992; Nerve, 1993) as a powerful tool for predicting flow fields inside jet ejectors. Fluent uses a mass-averaged segregated solver to solve the fundamental transport equations such as mass continuity, momentum conservation, and momentum conservation

for a compressible, Newtonian fluid (the Navier-Stokes equation). The governing equations are discretized in space using a finite-volume differencing formulation, based upon an unstructured grid system. The standard k-ε turbulent method was employed to solve the governing equations. The reliability of CFD modeling was examined by comparing simulation results with an experiment results as reported in Part 1 of this series. With no adjustable parameters, the model deviation was only 8.19%, thus confirming its reliability.

The performance of the optimum jet ejector design is compared with a conventional jet ejector provided by Graham Corporation to confirm the ejector performance improvement. Finally, the simulation results are compared with the results from an actual jet ejector apparatus to confirm the results reliability.

CHAPTER II

LITERATURE REVIEW

Design and Optimization

In the past, when engineers designed jet ejectors, either a "rule-of-thumb" or "trial-and-error" approach was used. Both approaches may provide unsatisfactory performance, and thus consume too much power, material, and labor.

Conventional jet ejectors are classified by the dimension of the convergence section. There are two types:

1. Constant-pressure jet ejector
2. Constant-area jet ejector

DeFrate and Hoerl (1959) and Kim et al. (1999) discovered that the constant-pressure configuration provides a better performance than the constant-area configuration, because turbulent mixing in the jet-ejector is achieved more actively under an adverse pressure gradient, which occurs in the constant-area jet ejector, rather than under constant pressure (Kim et al., 1999). Stronger turbulent mixing dissipates the ejector performance. DeFrate and Hoerl (1959) provided the mathematical functions, which are valid for both configurations. The mathematical functions are used to calculate:

1. Optimum motive- and propelled-stream velocity as a function of expansion ratio for an arbitrary molecular weight and temperature
2. Nozzle diameter ratio (D_N/D_P) as a function of entrainment ratio

Jet ejectors are classified into two types, depending on their convergence configuration:

1. Constant-pressure jet ejector
2. Constant-area jet ejector

The different between both types is shown in Figure 1.

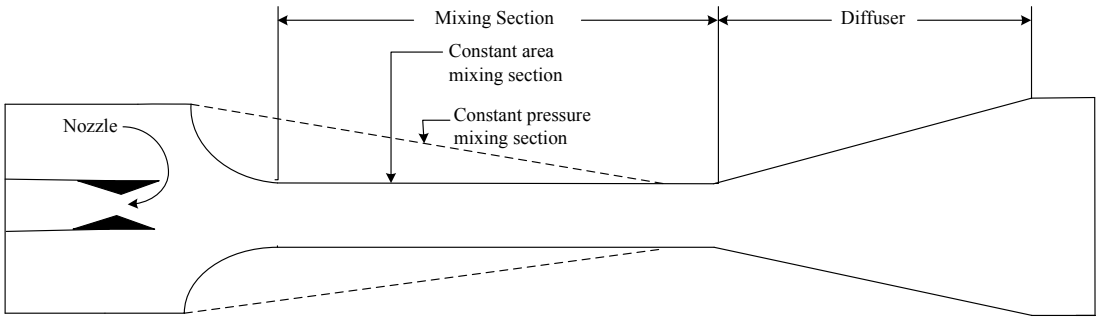

Figure 1. Jet ejector type.

The jet ejector performance is mainly affected by mixing, turbulence, friction, separation, and energy consumption in the suction of the propelled stream. To maximize jet ejector performance, enhancing turbulent mixing should be a major consideration. The literatures indicate that the nozzle geometry should be well-designed to boost the tangential shear interaction between the propelled and motive stream. Also both streams should blend completely inside the throat. The jet ejector should be designed properly to diminish turbulence effects.

Each part of a jet ejector is explained in the following section. Figure 2 indicates the geometric symbols used in the following section.

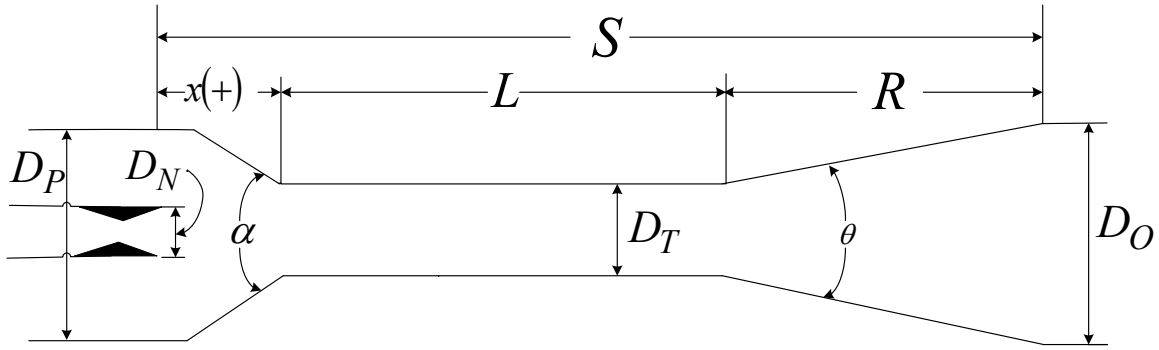

Figure 2. Symbols in jet ejector (Kroll, 1947).

Convergence Section

According to Kroll (1947), Engdahl and Holton (1943); Mellanby (1928); Watson (1933) found that the best design for the convergence section is a well-rounded, bell-mouthed entry. A conical or tapered entry is recommended to have an angle, α, greater than 20 degrees, because the nozzle jet, which has a general angle of about 20 degrees, will not create objectionable shock and eddy losses at the convergence inlet (Mellanby, 1928). Watson (1933) did an experiment and stated that 25 degrees is about the best convergence angle.

Regarding the well-rounded geometry, a conical entry reduces the flow 2%, whereas a coupling and sharp entry reduce the flow 4 and 11%, respectively .

Throat Section

Kroll (1947) also discusses that Mellanby (1928) and Watson (1933) reported that diffusers with a throat section created a greater vacuum than diffusers without a throat

section. Mellanby (1928) also showed that a parallel throat throughout is inferior, but still much better than no parallel throat at all.

The length of the throat section must be designed properly. It should be sufficiently long to create a uniform velocity profile before the entrance of the divergence section. The uniform velocity decreases the total energy losses in the divergence section, thus obtaining better high-pressure recovery (Berge et al., 2000) (also cited in Kroll (1947)).

Two literature sources cited in Kroll (1947) (Duperow and Bossart, (1927); and Keenan and Neumann, (1942)) reported that an optimum throat length is about 7 times the throat diameter, whereas Engdahl (1943) came across with another optimum value of 7.5 times the throat diameter. Additionally, lengths of 5 to 10 times the throat diameter provided within 3% of optimum performance. Although the optimum length increased slightly with pressure and throat diameter, the increase was less than 1 diameter even when these factors were doubled (Keenan and Newmann, 1942). Engdahl (1943) reported that any length between 4 and 14 throat diameters will give within 4% of optimum performance. According to many literature sources, the length should be 7 to 9 times the throat diameter for the best performance.

The optimal throat diameter is sensitive to jet ejector parameters, especially the entrainment ratio. A small change in throat diameter creates a huge change in the entrainment ratio. If the throat area is too large, fluid leaks back into system; if it is too small, choking occurs. So, the throat diameter must be designed properly to obtain the best performance.

Divergence Section

Kroll (1947) indicated that the angle of the divergent section, θ, is usually 4 to 10 degrees. Too rapid a divergence immediately after the throat is not recommended (Kroll, 1947). The divergent length, say from 4 to 8 times the throat diameter, is desired for pressure recovery. The length, however, may be as short as twice the throat diameter if necessary. It was discovered that eliminating the divergence section reduced the entrainment ratio (m_m/m_p) by about 20%.

Nozzle

Two factors of the nozzle influence jet ejector performance:

1. Nozzle design
2. Nozzle position

Fewer researchers have studied the effect of nozzle design on jet ejector performance than nozzle position. Hedges and Hill (1974) studied the influence of nozzle design on jet ejector performance. In their experiment, two conically diverging nozzles were tested, but differing in the divergence angle. The exit and throat diameters of the nozzle were fixed in both cases. The experimental results show that the overall jet ejector performance was not influenced by the nozzle design. According to Kroll (1947), a study done by Engdahl and Holton (1943) confirms the above statement. They found that the nozzle, which was designed by conventional methods for a specific pressure, performed only slightly better than a simple straight-hole nozzle at pressure up to 170 psig. Also, a machined nozzle with a convergence section and a 10 degree angle of divergence was only

3 to 6% better than a 100-psig small pipe-cap nozzle made by drilling a hole in a standard pipe cap. However, altering the nozzle design affects the motive-stream velocity. This was studied explicitly by Berkeley (1957). He also found that under normal circumstances, the expansion of motive stream in the ejector of a well-designed nozzle is almost always a fairy efficient part of the overall flow process. Therefore, very little energy is lost in the nozzle. But the task of efficiently converting velocity back into pressure is very difficult because energy is lost in this process. Additionally, Kroll (1947) reported that a poorly shaped nozzle causes unnecessary shock losses and useless lateral expansion, which decrease jet ejector efficiency tremendously.

The position of the nozzle has a greater effect on jet ejector performance than its design. A number of researchers investigated the optimum position of the nozzle in a jet ejector. Croft and Lilley (1976); and Kim et al. (1999) report that turbulence in the mixing tube decreases when the nozzle is placed right at the entrance of the throat section; however, Croft and Lilley (1976) also discovered that when the nozzle moves closer to the mixing tube, the entrainment ratio decreases. ESDU (1986) recommends placing the nozzle exit between 0.5 and 1.0 lengths of throat diameter upstream of the mixing chamber. Not only the jet ejector performance, but also the mixing distance of the motive and propelled streams is affected by the nozzle position. Kroll (1947) has suggested that nozzle position should be adjustable to obtain the best performance using field adjustments. Further, it is important to have the nozzle centered with the throat tube. He also recommended that the nozzle should be cleaned as often as possible for best performance.

Entrainment Ratio

An experiment conducted by Mellanby (1928) concluded that for all practical purposes, the entrainment ratio is independent of the inlet position of the propelled stream. Holton (1951) discovered that the entrainment ration is a function of the molecular weight of the fluid, but independent of pressure, and jet ejector design. Figure 3 shows the correlation between the entrainment ratio and molecular weight. Furthermore, Holton and Schulz (1951) discovered that the entrainment ratio is a linear function of operating temperature, but independent of pressure and jet ejector design. Figure 4 displays the effect of the operating temperature on the entrainment ratio.

$$\text{Entrainment Ratio} = \frac{\text{mass flow rate of the propelled stream}}{\text{mass flow rate of the motive stream}} \qquad (1)$$

Kroll (1947) had summarized the results of optimized jet ejector geometry from a number of literature sources (see Table 1).

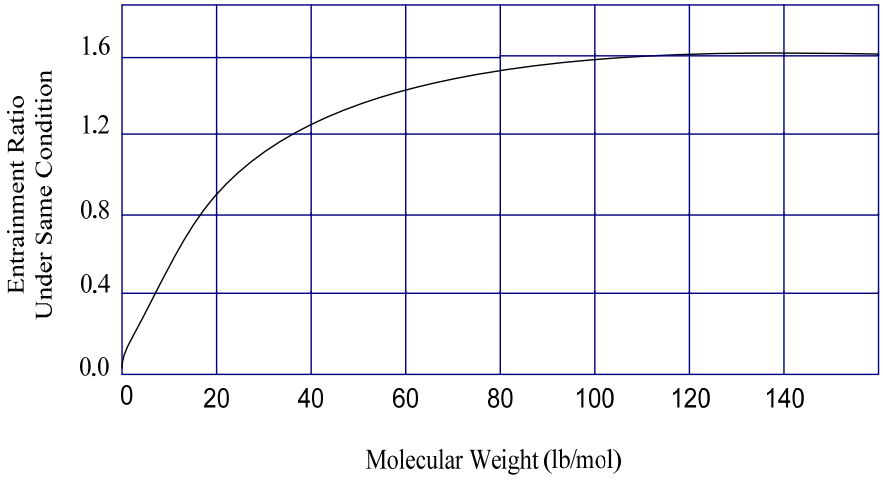

Figure 3. Entrainment ratio as a function of molecular weight (Holton, 1951).

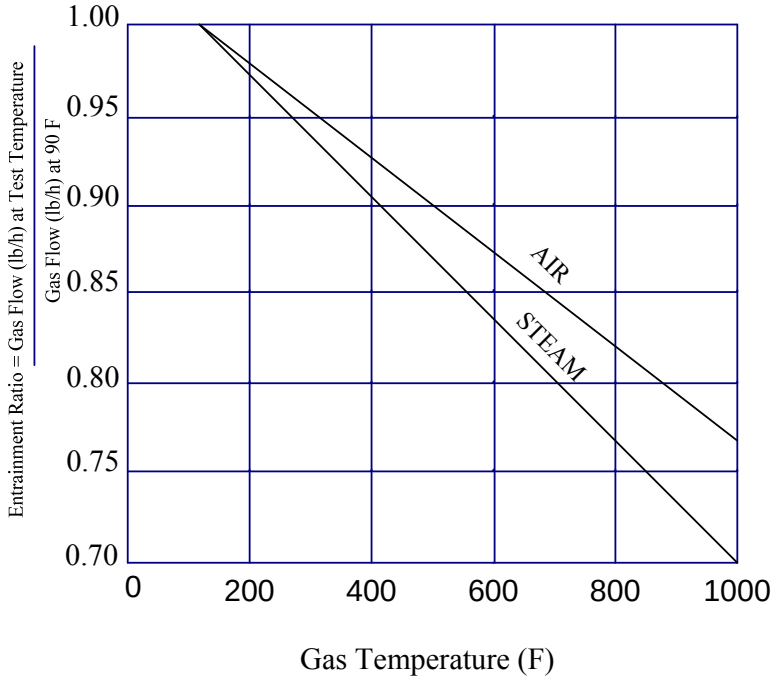

Figure 4. Entrainment ratio as a linear function of temperature for air and steam (Holton and Schultz, 1951).

Table 1. Summary of literature results about the optimization of the jet ejector (Kroll, 1947).

Reference	**Length of**				**Angle of Diffuser (degree)**	
Air-Jet Air Pumps	Throat	Divergence	Nozzle outlet to discharge	Nozzle outlet to throat	Convergence	Divergence
Symbol	***T***	***R***	***S***	***X***	***α***	***θ***
Keenan and Neumann (1942)	7 D_T	-	7.5 D_T	0.5 D_T	well rounded	-
Mellanby (1928)	4 D_T	10 D_T	-	variable	25	12
Kravath (1940)	1 D_T	12 D_T	15 D_T	2 D_T	28	5
Miller (1940)	-	-	-	5 D_T	-	16
SteamJet Air Pumps						
DuPerow and Bossart (1927)	-	-	6 D_T	1.2 D_T	-	7
Royds and Johnson (1941)	10 D_T	15 D_T	-	-	well rounded	-
Langhaar (1946)	3 D_T	4 D_T	10 D_T	3	24	10
Watson (1933)	2 D_T	6.7 D_T	12.3 D_T	3.6 D_T	28	8

Operating and Maintenance

A number of literature references state that pressure is the most critical variable when operating the jet ejector. The actual operating pressure should be evaluated closely during the operation. A jet ejector will not operate properly, causing a broken or unstable vacuum, if it is even a few hundred pascal below its design motive pressure (Knight, 1959). Due to that reason, a steam-pressure gage is highly recommended to be located on the steam chest of the ejectors to measure the inlet pressure of the propelled stream.

Three principles should always be followed for controlling steam jet ejectors (Knight, 1959):

1. Each jet ejector in a system operates along a fixed curve of suction pressure versus capacity for a given discharge pressure.
2. Each jet ejector has a fixed minimum suction pressure for a given discharge pressure, below which the jet ejector flow will be disrupted i.e., a pressure at which vapor flow in the diffuser will be reversed, operation below the break pressure is unstable, but if suction pressure increases above the break pressure, a greater pressure is attained at which stable operation returns, with normal flow in the diffuser.
3. Each jet ejector has a maximum discharge pressure for a given load, above which the jet ejector flow will be disrupted.

Knight (1959) also presented five ways for automatically controlling the pressure. The advantage and disadvantage of each approach were discussed in the literature.

Finally, Berkeley (1957) introduced six variables that should be considered when selecting a particular design of a steam jet ejector:

1. Suction pressure required
2. Amount of steam available
3. Amount of water available
4. Fluid to be evacuated
5. Equipment cost
6. Installation cost

Internal Flow Field

To enhance jet ejector performance, understanding the flow field mechanism inside the jet ejector is useful. Reinke et al. (2002) found that further away from the nozzle exit, the velocity profile is more uniform across the cross section. Because the viscous action of the jet fluid transfers its kinetic energy to the surroundings, fluid moves slower as the distance increases. The internal behavior of the jet ejector – particularly in the mixing section between the primary and secondary flows and also the effect of nozzle axial position – were studied by Croft and Lilley (1976). The energy contours, which are presented in the literature, reveal that at the mixing point, there is a high rate of thermal energy generation due to the high turbulence length scale in the mixing position. Also, the turbulent length scale decreases gradually through the throat section. This indicates that energy transfers from the motive stream to the propelled stream quickly. Turbulence length scale is a physical quantity related to the size of the large eddies containing energy in turbulent flows (Fluent, 2001). In fully developed flows in pipe, the turbulence length scale is restricted by the pipe diameter.

The flow velocity, temperature, and pressure inside the throat section – an effect of these parameters on the jet ejector performance inside the throat section – were studied by Djebedjian et al. (2000). The velocity distribution indicates the degree of mixing between motive and propelled streams and the quantity of entrained fluid. The length of the mixing tube creates a huge effect for producing a uniform velocity profile at the entrance of the divergence section. The fluid velocity profile inside the throat section is presented in Figure 5A. The pressure increases significantly in the throat and the divergence section as

shown in Figure 5B. The static temperature increases because heat is generated from kinetic energy losses in an energy-exchange process. As the fluid velocity decreases, the static temperature increases. The static temperature profile inside the throat section is presented in Figure 5C. The profiles of the fluid velocity and the static temperature are identical but opposite direction in magnitude.

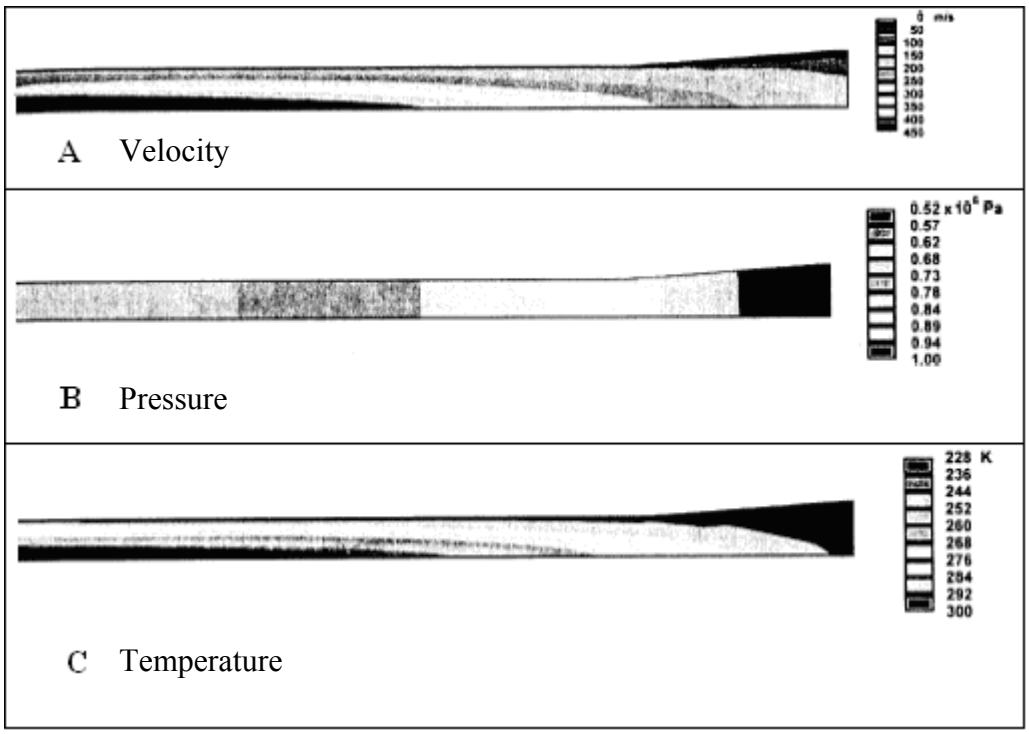

Figure 5. Flow variable profile inside the throat section, A) velocity, B) pressure, C) temperature (Djebedjian et al., 2000).

Shock Wave

When the motive-stream velocity exceeds the speed of sound, shock waves are unavoidable inside jet ejectors. Shock waves convert velocity back to pressure, but in an inefficient manner. Shock waves are more severe as the fluid velocity at the diffuser

entrance increases. Generally, the motive stream is accelerated to a supersonic velocity through the convergent-divergent nozzle. Then, inside the throat section, the propelled stream is induced by a strong shear force with the motive stream leading to the resulting deceleration of the motive stream. The shock wave occurs in this step. The shock wave system interacts with the boundary layer along the jet ejector surface. The flow inside the ejector is exposed to a strong invicid-viscous interaction. The operating characteristics and performance of a supersonic ejector are difficult to predict using conventional gas dynamic theory. Consequently, the discharge pressure is limited to a certain value. DeFrate and Hoerl (1959) provided mathematical formulations to calculate pressure before and after the shock wave in the throat section, and the subsonic Mach number after the shock occurs. Kim et al. (1999) researched the shock wave inside jet ejectors explicitly. They studied the effect of throat area on the shock wave (see Figure 6). As the area of the throat section increases, a Mach stem reduces to an oblique shock wave. Reflections of the oblique shock result in a multiple oblique shock system (Kim et al., 1999). Mach stem is a shock front formed by the fusion of the incident and reflected shock fronts from an explosion. In an ideal case, the mach stem is perpendicular to the reflecting surface and slightly forward. They also found that the throat dimension strongly affects the shock system inside the mixing tube. Their result indicates that the interaction between the shock system and the wall boundary layer in a constant-pressure jet ejector is noticeably stronger than a constant-area jet ejector. Therefore, it is expected that the flow would be subject to a stronger turbulence field in a constant-pressure (Figures 6A – D), rather than constant-area geometry (Figure 6E). This reduces the jet ejector performance significantly.

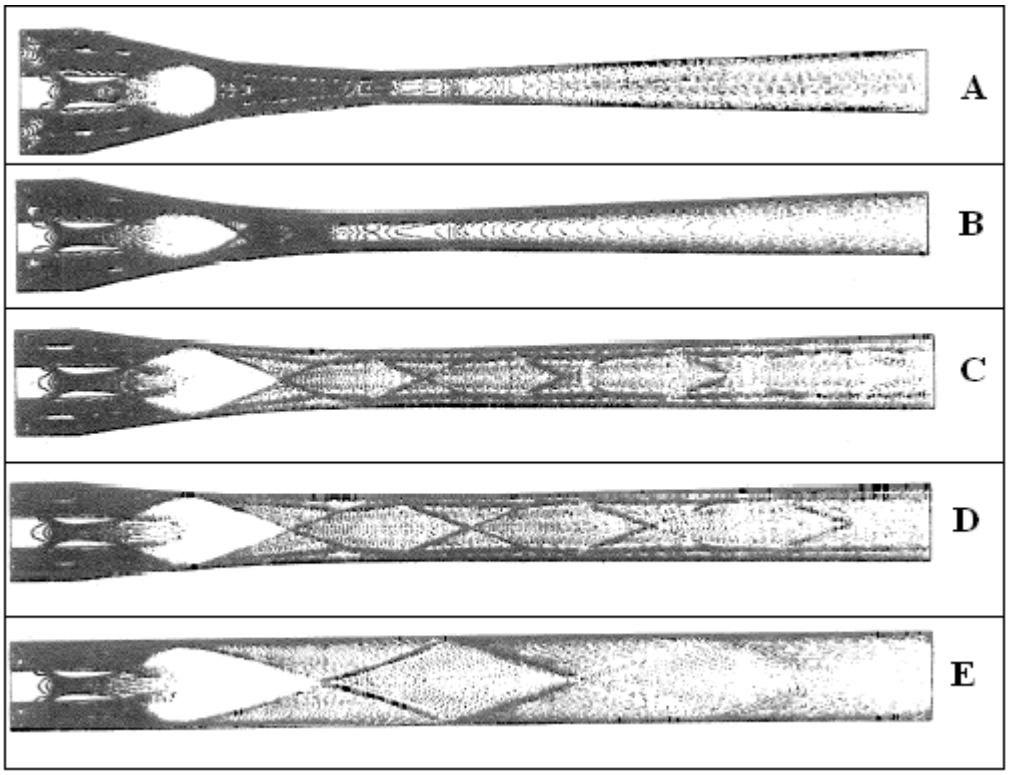

Figure 6. Iso-Mach contours for various ejector throat area ratios (Kim et al. 1999).

The shock wave occurs when the fluid velocity decreases to subsonic velocity. The pressure gradient changes suddenly in the shock wave area. Figure 7 illustrates the shock wave occurring inside the jet ejector.

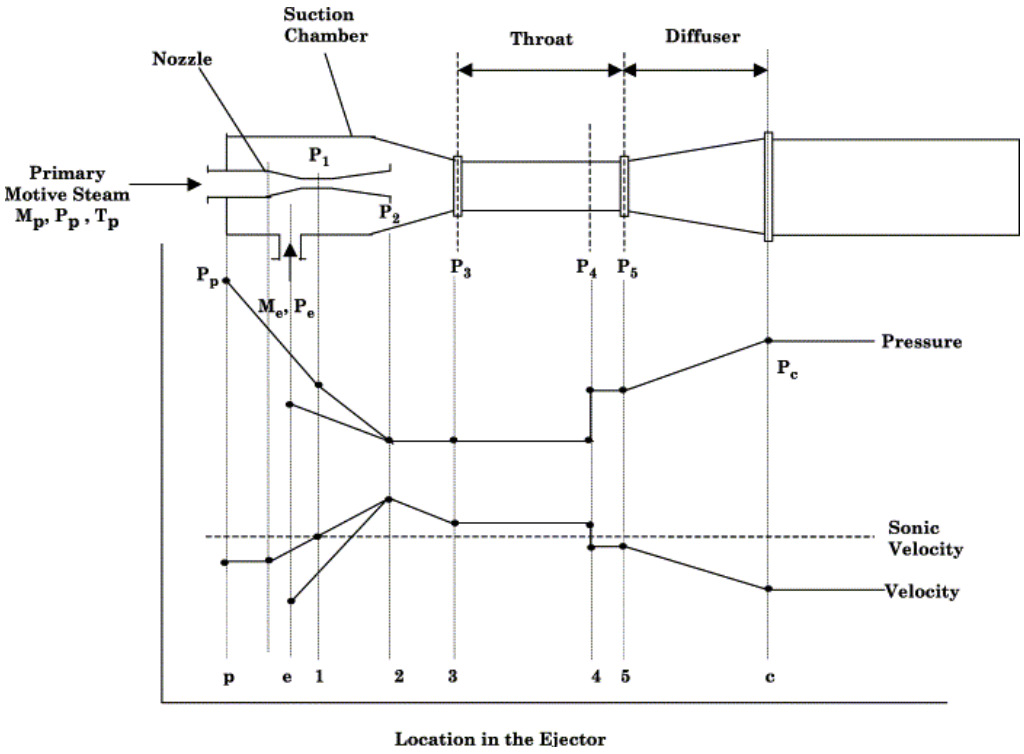

Figure 7. Variation in stream pressure and velocity as a function of location along the ejector (El-Dessouky et al., 2002).

Multi-Stage Jet Ejector System

A single jet ejector has a limiting capacity due to its shape, and also has practical limits on the overall compression ratio and throughput it can deliver. To enhance the compression ratio, two or more ejectors can be arranged in series. But for greater throughput capacity, two or more ejectors can be arranged in parallel. For these reasons, a multi-stage jet ejector system is considered.

The multi-stage jet ejector system contains:

1. Jet ejector
2. Condenser used for condensable fluid only
3. Interconnecting piping

A recent study indicates that five and six stages can produce almost any desired suction pressure. They have carved a unique and popular place in industry where large volumes of gases must be evacuated. Croll (1998) has suggested the capacities and operating ranges of the multi-stage jet ejector system, which are summarized in Table 2.

As the design pressure decreases, the number of ejector stages increases because the suction pressure of an ejector is further affected by the surrender of the energy from the motive stream to the propelled stream.

Table 2. Capacities and operating ranges of a multistage jet ejector (Croll, 1998).

System Type	Lowest Recommended Suction Pressure (kPa)
One-stage	10,000
Two-stage	1,600
Three-stage	130
Four-stage	25
Five-stage	2.5
Six-stage	0.4
Ejector and liquid-ring pump (Integrated pumping system)	20

In jet-ejector design and specification, it is convenient to divide sub-atmospheric pressure into four regions as shown in Table 3 (Croll, 1998).

Table 3. Sub-atmospheric pressure regions (Croll, 1998).

Region	Pressure range (Pa)
Rough vacuum	101,325 – 130
Medium vacuum	130 - 0.13
High vacuum	0.13 - 0.000013
Ultrahigh vacuum	below 0.000013

Most of the applications in chemical engineering are in the rough vacuum region. For example, the normal range of vacuum distillation, evaporation, drying, and filtration are covered in this range.

For selecting a multi-stage jet ejector system, five factors stated below must be satisfied. Many systems will be eliminated after the first two factors.

1. Suction pressure and capacity
2. Reliability and easy maintenance
3. Purchase, installation, and operating costs
4. Environmental restrictions
5. Air leakage

The reasons for these factors are explained explicitly in Croll (1998).

A diagram used for selecting a multi-stage jet ejector system is presented in Berkeley (1957). The diagram can be applied only to non-condensable gas loads. In case a portion of the load to the system is a condensable vapor, it is necessary to analyze the particular operating condition to determine the correct design for optimum economy. In some cases, the gas load to the ejector is reduced considerably by using a pre-condenser to

condense a large portion of the vapor before flowing into the system. Another advantage of using a condenser is that it increases the system reliability, because the system is protected against solid and liquid carryover, and also it reduces the concentration vapor in the load. Jet ejectors can be damaged permanently from excess moisture. Steam quality of less than 2% liquid is tolerable in most systems (Croll, 1998). Often the absolute pressure is too small to use a pre-condenser and it is necessary to compress or boost the vapor to a pressure where a large portion of the condensing can be done in an inter-condenser (Berkeley, 1957). Small secondary ejectors are utilized to compress the non-condensable vapor.

For a multi-stage jet ejector system handling air or other non-condensable gases, the best design is evaluated by the minimum steam and water requirement for its operation, which can be calculated from the diagram in Berkeley (1957). In cases where a large portion of the load is a condensable vapor, the cost of steam and water consumption will determine the best design. The equipment cost will usually change within the range of steam and water cost. Therefore, the operating cost has more influence than the initial cost in selecting the finest system.

CHAPTER III

THEORY

Conventional Jet Ejector

Jet ejectors are popular in the chemical process industries because of their simplicity and high reliability. They are widely used to generate vacuums with capacity ranges from very small to enormous. Due to their simplicity, constant-pressure jet ejectors that are properly designed for a given situation are very forgiving of errors in estimated quantities and of operational upsets. Additionally, they are easily changed to give the exact results required (Mains and Richenberg, 1967).

Jet ejectors provide numerous advantages, which are summarized below:

- They require little maintenance because there are no moving parts to break or wear.
- They have lower capital cost compared to mechanical devices because of their simple design.
- Their design is very straightforward.
- They are easily installed and require little supervision.

On the other hand, the major disadvantages of jet ejectors follow:

- They are designed to perform at a particular optimum point. Deviation from this optimum point can dramatically reduce efficiency.
- They have a low thermal efficiency at high compression ratios.

Jet Ejector Application

Due to their simplicity, jet ejectors have been used for various purposes. A number of the principle applications are listed below (Schmitt, 1975).

1. *Extraction*: suction of the induced fluid.
2. *Compression*: compression of the induced fluid using a motive fluid.
3. *Ventilation and air conditioning*: extraction and discharge of gas near atmospheric pressure with small compression ratio.
4. *Uniform mixing of two streams*: providing a uniform concentration or temperature in a chemical reaction
5. *Conveyance*: pneumatic or hydraulic transport of solids.
6. *Thermo-compression desalination*: pressurizing water vapors from evaporating saline water (Porteous, 1983).

Operating Principle

As shown in Figure 8, the conventional jet ejector design has four major sections:

1. nozzle
2. suction chamber
3. throat
4. diffuser

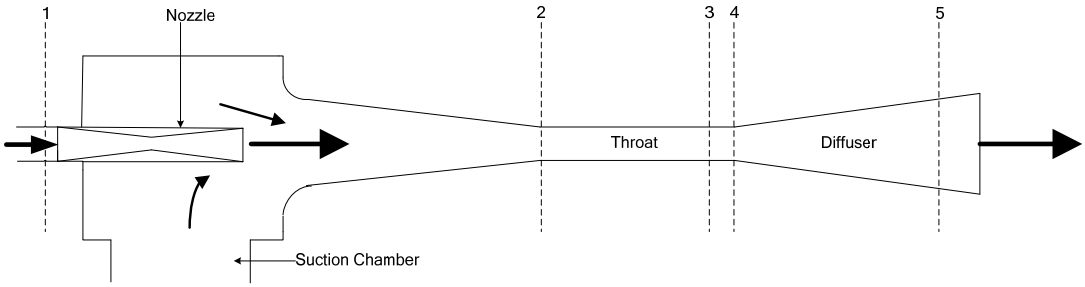

Figure 8. Conventional jet ejector design.

The operating principle of jet ejectors is described below:

1. Subsonic motive stream enters the nozzle at Point 1. It flows to the converging section of the nozzle, its velocity increases, and its pressure decreases. At the nozzle throat, the stream reaches sonic velocity. In the diverging section of the nozzle, the velocity increases to supersonic.
2. The entrained propelled fluid enters the ejector, flowing to Point 2. Its velocity increases and its pressure decreases.
3. The motive stream and entrained propelled stream begin to mix within the suction chamber; mixing is completed in the throat.
4. Inside the throat, a shock wave forms when the mixture velocity reduces to a subsonic condition. The back-pressure resistance can cause condensation at Point 3.
5. The mixture flows into the diverging section of the diffuser where the kinetic energy of the mixture is transformed into pressure energy. At Point 5, the pressure of the emerging fluid is slightly higher than at Point 3 (El-Dessouky et al., 2002).

All jet ejectors, whether they are condensing or noncondensing, operate on this principle. They can be combined into multiple stages, each stage being another compressor (Mains and Richenberg, 1967).

Computational Fluid Dynamics

Since the 1950s, due to improvements in the speed of computers and their memory size, computational fluid dynamics (CFD) has emerged as a valuable tool. CFD is primarily used for flow-based physical simulation, process evaluation, and component design. CFD, when implemented properly, is a low-cost, rapid, non-intrusive, parametric test method. As a design tool, it permits developments with greater reliability and repeatability, at a fraction of the cost and time of traditional design approaches that involve empiricism, followed by prototyping and testing (Habashi, 1995).

CFD has five major advantages compared with experimental fluid dynamics:

1. Significantly reduce lead time in design and development
2. Simulate flow conditions not reproducible in experimental model tests
3. More detailed and comprehensive information
4. More cost-effective than wind-tunnel testing
5. Lower energy consumption

Because of computer developments, CFD can solve more complex problems, which require more details, and ask for more precision.

Fluent Software

Fluent is a state-of-the-art computer program for modeling fluid flow and heat transfer in complex geometries (Fluent, 2001). It obtains the computational solution in two stages, as shown schematically in Figure 9.

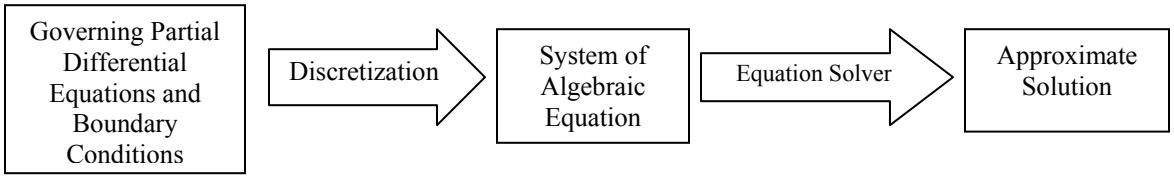

Figure 9. Overview of the computational solution procedure (Fletcher, 1991).

The first stage is discretization where continuous partial differential equations are converted into a discrete system of algebraic equations. In the second stage, a numerical solver is selected to solve a discrete system obtained from the first stage. The solution of the system of algebraic equations is obtained as a consequence.

Discretization

Discretization is a process that converts the governing partial differential equations to a system of algebraic equations. Several techniques are available in CFD software. The most common are finite difference, finite element, finite volume, and spectral methods (Fletcher, 1991).

The finite-volume technique is used in this study. Discretization of the governing equations is demonstrated easily by considering transport of a scalar quantity (ϕ) in the

steady-state conservation equation. The steady-state conservation equation written in integral form for an arbitrary control volume (V) is expressed in Equation 2.

$$\oint \rho\phi\vec{v} \cdot d\vec{A} = \oint \Gamma_\phi \nabla\phi \cdot d\vec{A} + \int_V S_\phi dV \tag{2}$$

where,

ρ = density $\left(\text{kg/m}^3\right)$

$\vec{v}$ = velocity vector $\left(u\hat{i} + v\hat{j}\right)$ $\left(\text{m/s}\right)$

$\vec{A}$ = surface area vector $\left(\text{m}^2\right)$

Γ_ϕ = diffusion coefficient for ϕ $\left(\text{kg/}\left(\text{m} \cdot \text{s}\right)\right)$

$\left(\nabla\phi\right)$ = gradient of ϕ $\left(\left(\frac{\partial\phi}{\partial x}\right)\hat{i} + \left(\frac{\partial\phi}{\partial y}\right)\hat{j}\right)\left(\text{m}^{-1}\right)$

S_ϕ = source of ϕ per unit volume $\left(\text{kg/}\left(\text{m}^3 \cdot \text{s}\right)\right)$

Equation 2 is applied to each control volume, or cell, in the computational domain (Fluent, 2001). Discretization of Equation 13 gives rise to Equation 3.

$$\sum_f^{N_{faces}} \rho_f \vec{v}_f \phi_f \cdot \vec{A}_f = \sum_f^{N_{faces}} \Gamma_\phi \left(\nabla\phi\right)_n \cdot \vec{A}_f + S_\phi V \tag{3}$$

where,

N_{faces} = number of faces enclosing cell

ϕ_f = value of ϕ convected through face f

$\rho_f \vec{v}_f \cdot \vec{A}_f$ = mass flux through the face $\left(\text{kg/s}\right)$

$\vec{A}_f$ = area of face f $\left(\left|A\right| = \left|A_x\right|\hat{i} + \left|A_y\right|\hat{j}\right)$ $\left(\text{m}^2\right)$

$(\nabla\phi)_n$ = magnitude of $\nabla\phi$ normal to face f $\left(\text{m}^{-1}\right)$

V = cell volume $\left(\text{m}^3\right)$

Figure 10 illustrates the discretization of a scalar transport equation by a finite-volume technique.

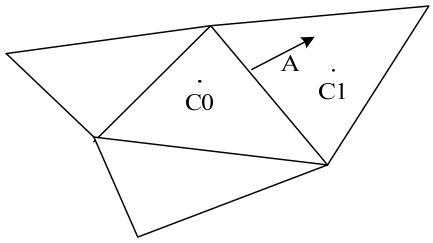

Figure 10. Control volume used to illustrate discretisation of a scalar transport equation (Fluent, 2001).

Discrete values of the scalar ϕ are stored at the cell center (C_o and C_1) in Figure 10. The connection terms in Equation 3 requires face value (ϕ_f). The face value is calculated by using an upwind scheme, whereas the diffusion terms in Equation 2 are central-differenced and second-order accurate.

Upwinding means that the face value (ϕ_f) is calculated from the cell-center value (ϕ) of the cell upstream relative to the direction of the velocity ($\vec{v}_n$) in Equation 3.

There are four upwind schemes available in Fluent:

1. First-Order Upwind
2. Second-Order Upwind
3. Power Law
4. Quick

First-Order Upwind Scheme

The face value (ϕ_f) is set equal to the cell-center value (ϕ) of the upstream cell.

Second-Order Upwind Scheme

The face value (ϕ_f) is calculated by the following equation:

$$\phi_f = \phi + \nabla\phi \cdot \nabla\vec{S} \tag{4}$$

where,

$\nabla\phi$ = gradient of the upstream cell $\left(\mathrm{m}^{-1}\right)$

$\nabla\vec{S}$ = displacement vector from centroid of the upstream cell to its face $\left(\mathrm{m}\right)$

The gradient is evaluated by the divergence theorem, which is written in discrete form as

$$\nabla\phi = \frac{1}{\mathrm{V}} \sum_{f}^{\mathrm{N_{faces}}} \widetilde{\phi}_{\mathrm{f}} \vec{A} \tag{5}$$

where,

$\widetilde{\phi}_f$ = converge face values

The face values ($\widetilde{\phi}_f$) are computed by averaging the cell-center value (ϕ) from two cells adjacent to the face.

Power Law Scheme

The face value (ϕ_f) is interpolated by using the exact solution of a one-dimensional convection diffusion equation

$$\frac{\partial}{\partial x}(\rho u \phi) = \frac{\partial}{\partial x}\Gamma\frac{\partial \phi}{\partial x} \tag{6}$$

where Γ and ρu are constant across the interval ∂x.

Equation 6 is integrated giving rise Equation 7. Equation 7 explains how the cell-center value (ϕ) varies with *x*:

$$\frac{\phi(x)-\phi_o}{\phi_L-\phi_o} = \frac{\exp\left(\mathrm{Pe}\frac{x}{L}\right)-1}{\exp(\mathrm{Pe})-1} \tag{7}$$

where,

ϕ_o = ϕ at the first point

ϕ_L = ϕ at final point

Pe = Peclet number = $\frac{\rho u L}{\Gamma}$

The variation of $\phi(x)$ between *x*=0 and *x*=*L* is demonstrated in Figure 11 for a variety of Peclet numbers.

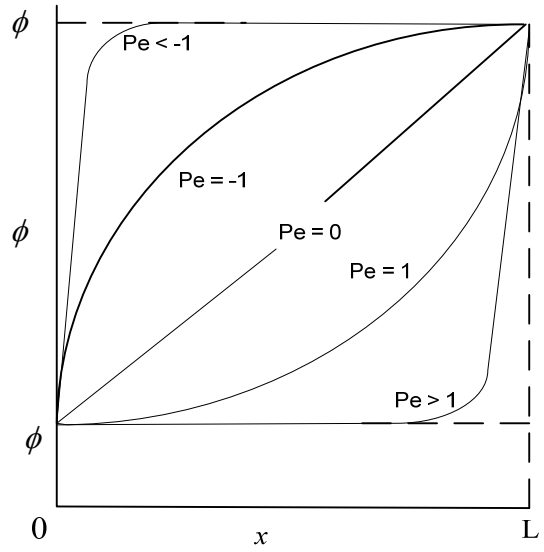

Figure 11. Variation of a variable ϕ between x=0 *and* x=L (Fluent, 2001).

Equation 7 is used as an equivalent "Power Law" format in Fluent, as its interpolation scheme.

Quick Scheme

Quick scheme is based on a weight average of second-order-upwind and central interpolations of the variable. A one-dimensional control volume is displayed in Figure 12.

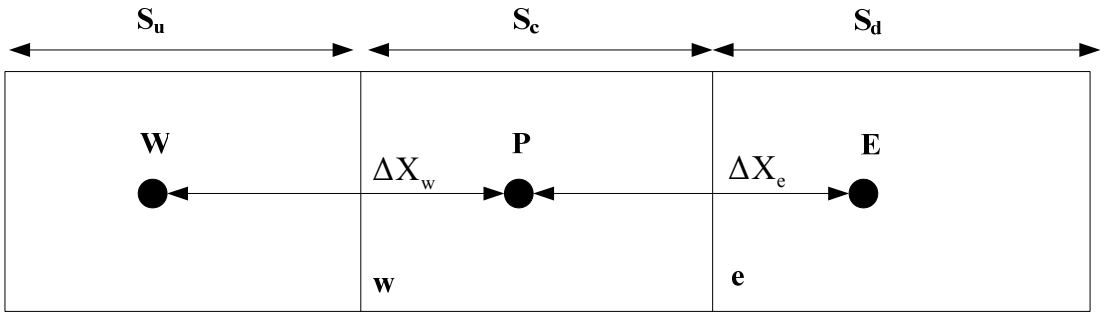

Figure 12. One-dimensional control volume (Fluent, 2001).

For the face *e* in Figure 12, if the fluid flows from left to right, such a value can be written as (Fluent, 2001).

$$\phi_e = \theta\left[\frac{S_d}{S_c + S_d}\phi_P + \frac{S_c}{S_c + S_d}\phi_E\right] + (1-\theta)\left[\frac{S_u + 2S_c}{S_u + S_c}\phi_P - \frac{S_c}{S_u + S_c}\phi_W\right] \qquad (8)$$

Seta (θ) is set at $\frac{1}{8}$ in a conventional quick scheme.

Pressure-Velocity Coupling

In Fluent, there are three options available for the pressure-velocity coupling algorithms, which are

1. SIMPLE; Semi-Implicit Method for Pressure-Linked Equations
2. SIMPLEC; SIMPLE-Consistence
3. PISO; Pressure-Implicit with Splitting of Operators

Because the SIMPLE algorithm is applied in this study, the SIMPLE algorithm is presented further in detail.

SIMPLE

The SIMPLE algorithm uses a relationship between velocity and pressure corrections to enforce mass conservation and to obtain the pressure field. The steady-state continuity and momentum equations in integral form are considered as the first step as shown in Equations 9 and 10, respectively.

$$\oint \rho \vec{v} \cdot d\vec{A} = 0 \tag{9}$$

$$\oint \rho \vec{v}\vec{v} \cdot d\vec{A} = -\oint \rho \phi \vec{I} \cdot d\vec{A} + \oint \bar{\bar{\tau}} \cdot d\vec{A} + \int_V \vec{F} dV \tag{10}$$

where,

$\vec{I}$ = identity matrix

$\bar{\bar{\tau}}$ = stress tensor $\left(\text{kg}/\left(\text{m} \cdot \text{s}^2\right)\right)$

$\vec{F}$ = force vector $\left(\text{N}\right)$

The continuity equation is integrated over the control volume in Figure 10. Equation 9 transforms to Equation 11.

$$\sum_f^{N_{faces}} J_f A_f = 0 \tag{11}$$

where,

J_f = mass flux through face f $\left(\text{kg}/\left(\text{m}^2 \cdot \text{s}\right)\right)$

The mass flux (J_f) is computed by

$$J_f = \hat{J}_f + d_f \left(P_{c0} - P_{c1}\right) \tag{12}$$

where,

$\hat{J}_f$ = mass flux containing the influence of velocities $\left(\text{kg}/\left(\text{m}^2 \cdot \text{s}\right)\right)$

d_f = a function of momentum equation on either side of f $\left(\text{s}/\text{m}\right)$

P_{c0} = pressure in cell C_0 on either side of the face $\left(\text{kg}/\left(\text{m} \cdot \text{s}^2\right)\right)$

P_{c1} = pressure in cell C_1 on either side of the face $\left(\text{kg}/\left(\text{m} \cdot \text{s}^2\right)\right)$

If the momentum equation is solved by using a guessed pressure field (P^*), Equation 12 will be modified to Equation 13.

$$J_f^* = \hat{J}_f^* + d_f\left(P_{c0}^* - P_{c1}^*\right) \tag{13}$$

However, the resulting face flux (J_f^*) does not satisfy the continuity equation. Therefore, a correction $J_f^{'}$ is added to the resulting face flux to satisfy the continuity equation as shown in Equation 14.

$$J_f = J_f^* + J_f^{'} \tag{14}$$

The SIMPLE algorithm postulates that the correction ($J_f^{'}$) can be written as (Fluent, 2001).

$$J_f^{'} = d_f\left(P_{c0}^{'} - P_{c1}^{'}\right) \tag{15}$$

where,

$P^{'}$ = the cell pressure correction $\left(\text{kg}/\left(\text{m}\cdot\text{s}^2\right)\right)$

When a solution is obtained, the face flux and the cell pressure are interpolated using Equation 16 and 17 respectively.

$$J_f = J_f^* + d_f\left(P_{c0}^{'} - P_{c1}^{'}\right) \tag{16}$$

$$P = P^* + \alpha_P P^{'} \tag{17}$$

where,

α_P = the under-relaxation factor for pressure

Ultimately, the corrected face flux (J_f) satisfies the discrete continuity equation. Equation 16 presents the corrected face flux which satisfies the discrete continuity equation during iteration.

Equation Solver

Equation solver is applied in the step of solving the system of algebraic equations to obtain an approximate solution as shown in Figure 9.

Fluent provides two different equation solvers:

1. Segregated solver
2. Coupled solver

These two alternatives are used to solve the continuity, momentum, energy, and species equation. The segregated solver solves these equations segregated from one another. But the coupled solver solves them coupled together. Regardless of the types of solvers, the control-volume technique is always applied. The procedure is explained below:

1. Divide the domain into discrete control volumes by using a computational grid
2. Integrate the governing equations on the individual control volumes to generate algebraic equations for the dependent variable such as velocities, pressure, temperature, and conserved scalar quantities.
3. Linearize the discretized equations and the resultant linear equation system to updated values of the dependent variables.

Segregated Solver

The segregated solver solves the governing equation separately. Each iteration step is presented in Figure 13 and is explained below.

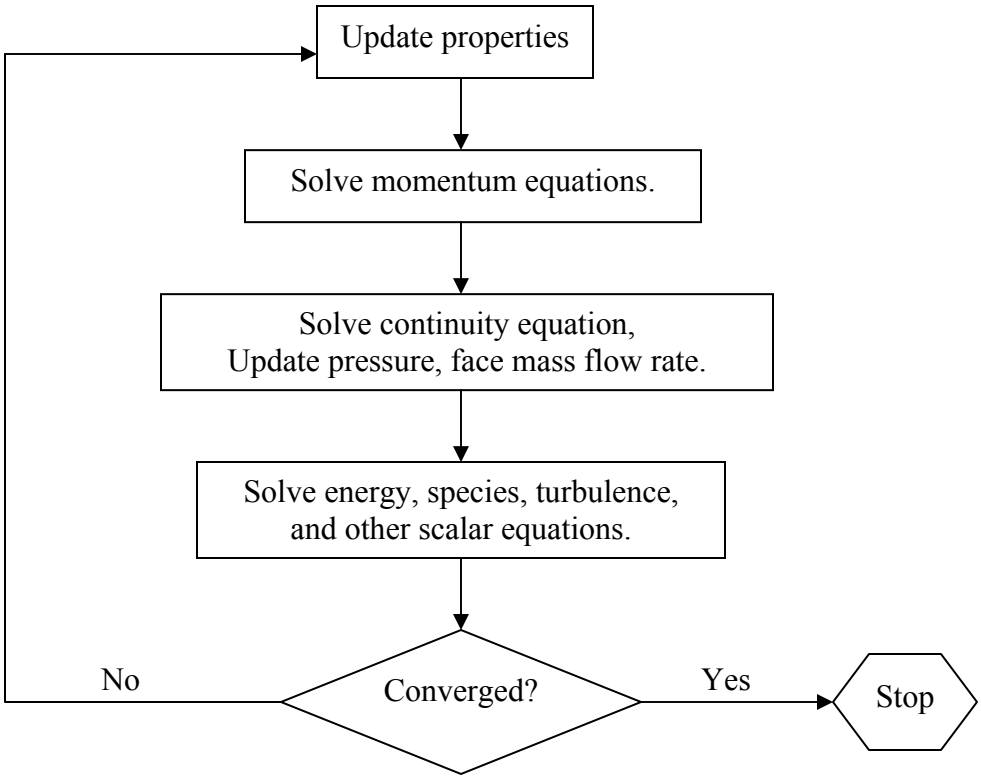

Figure 13. Procedure of the segregated solver.

1. Update fluid properties, based on the current solution. For the first iteration, the fluid properties will be updated from an initialized solution.
2. Solve momentum equations by using current values for pressure and face mass fluxes for updating the velocity field.

3. Solve the continuity equation to update, pressure, velocity fields and the face mass fluxes.
4. Solve equations for scalar quantities, such as turbulence, energy, species, and radiation by using the previously updated values of the other variables.
5. (Optional) Update the source terms in the appropriate continuous phase equations with a discrete phase trajectory calculation.
6. Check for convergence condition.

Coupled Solver

The governing equations of continuity, momentum, energy, and species transport are solved simultaneously in the coupled solver; whereas, the governing equations for additional scalars will be solved segregated from one another. Each iteration step is shown in Figure 14 and explained below.

1. Update fluid properties, based on the current solution. For the first iterations, the fluid properties will be updated based on an initialized solution.
2. Solve the continuity, momentum, energy, and species equations simultaneously.
3. Solve equations for scalars, such as turbulence and radiation by using the previously updated values of the other variables.
4. (Optional) Update the source terms in the appropriate continuous phase equations with a discrete phase trajectory calculation.
5. Check for convergence condition.

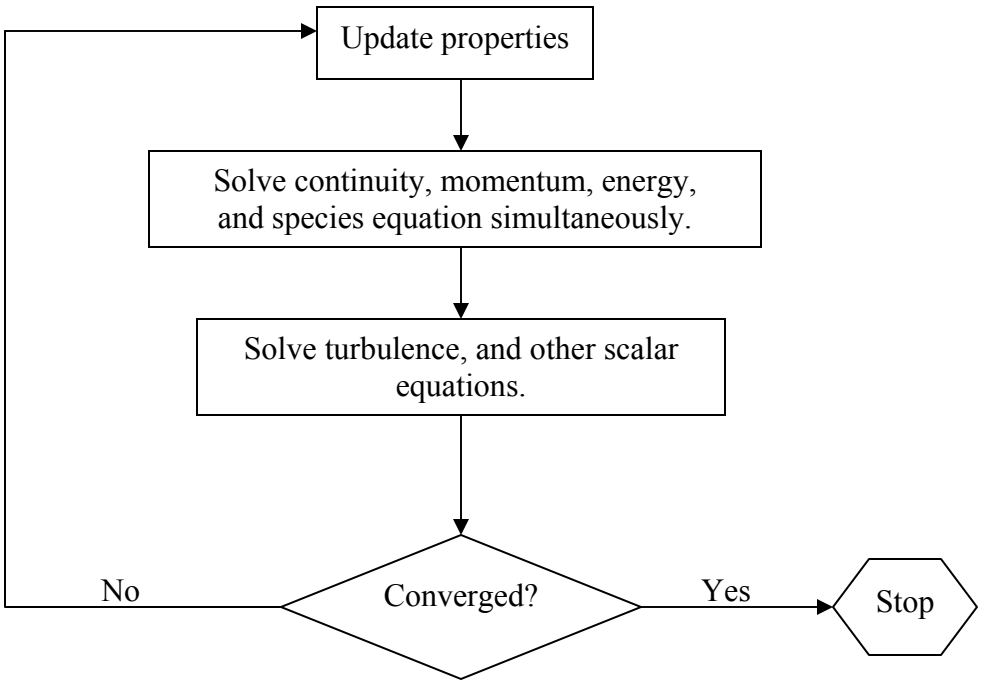

Figure 14. Procedure of the coupled solver.

Turbulence Modeling

Fluid flow with a very high velocity and high Reynolds number is called turbulent flow. Because the jet ejector motive stream is turbulent, a turbulence model must be considered for calculating fluid properties in Fluent.

In turbulent flow, velocity fields fluctuate. These fluctuations mix with transport quantities such as momentum, energy, and species concentration; consequently, the transport quantities fluctuate as well. The exact governing equation; however, can be time-averaged or ensemble-averaged to cancel the small fluctuations. A modified set of equations is created from this operation. Unknown variables are generated in the modified

equations, and these variables are determined as known quantities by using the turbulence model.

In Fluent, there are five turbulence models available:

1. Spalart-Allmaras model
2. *k*-*ε* models
    - Standard *k*-*ε* model
    - Renormalization-group (RNG) *k*-*ε* model
    - Realizable *k*-*ε* model
3. *k*-*ω* models
    - Standard *k*-*ω* model
    - Shear-stress transport (SST) *k*-*ω* model
4. Reynolds stress model (RSM)
5. Large eddy simulation (LES) model

The advantages and disadvantages of each model are described in the following section. Also, the reasons for selecting the standard *k*-*ε* model are addressed. Finally, the mathematical algorithm of standard *k*-*ε* is presented.

Because there is no single model that is universally accepted for all classes of problems, the choice of turbulence model depends on considerations such as the physics encompassed in the flow, the established practice for a specific class of problem, the level of accuracy required, the available computational resources, and the amount of time available for the simulation.

Spalart-Allmaras Model

Spalart-Allmaras model is mainly applied to aerospace applications. The model involves wall-bounded flows and gives good results for boundary layers subjected to adverse pressure gradients. It is popular in turbo-machinery applications. Because the near-wall gradients of the transported variables in the model are much smaller than the ones in k-ε or k-ω models, the model is less sensitive to numerical error.

Standard k-ε Model

Standard k-ε model is considered the simplest "complete model" of turbulence. This model is widely used in industrial flow simulation due to robustness, economy, and reasonable accuracy for a wide range of turbulent flows. It is the workhorse of practical engineering flow calculations.

Renormalization-Group (RNG) k-ε Model

The RNG model is improved from the standard k-ε model by using a rigorous statistical technique. It is similar to the standard k-ε model, but includes the following refinements:

1. An additional term in its ε equation is added that significantly improves the accuracy for rapidly strained flows.
2. The effect of swirl on turbulence is included, enhancing accuracy for swirling flows.
3. An analytical formula for turbulent Prandtl numbers is provided

4. An analytically derived differential formula for effective viscosity is provided, so low-Reynolds-number is accounted for.

These features produce more reliability and accuracy in the model than the standard *k-ε* model. However, these additional features are not required in this study.

Realizable k-ε Model

The realizable *k-ε* model is different from the standard *k-ε* model in two important ways:

1. It contains a new formula for turbulent viscosity.
2. The transport of the mean-square vorticity fluctuation is included in this model.

This model provides superior performance for flow involving rotation, boundary layers under strong adverse pressure gradients, separation, and recirculation. Because the fluid flow in a jet ejector does not require any above additional features, this model is not applied.

Standard k-ω Model

Standard *k-ω* model is derived for low-Reynolds-number flow, compressibility, and shear flow spreading. In our problem, the Reynolds number is very high especially at the nozzle, so this model is not selected.

Shear-Stress Transport (SST) k-ω Model

SST *k-ω* model is created to blend the robust and accurate formulation of the *k-ω* model in the near-wall region effectively with the free-stream independence of the *k-ε* model in the far field.

The SST *k-ω* model is close to the standard *k-ω* model, but includes the following additional refinements:

1. A blending function is formulated by multiplying both the standard *k-ω* model and the transformed *k-ε* model. The blending function is designed to be one in the near-wall region, and zero away from the surface.
2. A damped cross-diffusion derivative term in the *ω* equation is accounted in the SST *k-ω* model.
3. The transport of the turbulent shear stress is accounted by modifying the definite of the turbulent viscosity.

The SST *k-ω* model is more accurate and reliable than the standard *k-ω* model due to these features, and it is applied for low-Reynolds-number flow only.

Reynolds Stress Model (RSM)

RSM is designed for the effects of streamline curvature, swirl, rotation, and rapid changes in strain rate. The examples relating to these flow characteristics are cyclone flow, highly swirling flow in combustor, rotating flow passage, and the stress-induced secondary flows in duct.

Large Eddy Simulation Model (LES)

The LES model is used for unsteady-state, high-Reynolds-number turbulent flow in complex geometries. The strength of this model is that an error included by the turbulence model is small; however, it requires the large computational resources to resolve the energy-containing turbulent eddies.

CPU Time and Solution Behavior

The relative CPU time required for each model is summarized in Table 4.

Table 4. Comparison of CPU time consuming of each turbulence model.

Turbulence Model	CPU Time Requirement
S-A	1 (least)
Standard k-ε	2
Standard k-ω	2
Realizable k-ε	3
RNG k-ε	4
SST	4
RSM	5
LES	6 (most)

Due to an additional transport equation, the standard k-ε model requires more computational effort than the Spalart-Allmaras model. The realizable k-ε model requires slightly higher CPU resource than the standard k-ε model. The RNG k-ε model needs 10 –

15% more computational effort than the standard *k-ε* model. The *k-ω* models require almost the same CPU resource as the *k-ε* models. On average, RSM requires 50 – 60% more computational effort compared to the *k-ε* and *k-ω* models and 15 – 20% more memory is required.

. Because of finite computational resources and the flow behavior in jet ejectors does not require the RSM and LES models, the standard *k-ε* model is the best compared to other schemes, so the standard *k-ε* model was applied throughout the study.

Mathematical Algorithm of the Standard k-ε Model

The standard *k-ε* model is a semi-empirical model for turbulent kinetic energy, *k*, and its dissipation rate, *ε*. The model assumes that the effects of molecular viscosity are negligible and the flow is fully turbulent.

The turbulence kinetic energy, *k*, and its dissipation rate, *ε*, are calculated from

$$\frac{\partial}{\partial t}(\rho k)+\frac{\partial}{\partial x_i}(\rho k v_i)=\frac{\partial}{\partial x_j}\left[\left(\mu+\frac{\mu_t}{\sigma_k}\right)\frac{\partial k}{\partial x_j}\right]+G_k+G_b-\rho\varepsilon-Y_M+S_k \qquad (18)$$

and

$$\frac{\partial}{\partial t}(\rho \varepsilon)+\frac{\partial}{\partial x_i}(\rho \varepsilon v_i)=\frac{\partial}{\partial x_j}\left[\left(\mu+\frac{\mu_t}{\sigma_\varepsilon}\right)\frac{\partial \varepsilon}{\partial x_j}\right]+C_{1\varepsilon}G_k\frac{\varepsilon}{k}-C_{2\varepsilon}\rho\frac{\varepsilon^2}{k}+S_\varepsilon \qquad (19)$$

where,

t = time (s)

ρ = density $(\mathrm{kg/m^3})$

k = turbulence kinetic energy $((\mathrm{J\cdot m^3})/\mathrm{kg})$

v = velocity $(\mathrm{m/s})$

x = distance (m)

μ = viscosity $(\mathrm{kg/(m \cdot s)})$

μ_t = turbulence viscosity $(\mathrm{kg/(m \cdot s)})$

G_k = generation of turbulence kinetic energy due to the mean velocity gradients (J)

G_b = generation of turbulence kinetic energy due to buoyancy force (J)

ε = rate of dissipation rate $((\mathrm{J \cdot m^3})/(\mathrm{kg \cdot s}))$

Y_M = contribution of the fluctuating dilation in compressible turbulence to the overall dissipation (J)

$C_{1\varepsilon}$ = model constant = 1.44

$C_{2\varepsilon}$ = model constant = 1.92

σ_k = turbulent Prandtl number for k = 1.0

σ_ε = turbulent Prandtl number for ε = 1.3

S_k = user-defined source term for k (J)

S_ε = user-defined source term for ε (J)

μ_t = turbulent viscosity $(\mathrm{kg/(m \cdot s)})$

Turbulent viscosity is calculated by Equation 8.

$$\mu_t = \rho C_\mu \frac{k^2}{\varepsilon} \tag{20}$$

where,

C_μ = model constant = 0.09

Dimensionless Forms of Fluid Transport Equations

Dimensionless quantities are universal, and independent of operating variables, such as fluid, geometric scale, operating pressure, etc. Therefore, all parameters in the research are converted to the dimensionless terms. The objective of this section is to demonstrate that the fluid transport equations can be transformed into dimensionless forms. This confirms that the dimensionless principle can relate to the research. The fluid transport equations such as the mass (continuity), momentum, and energy conservation equations are demonstrated in this section.

The mass conservation equation, or continuity equation, for the compressible flow is:

$$\frac{\partial \rho}{\partial t} + \overline{\nabla} \cdot \left(\rho \, \bar{v}\right) = 0 \tag{21}$$

where,

ρ = fluid density $\left(\text{kg/m}^3\right)$

t = time $\left(\text{s}\right)$

$\bar{v}$ = fluid velocity in a vector notation $\left(\text{m/s}\right)$

$\overline{\nabla}$ = gradient operator

Momentum conservation for compressible flow in vector notation is (Happel and Brenner, 1965).

$$\rho\frac{Dv}{Dt} = -\overline{\nabla}P_{static} + \mu\nabla^2\overline{v} + 2\overline{\nabla}\mu\cdot\overline{\nabla}\overline{v} + \overline{\nabla}\mu\times\left(\overline{\nabla}\times\overline{v}\right) + \frac{1}{3}\mu\overline{\nabla}\left(\overline{\nabla}\cdot\overline{v}\right)$$

$$-\frac{2}{3}\left(\overline{\nabla}\cdot\overline{v}\right)\overline{\nabla}\mu + K\overline{\nabla}\left(\overline{\nabla}\cdot\overline{v}\right) + \left(\overline{\nabla}\cdot\overline{v}\right)\overline{\nabla}K + \rho\ g + j\times\overline{B} \qquad (22)$$

where,

$\frac{D}{Dt}$ = material derivation

P_{static} = static pressure $\left(\text{Pa}\right)$

μ = fluid viscosity $\left(\text{N}\cdot\text{m}\right)$

∇^2 = LaPlacian operator

K = bulk viscosity $\left(\text{N}\cdot\text{m}\right)$

g = acceleration due to gravity $\left(\text{m/s}^2\right)$

j = current

$\overline{B}$ = magnetic field

The effects of K on fluid dynamics are difficult to detect and usually ignored (Deen, 1998). Also, there is no magnetic field in our system, so the final term is negligible. To simplify Equation 22, the dynamic pressure term is introduced to replace the static

pressure and the gravity force term in the equation. The relationship of the dynamic pressure can be written as (Deen, 1998):

$$\overline{\nabla} P_{dynamic} = \overline{\nabla} P_{static} - \rho\ \bar{g} \tag{23}$$

where,

$$P_{dynamic} = \text{dynamic pressure } (\text{Pa})$$

So Equation 22 converts to Equation 24.

$$\rho \frac{Dv}{Dt} = -\overline{\nabla} P_{dynamic} + \mu \nabla^2 \bar{v} + 2\overline{\nabla}\mu \cdot \overline{\nabla}\bar{v} + \overline{\nabla}\mu \times \left(\overline{\nabla} \times \bar{v}\right) + \frac{1}{3}\mu \overline{\nabla}\left(\overline{\nabla} \cdot \bar{v}\right) - \frac{2}{3}\left(\overline{\nabla} \cdot \bar{v}\right)\overline{\nabla}\mu \tag{24}$$

The material derivation on the left-hand side is equivalent to Equation 25.

$$\rho \frac{Dv}{Dt} = \frac{\partial}{\partial t}\left(\rho\ \bar{v}\right) + \overline{\nabla} \cdot \left(\rho\ \bar{v}\bar{v}\right) \tag{25}$$

Equation 24 is substituted by Equation 25 and becomes Equation 26, which is the dimensional form of the momentum conservation equation.

$$\frac{\partial}{\partial t}\left(\rho\ \bar{v}\right) + \overline{\nabla} \cdot \left(\rho\ \bar{v}\bar{v}\right) = -\overline{\nabla} P_{dynamic} + \mu \nabla^2 \bar{v} + 2\overline{\nabla}\mu \cdot \overline{\nabla}\bar{v} + \overline{\nabla}\mu \times \left(\overline{\nabla} \times \bar{v}\right) + \frac{1}{3}\mu \overline{\nabla}\left(\overline{\nabla} \cdot \bar{v}\right) - \frac{2}{3}\left(\overline{\nabla} \cdot \bar{v}\right)\overline{\nabla}\mu \tag{26}$$

The Mass Conservation Equation (Continuity Equation)

A general form of the mass conservation equation in case of without any external force is

$$\frac{\partial \rho}{\partial t} + \overline{\nabla} \cdot \left(\rho\ \bar{v}\right) = 0 \tag{21}$$

The characteristic density and velocity are introduced to transform Equation 21 to the dimensionless form.

Define:

ρ_c = characteristic density = an inlet density of the fluid $\left(\text{kg/m}^3\right)$

U = characteristic velocity = an inlet velocity of the fluid $\left(\text{m/s}\right)$

t_c = characteristic time $\left(\text{s}\right)$

With dimensionless variables and differential operators defined as (Deen, 1998):

$$\tilde{\rho}=\frac{\rho}{\rho_c}, \quad \tilde{v}=\frac{\bar{v}}{\bar{U}}, \quad \tilde{t}=\frac{t}{t_c}, \quad \tilde{\nabla}=\bar{\nabla}L \tag{27}$$

where,

L = characteristic length = an inlet diameter of ejector $\left(\text{m}\right)$

For Equation 27, each term is converted to dimensionless form by multiplying and dividing each term by their characteristic parameters, and then rearranging the equation to the dimensionless parameters. Consequently, the dimensionless form of Equation 21 is presented in Equation 28.

$$\frac{\partial\tilde{\rho}}{\partial\tilde{t}}+\tilde{\nabla}\left(\tilde{\rho}\,\tilde{v}\right)= \quad 0 \tag{28}$$

The Momentum Conservation Equation

The general form of the momentum conservation equation is presented in Equation 26, which is

$$\frac{\partial}{\partial t}\left(\rho\ \bar{v}\right)+\bar{\nabla}\cdot\left(\rho\ \bar{v}\bar{v}\right)=-\bar{\nabla}P_{dynamic}+\mu\nabla^2\bar{v}+2\bar{\nabla}\mu\cdot\bar{\nabla}\bar{v}+\bar{\nabla}\mu\times\left(\bar{\nabla}\times\bar{v}\right)$$

$$+\frac{1}{3}\mu\bar{\nabla}\left(\bar{\nabla}\cdot\bar{v}\right)-\frac{2}{3}\left(\bar{\nabla}\cdot\bar{v}\right)\bar{\nabla}\mu \qquad (26)$$

The characteristic dynamic pressure and viscosity are additionally defined from the continuity equation in this case.

Define:

$$\prod = \text{characteristic dynamic pressure} = \frac{1}{2}\rho_c U^2\ \left(\text{Pa}\right)$$

$$\mu_c = \text{characteristic viscosity} = \text{inlet viscosity of the fluid}\ \left(\text{N}\cdot\text{m}\right)$$

Consequently, additional dimensionless variables and differential operators from Equation 26 are specified, which are

$$\tilde{P} = \frac{P_{dynamic}}{\prod},\quad \tilde{\mu}=\frac{\mu}{\mu_c},\quad \tilde{\nabla}^2=L^2\bar{\nabla}^2 \qquad (29)$$

The same procedure as the continuity equation is applied at this stage to transform Equation 26. The dimensionless form of the momentum conservation equation is Equation 30.

$$\left(\frac{\rho_c U}{t_c}\right)\frac{\partial}{\partial\tilde{t}}\left(\tilde{\rho}\ \tilde{v}\right)+\left(\frac{\rho_c U^2}{L}\right)\tilde{\nabla}\left(\tilde{\rho}\ \tilde{v}\tilde{v}\right)$$

$$=-\frac{\prod}{L}\tilde{\nabla}\tilde{P}+\left(\frac{\mu_C U}{L^2}\right)\left[\begin{array}{r}\tilde{\mu}\tilde{\nabla}^2\tilde{v}+2\tilde{\nabla}\tilde{\mu}\cdot\tilde{\nabla}\tilde{v}+\tilde{\nabla}\tilde{\mu}\times\left(\tilde{\nabla}\times\tilde{v}\right)\\ +\frac{1}{3}\tilde{\mu}\tilde{\nabla}\left(\tilde{\nabla}\cdot\tilde{v}\right)-\frac{2}{3}\left(\tilde{\nabla}\cdot\tilde{v}\right)\tilde{\nabla}\tilde{\mu}\end{array}\right] \qquad (30)$$

Equation 31 was multiplied by $\left(\frac{L^2}{\mu_c U}\right)$ gives to Equation 31.

$$\left(\frac{\rho_c U}{t_c}\right)\times\left(\frac{L^2}{\mu_c U}\right)\frac{\partial}{\partial\tilde{t}}\left(\tilde{\rho}\ \tilde{v}\right)+\left(\frac{\rho_c U^2}{L}\right)\times\left(\frac{L^2}{\mu_c U}\right)\tilde{\nabla}\left(\tilde{\rho}\ \tilde{v}\tilde{v}\right)\cdot$$

$$=-\frac{\prod}{L}\times\left(\frac{L^2}{\mu_c U}\right)\tilde{\nabla}\tilde{P}+\left[\begin{array}{r}\tilde{\mu}\tilde{\nabla}^2\tilde{v}+2\tilde{\nabla}\tilde{\mu}\cdot\tilde{\nabla}\tilde{v}+\tilde{\nabla}\tilde{\mu}\times\left(\tilde{\nabla}\times\tilde{v}\right)\\ +\frac{1}{3}\tilde{\mu}\tilde{\nabla}\left(\tilde{\nabla}\cdot\tilde{v}\right)-\frac{2}{3}\left(\tilde{\nabla}\cdot\tilde{v}\right)\tilde{\nabla}\tilde{\mu}\end{array}\right] \quad (31)$$

Each dimensionless term in Equation 31 is replaced by the dimensionless parameters presented below.

$$Re=\frac{\rho\, UL}{\mu_c},\quad St=\frac{t_c U}{L}$$

where,

Re = Reynolds number

St = Strouhal number

Therefore, the dimensionless term of the momentum conservation energy is presented in Equation 32.

$$Re\left[\frac{1}{Sr}\frac{\partial}{\partial\tilde{t}}\left(\tilde{\rho}\ \tilde{v}\right)+\tilde{\nabla}\left(\tilde{\rho}\ \tilde{v}\tilde{v}\right)\cdot\right]$$

$$=-\left(\frac{\prod L}{\mu_c U}\right)\tilde{\nabla}\tilde{P}+\left[\begin{array}{r}\tilde{\mu}\tilde{\nabla}^2\tilde{v}+2\tilde{\nabla}\tilde{\mu}\cdot\tilde{\nabla}\tilde{v}+\tilde{\nabla}\tilde{\mu}\times\left(\tilde{\nabla}\times\tilde{v}\right)\\ +\frac{1}{3}\tilde{\mu}\tilde{\nabla}\left(\tilde{\nabla}\cdot\tilde{v}\right)-\frac{2}{3}\left(\tilde{\nabla}\cdot\tilde{v}\right)\tilde{\nabla}\tilde{\mu}\end{array}\right] \quad (32)$$

Compressible Flow

Compressible flow occurs when the flow velocity is over Mach 0.3. In compressible flow, the pressure gradient is large; the variation of the gas density with pressure has a significant impact on the flow velocity, pressure, and temperature (Fluent, 2001).

In the research, the motive stream has the same behavior as compressible flow, because the motive stream flows out from the nozzle exit at supersonic velocity. The basic equation in compressible flow and the fluid transport equations are summarized in this section.

Basic Equations for Compressible Flows

The equations to calculate pressure and temperature in compressible flow are demonstrated, respectively. Both of them are expressed as a function of Mach number. The isentropic condition is applied in the equation.

$$\frac{P_o}{P} = \left(1 + \frac{\gamma - 1}{2} M^2\right)^{\frac{\gamma}{\gamma - 1}} \tag{33}$$

and

$$\frac{T_o}{T} = \left(1 + \frac{\gamma - 1}{2} M^2\right)^{\frac{\gamma}{\gamma - 1}} \tag{34}$$

where,

P_o = total pressure (Pa)

P = static pressure (Pa)

T_0 = total temperature (K)

T = static temperature (K)

γ = specific heat capacity ratio

M = Mach number

In compressible flow, fluid density changes as a function of pressure and temperature. For an ideal gas law, the fluid density can be calculated by Equation 35.

$$\rho = \frac{\left(P_{op} + P\right)}{\frac{R}{M_w}T} \tag{35}$$

where,

ρ = fluid density $\left(\mathrm{kg/m^3}\right)$

P_{op} = operating pressure (Pa)

P = local static pressure (Pa)

R = universal gas constant = 8.314 $\mathrm{J/(gmol \cdot K)}$

T = temperature (K)

MW = molecular weight $(\mathrm{g/gmol})$

The Mass Conservation Equation (The Continuity Equation)

According to Deen (1998), a general accounting equation is

$$\frac{\partial b}{\partial t} + \overline{\nabla} \cdot (bv) = -\overline{\nabla} \cdot f + B_V \tag{36}$$

where,

b = concentration of some quantity (per unit volume)

t = time (s)

$\overline{\nabla}$ = gradient operator

v = fluid velocity $(\mathrm{m/s})$

f = diffusive part of the flux of that quantity

B_V = rate of formation of the quantity per unit volume

In the continuity equation, the concentration variable is the total mass density, so b is replaced by fluid density. Because there is no net flow relative to the mass-average velocity, the diffusive flux for total mass is canceled $(f = 0)$ (Deen, 1998). Additionally, there are no mass sources or sinks in the jet ejector, so B_V is zero.

Thus, Equation 36 reduces to Equation 37.

$$\frac{\partial \rho}{\partial t} + \overline{\nabla} \cdot (\rho\, v) = 0 \tag{37}$$

The local mass conservation equation is called the mass continuity equation. In 2-D axi-symmetric geometry, the continuity equation is:

$$\frac{\partial \rho}{\partial t} + \frac{\partial}{\partial x}(\rho\ \bar{v}_x) + \frac{\partial}{\partial r}(\rho\ \bar{v}_r) + \frac{\rho\ \bar{v}_r}{r} = 0 \tag{38}$$

In Equation 38, x is the axial coordinate, r is the radial coordinate, $\bar{v}$ is the fluid velocity.

The Momentum Conservation Equation

From the governing conservation equation, the governing momentum conservation equation can be derived by the following step. Initially, *b* is substituted by momentum term ($\rho \bar{v}$) whereas the diffusive flux term (*f*) is replaced by the static pressure, the stress tensor and gravitational body force. In the jet ejector, the rate of formation B_v is zero. Consequently, the governing momentum conservation equation is presented in Equation 39.

$$\frac{\partial}{\partial t}\left(\rho\ \bar{v}\right)+\bar{\nabla}\cdot\left(\rho\ \bar{v}\bar{v}\right)=-\bar{\nabla}P+\bar{\nabla}\cdot\left(\bar{\bar{\tau}}\right)+\rho\ \bar{g} \tag{39}$$

where,

P = static pressure $\left(\text{Pa}\right)$

$\bar{\bar{\tau}}$ = stress tensor $\left(\text{J}\right)$

g = force per unit from gravity $\left(\text{m/s}^2\right)$

The stress tensor ($\bar{\bar{\tau}}$) for the compressible flows is presented in Equation 40.

$$\bar{\bar{\tau}}=\mu\left[\left(\bar{\nabla}\dot{v}+\bar{\nabla}\bar{v}^{T}\right)-\frac{2}{3}\bar{\nabla}\cdot\bar{v}I\right] \tag{40}$$

where,

μ = fluid viscosity $\left(\left(\text{kg}\cdot\text{m}^2\right)/\text{s}^2\right)$

I = unit tensor

For 2-D axi-symmetric geometry, the momentum conservation equations in axial and radial coordinates are presented in Equations 41 and 42, respectively (Deen, 1998).

In axial coordinate:

$$\frac{\partial}{\partial t}(\rho \bar{v}_x) + \frac{1}{r}\frac{\partial}{\partial x}(r\rho \bar{v}_x \bar{v}_x) + \frac{1}{r}\frac{\partial}{\partial r}(r\rho \bar{v}_r \bar{v}_x) = -\frac{\partial P}{\partial x} + \frac{1}{r}\frac{\partial}{\partial x}\left[r\mu\left(2\frac{\partial \bar{v}_x}{\partial x} - \frac{2}{3}(\bar{\nabla} \cdot \bar{v})\right)\right] + \frac{1}{r}\frac{\partial}{\partial r}\left[r\mu\left(\frac{\partial \bar{v}_x}{\partial r} + \frac{\partial \bar{v}_r}{\partial x}\right)\right] \quad (41)$$

In radial coordinate:

$$\frac{\partial}{\partial t}(\rho \bar{v}_r) + \frac{1}{r}\frac{\partial}{\partial x}(r\rho \bar{v}_x \bar{v}_r) + \frac{1}{r}\frac{\partial}{\partial r}(r\rho \bar{v}_r \bar{v}_r) = -\frac{\partial P}{\partial r} + \frac{1}{r}\frac{\partial}{\partial}\left[r\mu\left(\frac{\partial \bar{v}_x}{\partial r} + \frac{\partial \bar{v}_r}{\partial x}\right)\right] + \frac{1}{r}\frac{\partial}{\partial r}\left[r\mu\left(2\frac{\partial \bar{v}_r}{\partial r} - \frac{2}{3}(\bar{\nabla} \cdot \bar{v})\right)\right] - 2\mu\frac{\bar{v}_r}{r^2} + \frac{2}{3}\frac{\mu}{r}(\bar{\nabla} \cdot \bar{v}) + \rho\frac{\bar{v}_z^2}{r} \quad (42)$$

where,

$$\bar{\nabla} \cdot \bar{v} = \frac{\partial \bar{v}_x}{\partial x} + \frac{\partial \bar{v}_r}{\partial r} + \frac{\bar{v}_r}{r} \quad (43)$$

The Energy Equation

In compressible fluid, the energy equation is used corporately with the transported equations to calculate fluid properties. The governing energy equation is presented in Equation 44 (Fluent, 2001).

$$\frac{\partial}{\partial t}(\rho\ E) + \bar{\nabla} \cdot (\bar{v}(\rho\ E + p)) = \bar{\nabla} \cdot \left(k_{eff}\bar{\nabla}T - \sum_j h_j \bar{J}_j + (\bar{\bar{\tau}}_{eff}\bar{v})\right) + S_h \quad (44)$$

where,

E = internal energy (J)

k_{eff} = effective conductivity $(\mathrm{J/K})$

∇T = total temperature difference (K)

h_i = sensible enthalpy of species j (J)

$\bar{J}_j$ = diffusion flux of species j (J)

$\bar{\bar{\tau}}_{eff}$ = effective viscous dissipation $((\mathrm{J \cdot s})/\mathrm{m})$

S_h = volumetric heat sources (J)

The effective conductivity (k_{eff}) is a combination of the turbulent thermal conductivity and the conventional heat conductivity, whereas the internal energy is evaluated by

$$E = h - \frac{p}{\rho} + \frac{v^2}{2} \tag{45}$$

where,

h = sensible enthalpy (J)

The sensible enthalpy is defined for ideal gases as

$$h = \sum_j Y_j h_j \tag{46}$$

where,

Y_j = mass fraction of species j

h_j = sensible enthalpy of species j (J)

The sensible enthalpy of species j can be calculated by

$$h_j = \int_{T_{ref}}^{T} c_{P,j} dT \tag{47}$$

where T_{ref} is 298.15 K.

The viscous dissipation term is energy created by viscous shear force in the flow field, whereas the energy source term is negligible in the system.

All the equations stated above are used to calculate fluid properties in Fluent.

CHAPTER IV

MODEL VERIFICATION

Introduction

This chapter presents results of an experimental investigation and computational fluid dynamics (CFD) analysis of a constant-area jet ejector using air as the working fluid. Recently, CFD has been recognized as a powerful technique for simulating flow and calculating fluid properties (pressure, temperature, velocity, etc.). This paper begins with CFD model development and discreatation. In this stage, a study is conducted to provide the best CFD model with the most accurate results with the least computer time. The best CFD model was applied throughout the study to verify the accuracy and consistency of CFD results with experimental data from the jet ejector. With the same ejector geometry and operating conditions, the resulting deviation was expressed by comparing the mass flow rate of the experimental propelled stream to the CFD analysis for the same compression ratio. The nozzle exit velocity of the motive stream was 411 to 563 m/s, the propelled stream mass flow rate was 0.23 to 0.65 kg/s, and the compression ratio was 1.001 to 1.028.

By comparing CFD results to the experiment, CFD analysis showed high accuracy without the need for adjustable parameters. The overall deviation was 8.19%, thus confirming the CFD model as a highly reliable technique that is suitable for further studies on jet ejectors.

The ultimate objective of this dissertation is to optimize the efficiency of jet ejectors using CFD analysis. The main objective of this chapter is to present results of experimental

and numerical (CFD) analysis of a constant-area jet ejector that uses air as the working fluid. By ensuring that the CFD model properly represents reality, it makes the subsequent CFD optimizations more meaningful.

Methodology

Jet Ejector Experiment

Compressed air flowed through the nozzle system shown in Figure 15. The temperature and pressure were measured at the nozzle inlet and outlet (Table 5). The stagnation pressure P_{stag} was measured by inserting a pitot tube into the flowing gas stream exiting the nozzle shown in Figure 15. From these values, the velocity of the motive stream exiting the nozzle was calculated by using the compressible flow velocity Equation 48 (Vishwannathappa, 2001).

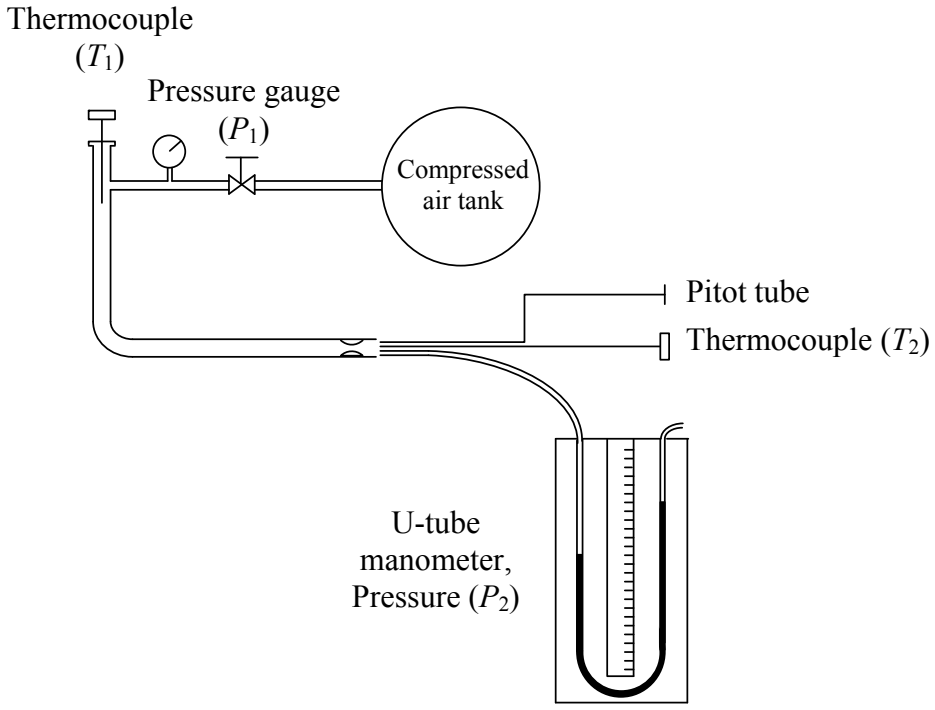

Figure 15. Experimental apparatus for measuring the nozzle efficiency.

where,

T_1 = nozzle inlet absolute temperature (K)

T_2 = nozzle outlet absolute temperature (K)

Table 5. Data obtained at the inlet and outlet of the nozzle (Figure 15).

Case	P_1 **(Pa)**	T_1 **(K)**	P_2 **(Pa)**	T_2 **(K)**	**Density (kg/m^3)**	v_1 **(m/s)**	$v_2 = v_m$ **(m/s)**	m_m **(kg/s)**	**Nozzle efficiency** η_N **(%)**
1	896,300	306	379,200	288	1.25	722	563	0.020	94.02
2	758,400	305	310,300	287	1.25	690	528	0.019	94.07
3	620,500	304	248,200	288	1.25	652	490	0.018	94.56
4	482,600	303	193,100	287	1.25	606	449	0.016	94.58
5	344,700	302	151,700	287	1.25	546	411	0.015	94.91

Note: Pressures P_1 and P_2 are gauge pressures.

$$v = \sqrt{\left(\frac{2\,\gamma}{\gamma - 1}\right)\left(\frac{P_s}{\rho}\right)\left[\left(\frac{P_{stag}}{P_s}\right)^{\left(\frac{\gamma-1}{\gamma}\right)} - 1\right]} \qquad (48)$$

(Note: P_s=101,325 Pa)

where,

P_s = static pressure (Pa)

P_{stag} = stagnation pressure (Pa)

ρ = density (kg/m^3)

γ = C_p/C_v = 1.4 for air, 1.3 for steam

v = velocity (m/s)

Air density is given by

$$\rho = \frac{MW\ \left(P_b + P_a\right)}{RT} \tag{49}$$

where,

P_a = barometric pressure (Pa)

P_a = guage pressure (Pa)

MW = molecular weight

R = gas constant (Pa·m^3/(mol·K))

T = absolute temperature (K)

The mass flow rate is given by

$$m = Av\rho \tag{50}$$

where,

A = outlet area (m^2)

m = mass flow rate (kg/s)

The nozzle efficiency (Vishwannathappa, 2001) is calculated as follows

$$\eta_N = \frac{\frac{1}{2} m_m \left(v_m^2 - v_1^2\right)}{m_m \left(\frac{2\gamma}{\gamma - 1}\right)\left(\frac{RT}{MW}\right)\left[\left(\frac{P_2}{P_1}\right)^{\left(\frac{\gamma-1}{\gamma}\right)} - 1\right]} \tag{51}$$

where,

η_N = nozzle efficiency

m_m = motive-stream mass flow rate (kg/s)

P_1 = nozzle inlet pressure (Pa)

P_2 = nozzle outlet pressure (Pa)

v_m = motive velocity (m/s)

v_1 = nozzle inlet velocity (m/s)

The efficiency of the jet ejector is given by

(52)

$$\eta_J = \frac{\frac{1}{2} m_t v_t^2 + m_p \frac{RT_p}{MW} + m_m \frac{RT_m}{MW} + m_m \left(\frac{\gamma}{\gamma - 1} \right) \frac{RT_p}{MW} \left[\left(\frac{P_{st}}{P_{sp}} \right)^{\frac{\gamma - 1}{\gamma}} - 1 \right] + m_m \left(\frac{\gamma}{\gamma - 1} \right) \frac{RT_m}{MW} \left[\left(\frac{P_{st}}{P_{sm}} \right)^{\frac{\gamma - 1}{\gamma}} - 1 \right]}{\frac{1}{2} m_p v_p^2 + \frac{1}{2} m_m v_m^2 + m_p \frac{RT_p}{MW} + m_m \frac{RT_m}{MW}}$$

where,

η_J = jet ejector efficiency

m_p = propelled-stream mass flow rate (kg/s)

m_t = outlet-stream mass flow rate (kg/s)

P_{sm} = motive-stream static pressure (Pa)

P_{sp} = propelled-stream static pressure (Pa)

P_{st} = outlet-stream static pressure (Pa)

T_m = motive-stream absolute temperature (K)

T_p = propelled-stream absolute temperature (K)

v_m = motive-stream velocity (m/s)

v_p = propelled-stream velocity (m/s)

v_t = outlet-stream velocity (m/s)

where all temperatures are measured at the jet ejector inlet. The derivation and verification of Equation 52 is described in Appendix A.

Figure 16 shows the schematic of the experiment apparatus. Pressurized air from a fixed-volume tank was supplied to the nozzle. The air exiting the nozzle passed through the jet ejector with various pinch valve closings (Figure 17). The inlet pressure, inlet temperature, pressure rise across the jet ejector, and outlet dynamic pressure were recorded for each run. The jet ejector was back pressurized by closing the pinch valve inch-by-inch as shown in Figure 17. The readings were recorded at each pinch valve closing. From these values, the velocity and mass flow rate through the jet ejector were calculated.

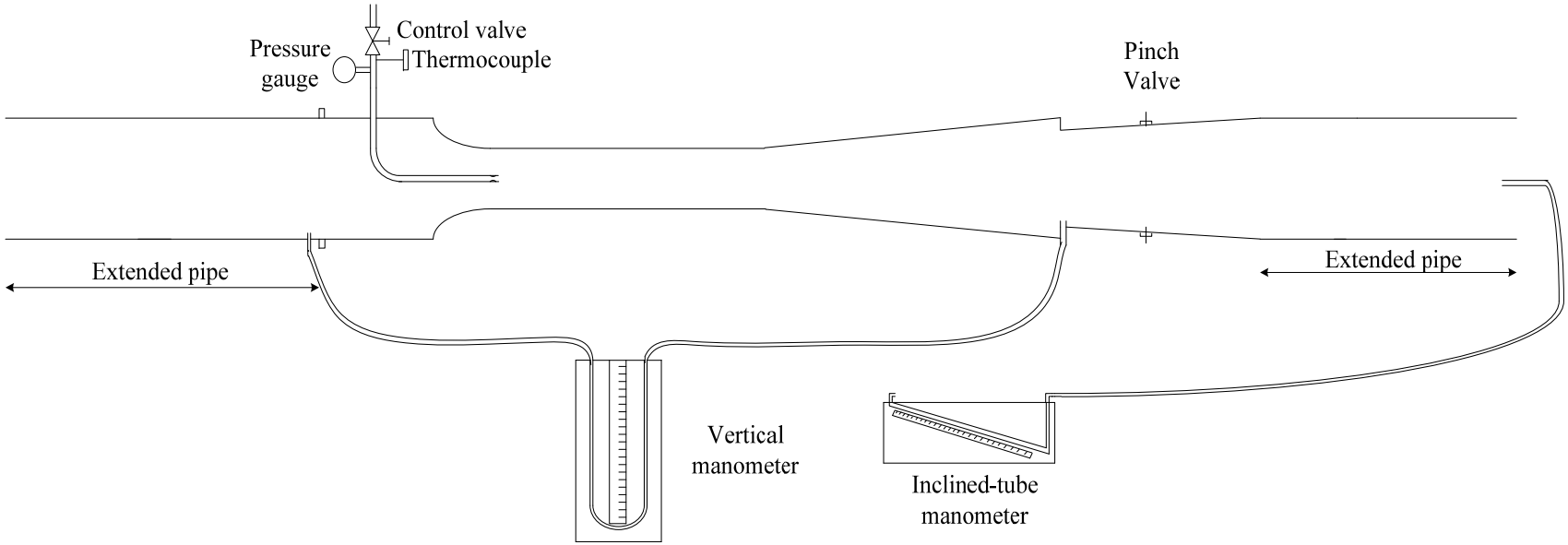

Figure 16. Experimental apparatus of jet ejector with no pinch valve closing.

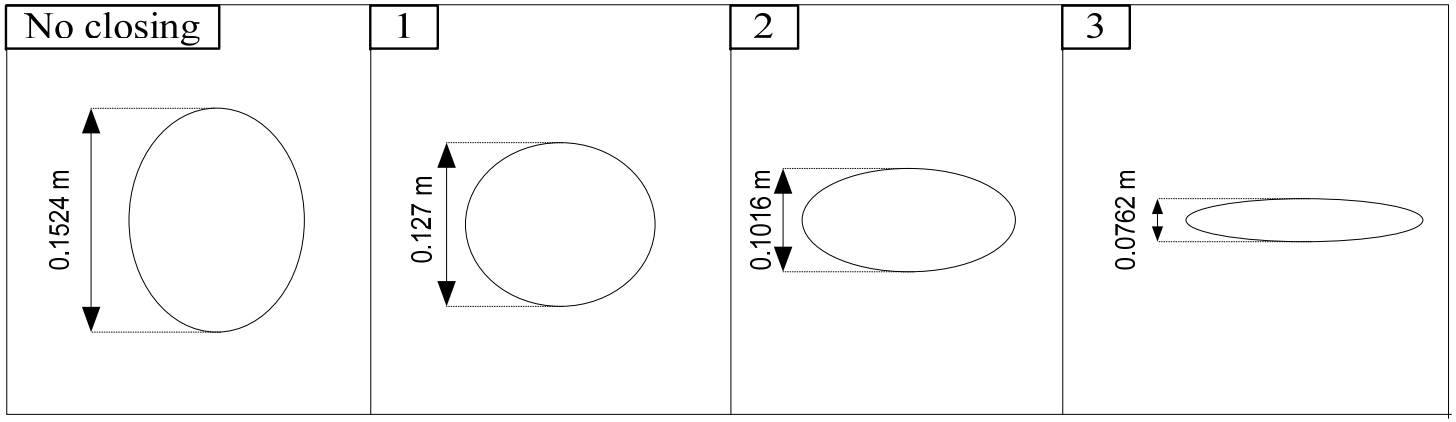

Figure 17. A schematic representation of pinch valve closings during the jet ejector experiment. The 6-in (0.1524-m) tube was closed inch-by-inch (5 in = 0.127 m, 4 in = 0.1016 m, 3 in = 0.0762 m) to create back pressure in the system.

Model Development

In the CFD study, the jet ejector model geometry matched the experimental apparatus. A grid was mapped to the model geometry using grid-generating software (GAMBIT). The grid size was optimized to be small enough to ensure that the CFD flow results were virtually independent of size, but large enough to ensure the model ran efficiently at an acceptable speed (Riffat and Everitt, 1999). A non-uniform grid was selected because it provided the greatest control of the number of cells and their localized density. For optimal meshing, the grid density increased near the wall and in areas where flow gradients were steep. This was accomplished by applying weighting factors to increase the grid density at these areas. Figure 18 shows the model grid size.

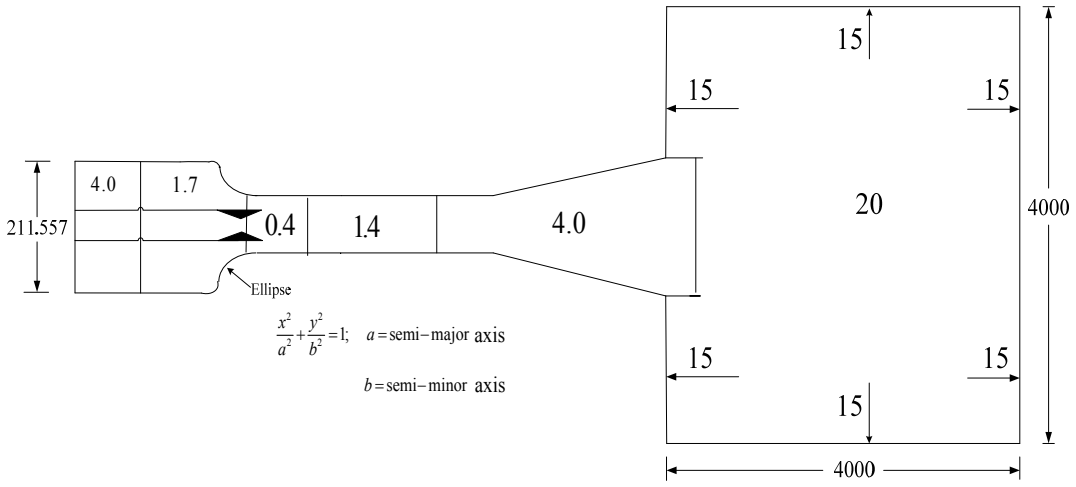

Figure 18. Grid size of an entire computational domain (unit: millimeter).

A good model provides high-accuracy results and consumes the least computational resource. As shown in Figure 19, three models were developed in the study. Table 6 summarizes two boundary condition cases that were tested for each model.

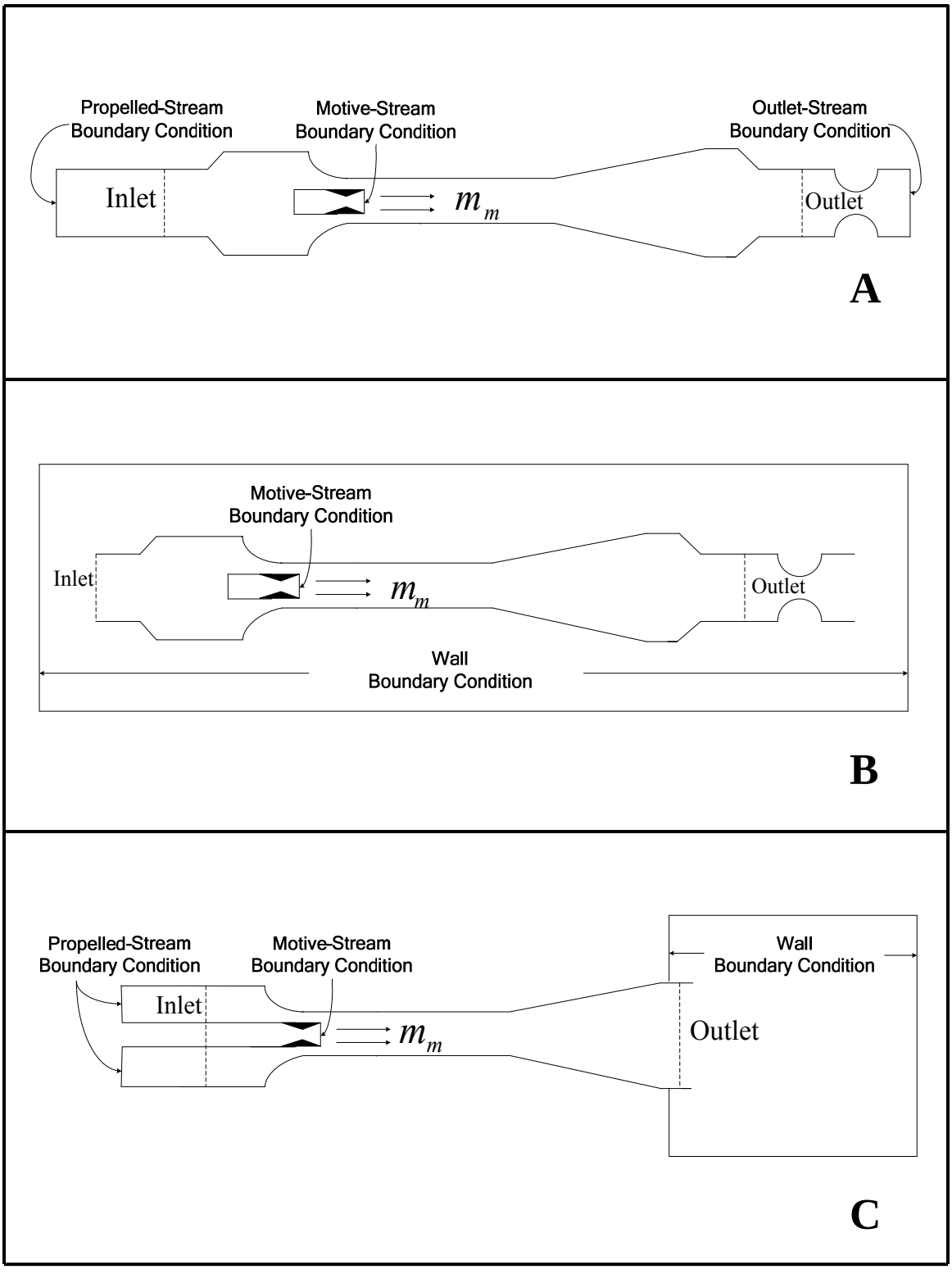

Figure 19. Various stages of model development. A) The first model, B) the second model, and C) the final model.

Table 6. Boundary condition specification of the CFD models.

Position	Applied boundary condition	
	Case 1	Case 2
Propelled-stream boundary condition	Mass flow rate	Total pressure
Motive-stream boundary condition	Mass flow rate	Mass flow rate
Outlet-stream boundary condition	Total pressure	Total pressure

Model Discretization

Discretization involves specifying the grid size and number of iterations. The grid size is examined by creating two different grid-size models (coarser and finer). Both models were simulated with various numbers of iterations (2,500, 4,500, and 6,000 iterations). The results using the finer grid size and 6,000 iterations are considered to be the most reliable; however, it consumes the most computational time and memory, so it is costly to employ. The preferred simulation model takes the least computational time yet provides accurate results. Once identified, it was applied throughout the study. This study verifies that the grid size and number of iterations were carefully selected to give valid results.

CFD Analysis

The simple jet-ejector geometry shown is Figure 19C was applied in this study. The motive-stream velocity in the model was identical to the experiment values. A number of cases with different propelled-stream mass flow rates were simulated. The experimental and CFD results were compared to determine the deviation. Table 7 summarizes the specified

parameters in the CFD model. The static pressure difference between the inlet and outlet of the jet ejector is reported and plotted as a function of propelled mass flow rate.

Table 7. Summarize parameter specification in CFD analysis.

Type	Selection
CFD modeling	
Model type	Two-dimensional axi-symmetric model
Numerical solver	Conventional equation (segregated solver)
Turbulence model	Standard *k*-ε model
Discretization technique	Finite volume
Discretization scheme	
Pressure	Standard scheme
Pressure-velocity coupling	SIMPLE
Density	Third-order MUSCL
Energy	Third-order MUSCL
Momentum	Third-order MUSCL
Turbulence kinetic energy	Third-order MUSCL
Boundary condition	
Propelled-stream inlet	Inlet mass flow rate
Motive-stream inlet	Inlet mass flow rate
Inlet and outlet of the box	Total pressure

In the applied CFD model, a large volume was placed at the jet ejector outlet. The pressure in the large volume corresponds to the pressure just upstream of the pinch valve. This modeling approach eliminated the need to simulate the pinch valve and introduce adjustable parameters that describe the pinch valve pressure drop. The motive-stream velocity was specified at the nozzle exit. For the propelled-stream boundary condition, the mass flow rate was specified. The pressure in the large volume P_o at the jet-ejector outlet is maintained constant at 101.3 kPa. and the inlet pressure P_p was allowed to float during the simulation. The total pressure boundary condition was specified for the large volume.

The deviation of the results between experiment and CFD analysis is given by

$$\%\ \text{Deviation} = \frac{(m_p)_{\text{exp}} - (m_p)_{CFD}}{(m_p)_{\text{exp}}} \times 100 \tag{53}$$

where,

$(m_p)_{\text{exp}}$ = propelled-stream mass flow rate of the experiment (kg/s)

$(m_p)_{CFD}$ = propelled-stream mass flow rate of CFD Modeling (kg/s)

Results and Discussion

Jet Ejector Experiment

As shown in Figure 15, the inlet pressure, inlet temperature, static pressure rise across the jet ejector, and outlet dynamic pressure were reported according to motive stream velocity and pinch valve position (Table 8). From these values, the velocity, mass flow rate through the jet ejector, and jet-ejector efficiency were calculated by applying Equations 48, 49, 50, and 52 (Table 8). The static pressure at the motive stream outlet, propelled stream inlet, and jet ejector outlet were reported for each motive stream velocity and pinch valve position (Table 9). The jet ejector experiment apparatus is shown in Figure 19.

Table 8. Data obtained at the outlet of the jet ejector for various pinch valve closings.

Jet ejector with no pinch valve closing										
m_m (kg/s)	v_m (m/s)	m_p (kg/s)	m_t (kg/s)	v_t (m/s)	Efficiency η_J (%)	m_p/m_m	Inlet press. (Pa)	Temp (K)	Dyn Pr (Pa)	ΔP (Pa)
0.020	563	0.65	0.67	29.6	93.67	32.5	896,300	302.1	548	685
0.019	529	0.61	0.63	27.7	94.53	32.2	758,400	301.9	478	638
0.018	490	0.55	0.57	25.2	95.29	30.7	620,500	301.4	399	468
0.016	449	0.50	0.52	22.9	96.21	31.5	482,600	300.6	329	359
0.015	411	0.45	0.46	20.5	96.88	29.7	344,700	300.1	262	234
Jet ejector with pinch valve closing 1										
m_m (kg/s)	v_m (m/s)	m_p (kg/s)	m_t (kg/s)	v_t (m/s)	Efficiency η_J (%)	m_p/m_m	Inlet press. (Pa)	Temp (K)	Dyn Pr (Pa)	ΔP (Pa)
0.020	563	0.61	0.63	27.8	93.77	30.5	896,300	303.3	483	857
0.019	528	0.57	0.59	25.9	94.60	30.1	758,400	303.5	418	732
0.018	490	0.53	0.55	24.0	95.30	29.6	620,500	303.4	359	608
0.016	449	0.47	0.49	21.8	96.21	29.6	482,600	303.0	296	468
0.015	411	0.43	0.44	19.3	96.85	28.3	344,700	302.8	232	326
Jet ejector with pinch valve closing 2										
m_m (kg/s)	v_m (m/s)	m_p (kg/s)	m_t (kg/s)	v_t (m/s)	Efficiency η_J (%)	m_p/m_m	Inlet press. (Pa)	Temp (K)	Dyn Pr (Pa)	ΔP (Pa)
0.020	563	0.57	0.59	26.2	93.78	28.5	896,300	303.8	428	1,153
0.019	528	0.54	0.56	24.4	94.58	28.5	758,400	303.8	374	1,029
0.018	490	0.50	0.52	22.8	95.27	27.9	620,500	303.4	324	842
0.016	449	0.45	0.47	20.7	96.17	28.4	482,600	302.7	267	623
0.015	411	0.42	0.43	18.7	96.83	27.7	344,700	302.0	219	436
Jet ejector with pinch valve closing 3										
m_m (kg/s)	v_m (m/s)	m_p (kg/s)	m_t (kg/s)	v_t (m/s)	Efficiency η_J (%)	m_p/m_m	Inlet press. (Pa)	Temp (K)	Dyn Pr (Pa)	ΔP (Pa)
0.020	563	0.37	0.39	17.2	91.92	18.5	896,300	300.3	184	2,179
0.019	528	0.36	0.38	16.7	93.09	19.0	758,400	299.0	174	1,853
0.018	490	0.34	0.36	16.1	94.00	19.0	620,500	297.8	162	1,557
0.016	449	0.33	0.35	15.5	95.39	20.9	482,600	296.5	149	1,121
0.015	411	0.33	0.34	15.0	96.32	21.7	344,700	296.5	139	795

Note: The inlet pressure is gauge pressure.

Table 9. Static pressures for various pinch valve closings (back pressures).

v_m (m/s)	P_{sm} (Pa)	P_{sp} (Pa)	P_{st} (Pa)
No pinch valve closing			
563	102,346	102,653	101,329
529	102,378	102,275	101,328
490	102,418	101,883	101,327
449	102,438	101,676	101,327
411	102,492	101,337	101,326
Pinch valve closing 1			
563	102,392	102,146	101,328
529	102,426	101,832	101,328
490	102,443	101,693	101,327
449	102,477	101,436	101,326
411	102,518	101,203	101,326
Pinch valve closing 2			
563	102,439	101,705	101,327
529	102,461	101,536	101,327
490	102,480	101,431	101,327
449	102,503	101,288	101,326
411	102,530	101,138	101,326
Pinch valve closing 3			
563	102,672	100,168	101,325
529	102,674	100,238	101,325
490	102,673	100,379	101,325
449	102,654	100,572	101,325
411	102,647	100,642	101,325

Model Development

In the first model (Figure 19A), the back pressure was controlled by a pinch valve, so an additional parameter to characterize the pressure drop was required, making the problem more complicated. Furthermore, the simulation results in Boundary Condition Case 1 (Table 6) were unstable due to over-specification. Further, for Boundary Condition Case 2, the model predictions were significantly different from the experimental results; the deviation was about 20%. For these reasons, the first model was rejected.

The second model is displayed in Figure 19B. Instead of specifying the boundary conditions at the propelled and outlet streams, the jet ejector was located in a large volume. The pressure in the volume was maintained constant at 101.3 kPa and the motive-stream velocity was defined at the nozzle exit. Because it consumed a lot of computational time and memory due to the large volume, and an additional adjustable parameter for the pinch valve was required, this model was impractical and inconvenient to implement.

The final model is displayed in Figure 19C. The large volume was placed at the jet ejector outlet only, rather than the entire domain. The computational time was reduced by 60% from the second model. Additionally, no pinch valve was required in the model, thus eliminating the need for an adjustable parameter that simulates the valve. The motive-stream velocity was specified at the nozzle exit and the pressure in the large volume was maintained constant at 101.3 kPa. This model provided stable results and consumed the least computational time, plus it did not require pinch valve simulation; therefore, this model was applied through the study.

Model Discretization

The grid size and number of iterations were examined in this experiment. The smaller the grid size, the more accuracy was obtained; however, the very fine grid consumed excessive computational resources as a consequence. Also, more iteration provides more accuracy, but required greater computational time and memory. Because jet ejector efficiency is used to determine the optimum condition, it was used to determine the proper grid size and number of iterations. The results with a number of iterations of coarser and finer grids are shown in Tables 10A and 10B, respectively.

Table 10. Simulation result of the model stability (A) coarse-grid model (B) fine-grid model .

.

(A) coarse-grid model

Number of iterations	Pressure (Pa)			Efficiency	Computational time (h)
	Motive	Propelled	Outlet		
2,500	97,842.3	98,124.1	101,325.5	0.9769	2
4,500	97,784.8	98,031.5	101,324.9	0.9783	3
6,000	97,784.7	98,031.5	101,325.0	0.9783	4

(B) fine-grid model

Number of iterations	Pressure (Pa)			Efficiency	Computational time (h)
	Motive	Propelled	Outlet		
2,500	97,792.5	98,061.1	101,325.3	0.9782	5
4,500	97,764.3	98,008.0	101,327.1	0.9786	7
6,000	97,762.1	98,003.4	101,327.2	0.9786	10

Regardless of the computational time consumed, the jet ejector efficiency of every case was almost the same (97%). The pressure difference among the cases was less than 130 Pa, which is very small compared to the outlet pressure of 101,325 Pa. The computational time presented in the last column varies widely among the cases due to the effect of grid size and number of iterations. The coarser grid (Figure 18) at 2,500 iterations consumed five times less computational resources than the finer grid at 6,000 iterations, but

the variation in efficiency was negligibly small, only 0.0017. So, the coarser grid size at 2,500 iterations was applied in the study.

CFD Analysis

The static pressure at the jet ejector inlet and outlet were reported according to the motive stream velocity and propelled stream mass flow rate. The static pressure rise across the jet ejector is the difference of the static pressure at the inlet and outlet of the jet ejector. Figure 20 demonstrates how accurately the CFD model predicted the static pressure difference obtained from experiments with various motive velocities.

The simulation results were obtained directly from first principles; no adjustable parameters were used. The simulation results closely agree with the experiment results in every case. The average overall deviation between the experiments and CFD analysis was 8.19%, thus confirming the model accuracy in simulating fluid flow. For each motive stream velocity and pinch valve position, Table 11 summarizes the percentage of mass flow rate deviation between the experiment and CFD simulation.

(A)

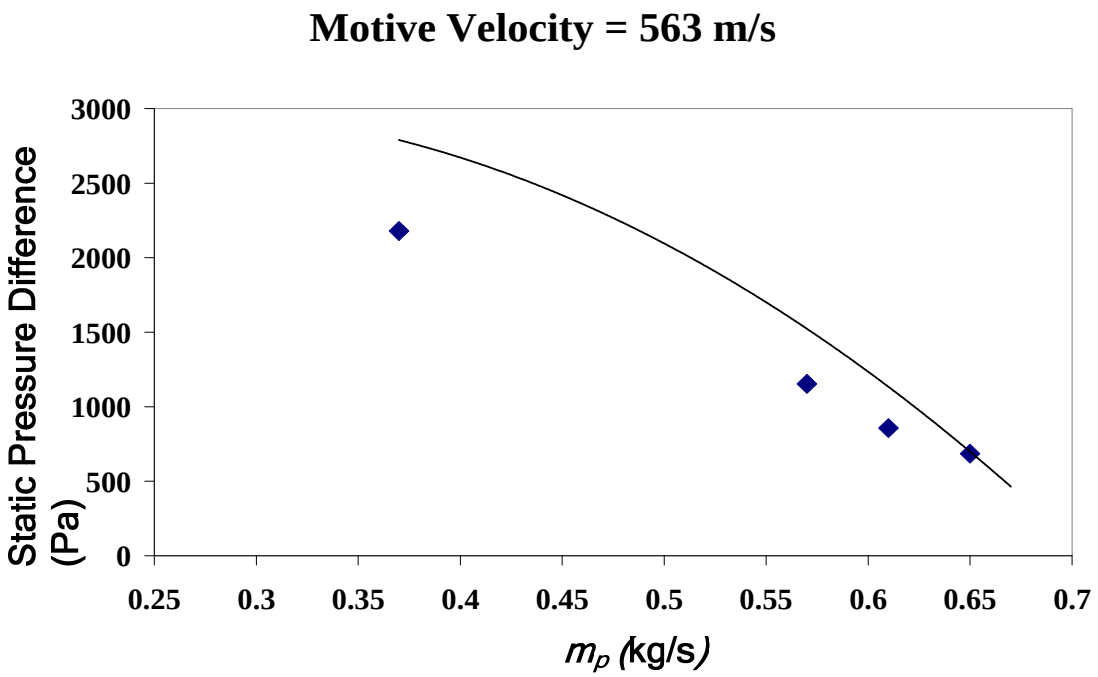

(B)

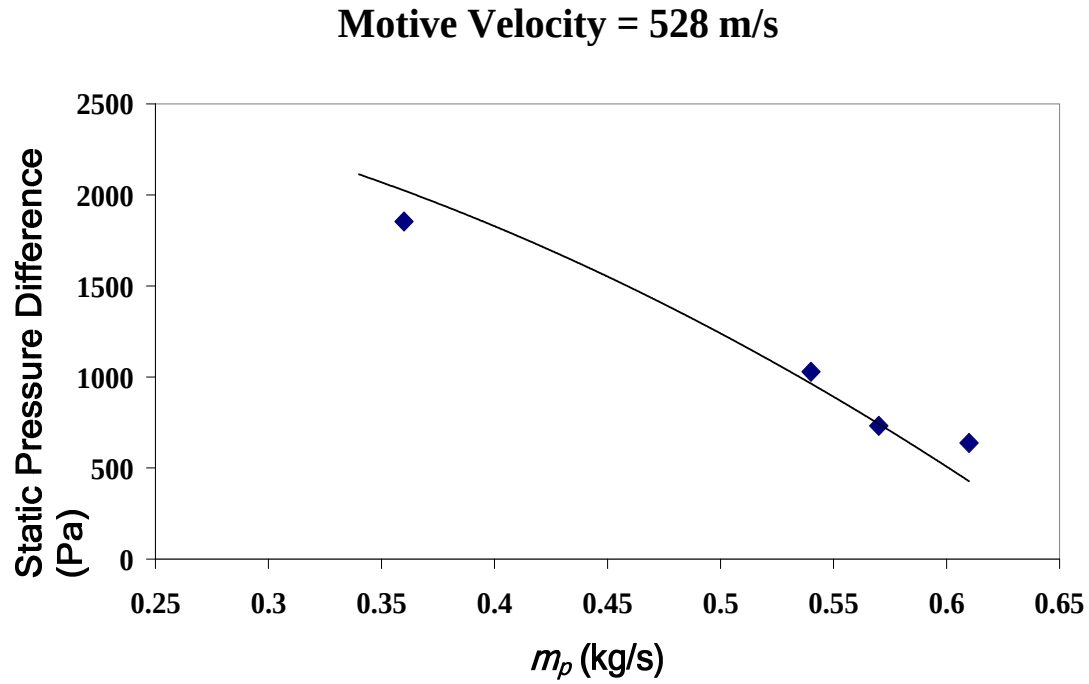

Figure 20. The experiment result comparing with the CFD result with various motive velocities. (A) 563 m/s, (B) 528 m/s, (C) 490 m/s, (D) 449 m/s, and (E) 411 m/s.

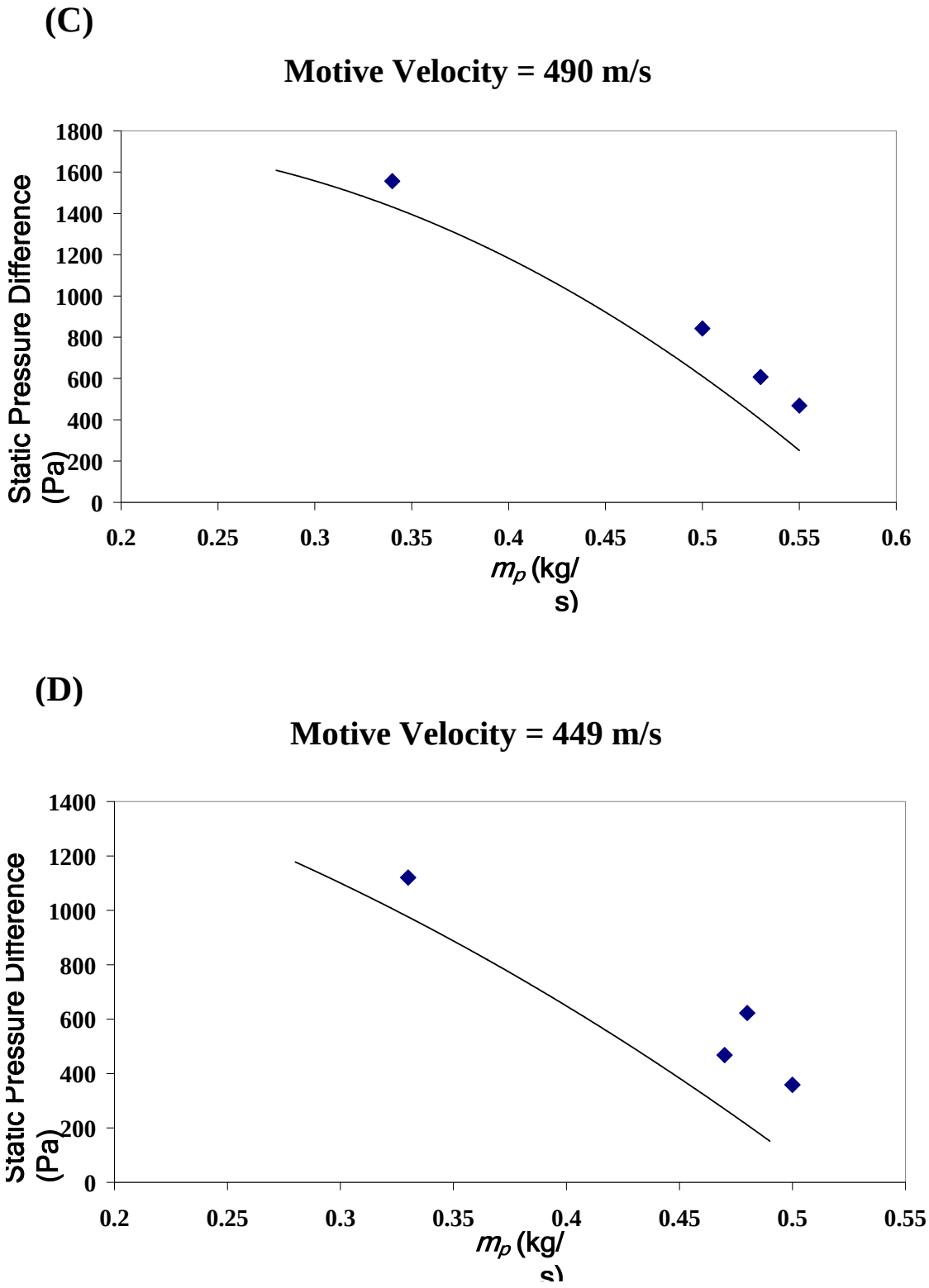

Figure 20. Continued.

(E)

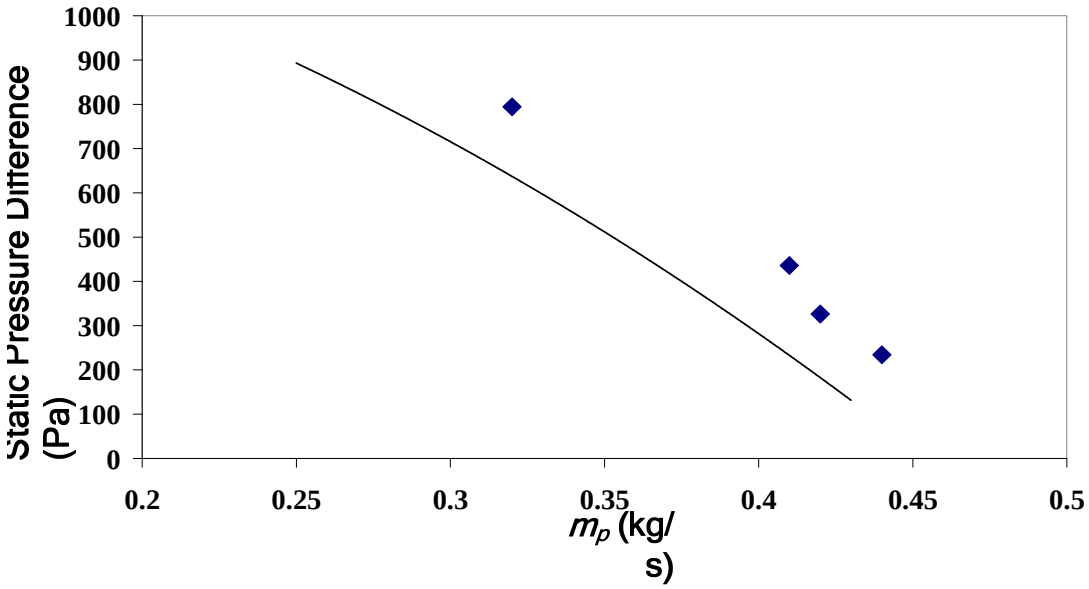

Figure 20. Continued.

Table 11. The percentage deviation between the experiment and CFD analysis for each motive stream velocity and pinch valve position.

v_m (m/s)	Pinch valve closing position*				Average Deviation (%)
	no closing	1	2	3	
563	1.54	4.92	7.02	27.03	10.13
529	3.28	1.75	1.85	8.33	3.81
490	3.64	5.66	14.55	14.71	9.64
449	6.00	6.38	8.89	12.12	8.35
411	6.82	7.14	9.76	12.50	9.05
				Overall average	8.19

*see Figure 17

Conclusion

This paper presents the results of a CFD model that simulates the flow field inside a constant-area jet ejector. Among the three standard alternatives, the k-ε turbulence model was selected. The model geometry and boundary conditions were selected to get accurate results with minimal computation time.

The simulation under-predicts the experimental results in the low-velocity region and over-predicts in the high-velocity region. The simulation agrees with the experimental results almost perfectly at a nozzle velocity of 528 m/s. On average, the model predicts the experimental data within 8.19% without using adjustable parameters. The ability to successfully model experimental jet ejector data supports the use of CFD modeling to optimize jet ejectors.

CHAPTER V

CONSTANT-PRESSURE VS CONSTANT-AREA JET EJECTOR OPTIMIZATION

Introduction

Constant-pressure jet ejectors are widely applied in the chemical process industries, even though constant-area designs have a simpler geometry and are easier to construct. This chapter compares the performance of both designs using steam as the working fluid.

The compression ratio and ejector efficiency were used to evaluate the jet ejector performance and determined the optimal design. Computational fluid dynamics (CFD) software, Fluent, was employed in this study to allow rapid optimization of each type. The CFD model was validated in a previous chapter. Using the optimal geometry with constant nozzle outer diameter on both designs, the compression ratio and efficiency between both configurations were compared. The nozzle velocity was 170 to 850 m/s (Mach 0.5 to 2.50) and the mass flow ratio was 0.023 to 100 kg motive/kg propelled. Comparing the optimal geometry for each, the constant-area jet ejector shows better performance on both compression ratio and efficiency. This study employs a new efficiency equation that is easily implemented using information readily available from CFD.

Methodology

Jet Ejector Optimization

The main objective is to optimize the jet ejector geometry, both the constant-pressure and constant-area designs, for a variety of motive-stream velocities and mass flow ratios. The mass flow ratio is defined by

$$\text{mass flow ratio} = \frac{\text{motive mass flow rate}}{\text{propelled mass flow rate}} \tag{54}$$

In this study, the motive-stream velocity ranges from 170 to 850 m/s (Mach 0.5 to 2.50) and the mass flow ratio ranges from 0.023 to 100 kg motive/kg propelled. This study is based on the experimental apparatus (Figure 21) investigated in the previous chapter. In the experimental apparatus, the nozzle diameter ratio D_N/D_P was 0.029. In the CFD simulations, this parameter was kept constant and was not investigated in this study. Figure 22 shows the optimal geometric parameters studied in the constant-pressure and constant-area designs.

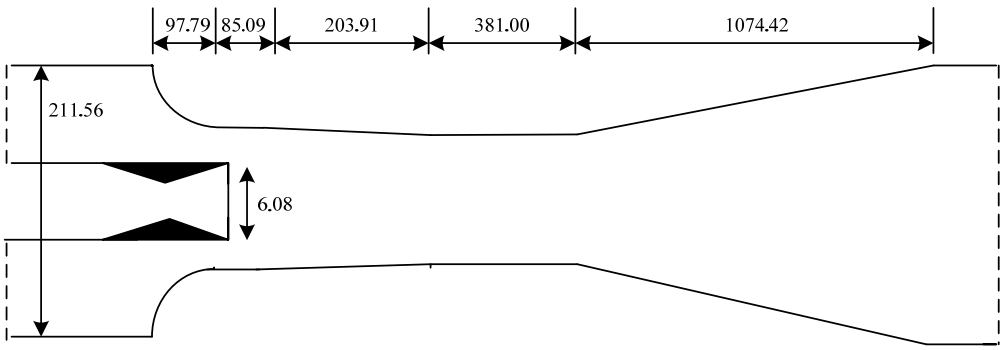

Figure 21. Base-case design (unit: millimeter).

According to the literature (e.g., ESDU, 1986), the optimum position to place a nozzle is near the beginning of the throat section. Therefore, the nozzle in the experiment is placed at the beginning of the throat section $(l = 0)$ and is not an optimized parameter. The convergence section connecting the jet ejector inlet and throat section does not exist in the constant-area jet ejector. Using the optimization procedure explained in the following section, the optimal geometries of both designs were obtained. The compression ratio and efficiency were compared to determine the better configuration. (Note: The derivation of the efficiency equation used in this study is explained later in the paper.) The geometric parameters are presented in dimensionless form by creating a ratio with jet-ejector inlet diameter D_P.

(A)

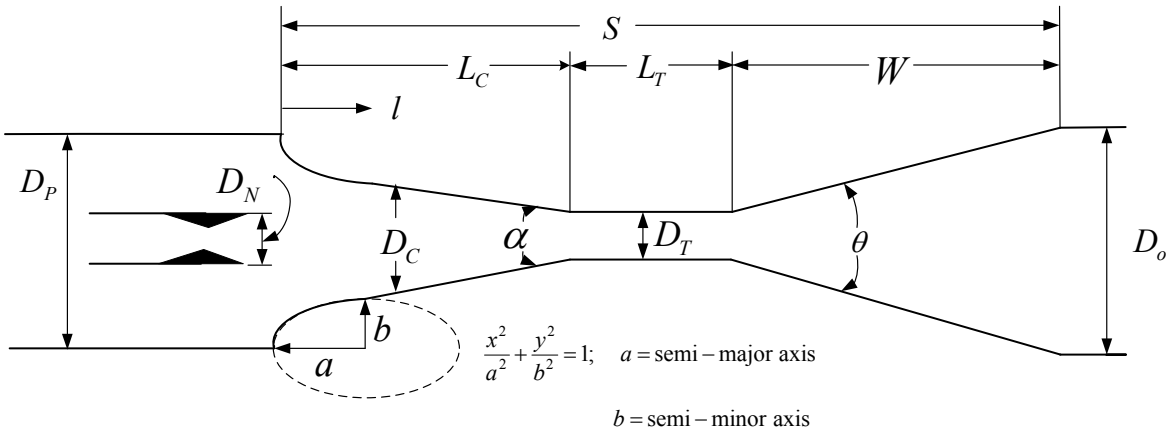

(B)

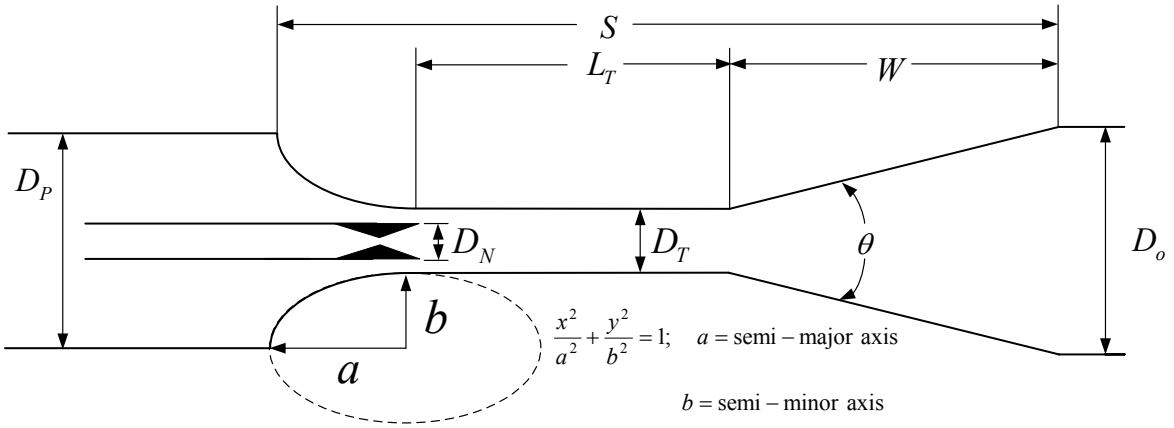

Figure 22. Symbols in jet ejector (A) constant-pressure (B) constant-area.

Optimization Procedure

Figure 23 illustrates the optimization procedure. The priority of optimized parameters is ranked by their effect on jet ejector performance.

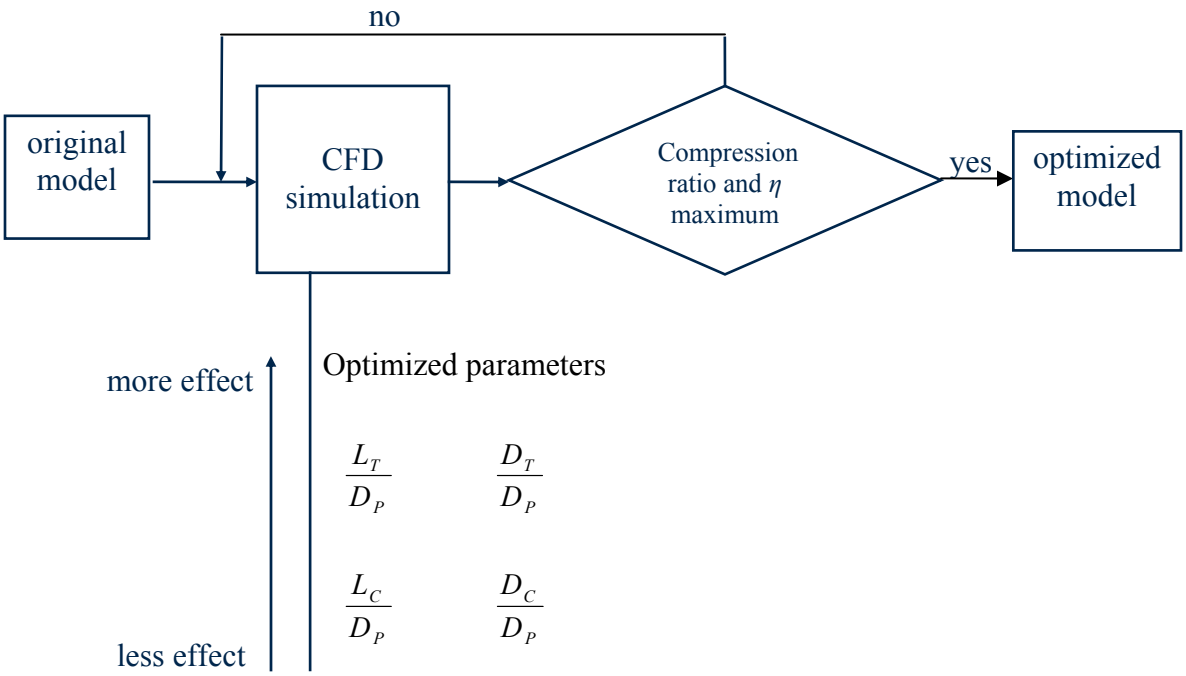

Figure 23. Optimization procedure.

From Figure 23, the length and diameter of the throat section provide the greatest impact on jet ejector performance, whereas the radius inlet curvature of the convergence section does not provide a great effect. The optimization procedure is described below:

1. From a base-case design (Figure 21), the optimized parameters are studied in ascending order of their effect (see Figure 23).
2. For a given flow, the geometric parameters are varied until the optimum efficiency is obtained. Fluid variables (e.g., pressure, velocity, density) are used to calculate the jet ejector efficiency. The maximum efficiency and compression

ratio is obtained when there is no deviation in compression ratio and efficiency from the previous iteration.

3. Eventually, an optimal geometry for a given motive-stream velocity and mass flow ratio is obtained.

The optimization procedure was done manually by making small adjustments of the jet ejector geometry and following the above hierarchy until achieving the optimum performance on both designs.

Results and Discussion

Comparing Constant-Pressure and Constant-Area Designs

In this study, both compression ratio and efficiency are employed to evaluate the jet ejector performance. Both the constant-area and constant-pressure designs were examined with the motive-stream velocity from Mach 0.5 to 2.5 and the mass flow ratio from 0.023 to 100 kg motive/kg propelled. Once the geometries were determined by following the optimization procedure, the compression ratio and efficiency were calculated. Figures 24 and 25 present the optimum compression ratio and efficiency of both designs for each motive velocity.

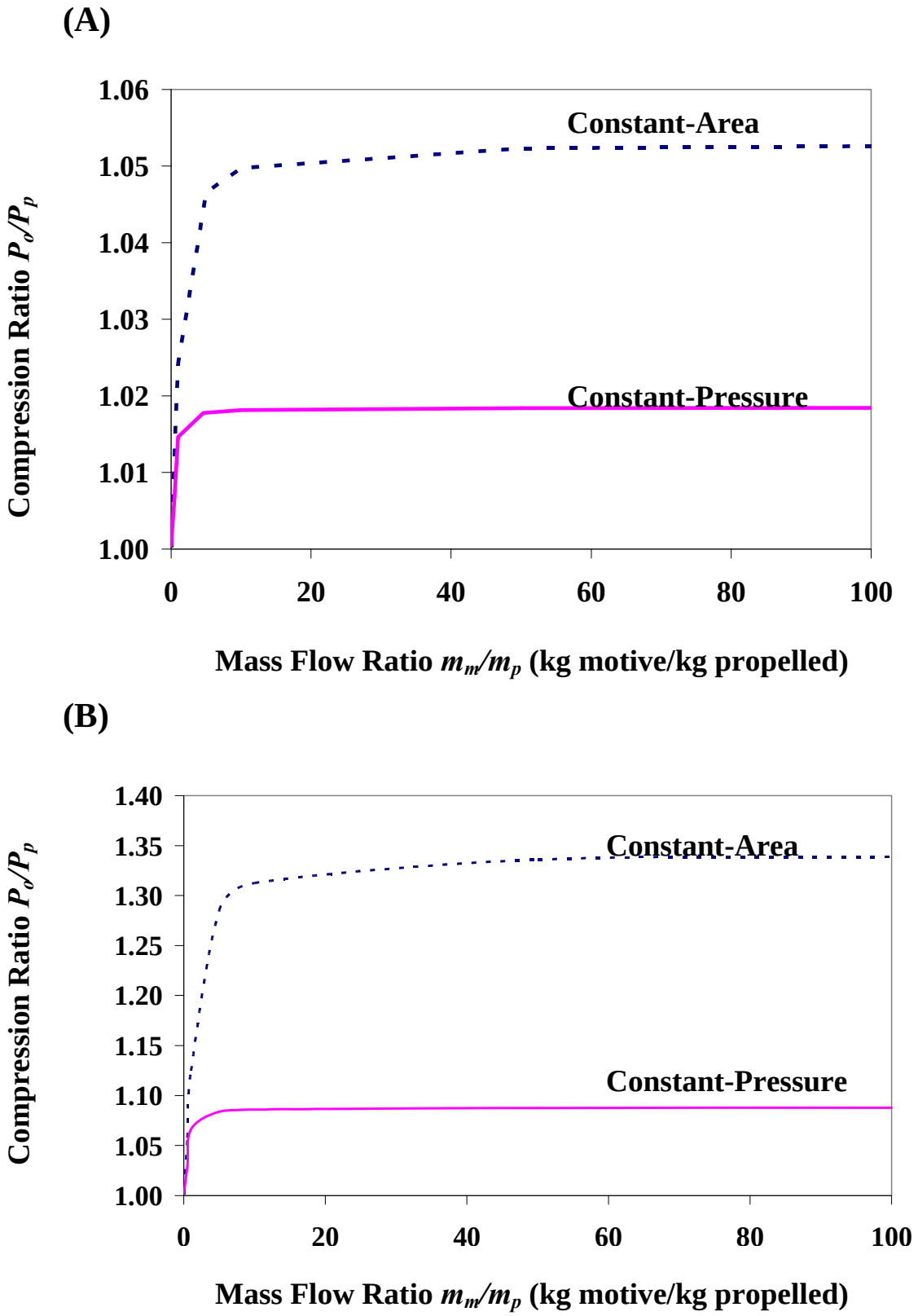

Figure 24. Compression ratio of optimal constant-pressure and constant-area jet ejectors with various motive velocities. Mach numbers: (A) 0.50, (B) 1.00, (C) 1.50, (D) 2.00, and (E) 2.50.

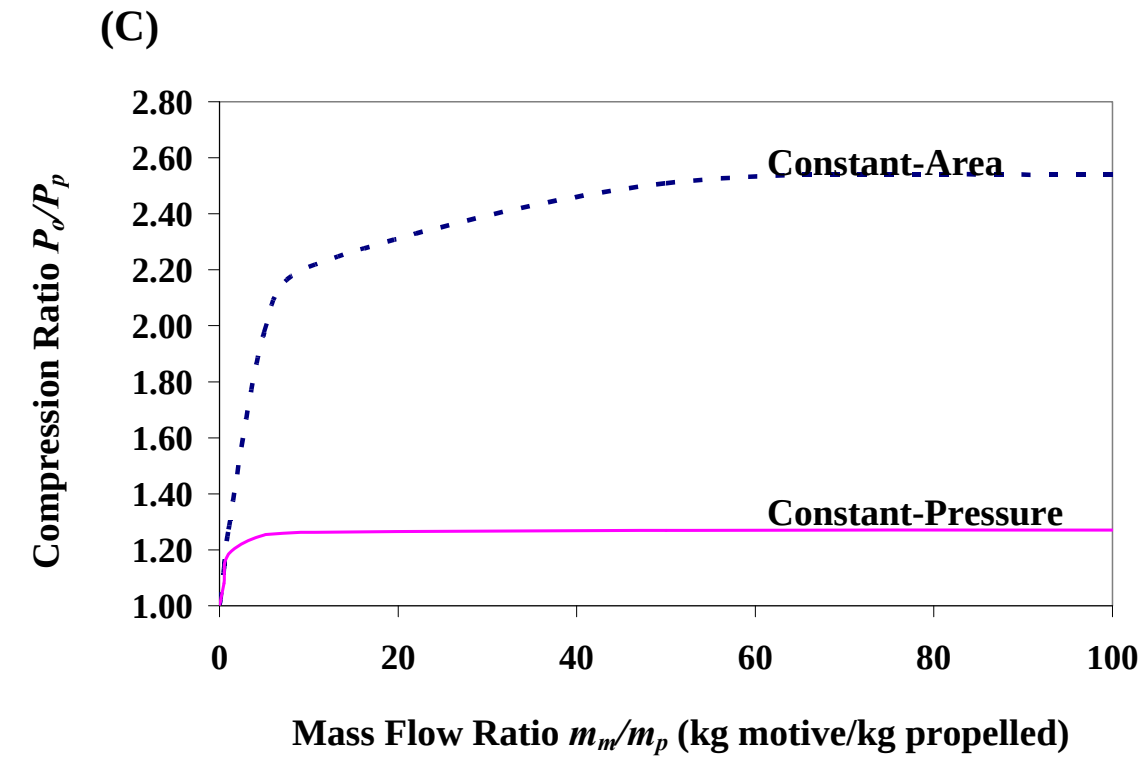

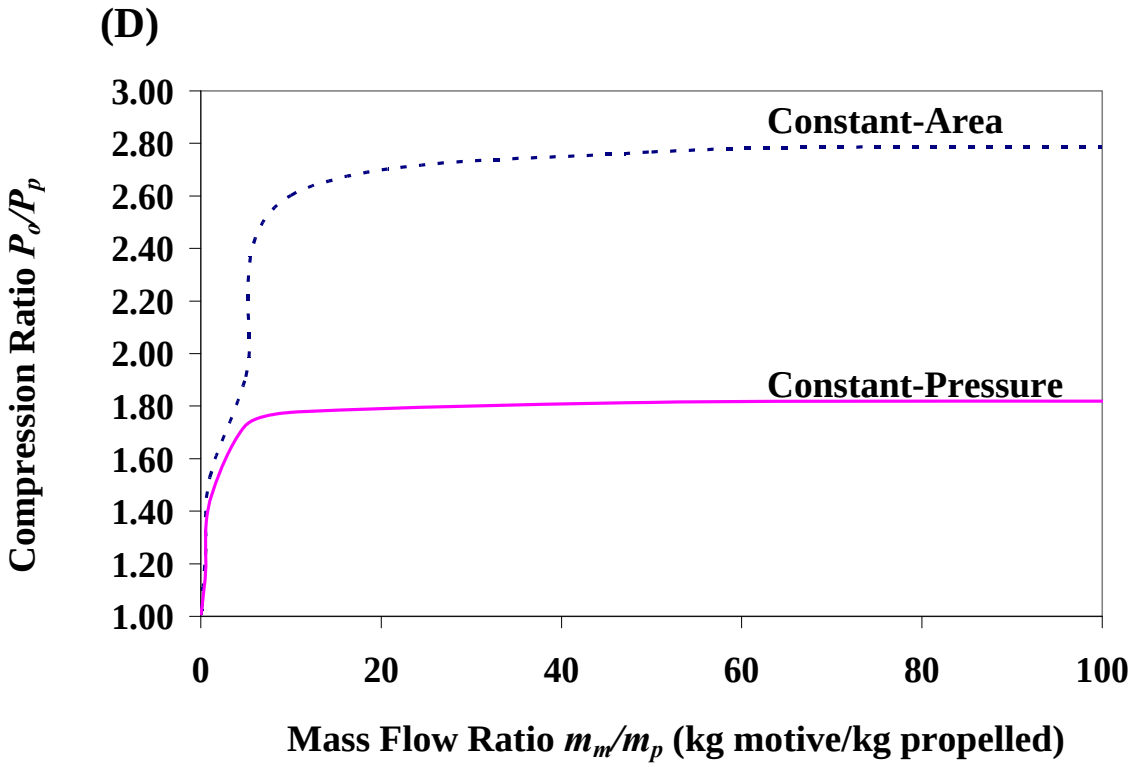

Figure 24. Continued.

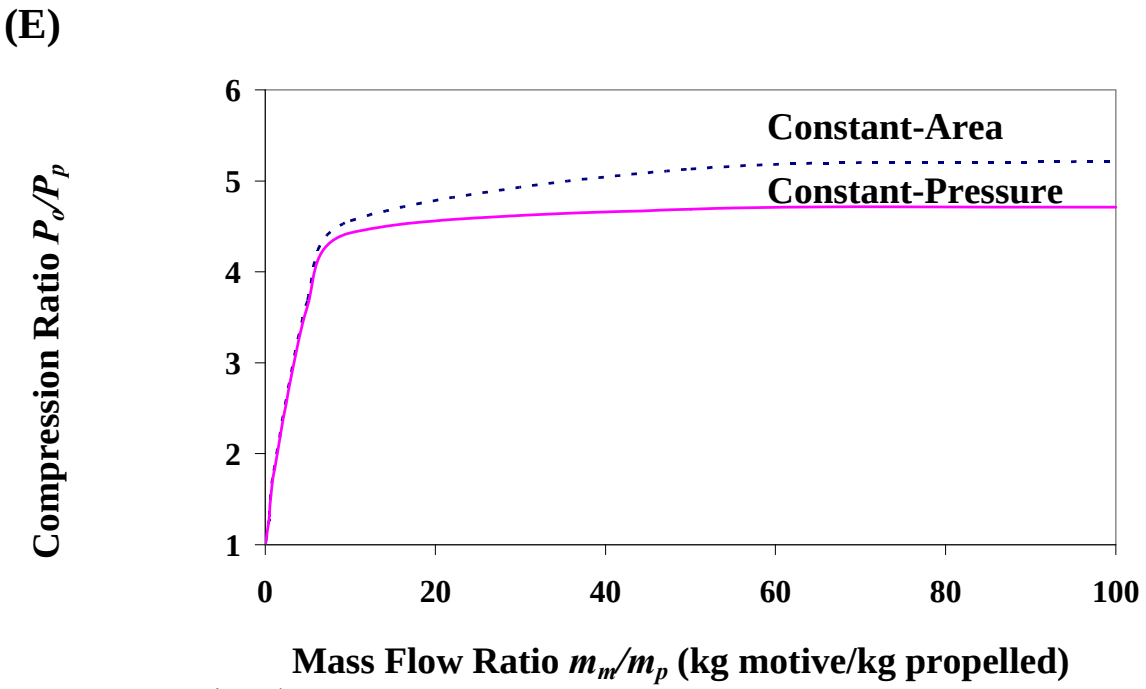

Figure 24. Continued.

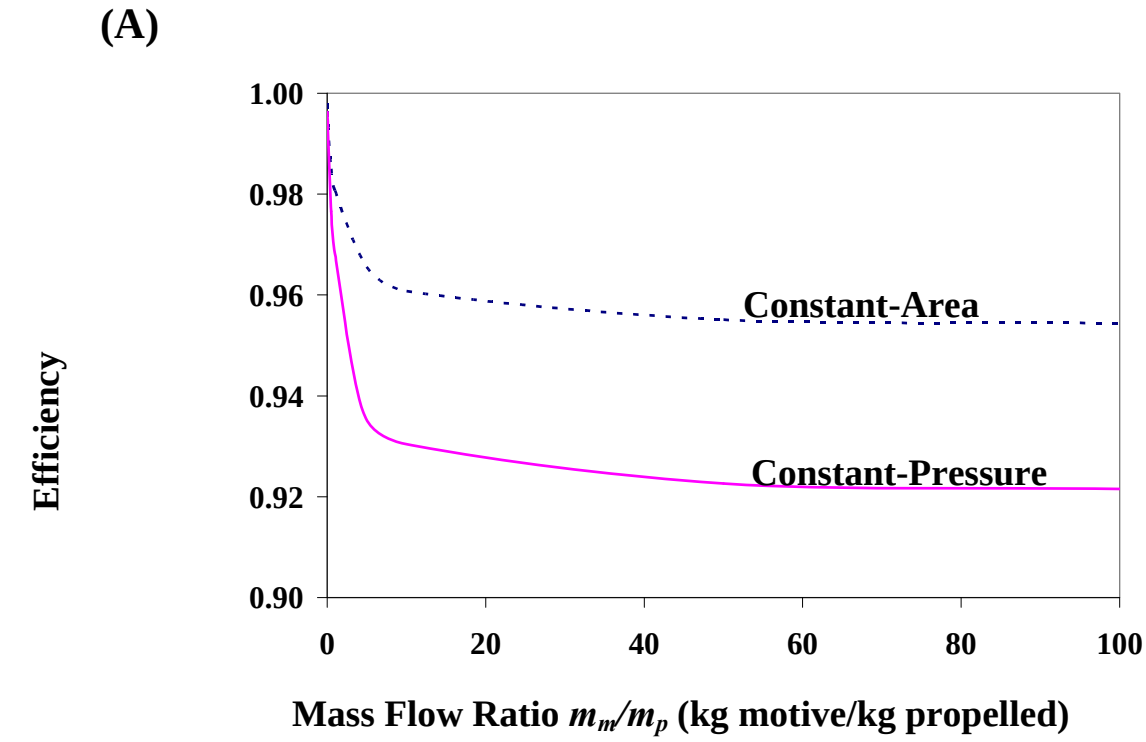

Figure 25. Efficiency of constant-pressure and constant-area jet ejectors with various motive velocities. Mach numbers: (A) 0.50, (B) 1.00, (C) 1.50, (D) 2.00, and (E) 2.50.

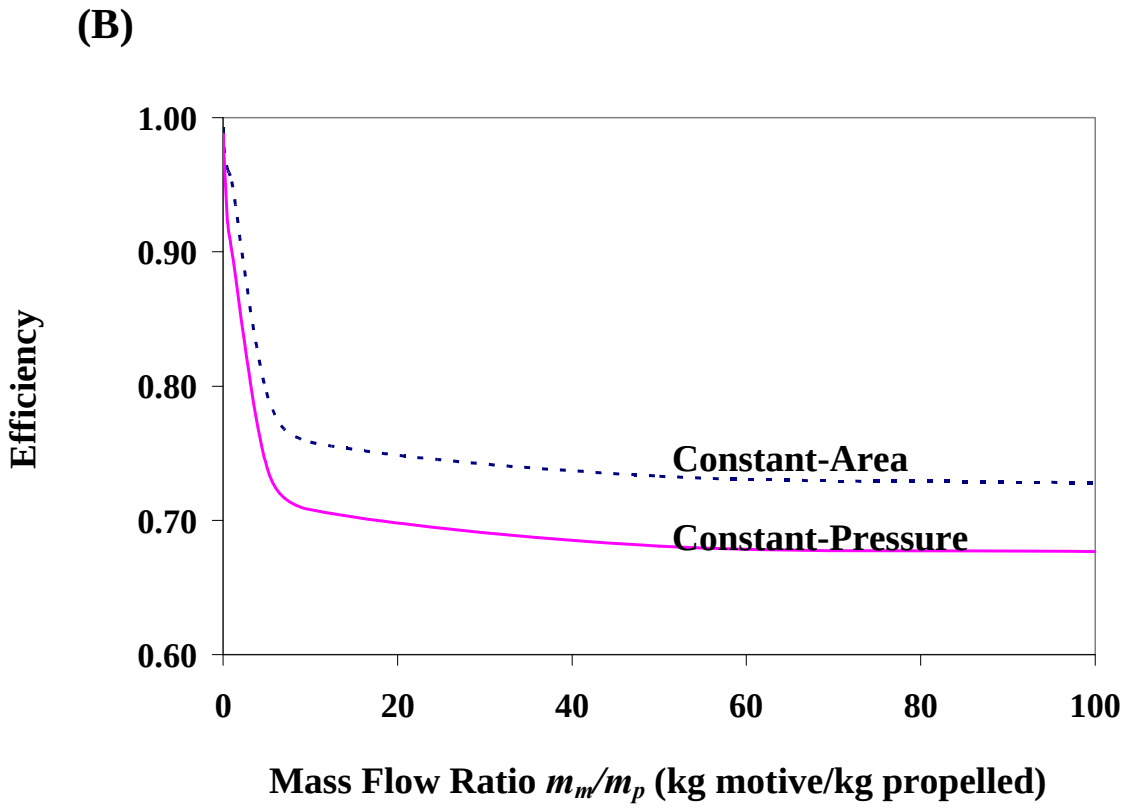

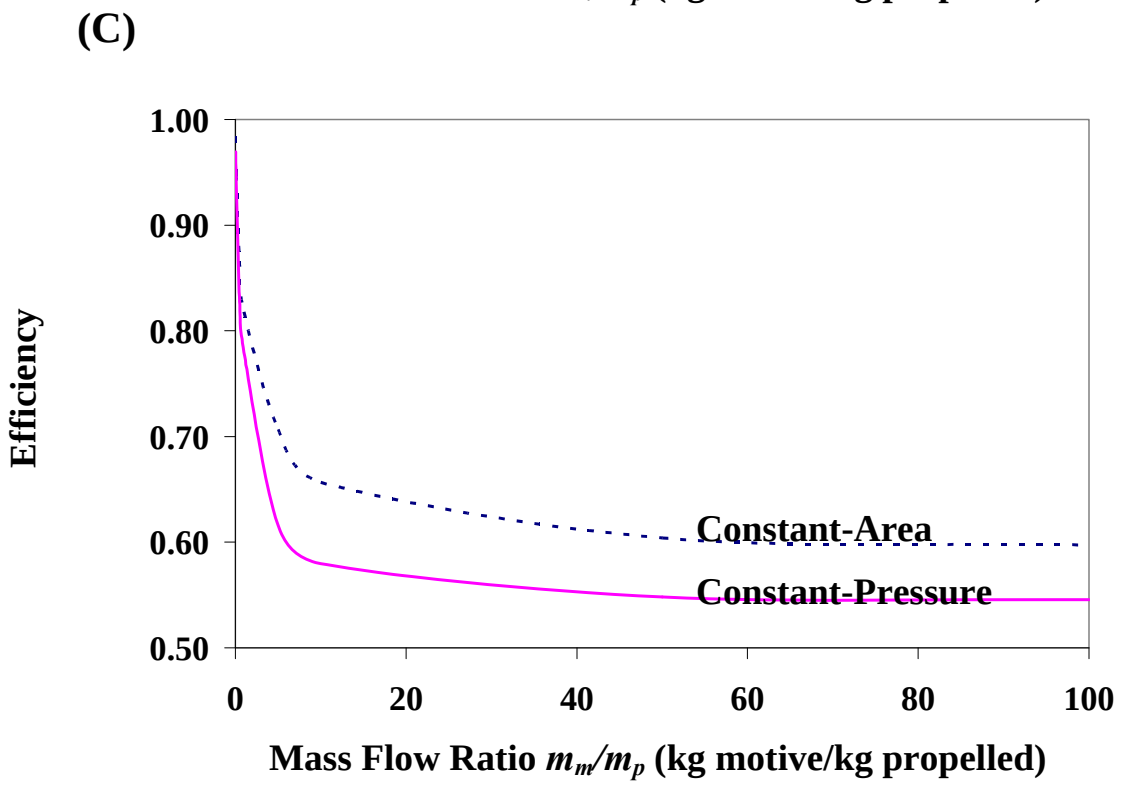

Figure 25. Continued.

(D)

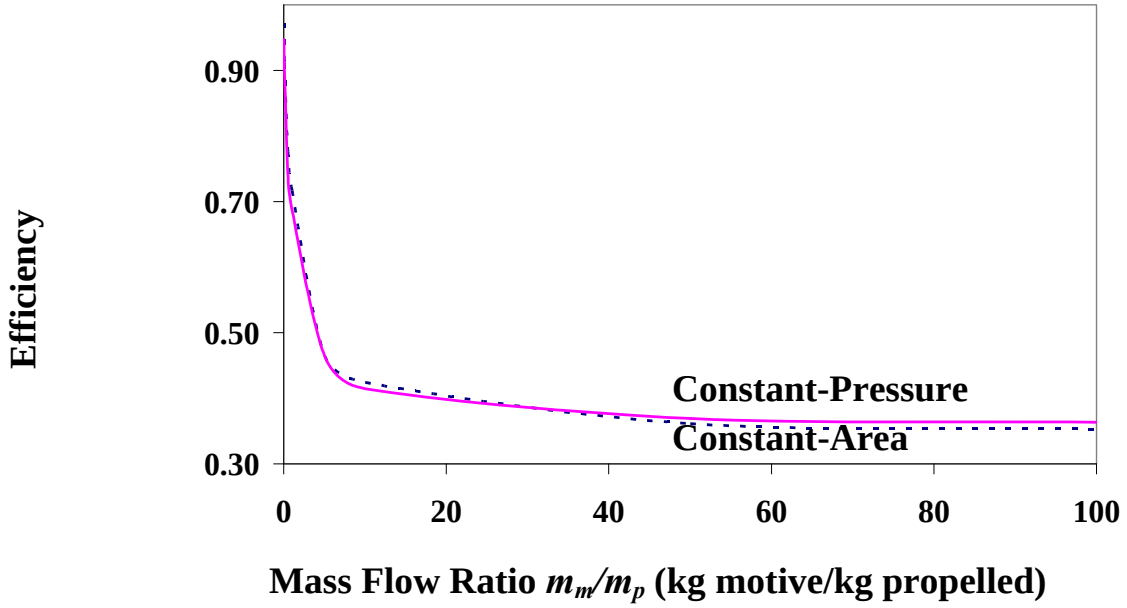

(E)

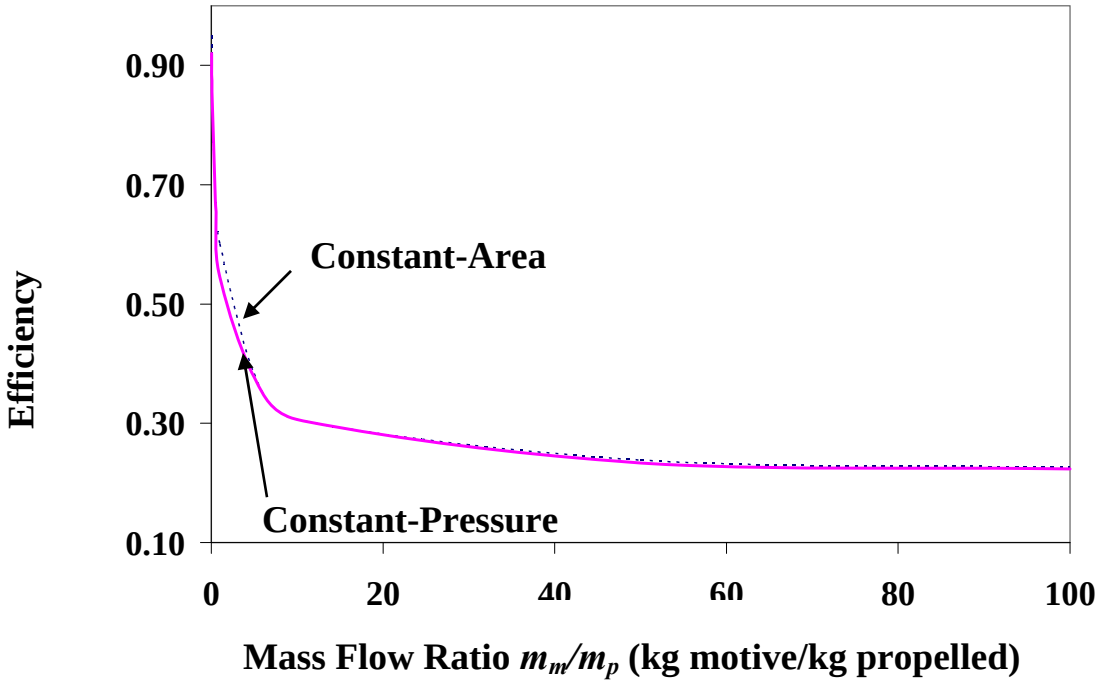

Figure 25. Continued.

The results show that the constant-area design produces both greater compression ratio and efficiency than the constant-pressure design. At all operating conditions, the constant-area jet ejector shows up to 45% higher compression ratio than the constant-pressure jet ejector. The higher compression ratio of the constant-area jet ejector is particularly pronounced in the low motive-velocity region and the improvement decreases once the motive velocity increases. The constant-area jet ejector produces up to 10% higher efficiency than the constant-pressure design. The greater efficiency is more pronounced in the low motive-velocity region.

For D_N/D_P = 0.029, Table 12 summarizes the optimal geometries for both the constant-area and constant-pressure jet ejectors as a function of motive velocity (Mach number) and mass flow ratio. Because the results are presented in dimensionless form as a ratio with inlet diameter, the results are valid for operating at any geometric scale.

Table 12. Summary of the optimal geometries for the constant-area and constant-pressure jet ejectors ($D_N/D_P = 0.029$).

Independent parameters		Optimized geometry					
		Constant-area		Constant-pressure			
Mach	Mass flow ratio (m_m/m_p)	Throat diameter ratio (D_T/D_P)	Throat length ratio (L_T/D_P)	Convergent diameter ratio (D_C/D_P)	Convergent length ratio (L_C/D_P)	Throat diameter ratio (D_T/D_P)	Throat length ratio (L_T/D_P)
0.50	0.02	0.95	2.7	-	-	-	-
	0.05	0.36	1.9	0.47	1.50	0.36	0.10
	0.10	0.20	1.0	0.31	0.60	0.20	0.10
	0.50	0.08	0.4	0.19	0.20	0.08	0.10
	1.0	0.06	0.3	0.18	0.20	0.07	0.10
	5.0	0.05	0.3	0.18	0.10	0.07	0.10
	10.0	0.05	0.3	0.18	0.10	0.07	0.10
	50.0	0.05	0.3	0.18	0.05	0.07	0.10
	100.0	0.05	0.3	0.18	0.05	0.07	0.10
1.00	0.02	0.95	2.7	-	-	-	-
	0.05	0.36	1.9	0.47	1.50	0.36	0.10
	0.10	0.21	1.0	0.31	0.60	0.20	0.10
	0.50	0.08	0.4	0.19	0.20	0.08	0.10
	1.0	0.06	0.3	0.18	0.20	0.07	0.10
	5.0	0.05	0.3	0.18	0.10	0.07	0.10
	10.0	0.05	0.3	0.18	0.10	0.07	0.10
	50.0	0.05	0.3	0.18	0.05	0.07	0.10
	100.0	0.05	0.3	0.18	0.05	0.07	0.10
1.50	0.02	0.95	3.0	-	-	-	-
	0.05	0.37	2.1	0.47	1.50	0.36	0.10
	0.10	0.22	1.1	0.35	0.80	0.24	0.10
	0.50	0.09	0.5	0.23	0.20	0.12	0.10
	1.0	0.07	0.5	0.20	0.20	0.09	0.10

Table 12. Continued.

Independent parameters		Optimized geometry					
		Constant-area		Constant-pressure			
Mach	Mass flow ratio (m_m/m_p)	Throat diameter ratio (D_T/D_P)	Throat length ratio (L_T/D_P)	Convergent diameter ratio (D_C/D_P)	Convergent length ratio (L_C/D_P)	Throat diameter ratio (D_T/D_P)	Throat length ratio (L_T/D_P)
1.50	5.0	0.05	0.5	0.18	0.10	0.07	0.10
	10.0	0.05	0.5	0.18	0.10	0.07	0.10
	50.0	0.05	0.4	0.18	0.05	0.07	0.10
	100.0	0.05	0.4	0.18	0.05	0.07	0.10
2.00	0.02	0.95	4.8	-	-	-	-
	0.05	0.40	2.5	0.51	2.00	0.40	0.15
	0.10	0.24	1.5	0.35	0.90	0.24	0.15
	0.50	0.11	0.7	0.23	0.20	0.12	0.15
	1.0	0.08	0.7	0.20	0.20	0.09	0.15
	5.0	0.08	0.7	0.18	0.15	0.07	0.15
	10.0	0.07	0.7	0.18	0.15	0.07	0.15
	50.0	0.07	0.7	0.18	0.15	0.07	0.15
	100.0	0.07	0.7	0.18	0.15	0.07	0.15
2.50	0.02	0.95	5.2	-	-	-	-
	0.05	0.51	3.0	0.55	2.20	0.44	0.20
	0.10	0.29	2.5	0.39	1.30	0.28	0.20
	0.50	0.15	1.2	0.23	0.40	0.12	0.20
	1.0	0.11	0.9	0.21	0.30	0.10	0.20
	5.0	0.09	0.9	0.18	0.25	0.07	0.20
	10.0	0.09	0.9	0.18	0.25	0.07	0.20
	50.0	0.09	0.9	0.18	0.25	0.07	0.20
	100.0	0.09	0.9	0.18	0.25	0.07	0.20

Figure 26 presents the optimal throat length ratio L_T/D_P and the optimal throat diameter ratio D_T/D_P at various mass flow ratio mm/mp and motive velocity.

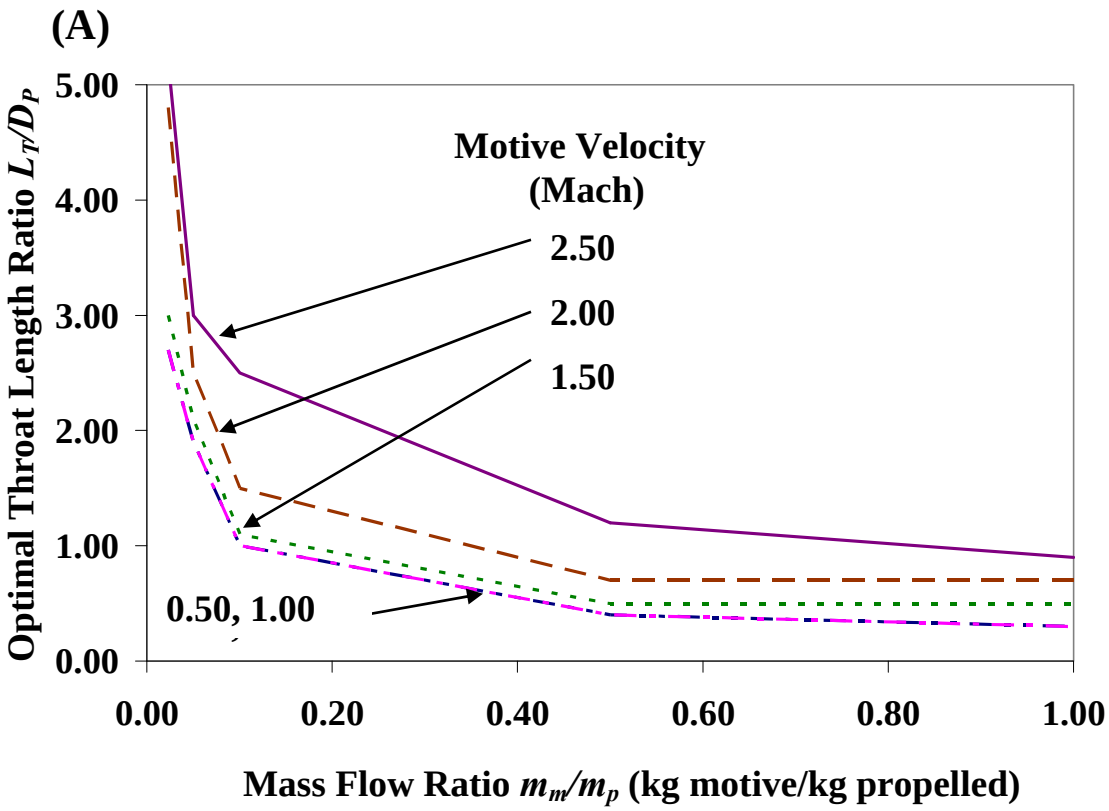

Figure 26. Optimal geometry of constant-area jet ejector (A) throat length, and (B) throat diameter.

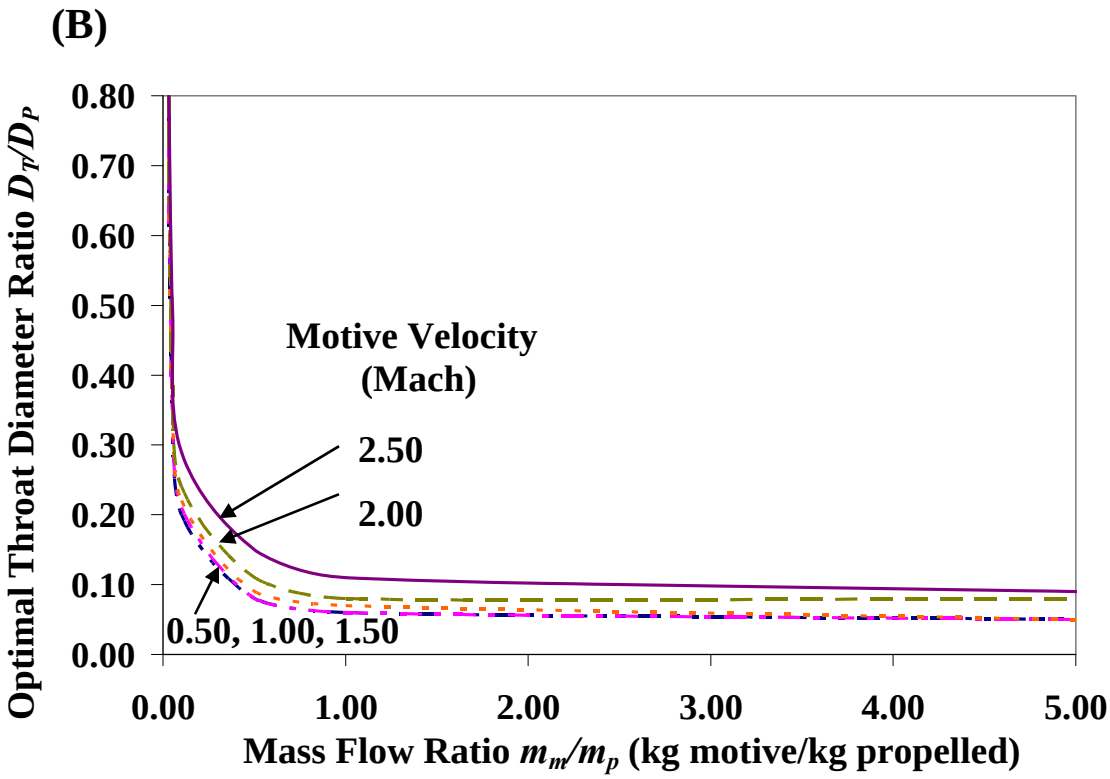

Figure 26. Continued.

Conclusion

Using CFD analysis, this paper compares constant-area and constant-pressure jet ejectors. Based upon compression ratio and efficiency, the constant-area design produces the best performance for all motive velocities and mass flow ratios investigated. At all operating conditions, the constant-area jet ejector shows up to 45% higher compression ratio than the constant-pressure jet ejector. The constant-area jet ejector produces up to 10% higher efficiency than the constant-pressure design. For a constant nozzle diameter ratio D_N/D_P = 0.029, the optimal geometries of both jet ejectors are reported in dimensionless form as a function of motive-stream velocity and mass flow ratio.

CHAPTER VI

CONSTANT-AREA JET EJECTOR OPTIMIZATION

Introduction

This chapter summarizes the optimization of constant-area jet ejectors using computational fluid dynamics (CFD). To achieve the greatest efficiency at each motive velocity and mass flow ratio, all parameters affecting jet ejector performance were thoroughly investigated, such as nozzle diameter, throat length, and throat diameter. At a given nozzle diameter (D_N/D_P = 0.029), the previous chapter indicates that a constant-area jet ejector provides greater compression ratio and efficiency than a conventional constant-pressure jet ejector at every operating condition; hence, the constant-area jet ejector is the focus of the optimization study in this chapter. In this study, the motive velocity ranged from 170 to 1104 m/s (Mach 0.50 to 3.25) and mass flow ratio from 0.02 to 100.0 kg motive/ kg propelled. The back pressure of the ejector is maintained constant at 101.3 kPa. The compression ratio and efficiency is reported according to the optimal geometry (throat length, throat diameter, and nozzle diameter) for each operating condition. In all cases, steam is used as the working fluid for both the motive and propelled streams. The outlet pressure was specified at 1 atm; the inlet pressure was under vacuum, depending upon the compression ratio. The procedure to apply the optimization results to design an optimal high-efficiency jet ejector for an arbitrary operating condition is explained.

Methodology

Figure 27 presents the optimization methodology. As mentioned earlier, the motive velocity and mass flow ratio were specified as independent parameters and varied over a wide range. The motive velocity ranges from 170 to 1104 m/s and the mass flow ratio is between 0.01 and 100 kg motive/ kg propelled.

Every procedure started with the original model (Figure 28) and its dimensions (Table 13). The initial conditions in the study were the minimum motive velocity (v_m = 170 m/s), minimum mass flow ratio (m_m/m_p = 0.01 kg motive/ kg propelled), and very small nozzle diameter ratio (D_N/D_P = 0.01). The throat diameter and length were adjusted until the optimum performance was found. This procedure determined the optimal ejector geometry for a particular motive velocity, mass flow ratio, and nozzle diameter ratio. Then, a higher mass flow ratio was explored, following the same pattern previously described until all mass flow ratios (0.01 to 100 kg motive/ kg propelled) were thoroughly explored. Next, the nozzle diameter ratio was adjusted, but the motive velocity remained constant, and the mass flow ratio was again varied from 0.01 to 100 kg motive/ kg propelled.

This process was continued until the optimum nozzle diameter ratio was discovered for a particular motive velocity. The optimum nozzle diameter gave the maximum compression ratio and efficiency for every mass flow ratio at a given motive velocity. Once the optimum nozzle diameter ratio was identified, then the process was repeated with another motive velocity within the range from 170 to 1104 m/s. According to the literature (e.g., ESDU, 1986), the optimum position to place a nozzle is near the beginning of the throat section; therefore, the nozzle in the experiment was placed at the

beginning of the throat section $(l = 0)$ and was not an optimized parameter. The geometric parameters are presented in dimensionless form by creating a ratio with jet-ejector inlet diameter D_P.

Results and Discussion

Table 14 presents the optimized geometry of the constant-area jet ejector. All parameters are categorized into three groups:

1. Independent parameters (operating parameters): motive velocity and mass flow ratio
2. Optimized geometric parameters: nozzle diameter ratio, throat diameter ratio, and length ratio
3. Dependent parameters: compression ratio and efficiency

The information is presented in motive-velocity order, which ranges from 170 to 1104 m/s

The optimized geometric and dependent parameters are presented in Figures 29A to 29D as function of motive velocity v_m and mass flow ratio m_m/m_p.

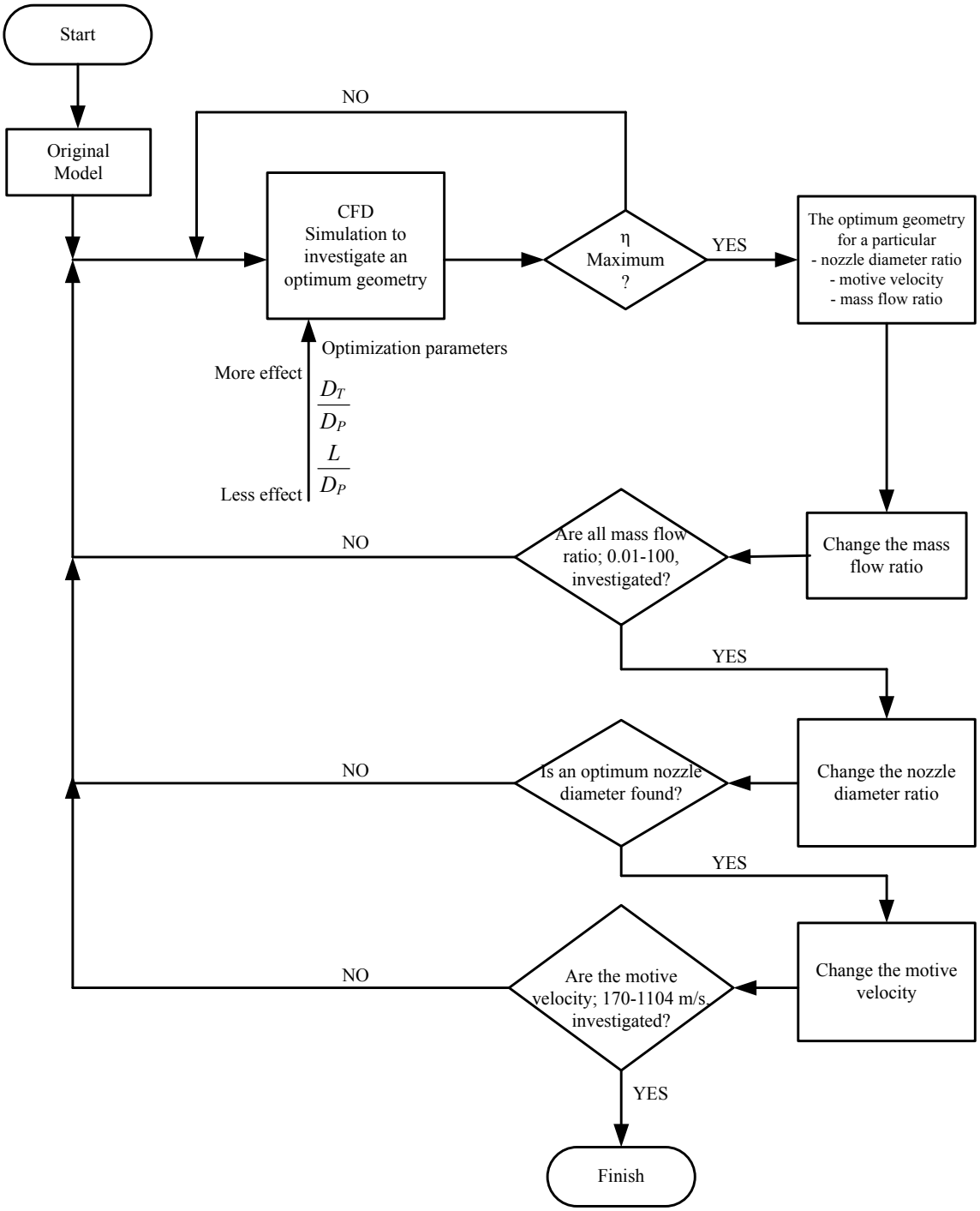

Figure 27. Optimization methodology.

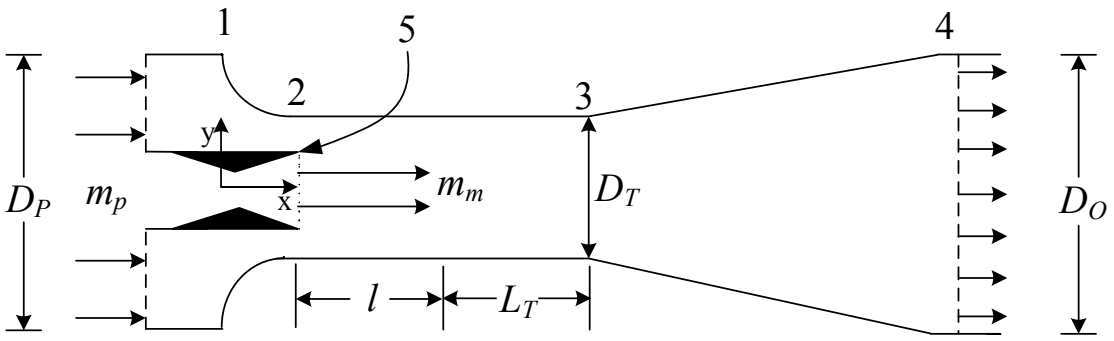

Figure 28. Jet ejector geometry in high-efficiency jet ejector.

Table 13. Jet ejector dimension according to points in Figure 28 (unit: millimeter).

Point number	x-coordinate	y-coordinate
1	0	105.78
2	97.79	42.28
3	1367.79	42.28
4	2442.21	105.78
5	97.79	3.04

Table 14. The optimization study result.

Independent parameters		Optimized geometric parameters			Dependent parameters	
Motive velocity v_m	Mass flow ratio m_m/m_p	Nozzle diameter ratio D_N/D_P	Throat diameter ratio D_T/D_P	Throat length ratio L_T/L_P	Compres-sion ratio P_o/P_p	Efficiency η
170 m/s (Mach 0.50)	0.03	0.05	0.950	4.0	1.0006	0.9977
	0.05		0.700	3.0	1.0006	0.9964
	0.10		0.348	2.2	1.0015	0.9940
	0.50		0.128	0.9	1.0113	0.9853
	1.00		0.098	0.6	1.0224	0.9818
	5.00		0.066	0.3	1.0559	0.9804
	10.00		0.062	0.3	1.0689	0.9810
	50.00		0.052	0.3	1.1004	0.9789
	100.00		0.052	0.3	1.1114	0.9783
340 m/s (Mach 1.00)	0.03	0.046	0.950	4.0	1.0025	0.9912
	0.05		0.650	3.1	1.0026	0.9863
	0.10		0.380	2.1	1.0066	0.9768
	0.50		0.120	1.2	1.0597	0.9447
	1.00		0.090	0.7	1.1195	0.9303
	5.00		0.056	0.4	1.4370	0.9051
	10.00		0.056	0.3	1.7819	0.8780
	50.00		0.054	0.3	2.2719	0.8695
	100.00		0.052	0.3	2.6175	0.8748

Table 14. Continued.

Independent parameters		Optimized geometric parameters			Dependent parameters	
Motive velocity v_m	Mass flow ratio m_m/m_p	Nozzle diameter ratio D_N/D_P	Throat diameter ratio D_T/D_P	Throat length ratio L_T/L_P	Compres-sion ratio P_o/P_p	Efficiency η
510 m/s (Mach 1.50)	0.03	0.044	0.95	4.5	1.0057	0.9804
	0.05		0.65	3.2	1.0061	0.9699
	0.10		0.38	2.3	1.0145	0.9474
	0.50		0.12	1.0	1.1450	0.8686
	1.00		0.098	0.7	1.3240	0.8254
	5.00		0.075	0.5	2.2827	0.6876
	10.00		0.072	0.5	2.8464	0.6332
	50.00		0.068	0.5	4.2732	0.5668
	100.00		0.068	0.5	4.6358	0.5542
680 m/s (Mach 2.00)	0.03	0.044	0.950	4.5	1.0110	0.9646
	0.05		0.750	3.5	1.0117	0.9473
	0.10		0.400	2.6	1.0289	0.9120
	0.50		0.144	1.4	1.2676	0.7890
	1.00		0.118	1.2	1.5541	0.7115
	5.00		0.100	0.7	3.0767	0.5181
	10.00		0.095	0.7	4.1293	0.4549
	50.00		0.088	0.7	7.8180	0.3786
	100.00		0.088	0.7	9.7421	0.3647

Table 14. Continued.

Independent parameters		Optimized geometric parameters			Dependent parameters	
Motive velocity v_m	Mass flow ratio m_m/m_p	Nozzle diameter ratio D_N/D_P	Throat diameter ratio D_T/D_P	Throat length ratio L_T/L_P	Compres-sion ratio P_o/P_p	Efficiency η
850 m/s (Mach 2.50)	0.05	0.044	0.95	5.2	1.0227	0.9198
	0.09		0.50	3.2	1.0484	0.8851
	0.10		0.50	3.2	1.0590	0.8789
	0.50		0.19	1.8	1.3922	0.6928
	1.00		0.155	1.7	1.6986	0.5768
	5.00		0.133	1.2	4.1297	0.3771
	10.00		0.130	1.0	6.0759	0.3093
	50.00		0.120	1.0	14.8304	0.2359
	100.00		0.120	1.0	21.7476	0.2219
1020 m/s (Mach 3.00)	0.03	0.030	0.950	5.0	1.0312	0.9277
	0.05		0.620	3.0	1.0348	0.8931
	0.09		0.440	2.7	1.0583	0.8347
	0.10		0.400	2.5	1.0706	0.8254
	0.50		0.178	1.7	1.4136	0.5689
	1.00		0.148	1.6	1.9201	0.4655
	5.00		0.129	1.5	5.2329	0.2566
	10.00		0.127	1.4	8.5142	0.2025
	50.00		0.123	1.1	33.0519	0.1323
	100.00		0.123	1.0	58.4498	0.1179

Table 14. Continued.

Independent parameters		Optimized geometric parameters			Dependent parameters	
Motive velocity v_m	Mass flow ratio m_m/m_p	Nozzle diameter ratio D_N/D_P	Throat diameter ratio D_T/D_P	Throat length ratio L_T/L_P	Compres-sion ratio P_o/P_p	Efficiency η
1104 m/s (Mach 3.25)	0.05	0.030	0.950	4.5	1.0498	0.8740
	0.075		0.900	3.5	1.0654	0.8378
	0.10		0.850	3.2	1.0790	0.7943
	0.25		0.300	2.1	1.2232	0.6390
	0.50		0.228	1.8	1.4396	0.4967
	1.00		0.185	1.7	1.7780	0.3826
	5.00		0.178	1.5	6.2830	0.2170
	10.00		0.175	1.5	10.9659	0.1605

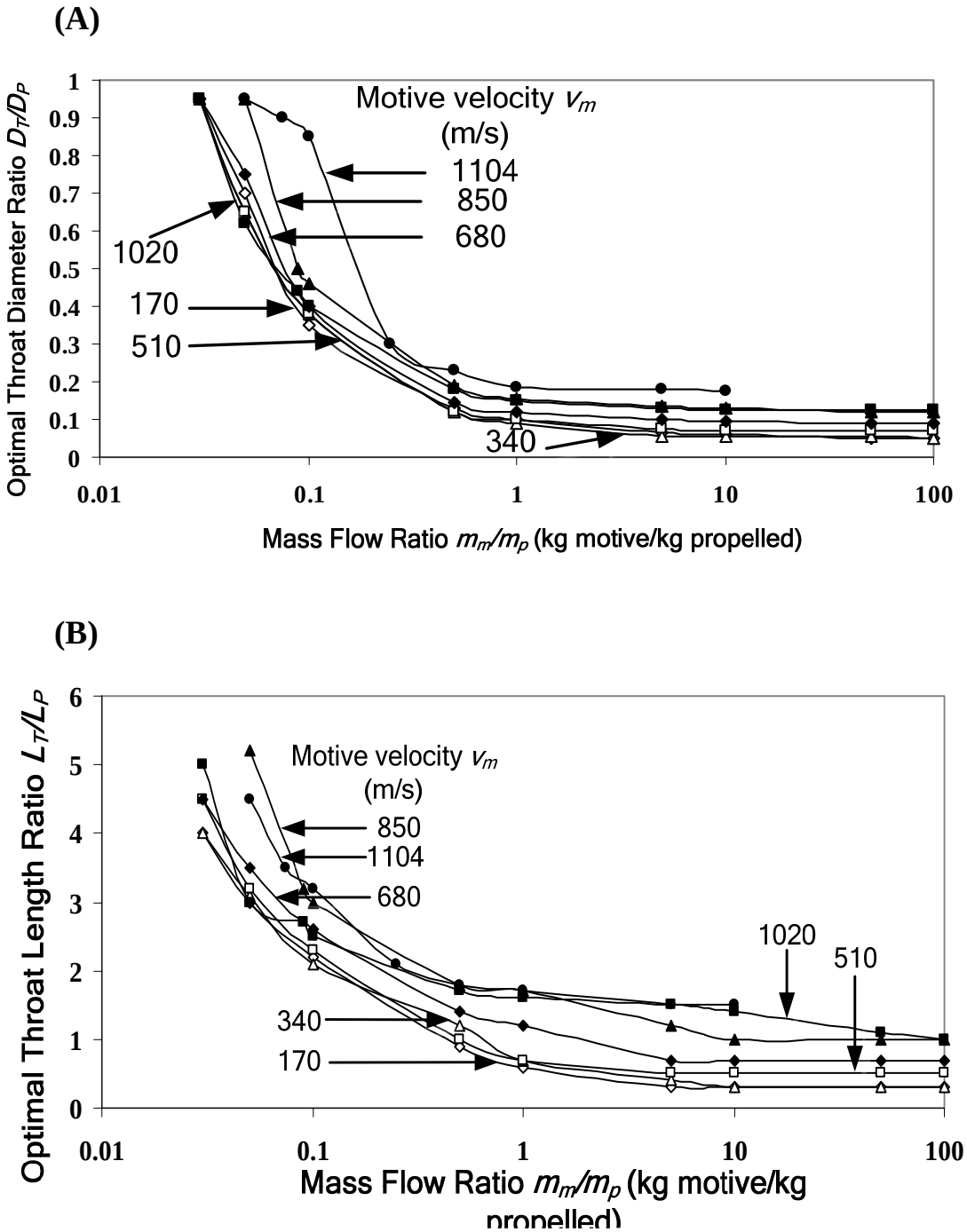

Figure 29. Optimized constant-area jet ejector. (A) Optimal throat diameter ratio D_T/D_P, (B) optimal throat length ratio L_T/D_P, (C) compression ratio P_o/P_p, and (D) efficiency.

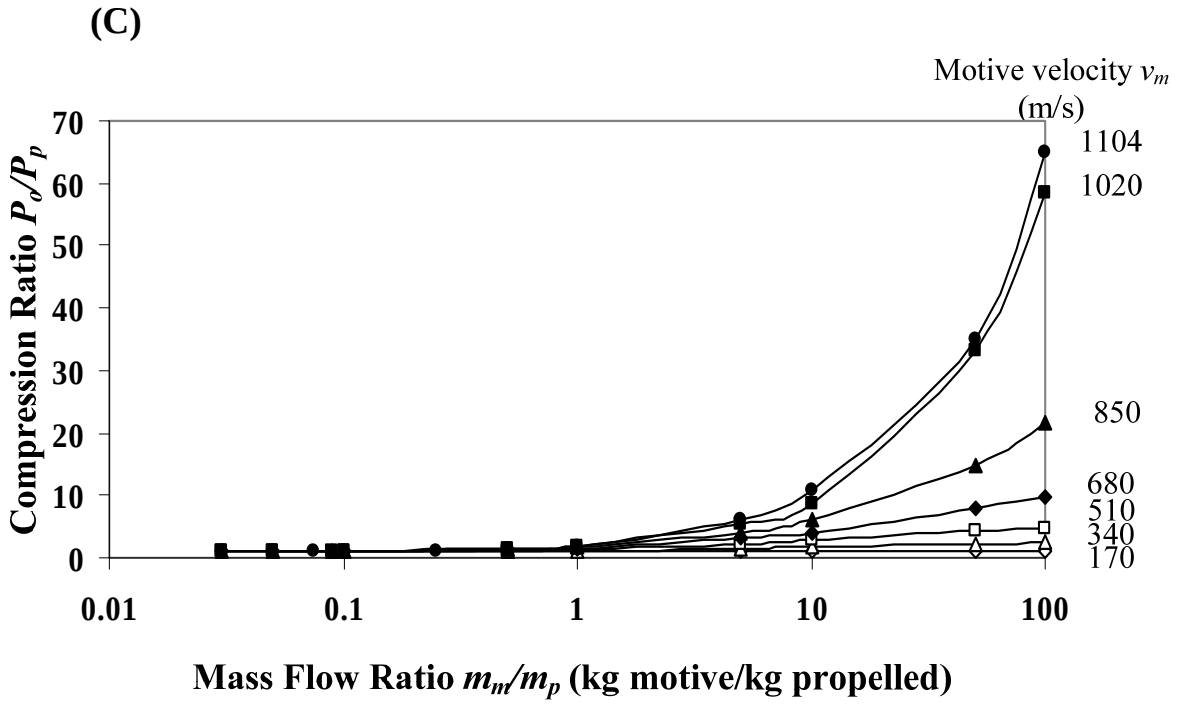

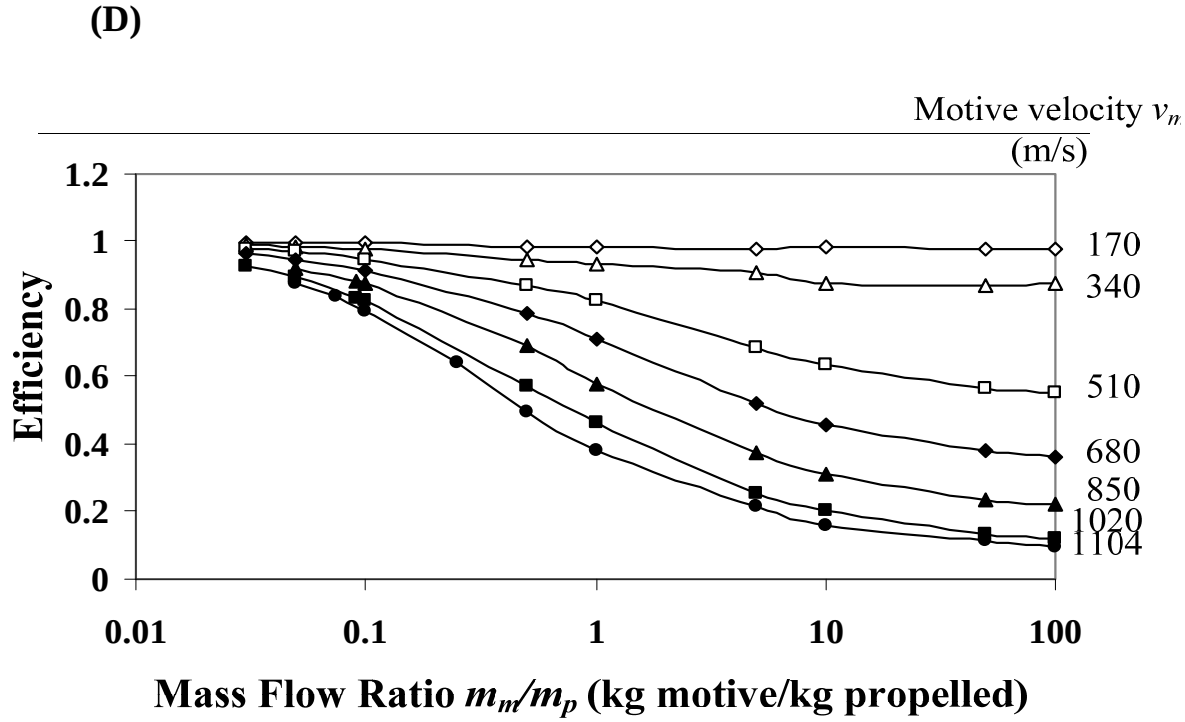

Figure 29. Continued.

Example

The procedure for implementing the results and selecting the optimal jet ejector geometry is explained in this example. A jet ejector using steam as a working fluid is operated at compression ratio 1.10, which would be typical in thermo-compression distillation.

1. From Table 14, search the optimization results that fall within the specified compression ratio region (see Table 15).

At a motive velocity of 170 m/s, the mass flow ratio is almost 50 kg motive/kg propelled to achieve the 1.10 compression ratio, which means a jet ejector that propels 1 kg/s of steam will consume 50 kg/s of motive steam. This does not make economic sense, even though the efficiency is very high (97.89%). Higher velocities (340 to 1104 m/s) use less motive steam, but have a lower efficiency.

2. Plot the compression ratio versus mass flow ratio for each motive velocity (Figure 30).

3. Draw a horizontal line through the desired compression ratio (Figure 31). (In the sample case, the compression ratio is 1.10.)

The horizontal line intersects each curve. At the intersection point, a vertical line was drawn to the *x*-axis, which indicates the required mass flow ratio for each motive velocity (Figure 32).

4. Plot the efficiency versus mass flow ratio at each motive velocity (Figure 33).

To identify the efficiency, draw a vertical line from the mass flow ratio obtained from Step 3 and then draw a horizontal line to the *y*-axis (Figure 34).

5. Summarize the compression ratio and efficiency information for each motive

velocity (Table 16).

Table 15. Results according to Step 1.

Motive velocity v_m (m/s)	Mass flow ratio m_m/m_p (kg motive/kg propelled)	Compression ratio P_o/P_p	Efficiency η
170	10	1.0689	0.9810
	50	1.1004	0.9789
	100	1.1114	0.9783
340	0.50	1.0597	0.9447
	1.00	1.1195	0.9303
510	0.10	1.0145	0.9474
	0.50	1.145	0.8686
680	0.10	1.0289	0.9120
	0.50	1.2676	0.7890
850	0.10	1.0590	0.8789
	0.50	1.3922	0.6928
1020	0.10	1.0706	0.8254
	0.50	1.4136	0.5689
1104	0.10	1.0790	0.7943
	0.25	1.2232	0.6390

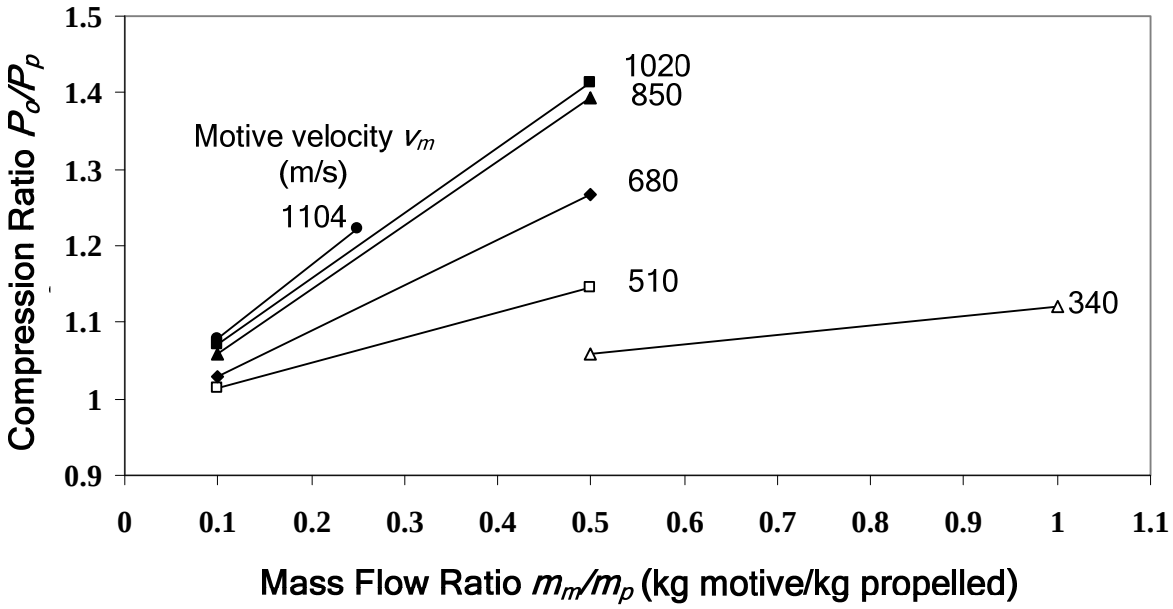

Figure 30. Relationship between compression ratio and mass flow ratio for each motive velocity.

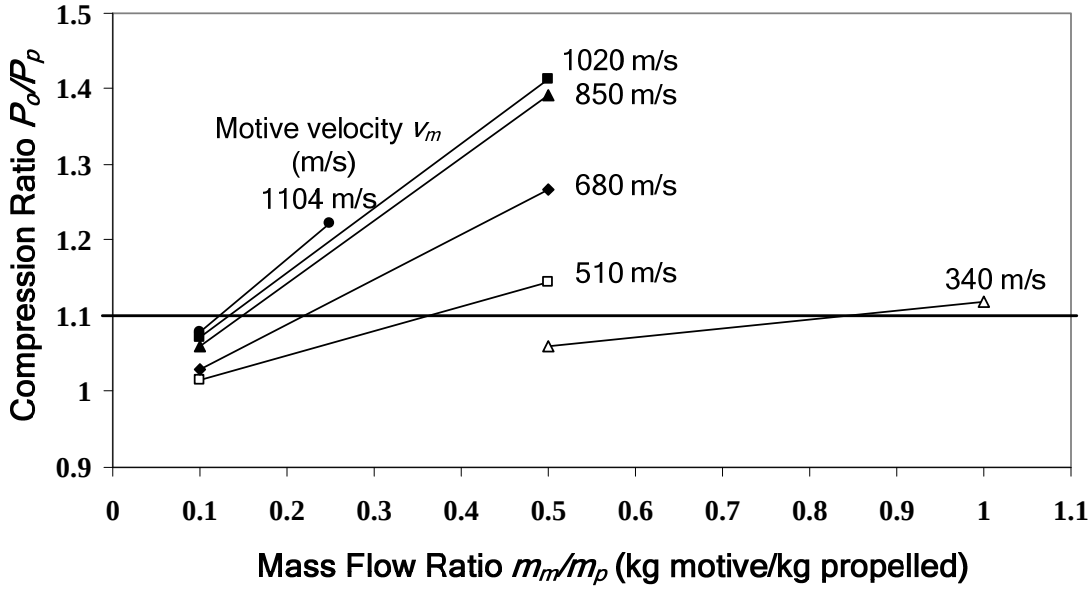

Figure 31. Graph for step 3.

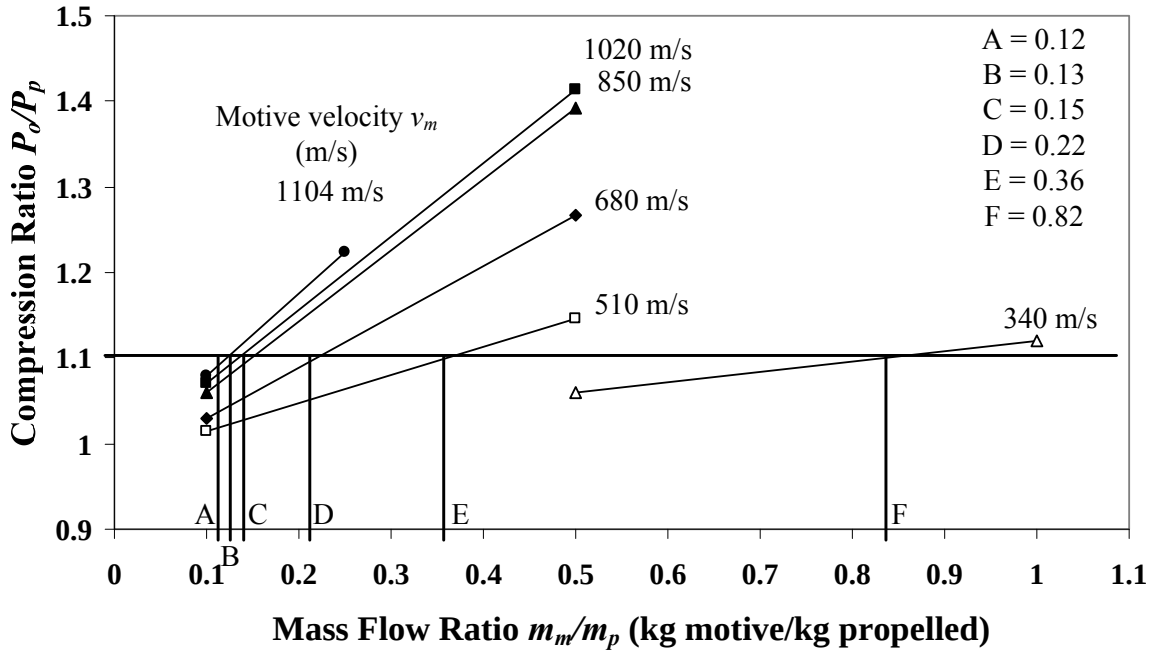

Figure 32. Required mass flow ratio for each motive velocity to achieve 1.10 compression ratio.

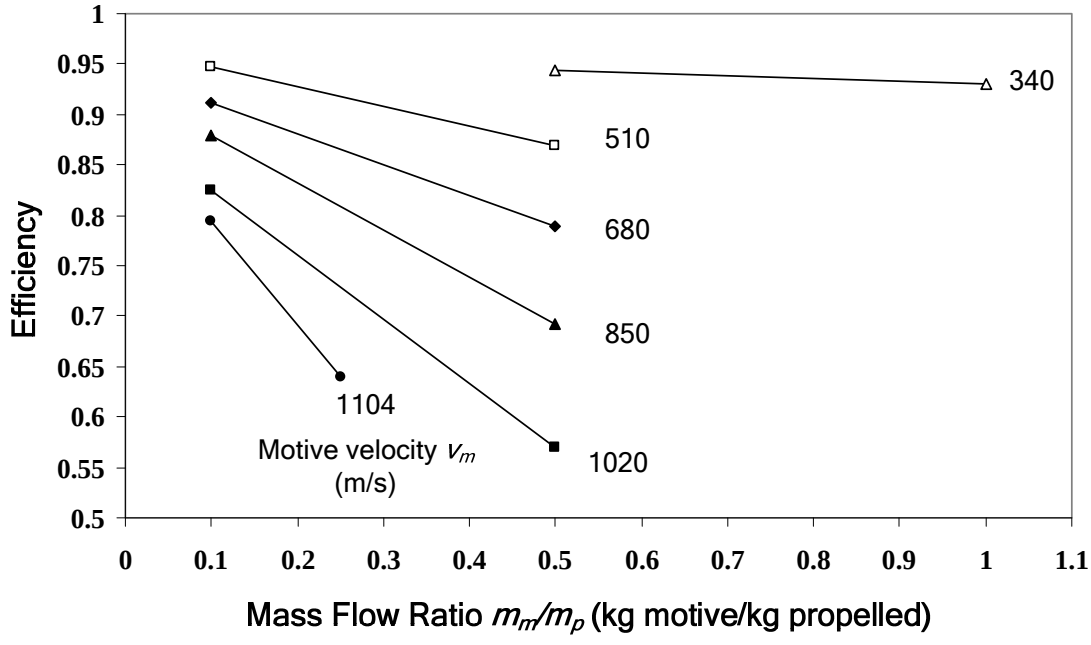

Figure 33. Relationship between efficiency and mass flow ratio for each motive velocity.

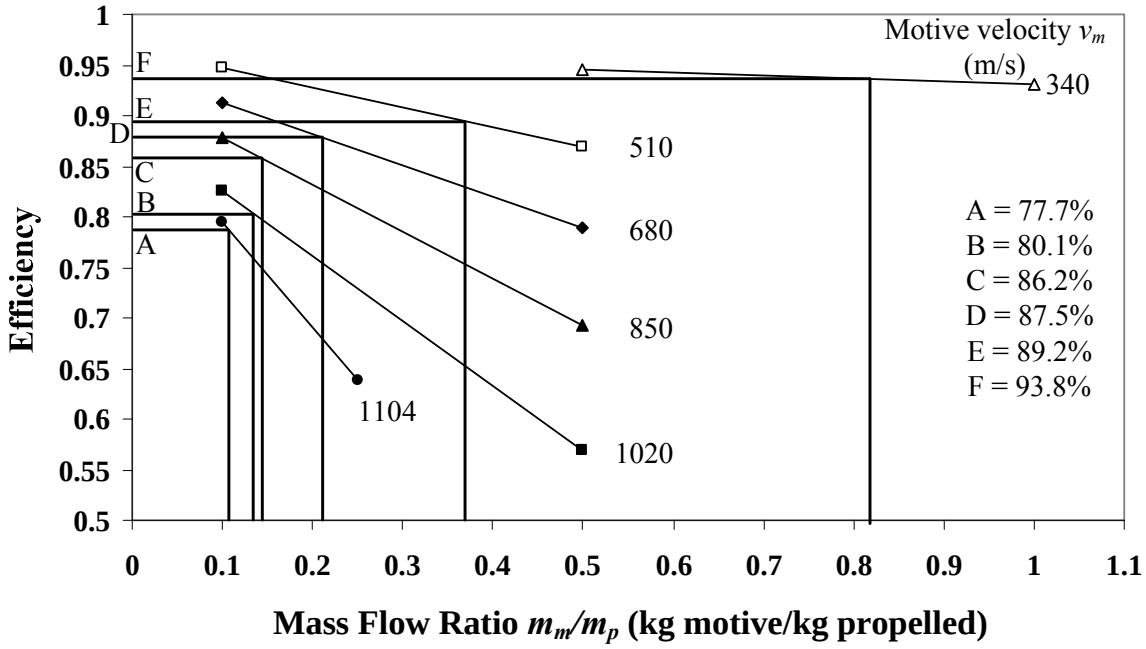

Figure 34. Efficiency of each motive velocity at compression ratio 1.10.

Table 16. Summary of the mass flow ratio and efficiency for each motive velocity at 1.10 compression ratio.

Required saturated steam pressure (atm)	Motive velocity v_m (m/s)	Mass flow ratio m_m/m_p (kg motive/kg propelled)	Efficiency η
1.69	340	0.82	93.8%
3.22	510	0.36	89.2%
6.21	680	0.22	87.5%
12.78	850	0.15	86.2%
31.42	1020	0.13	80.1%
60.66	1104	0.12	77.7%

The results in Table 16 indicate that for a 1.10 compression ratio, there are many possible operating conditions. The next step is to select the best motive velocity that consumes the smallest amount of motive steam, but still has a satisfactory efficiency. According to Table 16, the mass flow ratios at motive velocities between 340 and 680 m/s are high, so the operating costs are high. A suitable motive velocity should be between 850 and 1104 m/s. A motive velocity of 1104 m/s requires high-pressure, high-temperature steam. At some point, as the motive velocity increases, the required steam temperature and pressure will be so high as to be uneconomical. At a steam pressure of 12.78 to 31.42 atm, the motive velocity is 850 to 1020 m/s and the mass flow ratio is 0.15 and 0.13 kg motive/ kg propelled respectively, and the efficiency is 86.2% to 80.1%. The optimal geometry is obtained from either Table 14 (Figures 29A and 29B) for throat diameter and throat length respectively.

Conclusion

The optimal geometry of a high-efficiency constant-area jet ejector was determined. The motive velocities explored in this study range from 170 to 1104 m/s (Mach 0.5 to 3.25), which includes the 500 to 800 m/s conventional motive velocities used in industry (Lines and Smith, 1997). The mass flow ratio ranged from 0.02 to 100.0 kg motive/kg propelled, which is sufficiently broad to apply to nearly any jet ejector application. The dimensionless analysis makes the optimization results valid for any fluid, geometric scale, and operating condition. When the motive velocity is below Mach 1.5 (510 m/s), the optimized jet-ejector efficiency is above 90% for all nozzle diameters.

CHAPTER VII

NOZZLE OPTIMIZATION

Introduction

The focus of this chapter is to maximize efficiency and minimize motive stream consumption by optimizing the nozzle geometry in constant-area jet ejectors. There are two major parts to this study: (1) investigate the optimum nozzle diameter for each motive velocity and (2) determine the best nozzle design among simple and complex alternatives. A four-tube nozzle design provides the best efficiency and compression ratio. At a motive velocity of 1020 m/s and mass flow ratios above 1.00 kg motive/kg propelled, the four-tube jet ejector compression ratio increased more than 5% above a single-tube design. Below these conditions, the four-tube nozzle increased the compression ratio, but the increase was below 5%. Steam was used as the working fluid.

Methodology

This nozzle optimization is an extension of the previous optimizations of constant-area jet ejectors (see Chapters V and VI); therefore, the previously determined optimal geometries (throat length, throat diameter, and nozzle diameter) are used throughout this paper.

Optimal Single-Nozzle Diameter

The single-nozzle diameter was optimized for each motive velocity. The procedure began by adjusting the nozzle diameter ratio D_N/D_P for a given motive

velocity. The mass flow ratio was varied from 0.01 to 100 kg motive/kg propelled. Then, the motive velocity was adjusted to another value and the procedure was repeated until all motive velocities (170 and 1104 m/s) were investigated. This process was conducted until the optimal nozzle diameter ratio was discovered for a particular motive velocity. The optimal nozzle diameter gave the maximum compression ratio and efficiency for every mass flow ratio at a given motive velocity. The optimization was performed manually.

Optimal Multiple-Nozzle Designs

For each operating condition (motive velocity from 170 to 1104 m/s and mass flow ratio from 0.01 to 100 kg motive/kg propelled), the optimal constant-area jet ejector geometry for each operating condition is reported in Chapter VI of this series. The best nozzle design to accompany the optimal geometry is investigated in this section.

Three major nozzle configurations were utilized in this study:

1. Two stages (Figure 35A)
2. Annulus tube (Figure 35B)
3. Circular array (Figures 35C-G).

For all nozzle designs, the two key optimization parameters are *s* and *l*, which are defined in Figures 35 to 37. For the two-stage nozzle (Figure 35A), three area ratios (outer:inner) were considered: 1:3, 2:2, and 3:1. Because the geometries of all nozzle designs are similar, the optimal area ratio determined for the two-stage nozzle was used for the other nozzle designs also. The optimal results (compression ratio and efficiency) of each multiple nozzle design are compared with the optimal single nozzle of a constant-

area jet ejector. The ultimate objective is to identify the best nozzle design that maximizes both compression ratio and efficiency.

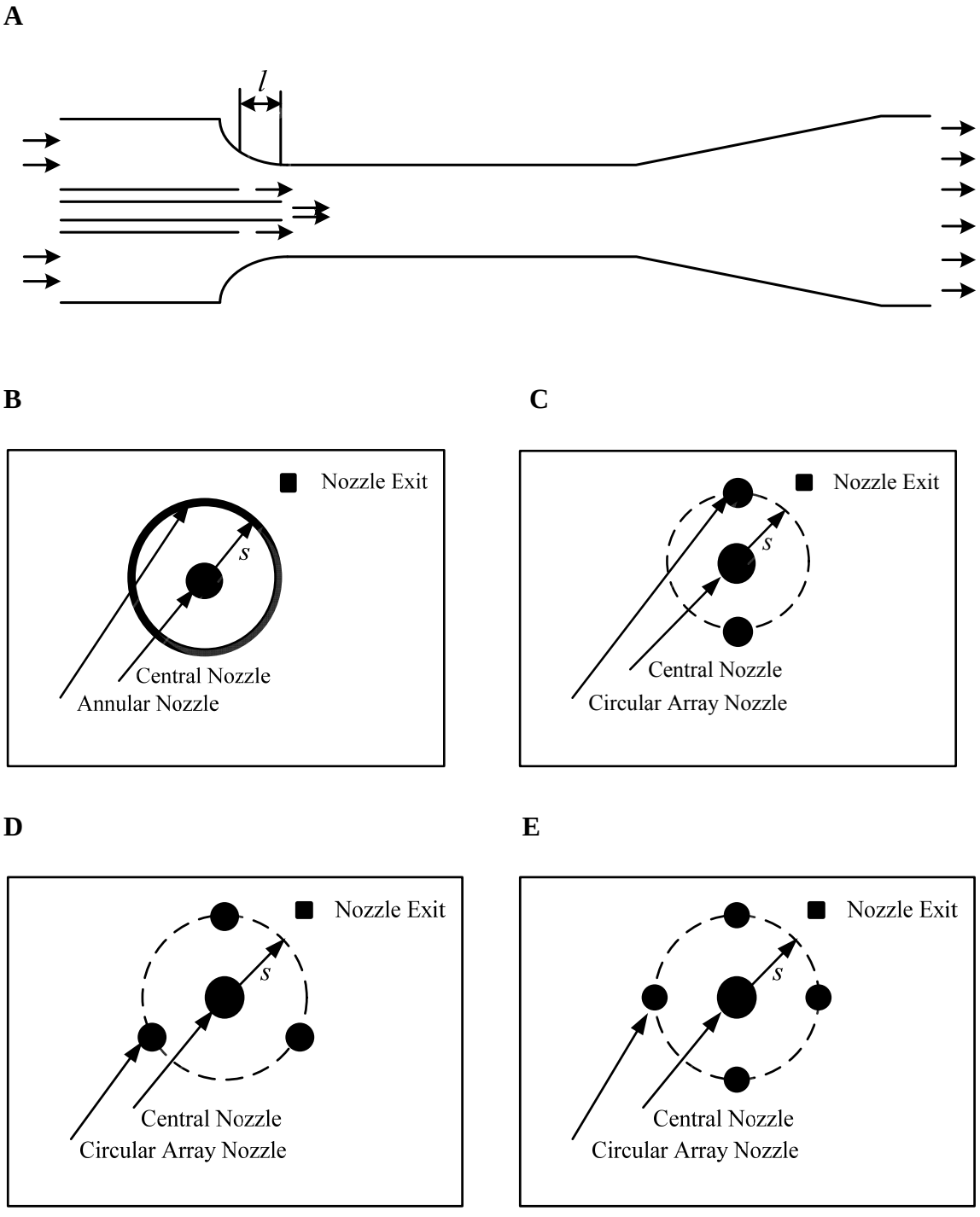

Figure 35. Nozzle configurations investigated. (A) Two stage (B) Annular (C) Two-tube circular array (D) Three -tube circular array (E) Four-tube circular array (F) Six-tube circular array (G) Eight-tube circular array.

F **G**

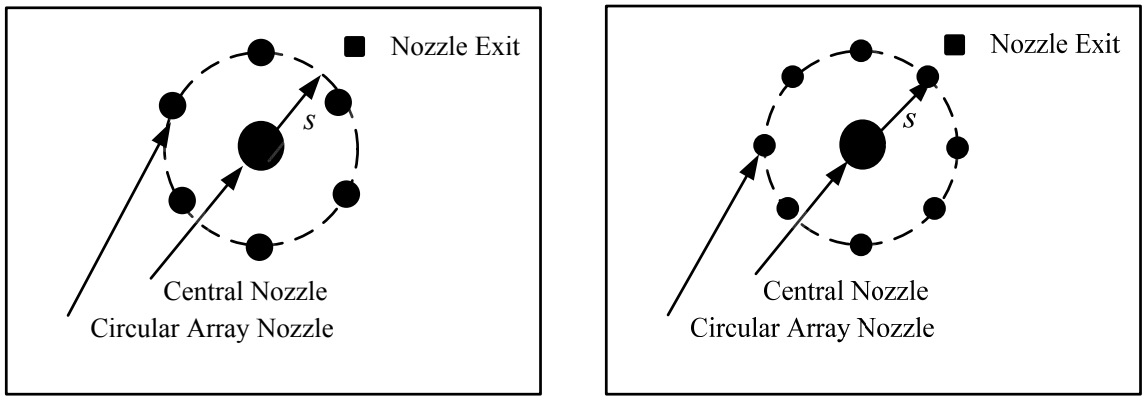

Figure 35. Continued.

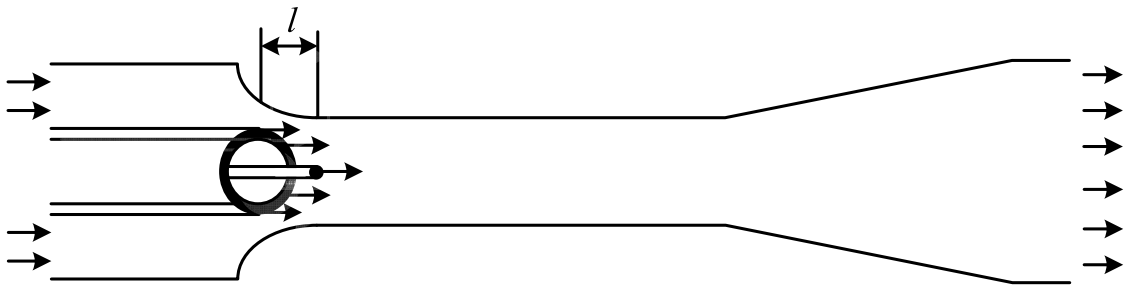

Figure 36. Definition of *l* in the annular nozzle design.

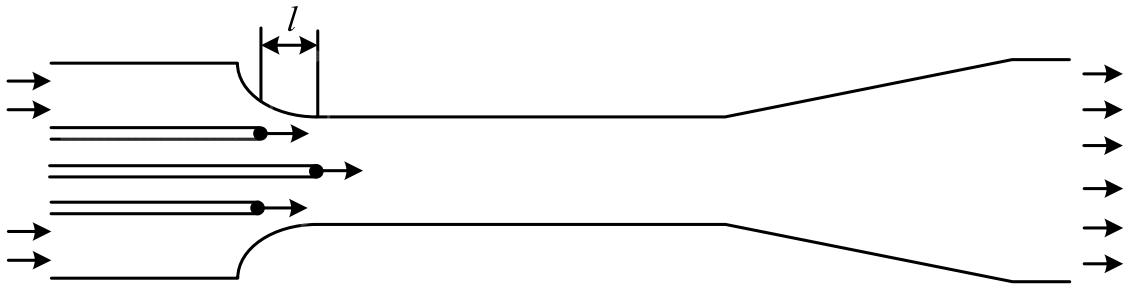

Figure 37. Definition of *l* in the multiple-tube circular array nozzle design.

Results and Discussion

Optimal Single-Nozzle Diameter

Figures 38 to 45 show the compression ratio and efficiency plotted against mass flow ratio (kg motive/kg propelled) for motive velocities ranging from 170 to 1104 m/s. The graphs show an optimal nozzle diameter ratio D_N/D_P for each motive velocity. In most cases, the efficiency is not significantly affected by nozzle size, especially when the nozzle diameter ratio is greater than 0.03. The compression ratio and efficiency are rarely different at low mass flow ratios, but the differences increase significantly at higher mass flow ratios, so these are used to determine the optimal nozzle diameter ratio. The efficiency and compression ratio are not much different when the nozzle diameter ratio is greater than 0.03, but at low nozzle diameter ratios (~0.01), the compression ratio and efficiency are dramatically lower. The optimal nozzle diameter ratio is smaller at higher motive velocities. At the lowest motive velocity (170 m/s), the optimal value is 0.05 whereas at the highest motive velocity (1104 m/s), the optimal value is 0.03. Table 17 summarizes the results of the optimal nozzle diameter.

Table 17. Optimal single-nozzle diameter.

Motive velocity		Optimal nozzle diameter ratio (D_N/D_P)
m/s	Mach number	
170	0.50	0.044
340	1.00	0.046
510	1.50	0.044
680	2.00	0.044
850	2.50	0.044
1020	3.00	0.030
1104	3.25	0.030

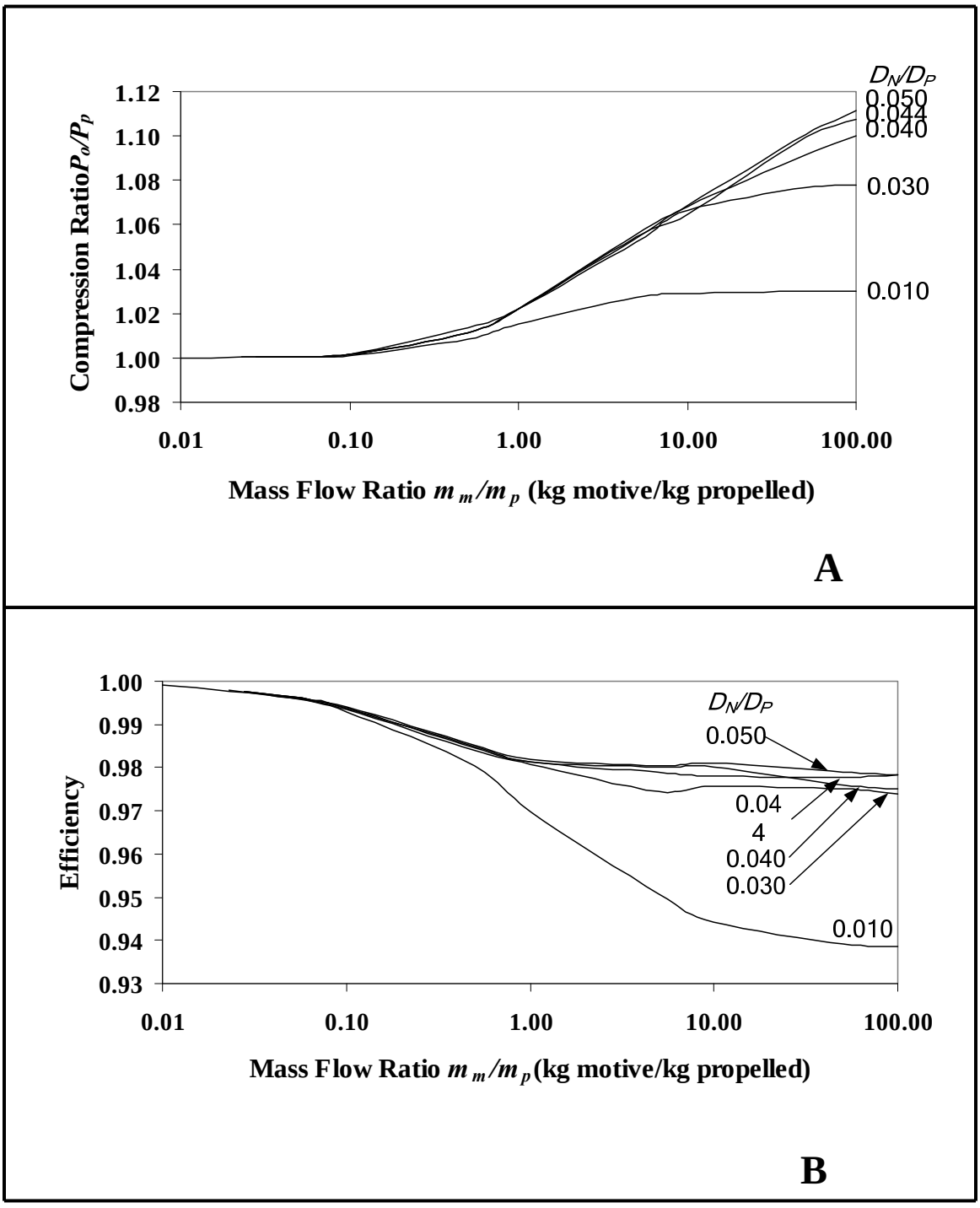

Figure 38. CFD simulation results for different nozzle diameter ratios at 170 m/s. A) Compression ratio B) Efficiency.
(Note: All curves are plotted using the optimal D_T/D_P and L_T/D_P determined in Chapter VI.)

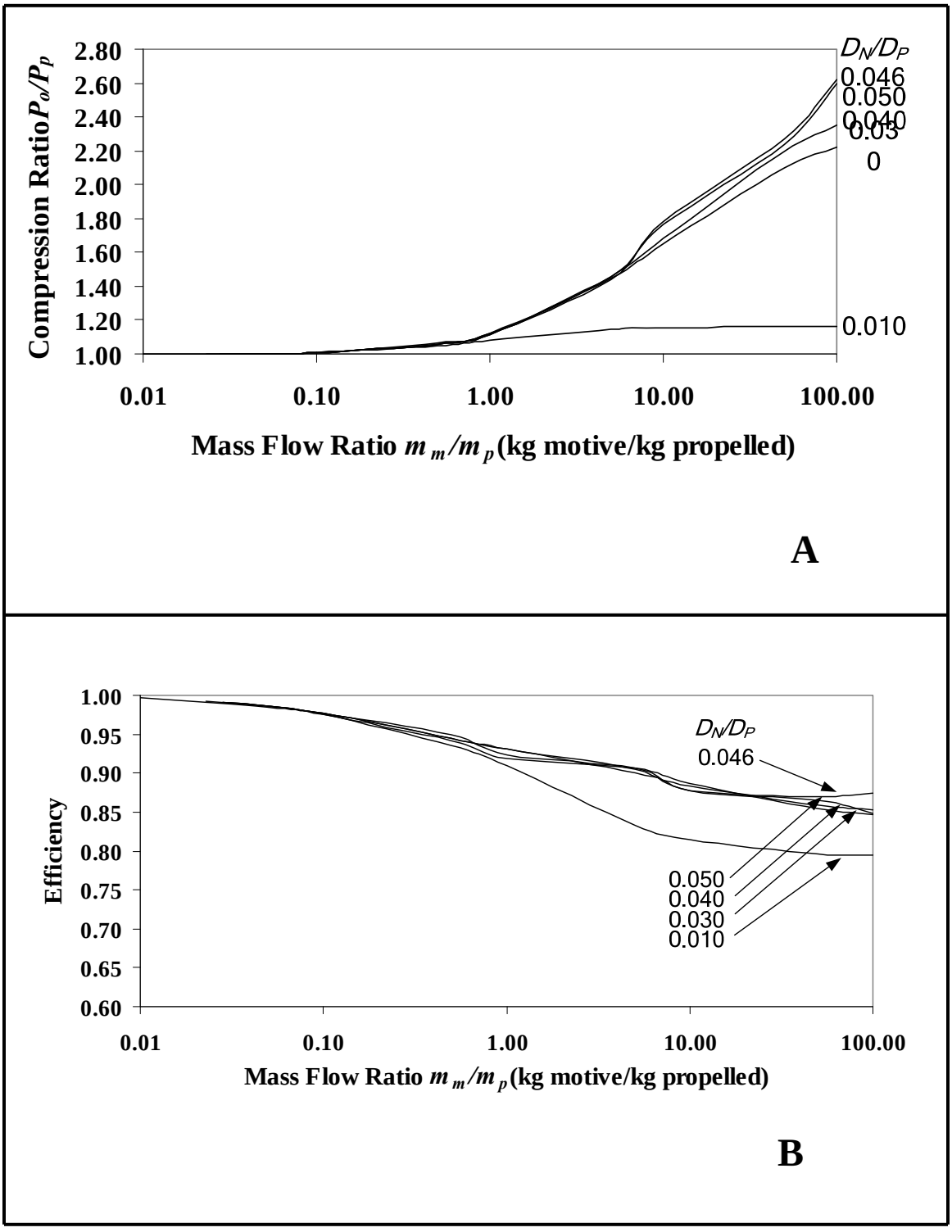

Figure 39. CFD simulation results for different nozzle diameter ratios at 340 m/s. A) Compression ratio B) Efficiency.
(Note: All curves are plotted using the optimal D_T/D_P and L_T/D_P determined in Chapter VI.)

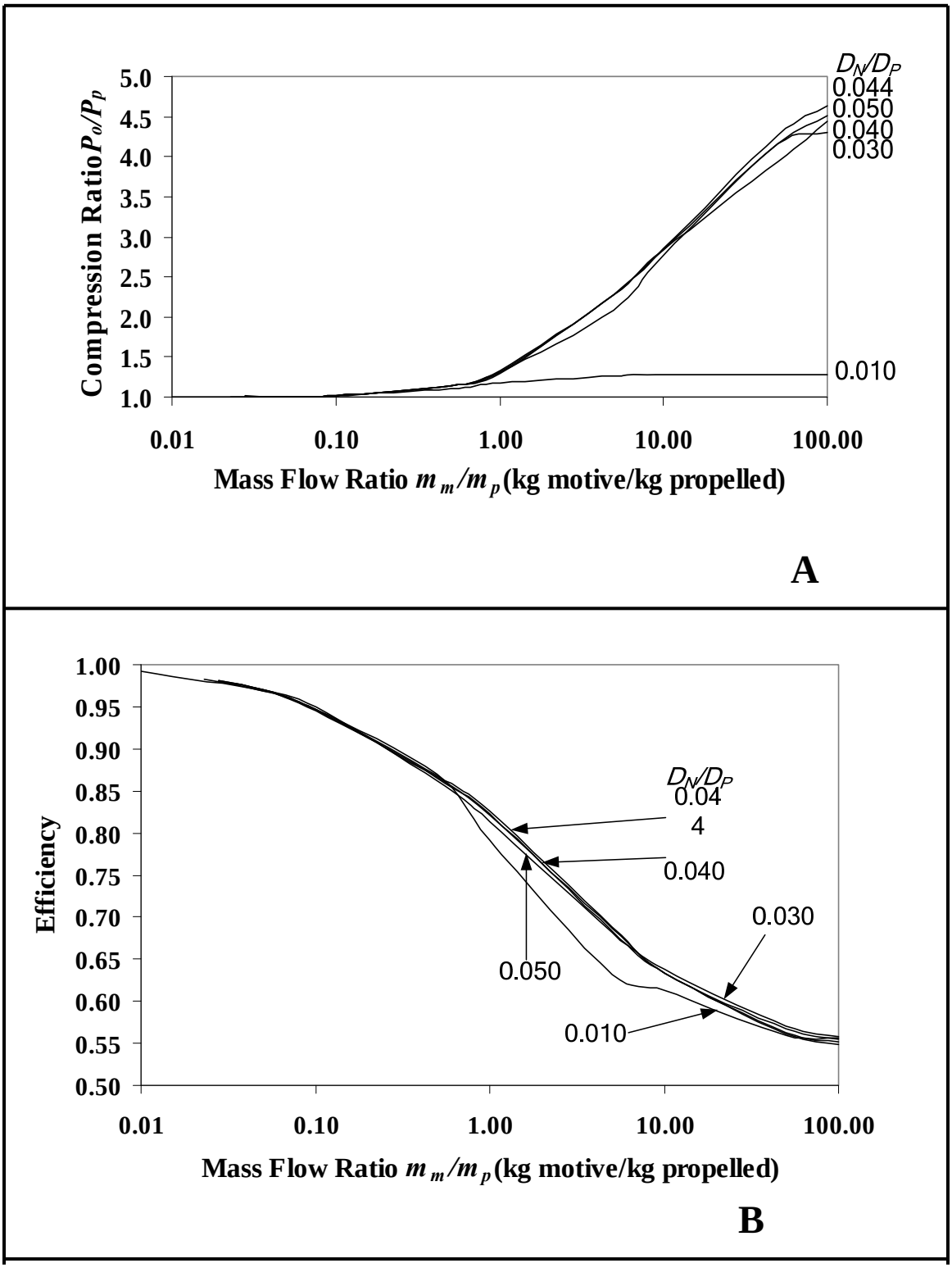

Figure 40. CFD simulation results for different nozzle diameter ratios at 510 m/s. A) Compression ratio B) Efficiency.
(Note: All curves are plotted using the optimal D_T/D_P and L_T/D_P determined in Chapter VI.)

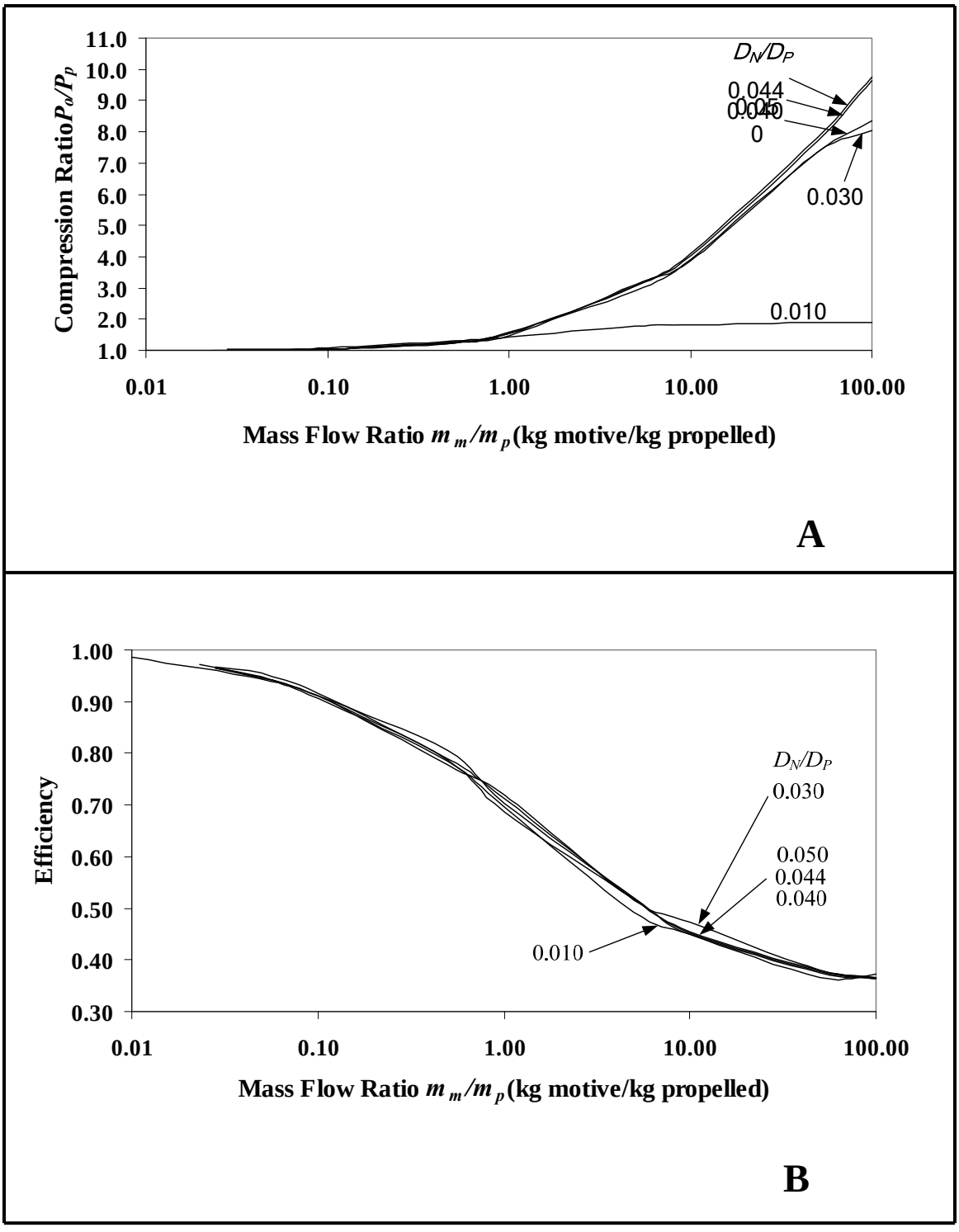

Figure 41. CFD simulation results for different nozzle diameter ratios at 680 m/s. A) Compression ratio B) Efficiency.
(Note: All curves are plotted using the optimal D_T/D_P and L_T/D_P determined in Chapter VI.)

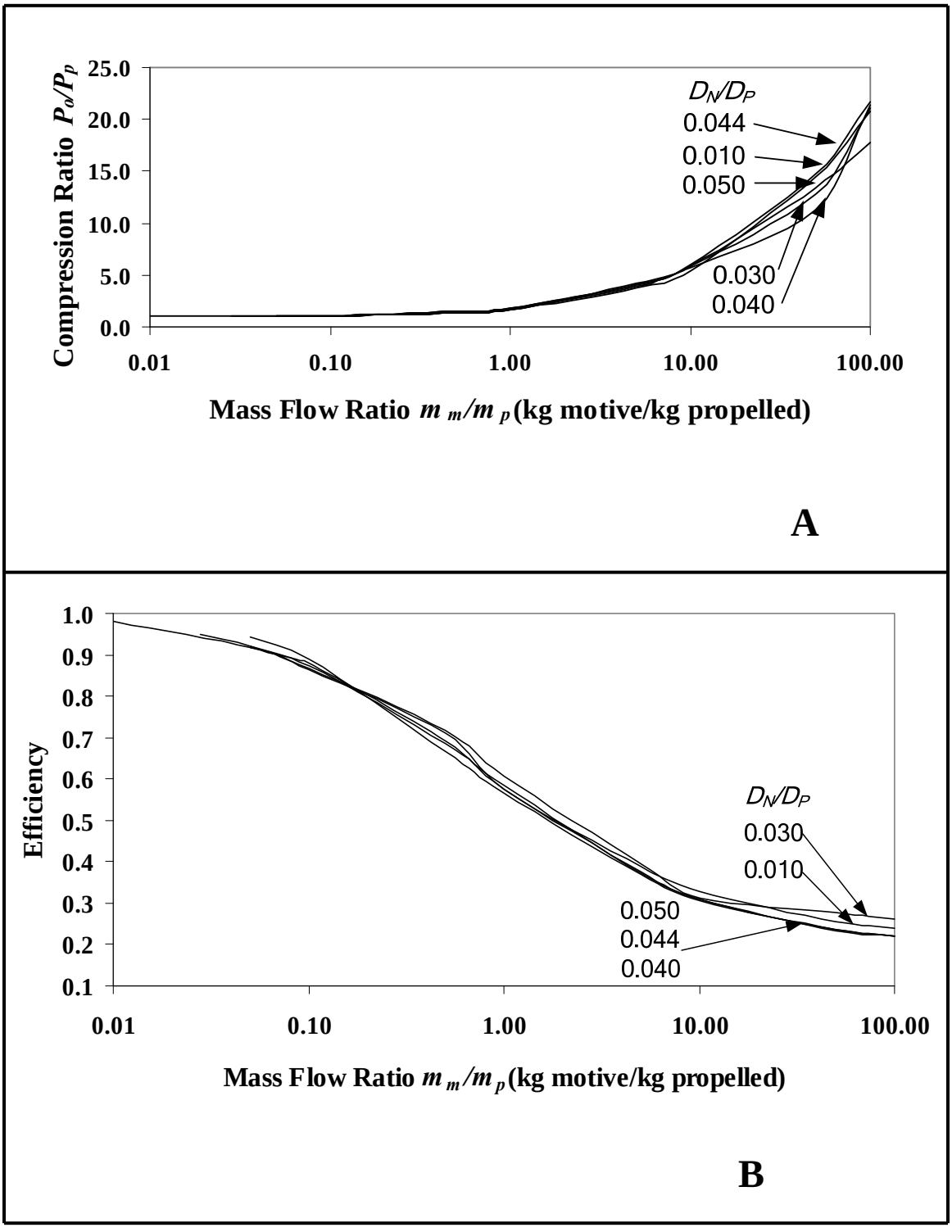

Figure 42. CFD simulation results for different nozzle diameter ratios at 850 m/s. A) Compression ratio B) Efficiency.
(Note: All curves are plotted using the optimal D_T/D_P and L_T/D_P determined in Chapter VI.)

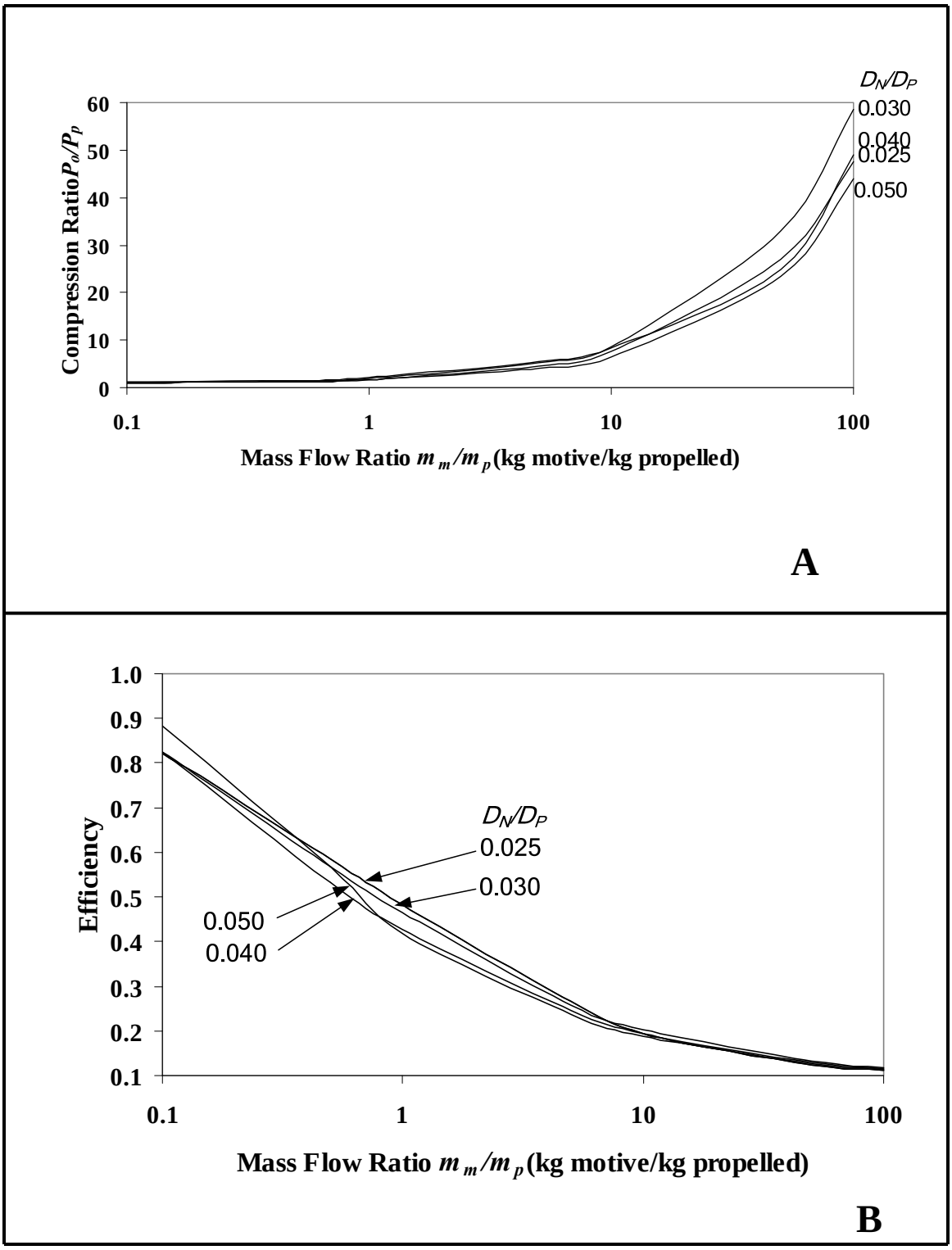

Figure 43. CFD simulation results for different nozzle diameter ratios at 1020 m/s. A) Compression ratio B) Efficiency.
(Note: All curves are plotted using the optimal D_T/D_P and L_T/D_P determined in Chapter VI.)

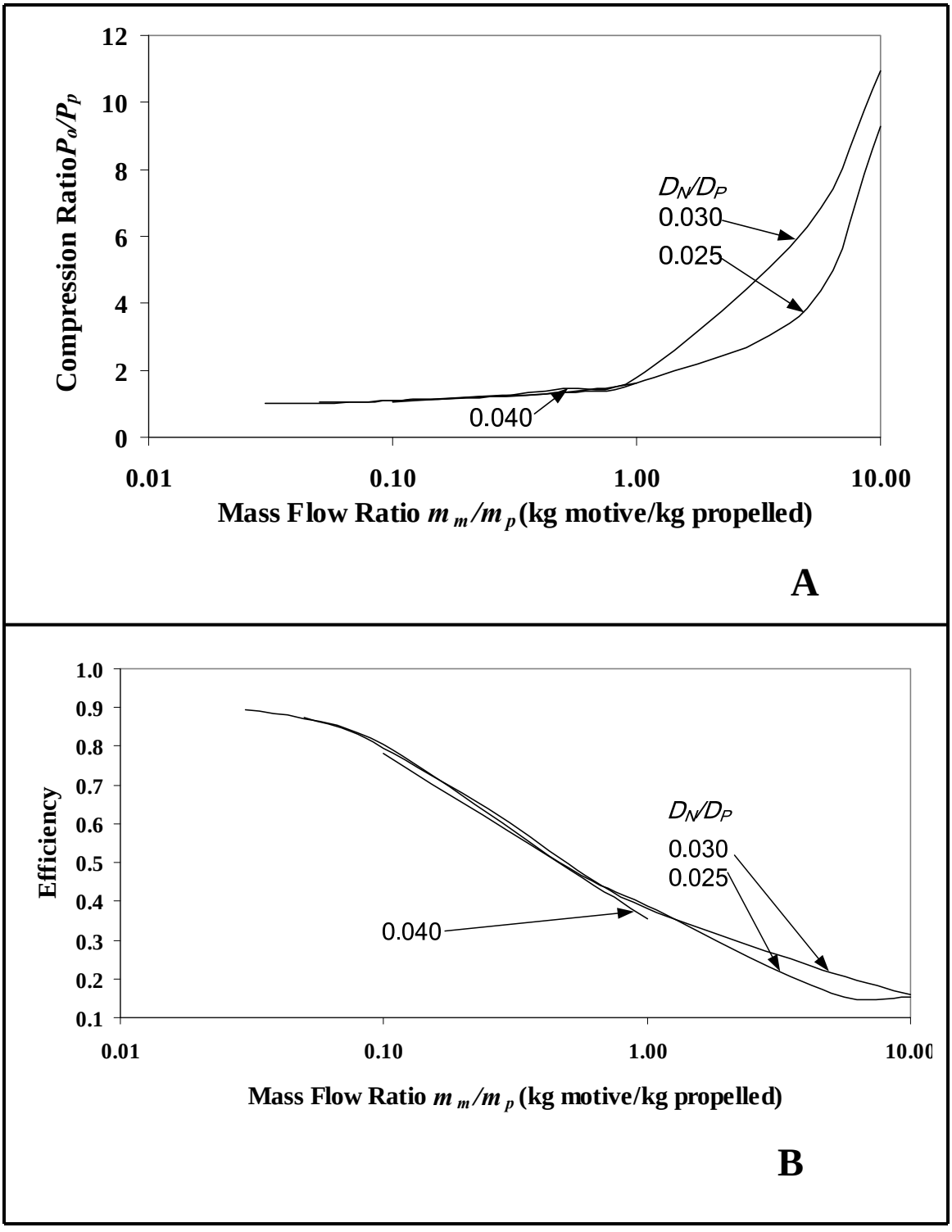

Figure 44. CFD simulation results for different nozzle diameter ratios at 1104 m/s. A) Compression ratio B) Efficiency.
(Note: All curves are plotted using the optimal D_T/D_P and L_T/D_P determined in Chapter VI.)

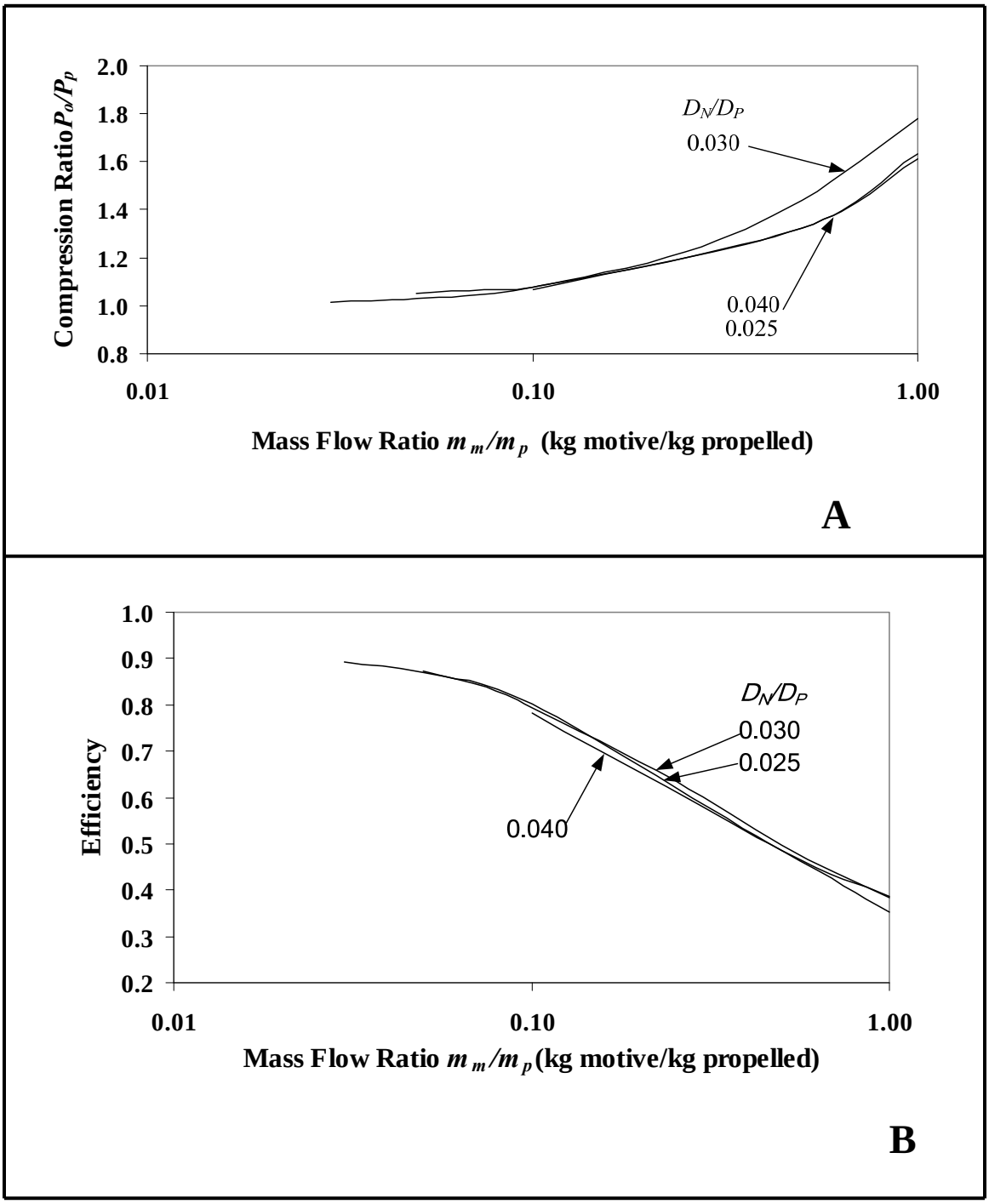

Figure 45. CFD simulation results for different nozzle diameter ratios at 1104 m/s. at mass flow ratio below 1. A) Compression ratio B) Efficiency.
(Note: All curves are plotted using the optimal D_T/D_P and L_T/D_P determined in Chapter VI.)

In the two-stage nozzle design (Figure 35A), the following were investigated: optimal distance between the outer and inner tube *l* and optimal area-ratio between the outer and inner tube.

The optimization results showed that there is no improvement on the two-stage nozzle at any operating condition. This could be explained as follows: The high-velocity motive stream exiting the outer nozzle contacts the surface of the inner nozzle, which increases friction and turbulence at the mixing position. Nonetheless, the area-ratio optimization shows that 3:1 (outer: inner) is the best. Because the other geometries are roughly similar, this same area ratio 3:1 (outer:inner) was employed in the other nozzle designs.

In the annular nozzle design (Figure 35B), *l* and *s* were varied with a constant area ratio (outer:inner) of 3:1. Nothing performed better than a conventional single-nozzle design.

For the circular arrays (Figures 35C to 35G), all five configurations were evaluated. In each configuration, *l* are *s* were optimized using the optimum area-ratio 3:1 (outer:inner) found from the previous study. The optimization was done using every operating condition (motive velocity and mass flow ratio). Table 18 summarizes the improved compression ratio for each nozzle design. The improvement is compared with the optimal single-nozzle design (Figure 21B).

The improvement is the greatest for the four-tube circular array, so it is the best among all the alternatives. Table 19 shows the improved compression ratio for each operating condition.

Table 18. Improved jet ejector compression ratio for circular array nozzle design.

Number of surrounding nozzles	Improved compression ratio (%)*
2	0.5449
3	0.8357
4	1.4214
6	1.2557
8	1.2782

*Compared to optimal single-nozzle design

Optimization of *l* shows that at the low mass-flow ratio region, the outer nozzles should be placed slightly behind the central tube (Figure 46A). The central tube is located right at the beginning of the throat section to enhance jet ejector performance. The optimal gap between the inner and outer nozzles is 0.04 to 0.08 D_P. At high mass flow ratios, the outer nozzles should have the same axial position as the central nozzle (Figure 46B). Table 20 summarizes the optimal *s*, throat length, and diameter for the four-tube circular array design. For scaling purposes, all results are presented in dimensionless form relative to the inlet diameter D_P. The total nozzle area of the circular array (the surrounding and central nozzles) equals the area of the optimal single nozzle.

Table 19. Improved compression ratio (%) of four-tube circular array compared to optimal single-nozzle design.

<table>
<tr><th>Motive velocity (m/s)
Mass flow ratio (kg motive/kg propelled)</th><th>170</th><th>340</th><th>510</th><th>680</th><th>850</th><th>1020</th><th>1104</th></tr>
<tr><td>0.03</td><td colspan="7" rowspan="2">The improvement is fairly small in this region.</td></tr>
<tr><td>0.05</td></tr>
<tr><td>0.10</td><td></td><td>0.15</td><td>0.17</td><td>0.14</td><td>0.25</td><td>0.25</td><td>0.26</td></tr>
<tr><td>0.50</td><td>0.12</td><td>0.13</td><td>0.18</td><td>0.18</td><td>2.33</td><td>2.56</td><td>2.58</td></tr>
<tr><td>1</td><td>0.47</td><td>0.70</td><td>0.51</td><td>0.37</td><td>4.77</td><td>5.27</td><td>5.63</td></tr>
<tr><td>5</td><td colspan="2" rowspan="4">Throat diameter (D_T) is too small to apply the surrounding nozzle design.</td><td>0.35</td><td>0.42</td><td>4.65</td><td>5.10</td><td>5.51</td></tr>
<tr><td>10</td><td>0.98</td><td>1.12</td><td>4.82</td><td>5.34</td><td>5.72</td></tr>
<tr><td>50</td><td>2.40</td><td>2.42</td><td>4.95</td><td>5.43</td><td>5.73</td></tr>
<tr><td>100</td><td>2.41</td><td>2.44</td><td>3.21</td><td>4.12</td><td>4.32</td></tr>
</table>

Table 20. The optimum constant-area jet ejector geometry with a four-tube circular array.

Motive velocity (m/s)	Mass flow ratio (kg motive/kg propelled)	(s/D_P)	(D_T/D_P)	(L_T/D_P)
170 (Mach 0.5)	0.03	0.070	0.95	3.2
	0.05	0.070	0.65	2.2
	0.10	0.064	0.34	1.7
	0.50	0.064	0.12	0.7
	1	0.060	0.09	0.6
	5	*	0.06	0.3
	10	*	0.06	0.3
	50	*	0.046	0.3
	100	*	0.046	0.3
340 (Mach 1.0)	0.03	0.070	0.95	3.2
	0.05	0.070	0.65	2.3
	0.10	0.070	0.38	2.1
	0.50	0.068	0.12	1.1
	1	0.060	0.09	0.6
	5	*	0.056	0.4
	10	*	0.056	0.3
	50	*	0.056	0.3
	100	*	0.052	0.3
510 (Mach 1.5)	0.03	0.070	0.95	4.0
	0.05	0.070	0.65	2.9
	0.10	0.064	0.38	2.2
	0.50	0.064	0.12	1.0
	1	0.064	0.098	0.7
	5	0.050	0.075	0.5
	10	0.050	0.072	0.4
	50	0.050	0.072	0.4
	100	0.050	0.072	0.4

Table 20. Continued.

Motive velocity (m/s)	Mass flow ratio (kg motive/kg propelled)	(s/D_P)	(D_T/D_P)	(L_T/D_P)
680 (Mach 2.0)	0.03	0.070	0.95	4.5
	0.05	0.070	0.75	2.9
	0.10	0.070	0.40	2.6
	0.50	0.067	0.144	1.3
	1	0.067	0.118	1.2
	5	0.067	0.10	0.7
	10	0.067	0.095	0.7
	50	0.060	0.088	0.7
	100	0.060	0.088	0.6
850 (Mach 2.5)	0.05	0.07	0.95	4.9
	0.10	0.07	0.50	3.0
	0.50	0.07	0.19	1.6
	1	0.07	0.155	1.7
	5	0.07	0.13	1.2
	10	0.067	0.13	1.2
	50	0.067	0.13	1.2
	100	0.067	0.13	1.2
1020 (Mach 3.0)	0.03	0.056	0.93	3.8
	0.05	0.056	0.62	3.5
	0.10	0.056	0.40	2.5
	0.50	0.056	0.178	1.9
	1	0.056	0.148	1.6
	5	0.056	0.134	1.3
	10	0.056	0,128	1.3
	50	0.056	0.123	1.1
	100	0.056	0.123	1.1

Table 20. Continued.

Motive velocity (m/s)	Mass flow ratio (kg motive/kg propelled)	(s/D_P)	(D_T/D_P)	(L_T/D_P)
1104 (Mach 3.25)	0.05	0.063	0.95	4.2
	0.10	0.063	0.85	3.2
	0.50	0.063	0.228	1.8
	1	0.063	0.185	1.7
	5	0.056	0.178	1.7
	10	0.056	0.178	1.4

(*) No optimum value because the throat diameter is too small to apply the surrounding nozzle design

Mass flow ratio (kg motive/kg propelled) \ Motive velocity (m/s)	170	340	510	680	850	1020	1104
Ma	0.5	1.0	1.5	2.0	2.5	3.0	3.25
0.03	The region that Configuration A provides greater performance than Configuration B.						
0.05							
0.10							
0.50							
1							
5			The region that Configuration B provides greater performance than Configuration A.				
10							
50							
100							

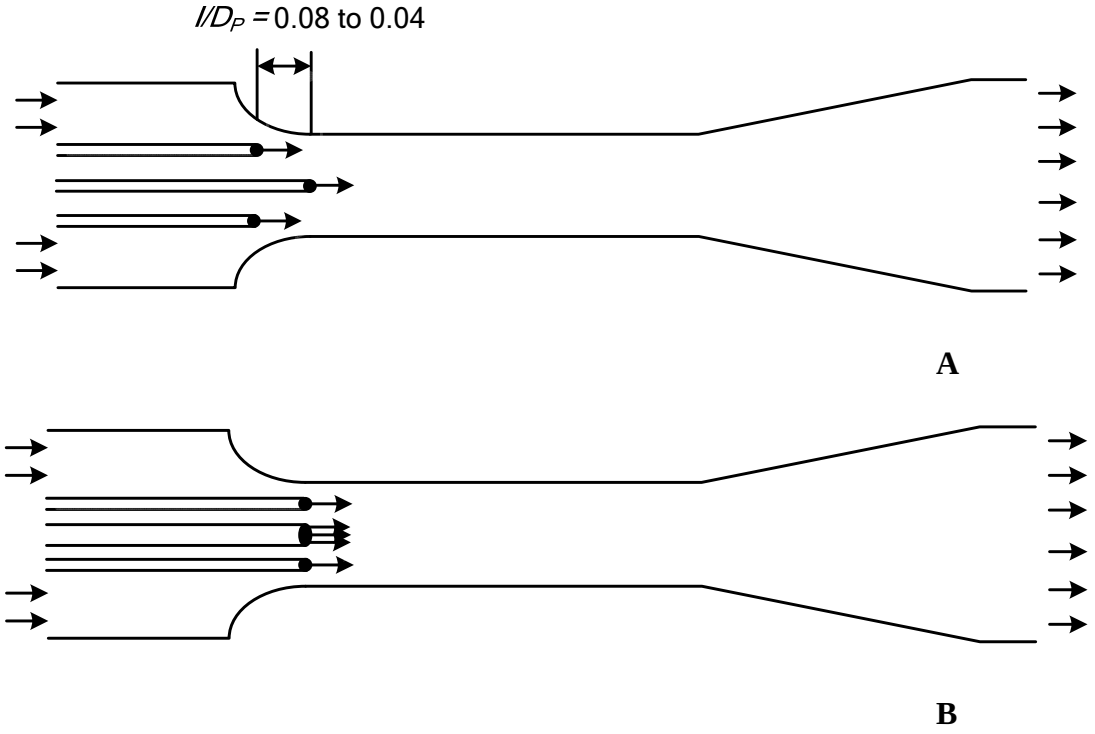

Figure 46. Optimal axial position for four-tube circular array.

Conclusion

Maximizing jet ejector performance involves minimizing wall friction and turbulent mixing between the propelled and motive streams. Minimizing the velocity difference between both streams at the mixing position is key to reducing turbulent mixing. The best nozzle design reduces the velocity differences and turbulence at the mixing point. The results show that the four-tube circular array provides the best jet ejector performance. At some operating conditions, the compression ratio increases more than 5%. At the optimal geometry, the surrounding tubes should be slightly behind the center tube. This allows the surrounding tubes to pre-accelerate the propelled stream before mixing with the motive stream from the center tube. This reduces the velocity difference between the propelled and motive stream at the mixing position, and increases jet ejector performance.

CHAPTER VIII

DIMENSIONLESS ANALYSIS

Introduction

The previous chapters of the optimization study studied steam as the working fluid in a constant-area jet ejector. An optimization was performed at a single scale. In this chapter, dimensionless analysis allows these optimization studies to be applicable for any geometric scale, outlet pressure, and fluid type, including both single- and double-component systems. Single-component systems have the same motive and propelled streams whereas double-component systems employ different motive and propelled streams. Identification of the appropriate dimensionless scaling parameters greatly increases the application of the previous optimization studies. The following dimensionless parameters were analyzed: mass flow ratio, momentum ratio, and Reynolds ratio. The Reynolds ratio failed to prove scalability with the double-component system, but the momentum ratio satisfied all testing conditions; therefore, the momentum ratio is the appropriate dimensionless scaling parameter. By specifying the momentum ratio and Mach number of the motive stream, the compression ratio can be predicted regardless of the working fluid, scale, and pressure.

The results presented in the previous chapters of the optimization study employed a constant-area jet ejector at a specific geometric scale operated using steam as the working fluid. The pressure was always 1 atm at the jet ejector outlet. To broaden the applicability of these results, dimensionless analysis can be used. The objective of this dimensionless analysis is to universalize the optimization results of the constant-area jet ejector for any geometric scale, operating pressure, and fluid type; including both single-

and double-component systems. No literature studying the dimensionless analysis of jet ejectors has been found, so this paper is a pioneering effort. Because there are no previous efforts to provide guidance, the challenge is to identify the appropriate dimensionless parameters by which scaling to other geometric scales, pressures, and fluids can be accomplished.

Methodology

The main objective of this chapter is to prove that when all parameters are expressed in dimensionless terms, the results are valid for any fluid, geometric scale, and operating pressure. If the dimensionless group analysis produces good agreement among all variables, the number of cases to be examined is reduced enormously. First, the definition of all dimensionless parameters – both geometric and fluid variables – are described. Then, a case study showing how to implement the dimensionless analysis is exemplified.

Dimensionless Geometric Parameters

All geometric parameters are converted to dimensionless form by dividing by the jet-ejector inlet diameter D_P (see Table 21). The outlet diameter of the jet ejector is specified to equal the inlet diameter.

Table 21. Geometric parameters in dimensionless term.

Parameter	Definition	Dimensionless formation
L_T	Length ratio	$\frac{L_T}{D_P}$
D_N	Nozzle diameter ratio	$\frac{D_N}{D_P}$
D_T	Throat diameter ratio	$\frac{D_T}{D_P}$
l	Nozzle position ratio	$\frac{l}{D_P}$

Dimensionless Fluid Variables

The fluid variables are converted to dimensionless terms (Table 22). Many dimensionless groups (e.g., mass flow rate ratio, Reynolds ratio, and momentum ratio) are considered in the analysis. Because the dimensionless pressure term of the propelled stream C_p and motive C_{pm} streams are calculated based on the optimal design, the objective of this analysis is to identify which dimensionless groups provide the same C_p and C_{pm} regardless of fluid type, geometric scale, and outlet pressure. The Reynolds number is incorporated in this analysis because it is recognized as the standard dimensionless group for fluid flow in pipes.

Two approaches were conducted to study the effect of the motive-stream velocity:

1. Maintain both the motive-stream Mach number and C_p constant
2. Maintain both the motive-stream velocity and C_p constant

An optimal constant-area jet ejector with 0.11 nozzle ratio is employed in the numerical experiments (see Chapter VI of this series for optimal geometry).

Table 22. Fluid variables in dimensionless formation.

Fluid variables	Dimensionless formation
Static pressure of inlet propelled stream C_p	$\frac{P_o - P_p}{\frac{1}{2}\rho_p v_p^2}$
Static pressure of the motive stream at the nozzle outlet C_{pm}	$\frac{P_o - P_m}{\frac{1}{2}\rho_m v_m^2}$
Velocity of inlet motive stream	$\frac{v_m}{\text{Speed of Sound}}$
Mass flow rate ratio	$\frac{m_m}{m_p}$
Momentum ratio	$\frac{m_m v_m}{m_p v_p}$
Reynolds ratio	$\left(\frac{\rho_m v_m D_n}{\mu_m}\right)\left(\frac{\mu_p}{\rho_p v_p D_p}\right)$

Figure 47 summarizes flow parameters. Validation of the appropriate dimensionless groups was performed in four steps. Figure 48 summarizes the procedure for the dimensionless group analysis.

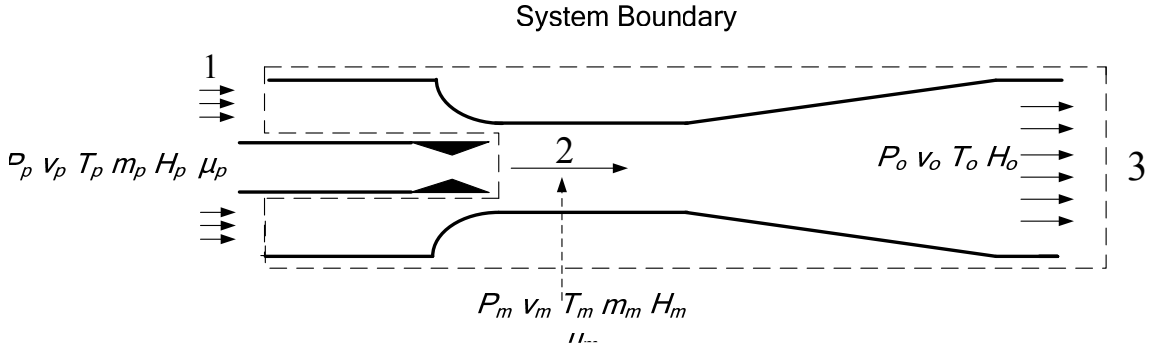

Figure 47. Flow parameters.

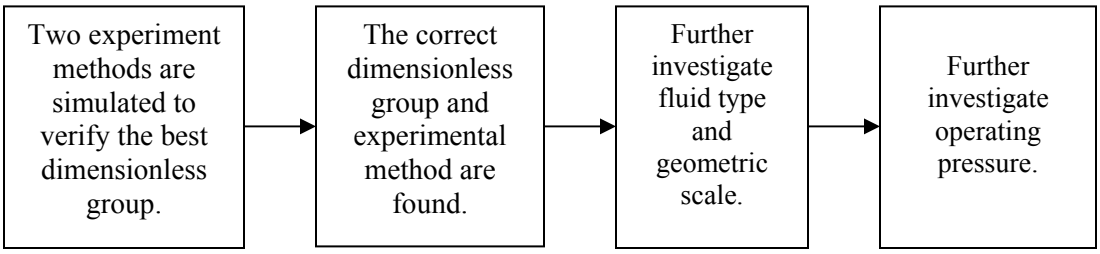

Figure 48. Procedure for the dimensionless group analysis.

Step 1. Air and steam are used as two different fluid types in a single-component system. The geometric scale of the constant-area jet ejector is compared at the 4× and 8× scales based on the dimensions in Figure 28 and Table 13. The outlet pressure is varied from 0.1 to 10.0 atm. Table 23 summarizes the specific conditions of each numerical study.

Table 23 Experimental conditions of each approach.

Experimental approach	Experimental conditions	
1	The velocity of the motive stream maintained at Mach 1.197	C_p value maintained constant at 31.99
2	The velocity magnitude of the motive stream maintained at 406.89 m/s	C_p value maintained constant at 31.99

Step 2. The best dimensionless groups among three alternatives (mass flow ratio, Reynolds ratio, and momentum ratio) are selected for further investigation in Step 2. Other fluid types and geometric scales are applied in this investigation. Table 24

summarizes the experiment condition. A constant exit pressure of 1 atm was employed in Step 2.

Table 24. Experimental conditions of the further investigation.

Experimental set	Operating pressure (atm)	Geometric scale	Fluid type
1	1.0	2×	Steam
2			Air
3			Hydrogen
4		4×	Carbon dioxide
5			Nitrogen

Step 3. This step is to verify the dimensionless parameters on a double-component system, i.e, the motive and propelled streams are different. Normally, jet ejectors are used in double-component systems; therefore, it is very important to prove that the optimization results apply. In this numerical experiment, the propelled materials are varied over a wide range of molecular weights, and include the following: hydrogen, methane, nitrogen, air, ethylene, ethane, oxygen, propylene, propane, and carbon dioxide. According to the literature, because they are commonly available in industrial environments, high-pressure steam and compressed air are used as the motive fluids in more than 90% of jet ejector applications. This step uses high-pressure steam and compressed air as the motive fluids, but the propelled fluid was varied. The results of the previous steps showed that the motive-stream Mach number is a better parameter than the

motive-stream velocity; therefore, the motive-stream Mach number was selected as an independent variable in this numerical experiment. Many dimensionless parameters (mass flow ratio, Reynolds ratio, and momentum ratio) were evaluated; the ones that were independent of the working fluid at constant C_p were appropriate for dimensionless analysis of the double-component system.

Step 4. In this step, the outlet pressure was fully investigated. The outlet pressure ranged from 0.01 to 10.0 atm. The scale was 2× and the fluid was steam. The motive-stream velocity varied from Mach 0.5 to 3.0 (the same domain studied in the optimization study reported in Chapters V and VI of this series). The deviations of C_{pm} and momentum ratio were calculated using the following equations:

$$\left(C_{pm}\right)_{deviate} = \frac{\left(C_{pm}\right)_{arb} - \left(C_{pm}\right)_{ref}}{\left(C_{pm}\right)_{ref}} \tag{55}$$

$$\left(\text{Momentum ratio}\right)_{deviate} = \frac{\left(\text{Momentum ratio}\right)_{arb} - \left(\text{Momentum ratio}\right)_{ref}}{\left(\text{Momentum ratio}\right)_{ref}} \tag{56}$$

where,

$\left(C_{pm}\right)_{deviate}$ = the deviation of C_{pm}

$\left(C_{pm}\right)_{arb}$ = C_{pm} value at arbitrary operating condition

$\left(C_{pm}\right)_{ref}$ = C_{pm} value of the operating pressure at 1 atm

$\left(\text{Momentum Ratio}\right)_{deviate}$ = the deviation of momentum ratio

$\left(\text{Momentum Ratio}\right)_{arb}$ = momentum ratio value at arbitrary operating condition

$\left(\text{Momentum Ratio}\right)_{ref}$ = momentum ratio value of the operating pressure at 1 atm

where the reference condition is at 1 atm, the pressure used in the optimization studies (Chapters V, VI, and VII).

Results and Discussion

Step 1. Table 25 shows the effect on dependent variables (efficiency, C_{pm}, Reynolds number ratio, momentum ratio) for the following independent variables: fluid selection (steam, air), scale (4×, and 8×), outlet pressure (0.1 to 10 atm), C_p (31.98) and Mach number (1.197) in a single-component system. Table 26 is nearly identical, except that motive velocity (407 m/s) was selected as an independent variable to replace Mach number. Studying these two tables, the following observations are clear: when Mach number is used as the independent variable, C_{pm}, Reynolds ratio, and momentum ratio are independent of scale, fluid type, and pressure (almost), within the error of the numerical simulation. This is not the case with motive velocity; thus, Mach number is preferred over motive velocity as an independent variable. Efficiency varies with fluid type, and is not an appropriate dimensionless group.

Step 2. This step investigates additional fluid types (hydrogen, nitrogen, steam, air, and carbon dioxide) and a new geometric scale (2×). The motive-stream Mach number (1.197) and C_p (31.99) are the same as Step 1. Table 27 summarizes the results. It shows that C_{pm}, Reynolds and momentum ratios are nearly independent of scale and fluid type. These results strengthen the conclusion that Mach number is a robust independent variable. Also the wide range in efficiency confirms that it is not a suitable dimensionless group. From Table 27, it is clear that the jet ejector efficiency increases when molecular weight increases.

Step 3. This step investigates dimensionless analysis of the double-component system. Tables 28 and 29 present the results when high-pressure steam and air, respectively, are used as the motive fluid. In this analysis, the steam-steam and air-air systems are used as the standard cases for steam and air motive fluid, respectively.

Tables 28 and 29 show that the mass flow ratio and Reynolds ratio change when the propelled working fluids change; however, the momentum ratio stays constant for both high-pressure steam and air systems; therefore, the momentum ratio is the best dimensionless parameter for the double-component system.

Regardless of the kind of working fluid, if a jet ejector is operated at the same motive-stream Mach number and momentum ratio, the dimensionless propelled-stream pressure term C_p will remain constant and predictable; thus, the compression ratio is predictable as well. This numerical experiment was done with both high-pressure steam and compressed air as motive fluids, which covers the majority of jet ejector applications.

Table 25. Result of maintaining constant motive-stream Mach number (1.197) and C_p (31.99).

Operating pressure (atm)	Efficiency				C_{pm}				Reynolds ratio				Momentum ratio			
	Steam		Air		Steam		Air		Steam		Air		Steam		Air	
	4×	8×	4×	8×	4×	8×	4×	8×	4×	8×	4×	8×	4×	8×	4×	8×
0.1	0.902	0.902	0.929	0.929	0.0052	0.0054	0.0052	0.0053	3.00	2.98	3.04	3.01	5.41	5.34	5.42	5.35
0.2	0.903	0.903	0.932	0.932	0.0055	0.0055	0.0053	0.0054	2.98	2.95	3.01	2.99	5.34	5.29	5.24	5.27
0.3	0.904	0.904	0.933	0.933	0.0055	0.0056	0.0054	0.0055	2.96	2.94	3.00	2.98	5.32	5.22	5.28	5.22
0.5	0.905	0.905	0.934	0.934	0.0057	0.0057	0.0055	0.0056	2.95	2.93	2.98	2.97	5.24	5.23	5.24	5.24
0.6	0.905	0.905	0.935	0.935	0.0057	0.0057	0.0055	0.0056	2.94	2.93	2.98	2.96	5.16	5.16	5.17	5.16
1.0	0.907	0.907	0.936	0.936	0.0058	0.0058	0.0056	0.0057	2.93	2.92	2.96	2.95	5.18	5.10	5.13	5.13
3.0	0.907	0.907	0.938	0.938	0.0059	0.0059	0.0058	0.0058	2.91	2.91	2.94	2.93	5.10	5.06	5.07	5.07
6.0	0.907	0.907	0.938	0.938	0.0059	0.0059	0.0058	0.0058	2.91	2.91	2.93	2.94	5.09	5.10	5.07	5.09
8.0	0.908	0.907	0.939	0.938	0.0057	0.0059	0.0057	0.0058	2.91	2.91	2.93	2.94	5.08	5.09	5.06	5.08
10.0	0.908	0.907	0.938	0.938	0.0057	0.0059	0.0057	0.0058	2.90	2.90	2.92	2.93	5.07	5.08	5.03	5.07

Table 26. Result of maintaining constant motive-stream velocity (407 m/s) and C_p (31.99).

Operating pressure (atm)	Efficiency				C_{pm}				Reynolds ratio				Momentum ratio			
	Steam		Air		Steam		Air		Steam		Air		Steam		Air	
	4×	8×	4×	8×	4×	8×	4×	8×	4×	8×	4×	8×	4×	8×	4×	8×
0.1	0.944	0.945	0.929	0.929	0.102	0.104	0.0052	0.0053	2.63	2.62	3.04	3.01	5.27	5.21	5.23	5.25
0.2	0.945	0.947	0.932	0.932	0.107	0.106	0.0053	0.0054	2.62	2.59	3.01	2.99	5.21	5.23	5.24	5.24
0.3	0.945	0.947	0.933	0.933	0.105	0.105	0.0054	0.0055	2.60	2.59	3.00	2.98	5.16	5.15	5.21	5.23
0.5	0.946	0.948	0.935	0.935	0.107	0.108	0.0054	0.0055	2.59	2.57	2.98	2.96	5.09	5.05	5.2	5.18
0.6	0.947	0.948	0.936	0.936	0.107	0.109	0.0055	0.0056	2.58	2.56	2.96	2.95	5.08	5.04	5.17	5.16
1.0	0.949	0.949	0.938	0.938	0.108	0.110	0.0056	0.0057	2.55	2.56	2.94	2.93	5.03	4.99	5.13	5.13
3.0	0.949	0.949	0.938	0.938	0.111	0.111	0.0058	0.0058	2.54	2.55	2.93	2.94	4.97	4.96	5.07	5.07
6.0	0.949	0.949	0.938	0.938	0.112	0.111	0.0058	0.0058	2.54	2.55	2.91	2.93	4.95	4.97	5.07	5.07
8.0	0.944	0.945	0.929	0.929	0.112	0.111	0.0058	0.0058	2.63	2.62	3.04	3.01	4.95	4.96	5.05	5.07
10.0	0.945	0.947	0.932	0.932	0.113	0.111	0.0062	0.0058	2.62	2.59	3.01	2.99	4.95	4.94	5.03	5.07

Table 27. Result of further investigation (motive-stream Mach number = 1.197, C_p = 31.99).

Independent parameters			Dependent parameters			
Operating pressure (atm)	Geometric scale	Fluid type	Efficiency	C_{pm}	Reynolds ratio	Momentum ratio
1.0	2×	steam	0.904	0.0055	2.95	5.26
		air	0.933	0.0057	2.98	5.21
		hydrogen	0.847	0.0056	2.96	5.20
	4×	nitrogen	0.931	0.0056	2.97	5.23
		carbon dioxide	0.985	0.0058	2.98	5.22

Table 28. Evaluation of dimensionless groups using high-pressure steam as the motive fluid; Mach number = 1.197.

Propelled stream material	C_p	Ratio (motive/propelled)			
		Mass flow ratio	C_{pm}	Reynolds ratio	Momentum ratio
Hydrogen	3863.71	0.52	0.00029	8.74	105.61
Methane	3863.63	0.45	0.00029	9.49	105.48
Steam	3862.47	0.50	0.00030	14.55	105.94
Nitrogen	3862.60	0.42	0.00030	15.80	105.21
Ethylene	3862.27	0.35	0.00030	6.85	106.12
Air	3862.92	0.38	0.00030	10.04	105.41
Ethane	3862.68	0.33	0.00031	5.86	105.86
Oxygen	3862.46	0.33	0.00030	11.95	106.40
Propylene	3862.53	0.28	0.00030	4.72	105.69
Carbon dioxide	3862.32	0.28	0.00030	4.29	106.88
Propane	3862.50	0.26	0.00031	4.29	106.35

Table 29. Evaluation of dimensionless groups using compressed air as the motive fluid; Mach number = 1.197.

Propelled stream material	C_p	Ratio (motive/propelled)			
		Mass flow ratio	C_{pm}	Reynolds ratio	Momentum ratio
Hydrogen	3862.51	0.58	0.00028	8.65	106.19
Methane	3862.44	0.55	0.00028	9.30	106.18
Nitrogen	3862.70	0.44	0.00027	10.49	106.45
Ethylene	3862.79	0.45	0.00027	6.37	106.17
Air	3862.86	0.52	0.00030	14.67	106.21
Ethane	3862.59	0.43	0.00033	5.41	106.13
Oxygen	3862.77	0.42	0.00028	11.16	106.38
Propylene	3862.40	0.39	0.00027	4.13	106.20
Carbon dioxide	3862.88	0.38	0.00029	6.48	106.30
Propane	3862.10	0.35	0.00028	3.77	106.33

Step 4. Step 1 analysis showed that C_{pm} and momentum ratios vary with outlet pressure. C_{pm} decreases with decreasing operating pressure, but momentum ratios increase with decreasing outlet pressure. In all cases, the change with pressure is relatively small considering the pressure changed by two orders of magnitude. The emphasis in Step 4 is to investigate the effect of outlet pressure on C_{pm} and momentum ratio. In this investigation, the motive stream varied from Mach 0.50 to 3.00, and C_p varied from 4.0 to 10,000,000. Figures 49(A) - (E) show the momentum ratio deviation for a given C_p and motive velocity at various outlet pressures and Figures 50(A) - (E)

show the C_{pm} deviation for a given C_p and motive velocity at various outlet pressures Table 30 summarizes the values of C_p, C_{pm} and momentum ratio of the optimal constant-area jet ejector geometry (Chapter VI). Table 30 summarizes dimensionless group of the optimal constant-area jet ejector geometry at 1-atm operating pressure from Chapter VI.

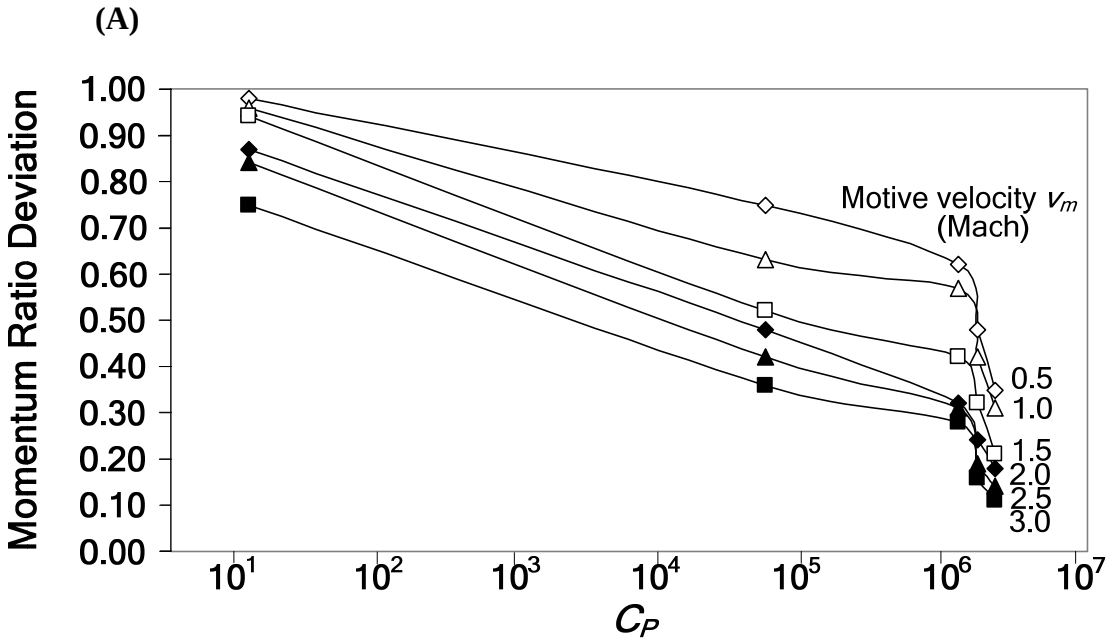

Figure 49. Momentum ratio deviation for a given C_p and motive velocity at various outlet pressure P_o. (A) 0.01 atm (B) 0.03 atm (C) 0.06 atm (D) 0.1 atm (E) 0.3 atm (F) 5 atm, and (G) 10 atm.

(B)

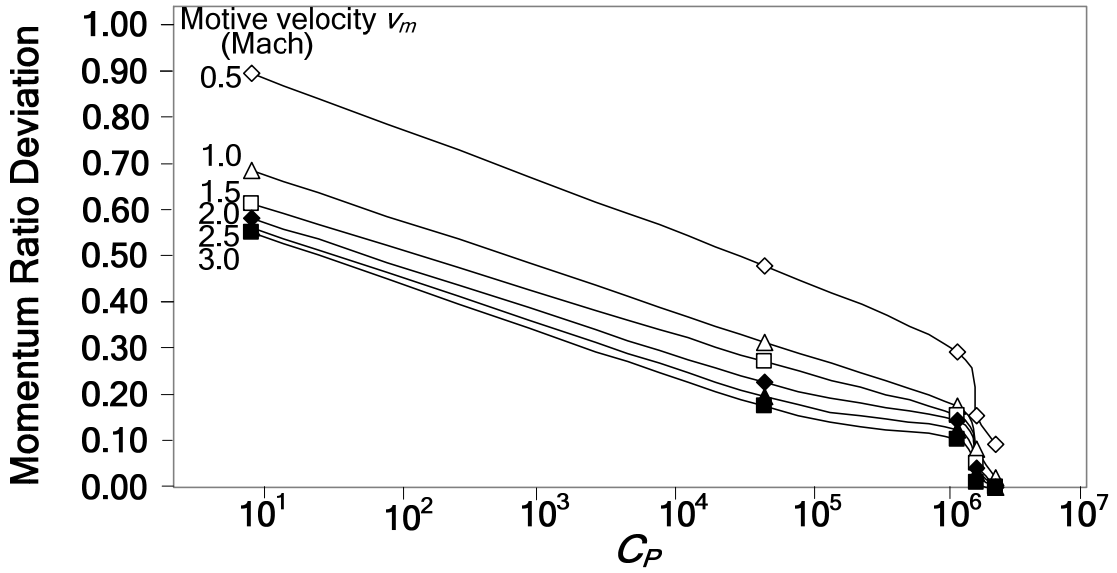

(C)

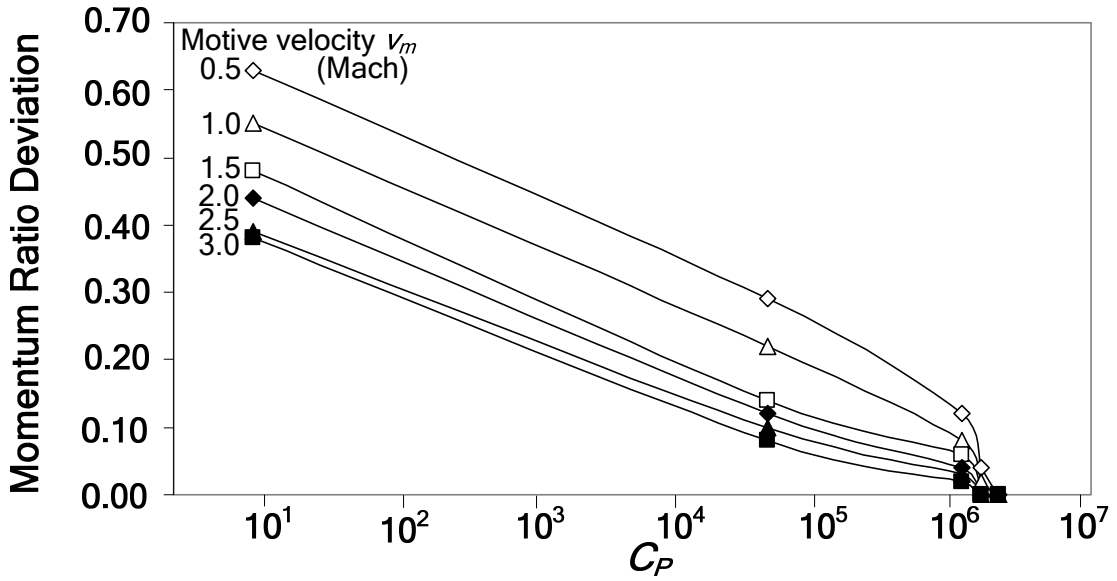

Figure 49. Continued.

(D)

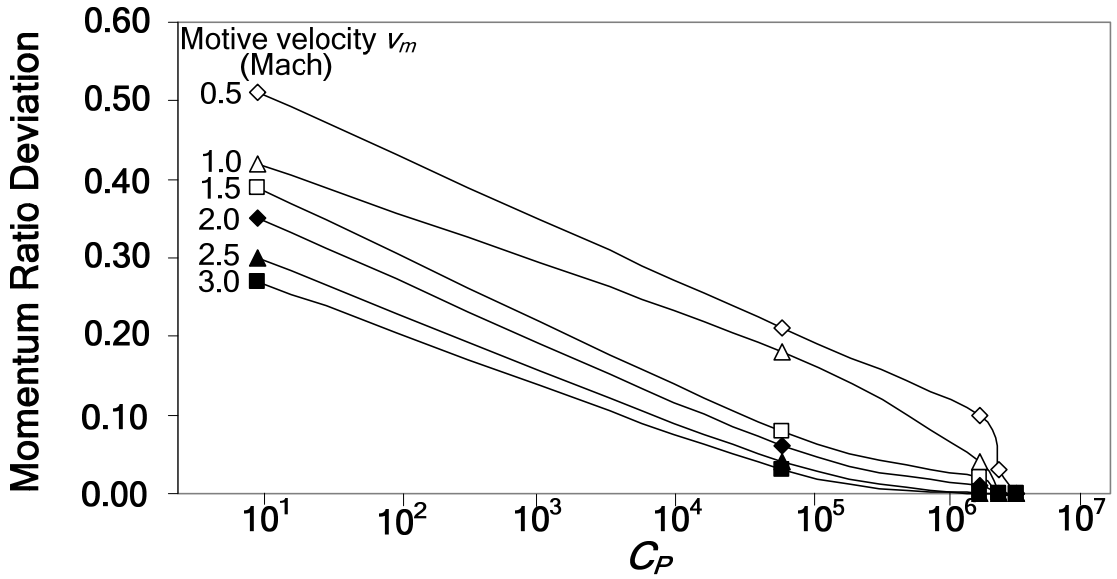

(E)

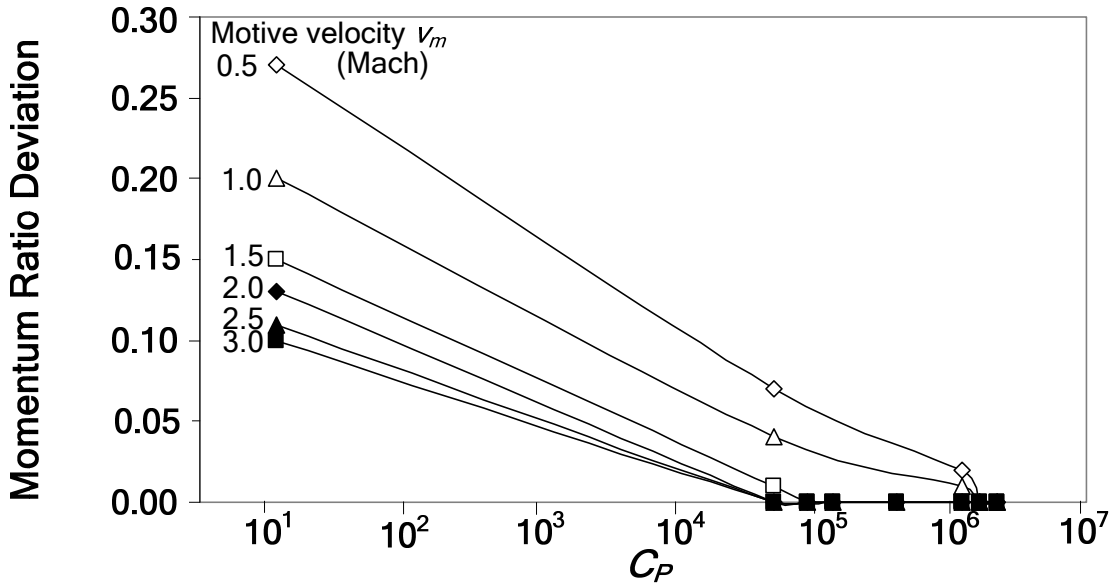

Figure 49. Continued.

(F)

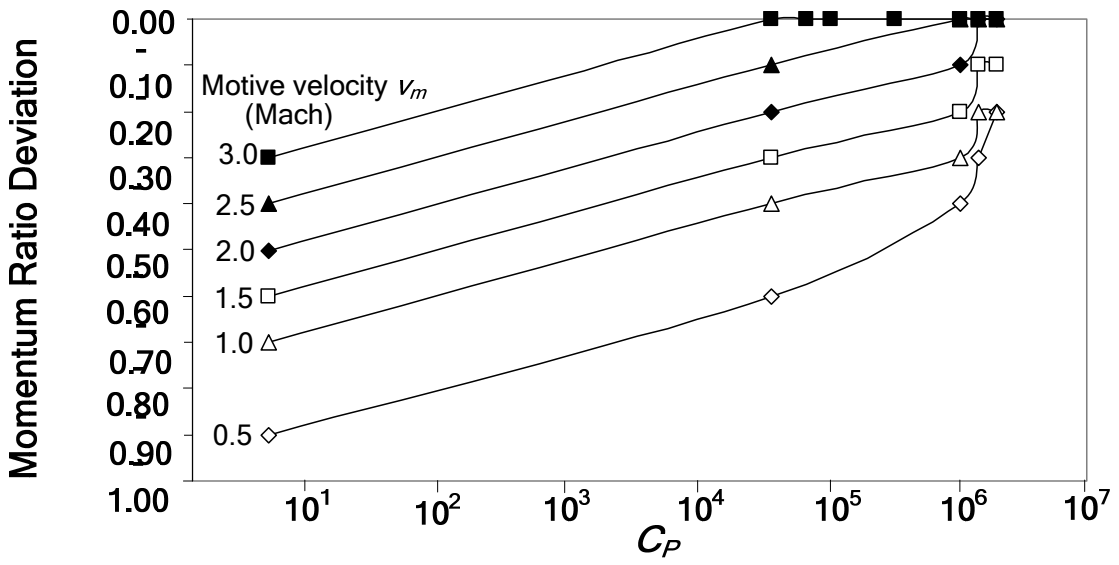

(G)

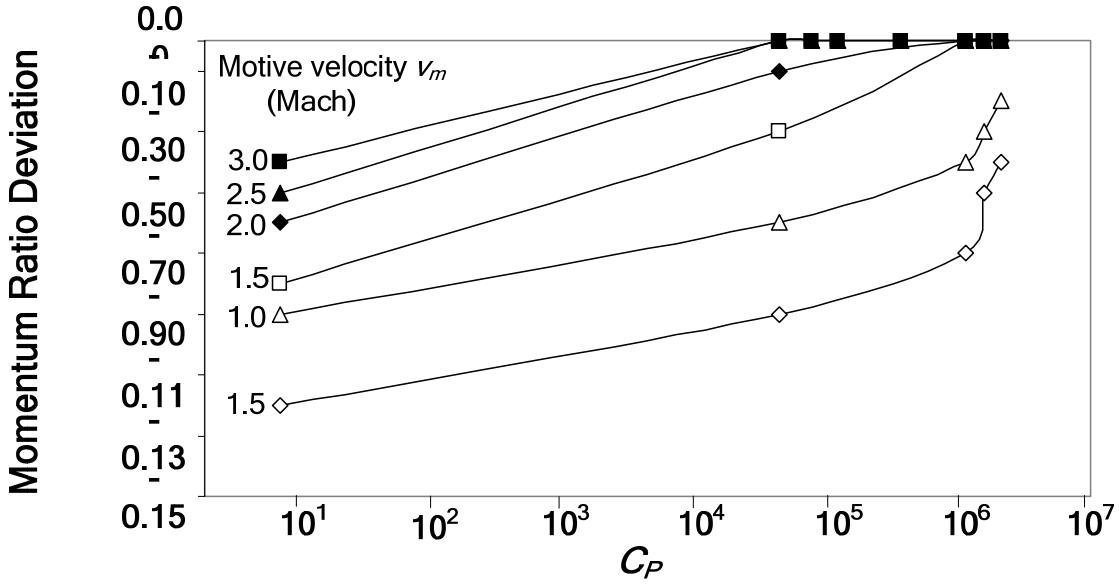

Figure 49. Continued.

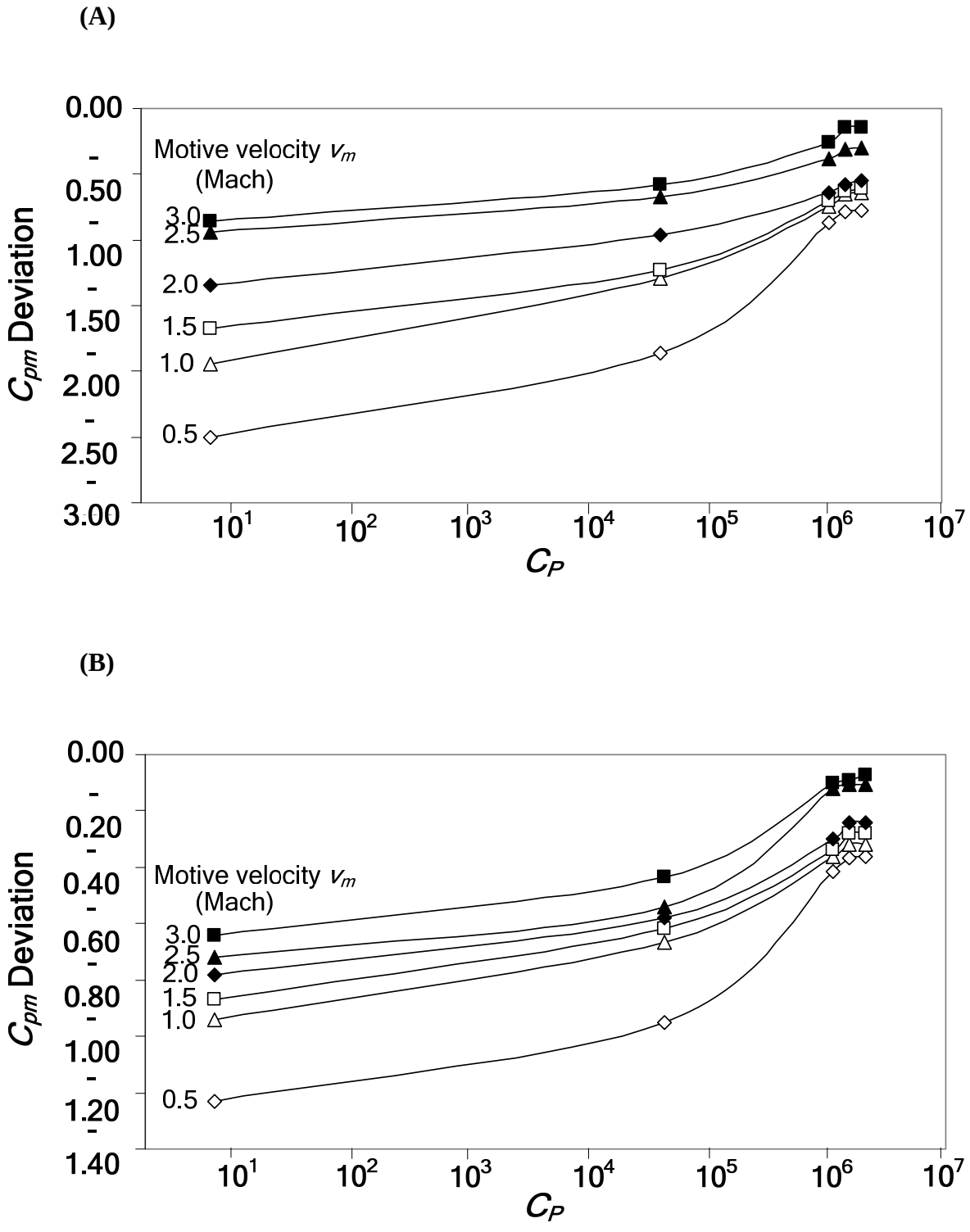

Figure 50. C_{pm} deviation for a given C_p and motive velocity at various outlet pressure P_o. (A) 0.01 atm (B) 0.03 atm (C) 0.06 atm (D) 0.1 atm (E) 0.3 atm (F) 5 atm, and (G) 10 atm.

(C)

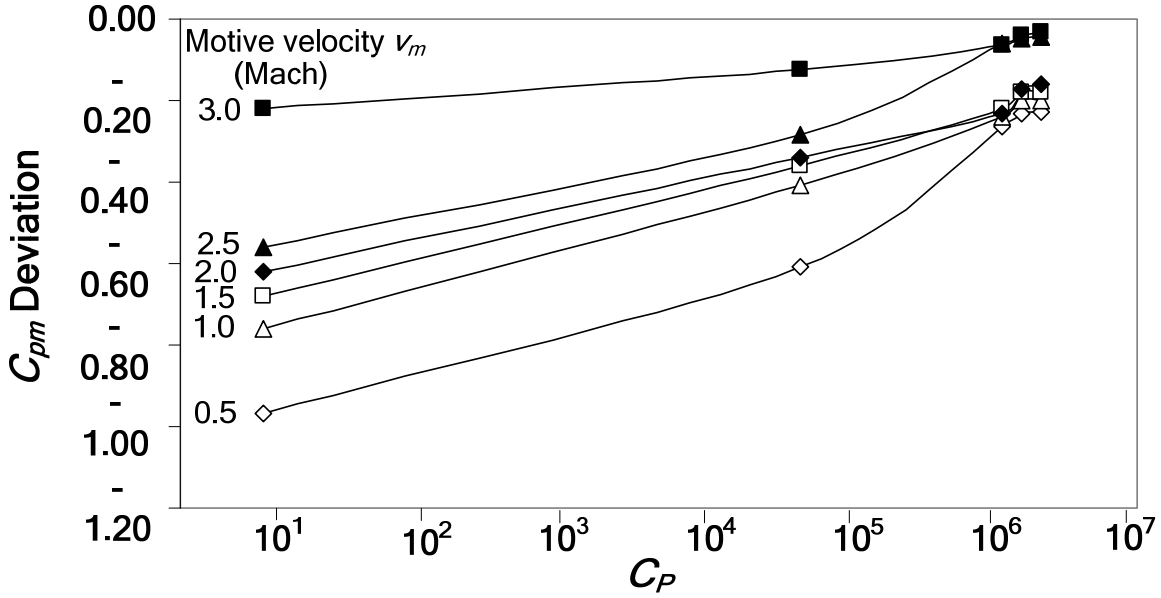

(D)

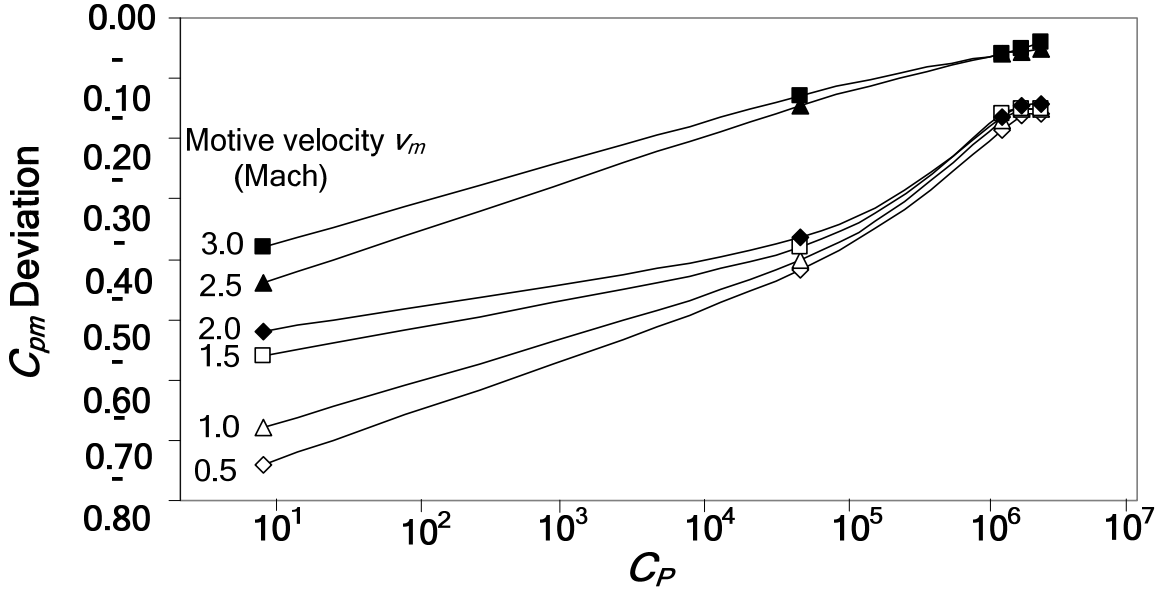

Figure 50. Continued.

(E)

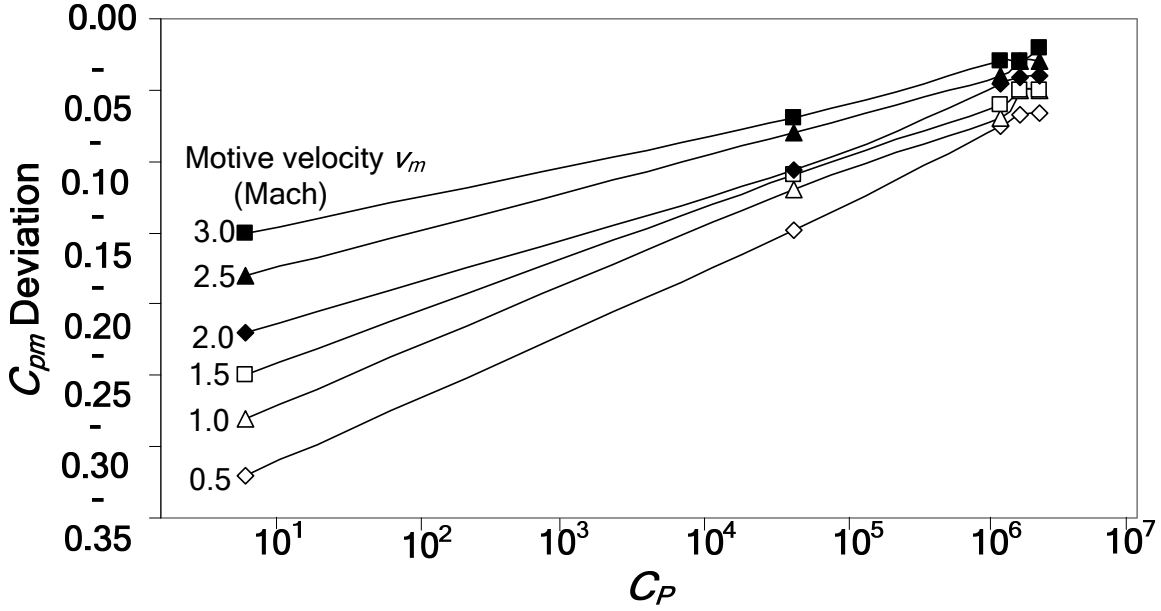

(F)

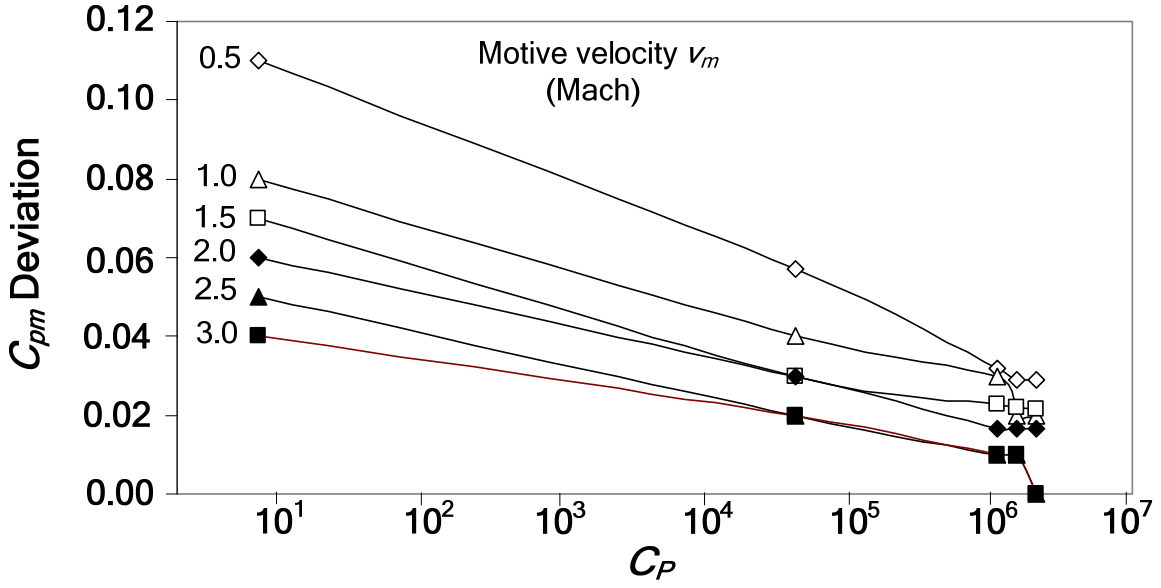

Figure 50. Continued.

(G)

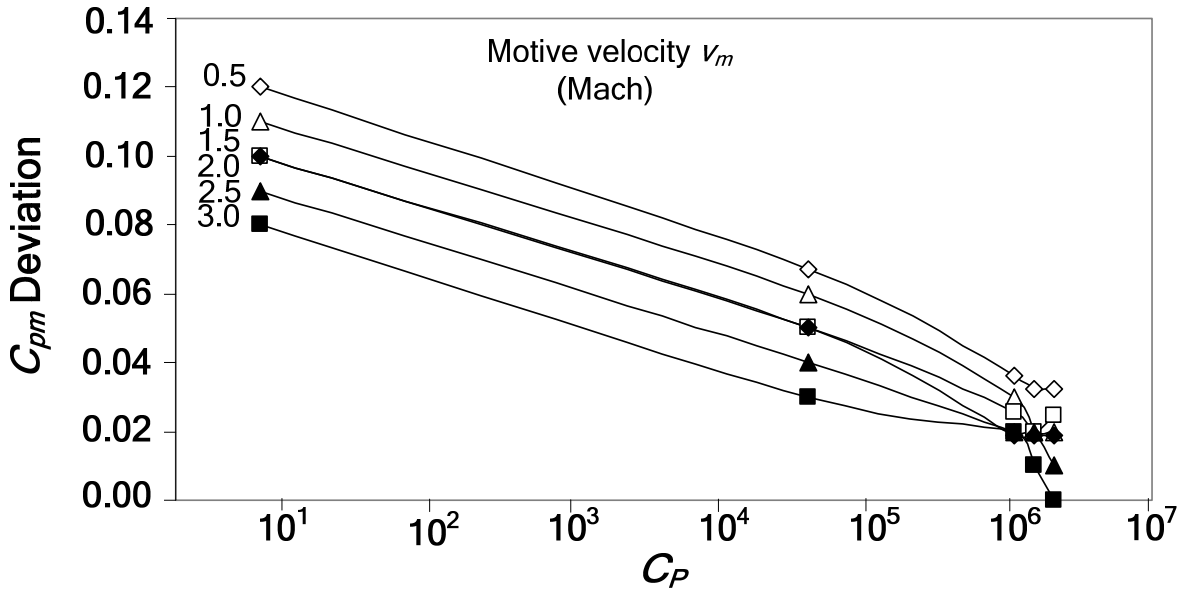

Figure 50. Continued.

Table 30. Dimensionless group of the optimal constant-area jet ejector geometry at 1-atm operating pressure from Chapter VI.

Motive velocity; m/s (Mach number) m_m	Mass flow ratio (kg motive/kg propelled) m_m/m_p	Dimensionless group		
		C_p	C_{pm}	Momentum ratio
170 m/s (0.5)	0.03	0.58	-0.00635	0.37
	0.05	1.50	0.00037	1.02
	0.10	14.54	0.0432	4.09
	0.50	2,745	0.241	101.19
	1.00	21,512	0.353	401.89
	5.00	942,720	0.699	8,416
	10.00	4,741,311	0.798	34,000
	50.00	23,012,848	0.845	314,815
	100.00	24,465,663	0.864	607,143
340 m/s (1.0)	0.03	0.71	-0.0203	0.41
	0.05	2.01	-0.0006	1.15
	0.10	20.32	0.0547	4.56
	0.50	4,259	0.281	109.40
	1.00	30,061	0.470	411.12
	5.00	648,467	0.953	7,981
	10.00	327,610	0.770	23,448
	50.00	9,386,938	0.930	500,000
	100.00	6,023,788	0.963	1,700,000

Table 30. Continued.

Motive velocity; m/s (Mach number) m_m	Mass flow ratio (kg motive/kg propelled) m_m/m_p	Dimensionless group		
		C_p	C_{pm}	Momentum ratio
510 m/s (1.5)	0.03	0.69	-0.0086	0.40
	0.05	2.03	0.000093	1.12
	0.10	19.05	0.00054	4.45
	0.50	3,729	0.0105	98.57
	1.00	24,998	0.0168	341.59
	5.00	832,382	0.0186	4,951
	10.00	3,103,807	0.0220	15,938
	50.00	58,688,252	0.0283	260,204
	100.00	222,760,363	0.0282	962,264
680 m/s (2.0)	0.03	0.53	-0.00639	0.33
	0.05	1.52	-0.00092	0.93
	0.10	14.50	-0.0018	3.67
	0.50	2,213	0.00326	74.53
	1.00	12,160	0.00464	242.77
	5.00	292,413	0.00524	3,080
	10.00	972,802	0.00557	9,140
	50.00	14,861,860	0.00643	120,996
	100.00	48,598,241	0.00657	386,364

Table 30. Continued.

Motive velocity; m/s (Mach number) m_m	Mass flow ratio (kg motive/kg propelled) m_m/m_p	Dimensionless group		
		C_p	C_{pm}	Momentum ratio
850 m/s (2.5)	0.05	1.04	-0.00008	0.69
	0.09	6.83	0.000018	2.19
	0.10	10.05	0.000061	2.67
	0.50	980.84	0.0002	51.63
	1.00	4,619	0.00076	166.57
	5.00	87,617	0.0017	1,713
	10.00	276,961	0.0011	4,786
	50.00	3,094,671	0.0020	48,461
	100.00	8,627,558	0.0021	132,193
1020 m/s (3.0)	0.03	0.60	-0.00018	0.33
	0.05	1.87	-0.00020	0.91
	0.09	9.64	-0.00013	2.84
	0.10	14.04	-0.00002	3.47
	0.50	1,178	0.00016	65.61
	1.00	5,683	0.00028	193.22
	5.00	92,380	0.00053	1,816
	10.00	236,957	0.00065	4,365
	50.00	1,685,006	0.00060	28,177

Table 30. Continued.

Motive velocity; m/s (Mach number) m_m	Mass flow ratio (kg motive/kg propelled) m_m/m_p	Dimensionless group		
		C_p	C_{pm}	Momentum ratio
1020 m/s (3.0)	100.00	3,823,083	0.00061	63,512
1104 m/s (3.25)	0.05	0.93	-0.00009	0.55
	0.075	2.34	-0.00016	1.18
	0.10	5.00	-0.00016	2.12
	0.25	72.85	-0.00008	12.39
	0.50	437.30	0.00005	44.44
	1.00	1,809	0.00009	128.30
	5.00	24,468	0.00011	902.26
	10.00	60,912	0.00015	2,080

Example

The objective of this example is to implement the dimensionless principle to design an optimal jet ejector for a specified operating condition. According to the dimensionless principle, the optimal jet ejector geometry (optimal nozzle diameter ratio D_N/D_P, optimal throat diameter ratio D_T/D_P, optimal throat length ratio, L_T/D_P) for any operating condition is predictable once the motive-stream Mach number and momentum ratio are selected.

Problem Statement

Design an optimal constant-area jet ejector geometry that operates with an outlet pressure of 0.01 atm and a compression ratio of 1.25. Compressed air is the motive-stream fluid and fed at Mach 2.0. Nitrogen is the propelled-stream fluid and is fed at velocity of 2 m/s.

Solution

The density of nitrogen and compressed air at the operating condition follow:

Nitrogen density $\rho_p = 0.009$ kg/m^3 ($P = 0.01$ atm and $T = 25$°C)

Air density $\rho_m = 0.024$ kg/m^3 ($P = 0.01$ atm, $T = 25$°C, and Mach = 2.0)

Compressed air velocity $v_m = 542.59$ m/s ($T = 25$°C, and Mach 2.0)

The procedure to solve the problem is explained below:

Dimensionless Propelled Pressure C_p

Given the compression ratio, propelled fluid density, and propelled stream velocity, the dimensionless propelled pressure C_p can be calculated:

$$P_o = 0.01 \text{ atm} \times 101{,}325 \text{ Pa/atm} = 1{,}013.25 \text{ Pa} \tag{57}$$

$$P_p = P_o / 1.25 = 1{,}013.25 \text{ Pa} / 1.25 = 811 \text{ Pa} \tag{58}$$

$$C_p = \frac{P_o - P_p}{1/2\,\rho_p v_p^2} = \frac{(1{,}013 - 811) \text{ Pa}}{1/2 \cdot (0.009 \text{ kg/m}^3) \cdot (2^2 \text{ m}^2/\text{s}^2)} = 11{,}199 \tag{59}$$

Knowing C_p, Table 30 provides the momentum ratio, and Table 14 (Chapter VI) provides the optimal throat diameter and throat length. For $C_p = 11{,}199$, interpolation is

required (see Figures 51(A) to 51(E)). Figure 51B shows the optimal throat diameter ratio D_T/D_P is 0.12 and Figure 51C shows the optimal throat length ratio L_T/D_P is 1.20.

Dimensionless Motive Pressure C_{pm}

At high vacuum (0.01 atm), the deviation factor of the dimensionless motive pressure C_{pm} is required. From Figure 50A, $(C_{pm})_{deviate}$ = -1.03 at C_p = 11,199 and Mach = 2.0. At atmospheric pressure, Figure 51(D) shows that momentum ratio is 0.0046; therefore, $(C_{pm})_{ref}$ = 0.0046. Rearranging Equation 56 allows C_{pm} at arbitrary condition (0.01 atm) to be calculated:

$$(C_{pm})_{arb} = (C_{pm})_{ref} + (C_{pm})_{deviate} \cdot (C_{pm})_{ref} \tag{60}$$

$$= 0.0046 + (-1.03 \cdot 0.0046) = -0.00014$$

Motive Stream Pressure P_m

Motive stream pressure P_m can be calculated as follows:

$$C_{pm} = \frac{(P_o - P_m)}{\frac{1}{2} \cdot \rho_m v_m^2} \tag{61}$$

Rearranging Equation 7 attain motive stream pressure P_m

$$P_m = P_o - C_{pm} \cdot \left(\frac{1}{2} \cdot \rho_m \cdot v_m^2 \right) \tag{62}$$

$$= 1{,}013 - (-0.00014) \cdot \left(\frac{1}{2} \cdot (0.024 \ \ \mathrm{kg/m^3}) \cdot (543^2 \ \mathrm{m^2/s^2}) \right)$$

$$= 1{,}013 \text{ Pa}$$

Momentum Ratio

At high vacuum (0.01 atm), the deviation factor of the momentum ratio is required. From Figure 49A, $(\text{Momentum Ratio})_{deviate}$ = 0.56 at C_p = 11,199 and Mach = 2.0. At atmospheric pressure, Figure 51(E) shows that momentum ratio is 350; therefore, $(\text{Momentum Ratio})_{ref}$ = 350. Rearranging Equation 55 allows the momentum ratio at arbitrary condition (0.01 atm) to be calculated:

$$(\text{Momentum Ratio})_{arb} = (\text{Momentum Ratio})_{ref} + (\text{Momentum Ratio})_{deviate} \cdot (\text{Momentum Ratio})_{ref} \tag{63}$$

$$= 350 + (0.56 \cdot 350) = 546$$

Optimum Nozzle Diameter Ratio D_N/D_P

From the momentum ratio, the optimal nozzle diameter ratio D_N/D_P can be found as follows:

$$(\text{Momentum Ratio})_{arb} = \frac{m_m v_m}{m_p v_p} = \frac{\rho_m A_N v_m^2}{\rho_p A_P v_p^2} = \frac{\rho_m D_N^2 v_m^2}{\rho_p D_P^2 v_p^2} = 546 \tag{64}$$

where,

A_N = nozzle area (m^2)

A_P = jet ejector inlet area (m^2)

$$\frac{D_N^2}{D_P^2} = 546 \cdot \frac{\rho_p v_p^2}{\rho_m v_m^2} = 546 \cdot \frac{0.009 \cdot 2^2}{0.024 \cdot 543^2} = 0.0028 \tag{65}$$

so,

$$\frac{D_N}{D_P} = \sqrt{0.0028} = 0.053$$

Summary

The values of each parameter are summarized below:

P_p = 811 Pa, P_m = 1,013 Pa, P_o = 1,013 Pa

v_m = 543 m/s, v_p = 2 m/s

$$\frac{D_N}{D_P} = 0.053, \quad \frac{D_T}{D_P} = 0.12, \quad \frac{L_T}{D_P} = 1.20$$

Validation

The solution to this problem was validated by CFD modeling. A constant-area jet ejector with 0.11 m inlet diameter D_P was simulated using the optimal geometry obtained in the problem. Further, the motive and propelled streams were specified using the above motive and propelled stream velocities. At an outlet pressure P_o of 1013 Pa, the CFD simulation predicted an inlet pressure P_p of 857 Pa (5.67% error) and motive pressure P_m of 1011 Pa (0.2% error).

Efficiency

The jet ejector efficiency was calculated by using Equation 52 in Chapter IV. The jet ejector efficiencies using both dimensionless analysis and CFD modeling were calculated and compared.

$$\eta = \frac{\frac{1}{2}\left(\dot{m}_m + \dot{m}_p\right)v_o^2 + \dot{m}_p\frac{RT_o}{(MW)_p} + \dot{m}_m\frac{RT_o}{(MW)_m} + \dot{m}_p\left(\frac{RT_o}{(MW)_p}\right)\frac{\gamma_p}{\gamma_p - 1}\left[\left(\frac{P_o}{P_p}\right)^{\frac{\gamma_p - 1}{\gamma_p}} - 1\right] + \dot{m}_m\left(\frac{RT_o}{(MW)_m}\right)\frac{\gamma_m}{\gamma_m - 1}\left[\left(\frac{P_o}{P_m}\right)^{\frac{\gamma_m - 1}{\gamma_m}} - 1\right]}{\frac{1}{2}\dot{m}_p v_p^2 + \frac{1}{2}\dot{m}_m v_m^2 + \dot{m}_p\frac{RT_p}{(MW)_p} + \dot{m}_m\frac{RT_m}{(MW)_m}}$$

Jet ejector efficiency using dimensionless analysis:

$$\eta = \frac{\left\{\begin{array}{l}\frac{1}{2}(0.02+0.0164)10.49^2 + 0.02\frac{8.314\cdot 300}{0.028} + 0.0164\frac{8.314\cdot 300}{0.029} \\ +0.02\left(\frac{8.314\cdot 300}{0.028}\right)\frac{1.4}{1.4-1}\left[\left(\frac{1013}{811}\right)^{\frac{1.4-1}{1.4}}-1\right] + 0.0164\left(\frac{8.314\cdot 300}{0.029}\right)\frac{1.4}{1.4-1}\left[\left(\frac{1013}{1013}\right)^{\frac{1.4-1}{1.4}}-1\right]\end{array}\right\}}{\frac{1}{2}0.02\cdot 2^2 + \frac{1}{2}0.0164\cdot 543^2 + 0.02\frac{8.314\cdot 300}{0.028} + 0.0164\frac{8.314\cdot 300}{0.029}}$$

$\eta = 0.642$

Jet ejector efficiency using CFD modeling:

$$\eta = \frac{\left\{\begin{array}{l}\frac{1}{2}(0.02+0.0164)10.49^2 + 0.02\frac{8.314\cdot 300}{0.028} + 0.0164\frac{8.314\cdot 300}{0.029} \\ +0.02\left(\frac{8.314\cdot 300}{0.028}\right)\frac{1.4}{1.4-1}\left[\left(\frac{1013}{857}\right)^{\frac{1.4-1}{1.4}}-1\right] + 0.0164\left(\frac{8.314\cdot 300}{0.029}\right)\frac{1.4}{1.4-1}\left[\left(\frac{1013}{1011}\right)^{\frac{1.4-1}{1.4}}-1\right]\end{array}\right\}}{\frac{1}{2}0.02\cdot 2^2 + \frac{1}{2}0.0164\cdot 543^2 + 0.02\frac{8.314\cdot 300}{0.028} + 0.0164\frac{8.314\cdot 300}{0.029}}$$

$\eta = 0.624$

The two efficiencies differ by only 1.8%. Based on this example, the dimensionless analysis provides a satisfactory prediction of jet ejector performance.

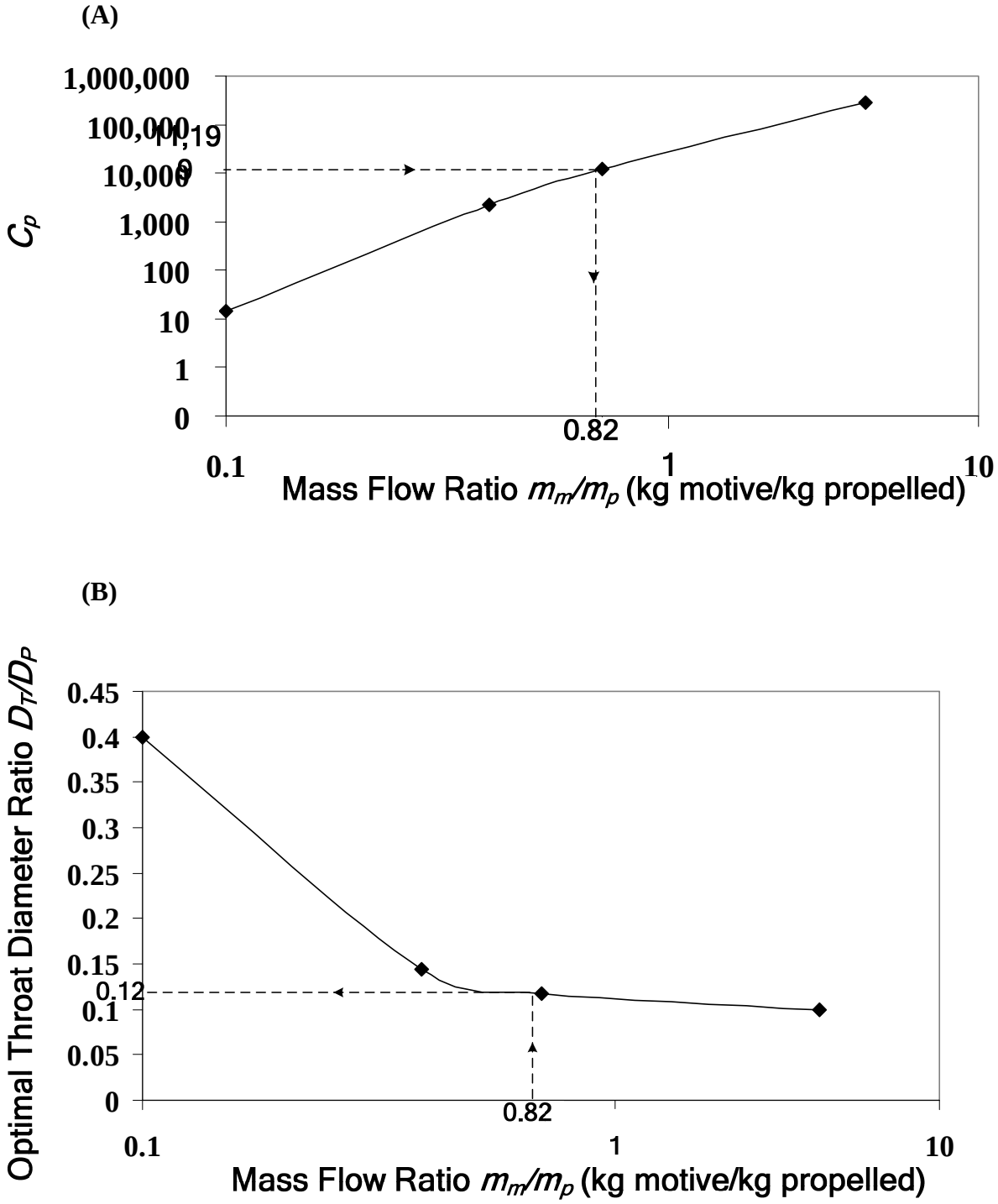

Figure 51. Interpolation of various parameters for the example problem. (A) C_p, (B) optimum throat diameter ratio, (C) optimum throat length ratio, (D) C_{pm}, and (E) Momentum ratio.

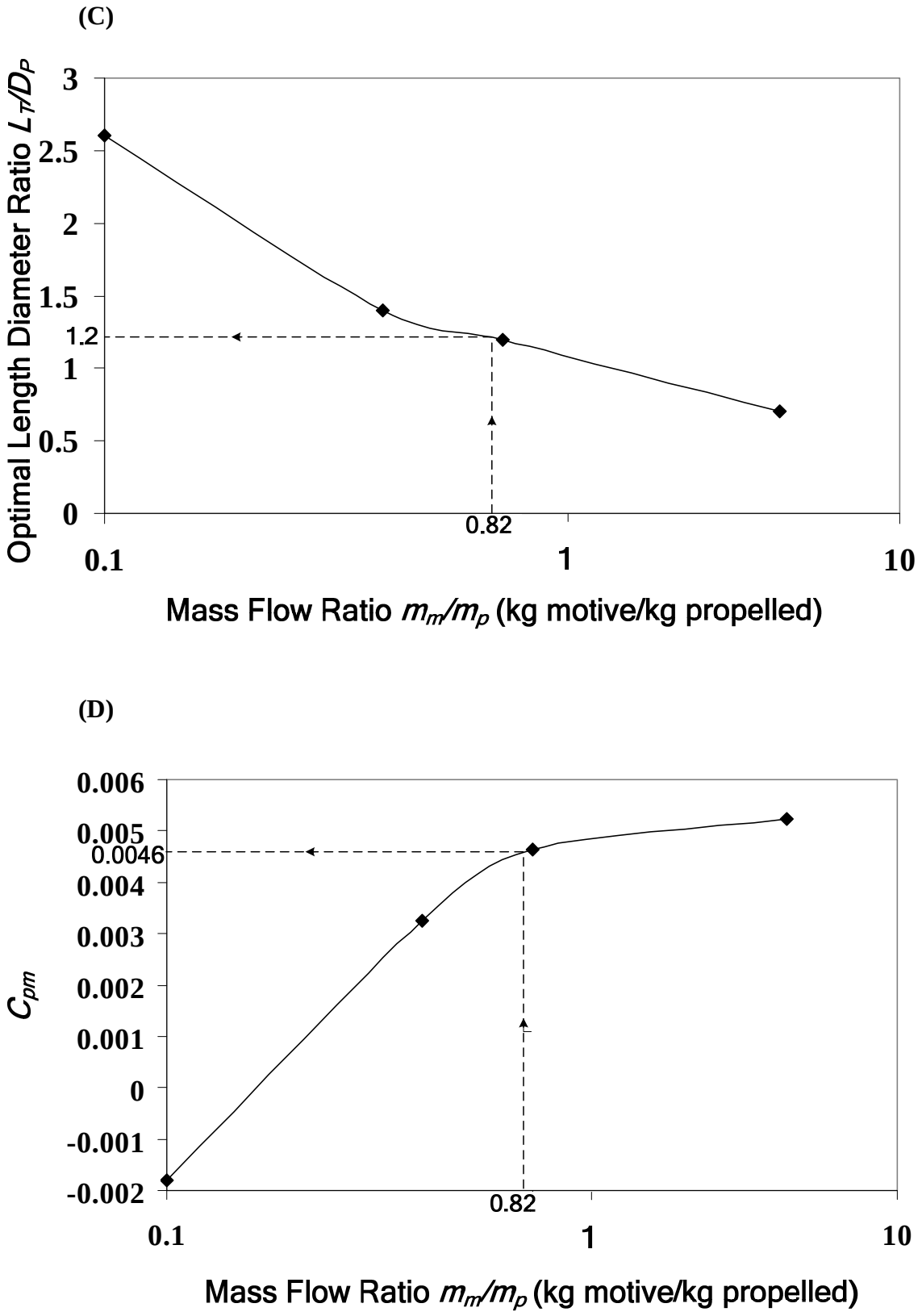

Figure 51. Continued.

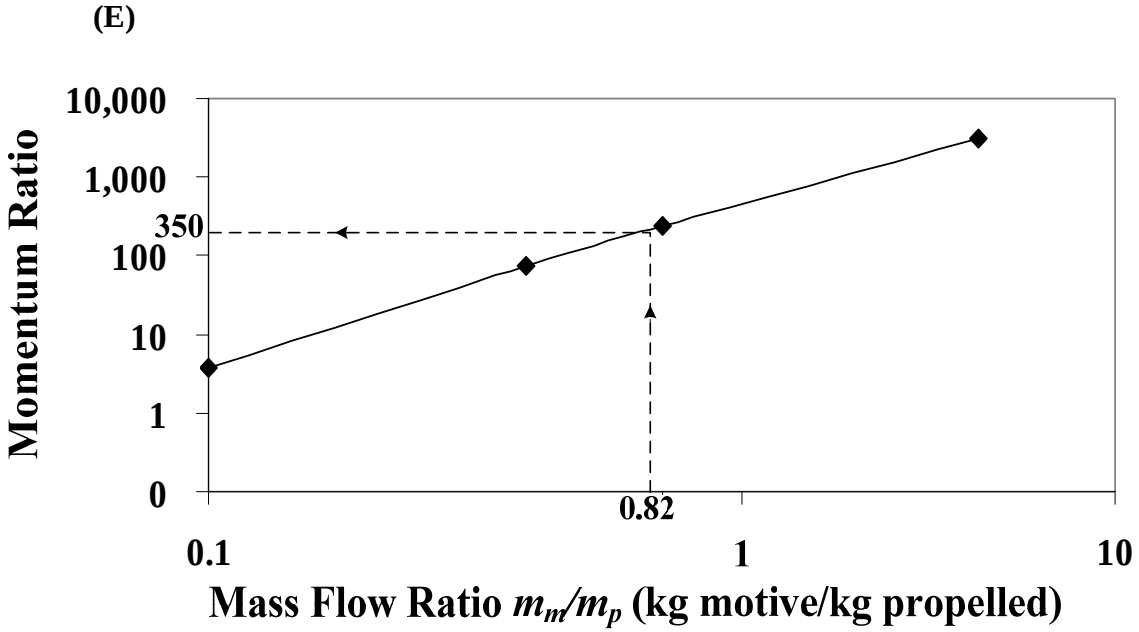

Figure 51. Continued.

Conclusion

This study shows how dimensionless groups can be used to design an optimal constant-area jet ejector for a variety of geometric scales, operating pressures, and fluids (including one- and two- component systems). For a given momentum ratio and motive-stream Mach number, the static pressure of the propelled stream is calculated from C_p. The inlet and outlet static pressures calculated from C_p allow the jet ejector efficiency to be calculated, regardless of the fluid type, using the efficiency equation (Equation 53 in Chapter IV) when the density, mass flow rate, pressure, velocity, and temperature of the propelled, motive, and outlet streams are known.

CHAPTER IX

EXPERIMENT COMPARISON BETWEEN OPTIMUM AND CONVENTIONAL JET EJECTOR

Introduction

Chapters V and VI investigate an optimal jet ejector design by using CFD simulation. Here, the optimal constant-area jet ejector is reduced to hardware and compared to a commercial constant-pressure jet ejector manufactured by Graham Corporation. This investigation compares both compression ratio (discharge/suction pressure) and efficiency. The motive velocity ranged from 298 to 390 m/s and mass flow ratio ranged from 0.45 to 9.00 kg motive/ kg propelled. Air was used as the working fluid. The optimal jet ejector shows superior performance to the conventional jet ejector on both compression ratio and efficiency at all operating conditions. The study showed that substituting an optimal jet ejector for a conventional jet ejector can reduce motive-stream consumption by 8.48% at the design condition (motive velocity 390 m/s and compression ratio 1.30) and up to 25% at motive velocity 298 m/s and compression ratio 1.20. The optimal jet ejector is more robust than a conventional jet ejector meaning it maintains good performance at off-design conditions. The optimum jet ejector results were compared with CFD results. CFD analysis showed high accuracy without the need for adjustable parameters. The overall deviation was 13.10% and 8.71% on compression ratio and efficiency, respectively.

Methodology

Figure 52 shows the experimental schematic. Compressed air was used as the motive fluid and was supplied through a converging-diverging nozzle located at the beginning of the throat section. Motive-stream velocity ranged from 298 to 390 m/s measured at the nozzle outlet. The same nozzle was used on both units; therefore, the measured performance is based strictly on the jet ejector itself. Table 31 summarizes ejector geometries of both the optimal and manufactured units.

Table 31. Summarize ejector geometries of both optimum and manufacture design.

	Optimum ejector	Manufacturer ejector
Jet ejector type	Constant area	Constant pressure
Inlet inside diameter (m)	0.0762	0.0762
Nozzle exit diameter (m)	0.0179	0.0179
Throat diameter (m)	0.0428	0.0381
Throat length (m)	0.2972	0.3048
Outlet inside diameter (m)	0.0762	0.0762

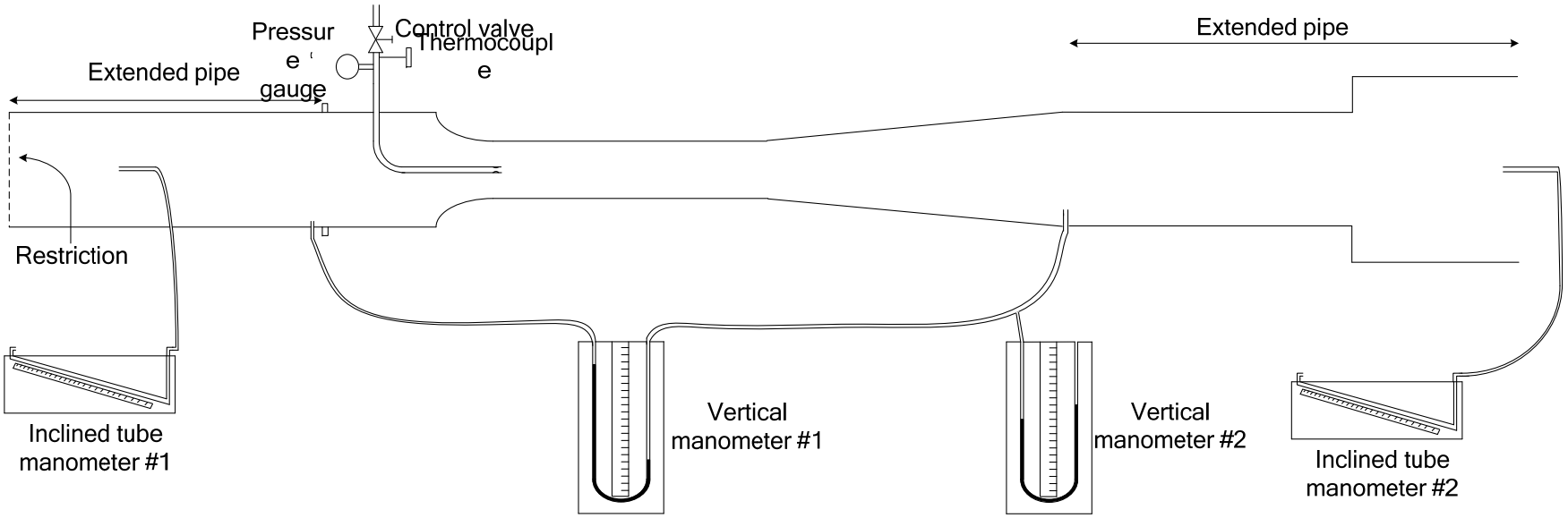

Figure 52. Experimental apparatus.

To vary the propelled mass flow rate, a restriction near the jet ejector inlet had a diameter that varied from 0.00635 to 0.0762 meters. Using identical instrumentation, the experiment was performed on both the optimal and conventional jet ejectors. The outlet pressure, the pressure difference between suction and discharge, and inlet and outlet flow velocities were measured. The fluid densities and mass flow rates of the motive, propelled, and discharge streams were calculated as explained below. Figure 53 shows the experimental procedure. For each jet ejector, the motive-stream velocity was initially set at the maximum velocity (390 m/s) as controlled by a pressure control valve. For each motive velocity tested, the restriction diameter varied from 0.00635 to 0.0762 meters (fully open) to adjust the propelled mass flow rate. Then, the motive velocity was changed to the next value until all motive velocities were investigated. The motive velocity ranged from 290 to 390 m/s. Flow, pressure, and velocity were measured for each run.

Pressure

Atmospheric, outlet, and inlet pressure were measured using vertical manometers. One vertical mercury manometer measured the pressure difference between the suction and discharge streams. The other vertical water manometer measured the pressure difference between the jet ejector outlet and atmospheric pressure. Using Equation 66, pressure was calculated from the liquid level differences in the mercury manometer.

$$\Delta P = \rho \; g \; \Delta h \tag{66}$$

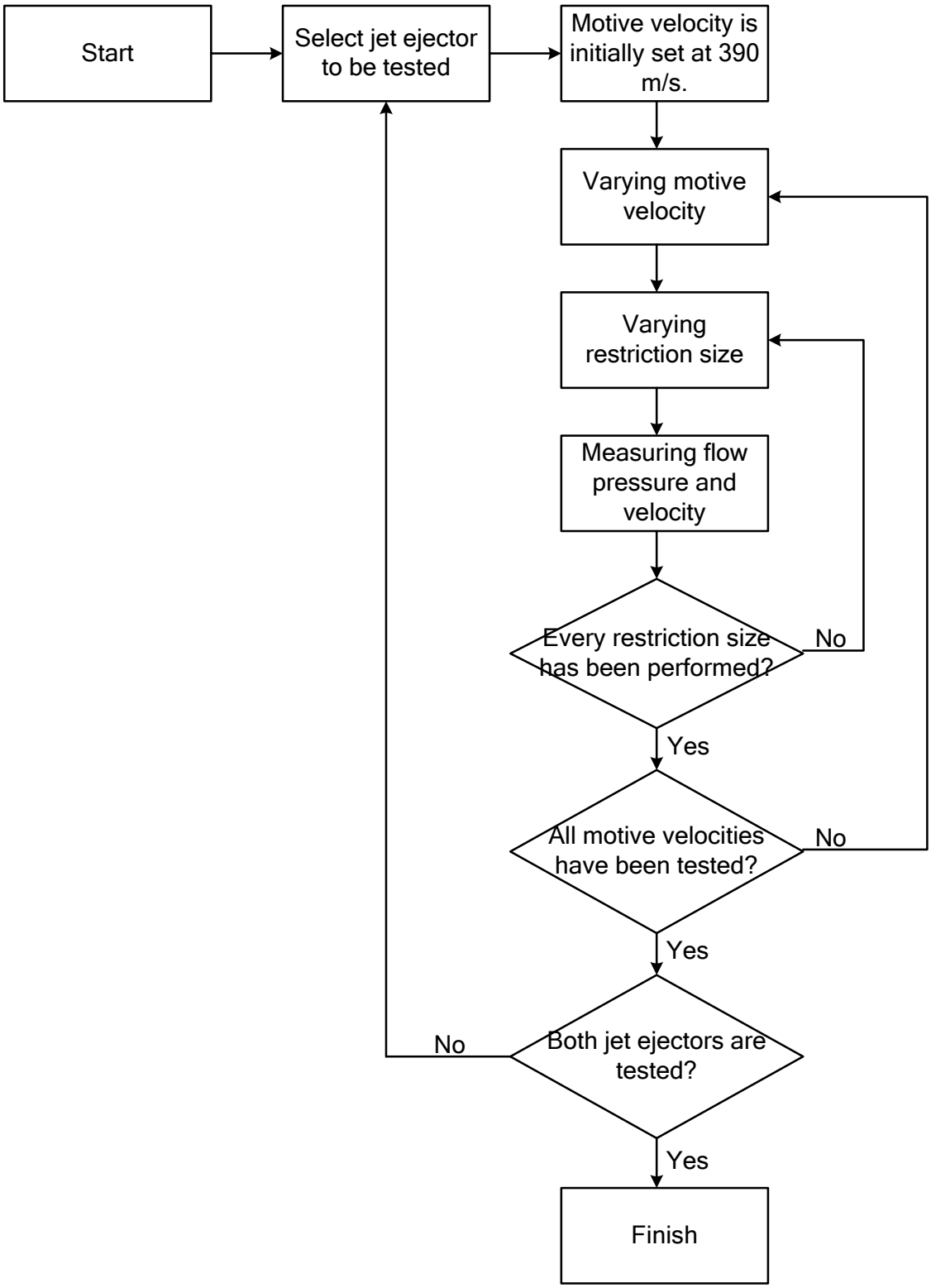

Figure 53. Experimental procedure.

The jet ejector discharge pressure was slightly greater than atmospheric pressure due to pressure drop in the outlet pipe. In addition, the discharge pressure was greater than the inlet pressure because of the suction created by the jet ejector. The barometric pressure was obtained from a weather website at the moment the experiment was performed.

Density

Air density is given by the ideal gas law.

$$\rho = \frac{MW \cdot P}{RT} \tag{67}$$

Mass Flow Rate

Mass flow rate is given by

$$m = Av\rho \tag{68}$$

Flow velocity v was measured by pitot tubes with 3-mm-diameter holes in a 8-mm-diameter tube (provided by Dwyer Instruments, Inc.) connected to inclined manometers. The velocity was measured upstream and downstream of the jet ejectors (Figure 52). The mass flow rate of the propelled and discharge streams were calculated using Equation 68. The motive-stream mass flow rate was calculated as the difference between the outlet and inlet streams.

$$m_m = m_o - m_p \tag{69}$$

Using a pitot tube, flow velocity was measured at various pipe radii on the same plane. The position of the pitot tube is shown in Figure 54 and summarized in Table 32. the mass flow rate was calculated by Equations 70 – 73.

$$m = \sum_{i=1}^{n} m_i = m_1 + m_2 + m_3 + m_4 + m_5 \tag{70}$$

$$\begin{aligned} m = {} & A_1 v_1 \rho + A_2 \left((v_1 + v_2)/2 \right) \rho + A_3 \left((v_2 + v_3)/2 \right) \rho \\ & + A_4 \left((v_3 + v_4)/2 \right) \rho + A_5 \left((v_5 + v_4)/2 \right) \rho \end{aligned} \tag{71}$$

Flow velocity at the wall is static, so $v_5 = 0$. Equation 71 is rearranged to

$$\begin{aligned} m = {} & A_1 v_1 \rho + A_2 \left((v_1 + v_2)/2 \right) \rho + A_3 \left((v_2 + v_3)/2 \right) \rho \\ & + A_4 \left((v_3 + v_4)/2 \right) \rho + A_5 \left(v_5/2 \right) \rho \end{aligned} \tag{72}$$

$$m = \pi \rho \begin{pmatrix} r_1^2 V_1 + \left((r_2^2 - r_1^2)(V_1 + V_2)/2 \right) + \left((r_3^2 - r_2^2)(V_2 + V_3)/2 \right) \\ + \left((r_4^2 - r_3^2)(V_3 + V_4)/2 \right) + \left((r_5^2 - r_4^2) V_4/2 \right) \end{pmatrix} \tag{73}$$

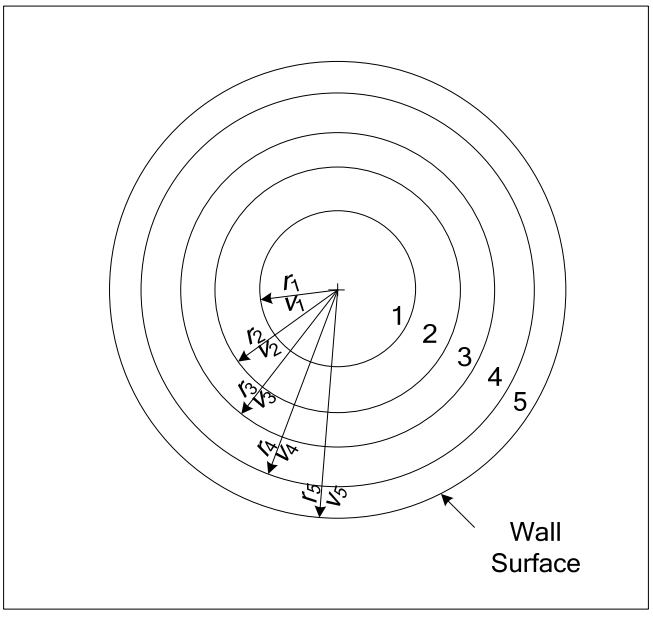

Figure 54. Measurement positions in pipe.

Table 32. Summarize the position of each point in the pipe.

Position of	Length (m)
r_1	0.0254
r_2	0.0381
r_3	0.0508
r_4	0.0722
r_5	0.0762

Velocity

Air velocity can be calculated by

$$v = \frac{m}{A\rho} \tag{74}$$

The maximum velocity that the pitot tube can read is 35 m/s, but the flow velocity exiting the jet ejectors exceeded this limit. Therefore, on the downstream side, the pipe diameter was enlarged from 0.0762 inch to 0.1524 meters to reduce the flow velocity to the measurable range. Figure 55 shows an example of velocity profile at the design condition.

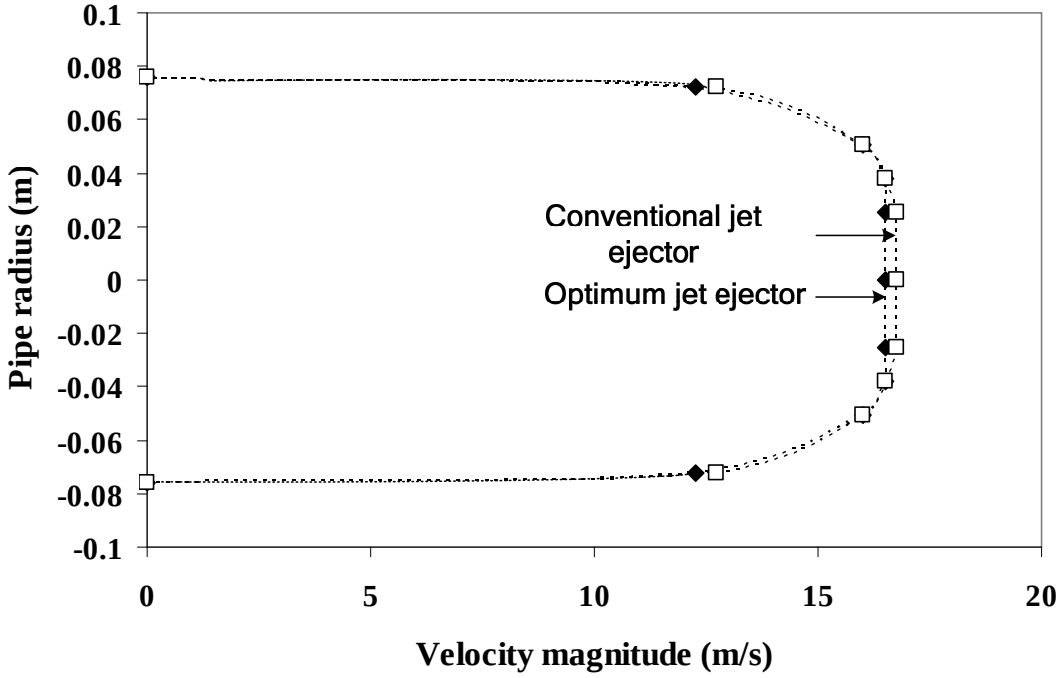

Figure 55. Velocity profile in pipe.

Efficiency

Ejector efficiency is calculated by rearranging Equation 52 in Chapter IV

$$\eta = \frac{\frac{1}{2}\left(\dot{m}_m + \dot{m}_p\right)v_o^2 + \dot{m}_p\frac{RT_p}{MW} + \dot{m}_m\frac{RT_m}{MW} + \dot{m}_p\left(\frac{RT_p}{MW}\right)\frac{\gamma}{\gamma-1}\left[\left(\frac{P_o}{P_p}\right)^{\frac{\gamma-1}{\gamma}} - 1\right] + \dot{m}_m\left(\frac{RT_m}{MW}\right)\frac{\gamma}{\gamma-1}\left[\left(\frac{P_o}{P_m}\right)^{\frac{\gamma-1}{\gamma}} - 1\right]}{\frac{1}{2}\dot{m}_p v_p^2 + \frac{1}{2}\dot{m}_m v_m^2 + \dot{m}_p\frac{RT_p}{MW} + \dot{m}_m\frac{RT_m}{MW}} \tag{75}$$

where all temperature are measured at the jet ejector inlet. The equation validation was presented in Appendix A. Figure 47 displays all parameters used in the efficiency equation.

CFD Analysis

The deviation of the compression ratios and efficiency between experiment and CFD analysis is given by

$$\text{Percent deviation} = \left(\frac{\text{Experiment} - \text{Modeling}}{\text{Experiment}} \right) \times 100 \qquad (76)$$

The simulation results were obtained directly from first principles; no adjustable parameters were used.

Results and Discussion

Jet ejector performance can be defined by both compression ratio and efficiency. Over a wide range of mass flow ratios and motive velocities, Figures 56(A) – (D) and Figures 56(A) – (D) show the compression ratios and efficiencies, respectively, for the optimal and conventional jet ejectors. Both jet ejectors are designed to provide maximum efficiency at compression ratio 1.30 and motive velocity 390 m/s. The optimal design is built according to the optimization results presented in Chapter VI. The jet ejector provided by Graham Corp. is commonly used in industry. As mentioned earlier, the same nozzle was used in both jet ejectors; therefore, the effect of nozzle selection on

jet ejector performance was eliminated. As shown in Figures 56(A) – (D), the compression ratio rapidly increases at low mass flow ratios and then gradually increases above mass flow ratios of 1.50 kg motive/kg propelled. The efficiency increases rapidly at low mass flow ratios, reaches the maximum, and then drops after the peak. At low mass flow ratios, the difference between the optimal and conventional jet ejectors is very small and difficult to observe, so Figures 58(A) – (D) enlarge this region. As shown in Figures 57 – 58, the optimal jet ejector produces greater compression ratio and efficiency than the conventional jet ejector at all operating conditions.

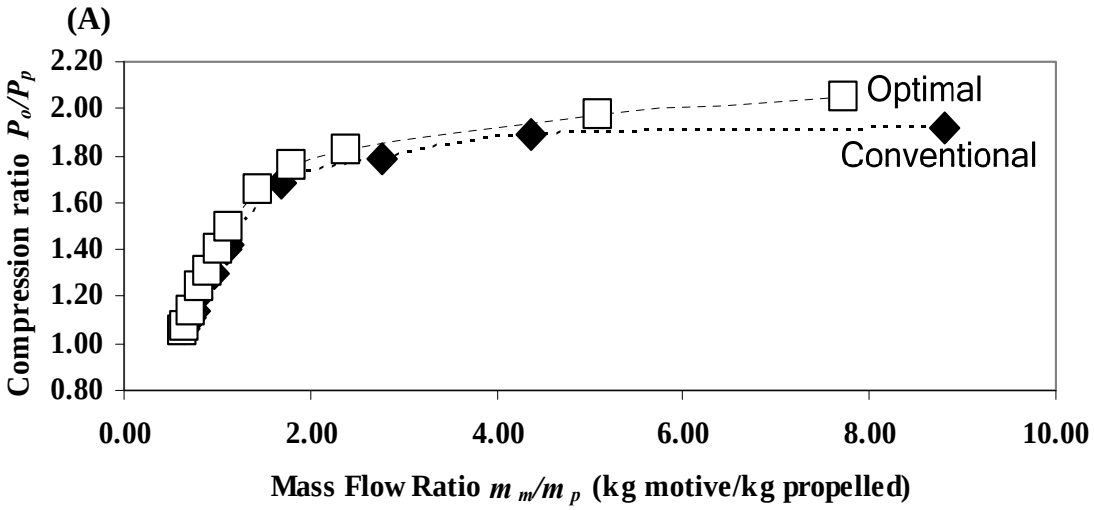

Figure 56. Compression ratio for a given mass flow ratio for optimal and conventional jet ejector at motive velocities (A) 390 m/s, (B) 370 m/s, (C) 320 m/s, and (D) 298 m/s.

(B)

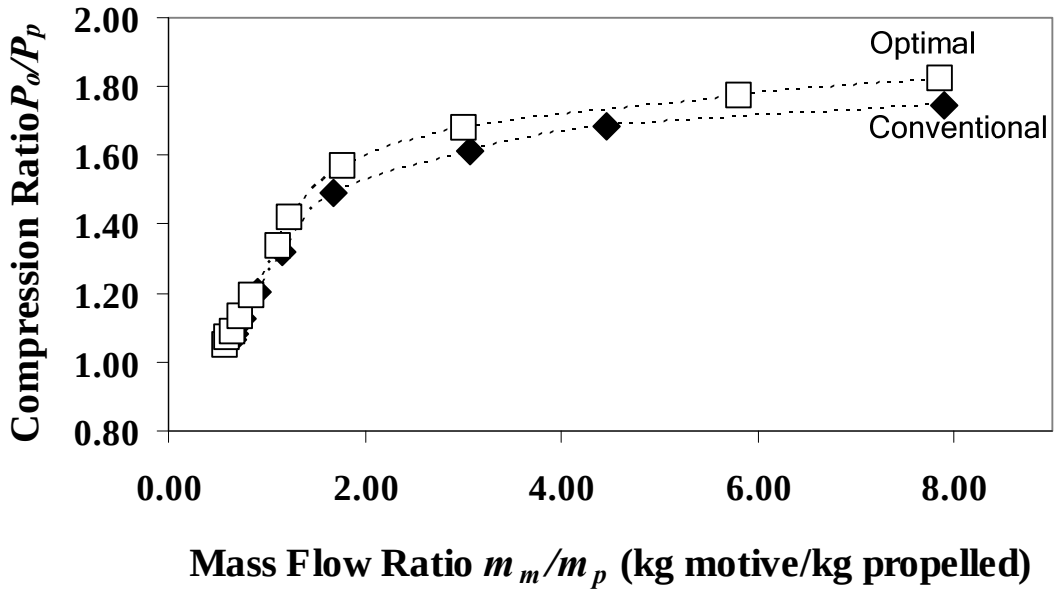

(C)

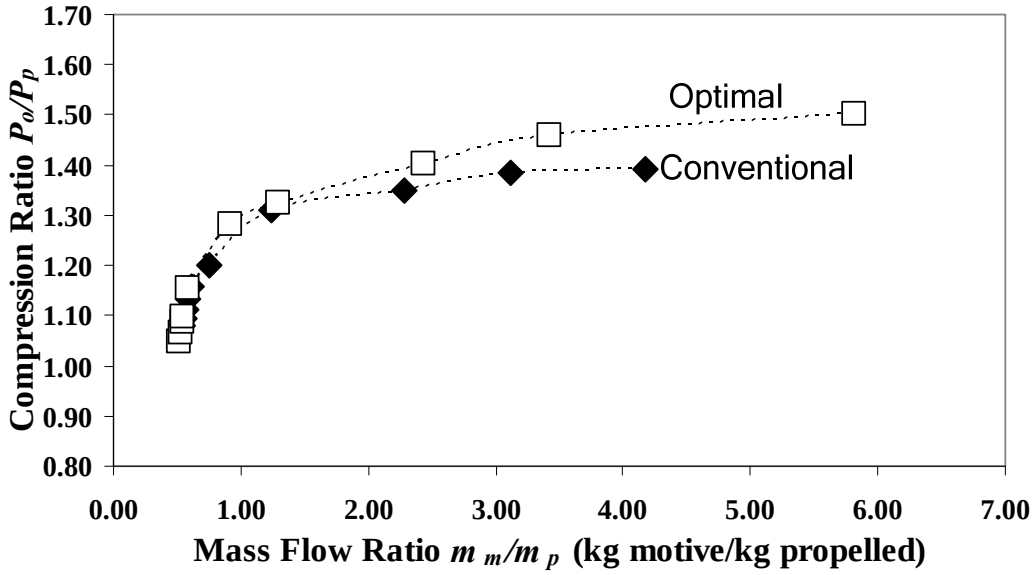

Figure 56. Continued.

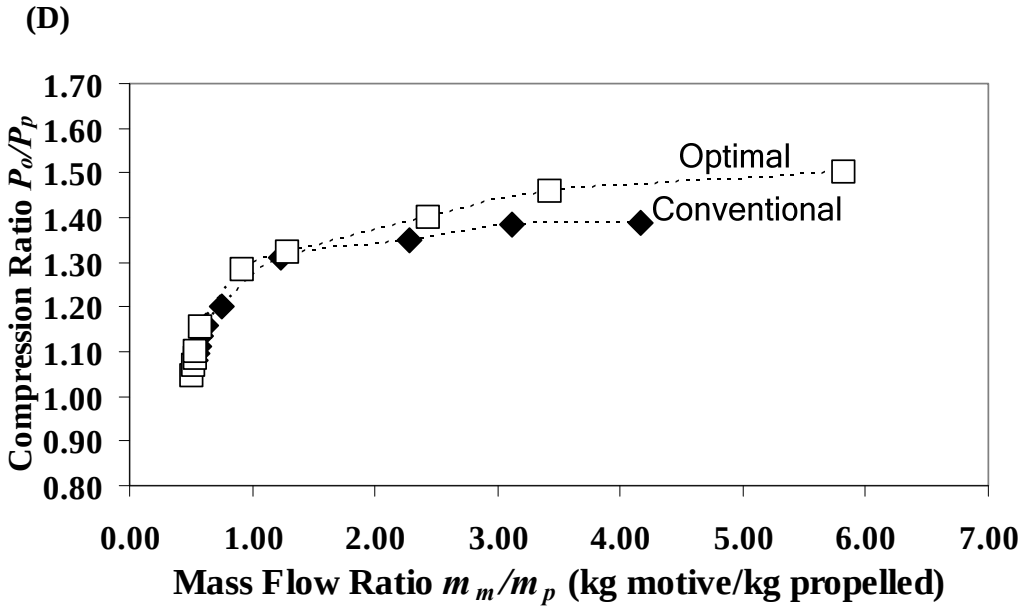

Figure 56. Continued.

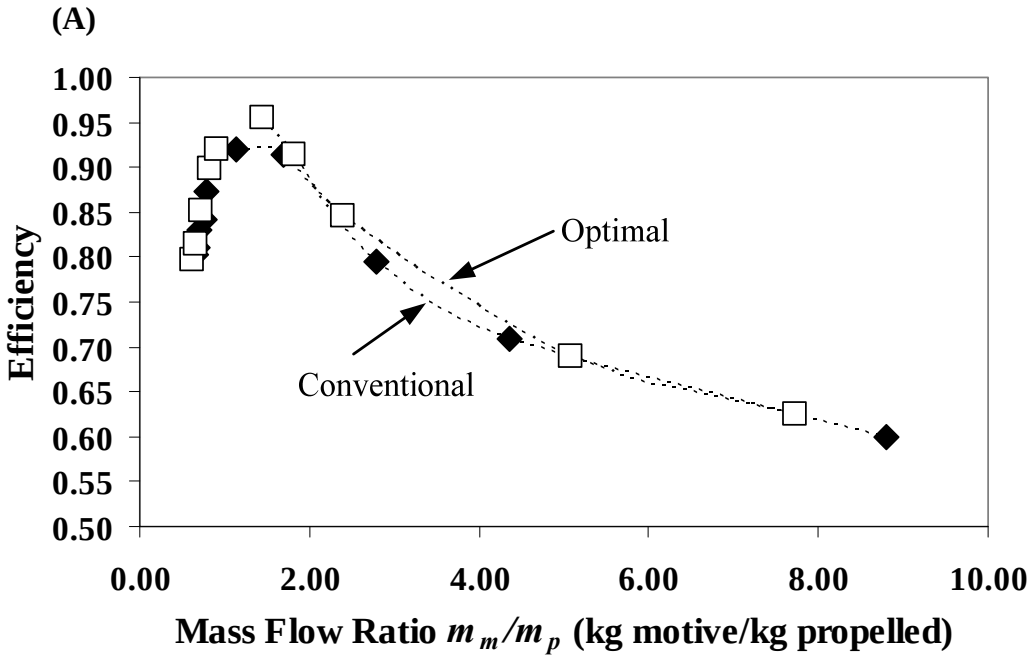

Figure 57. Efficiency for a given mass flow ratio for optimal and conventional jet ejector at motive velocities (A) 390 m/s, (B) 370 m/s, (C) 320 m/s, and (D) 298 m/s.

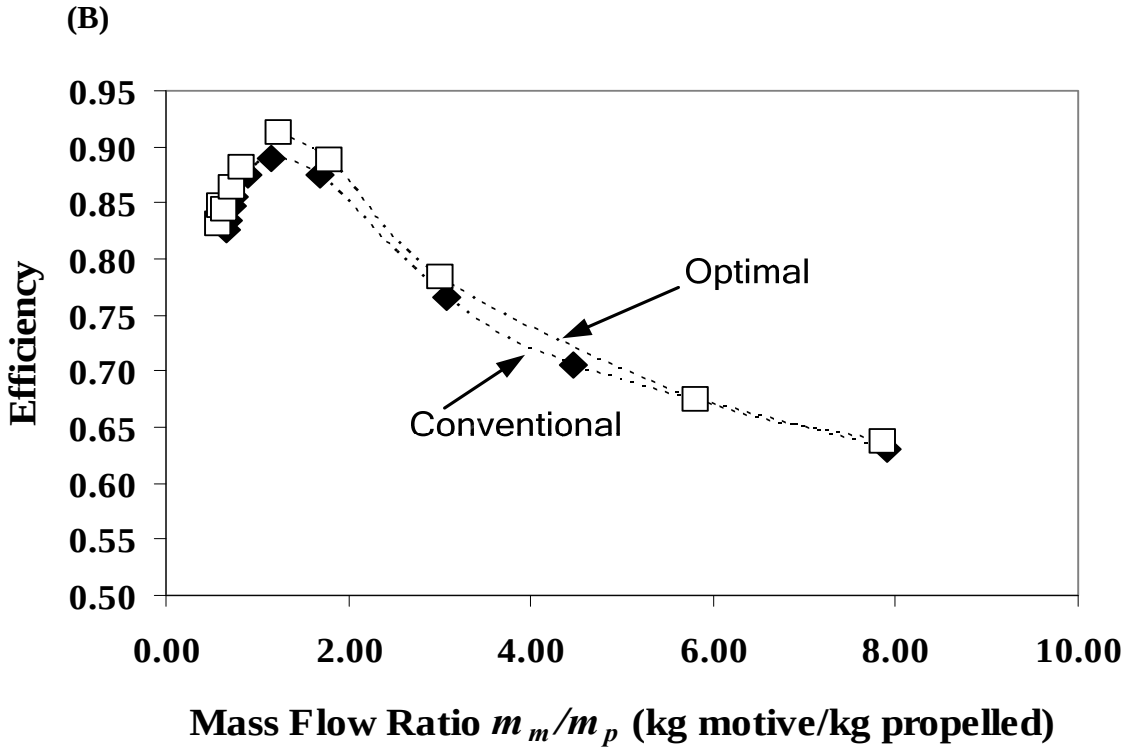

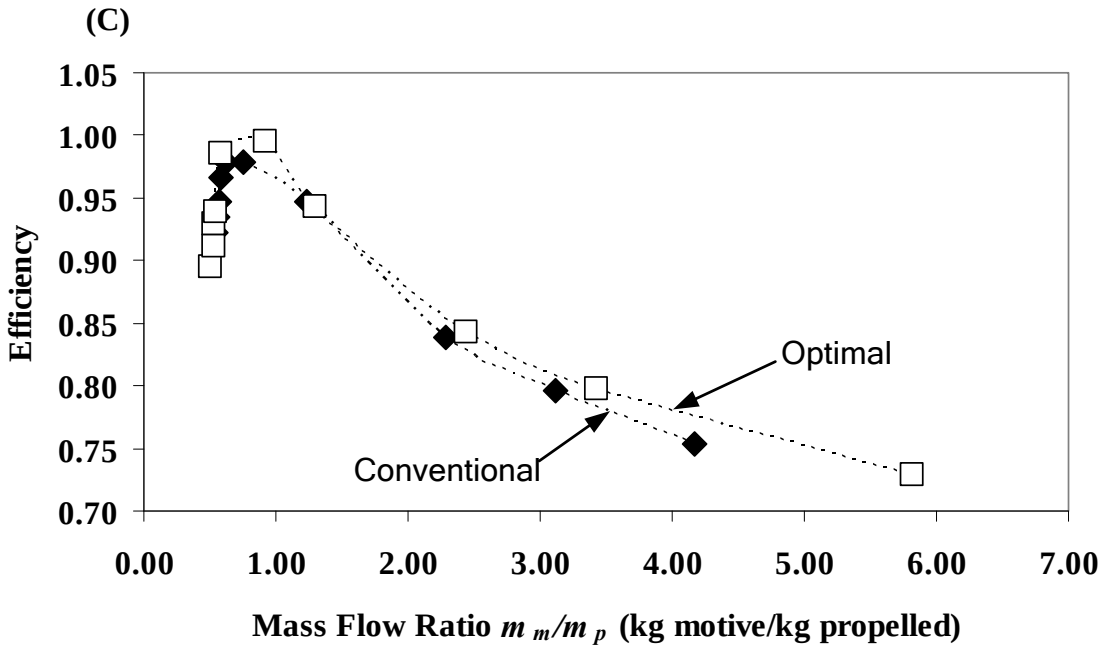

Figure 57. Continued.

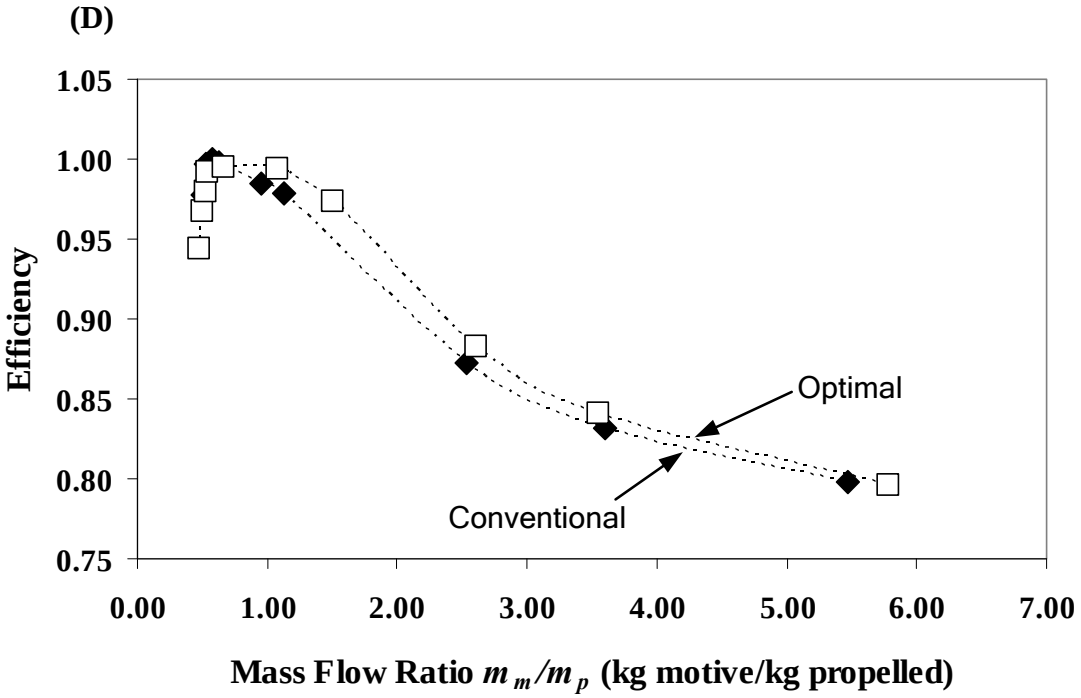

Figure 57. Continued.

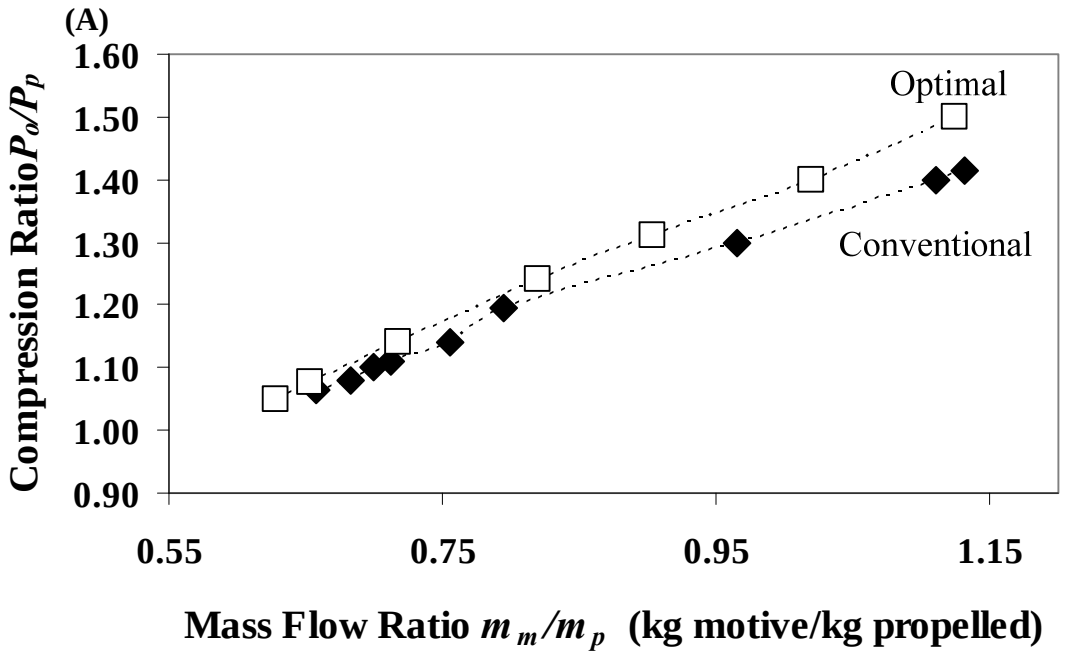

Figure 58. Enlarged view of the low-compression-ratio region of Figure 5 (A) 390 m/s, (B) 370 m/s, (C) 320 m/s, and (D) 298 m/s.

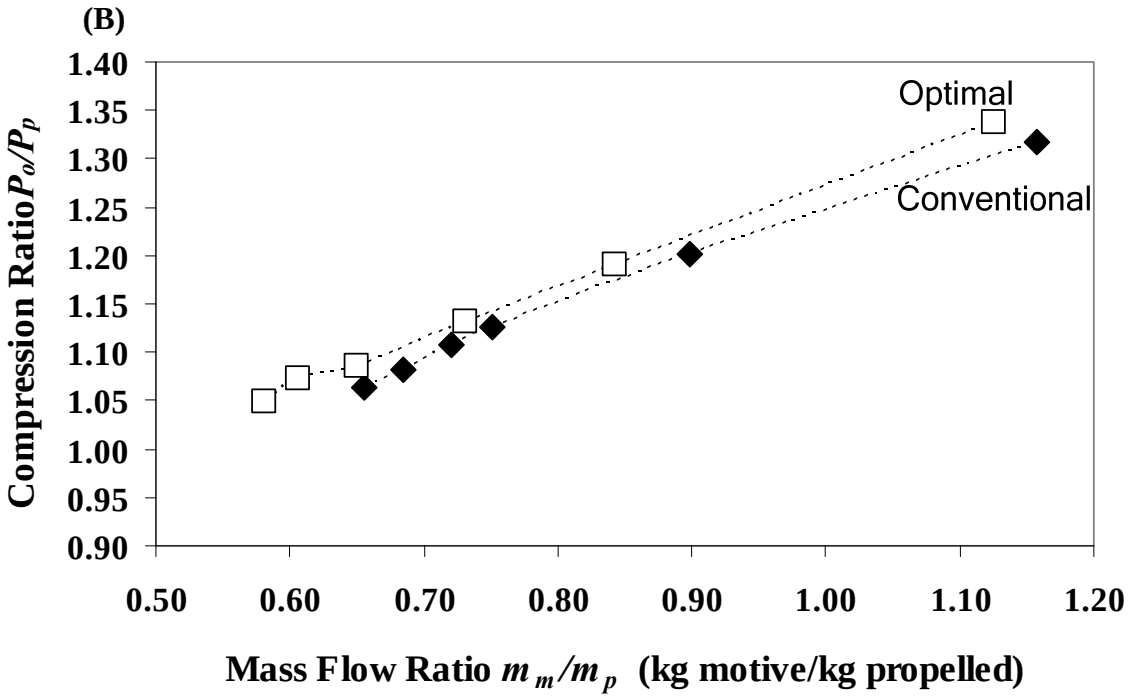

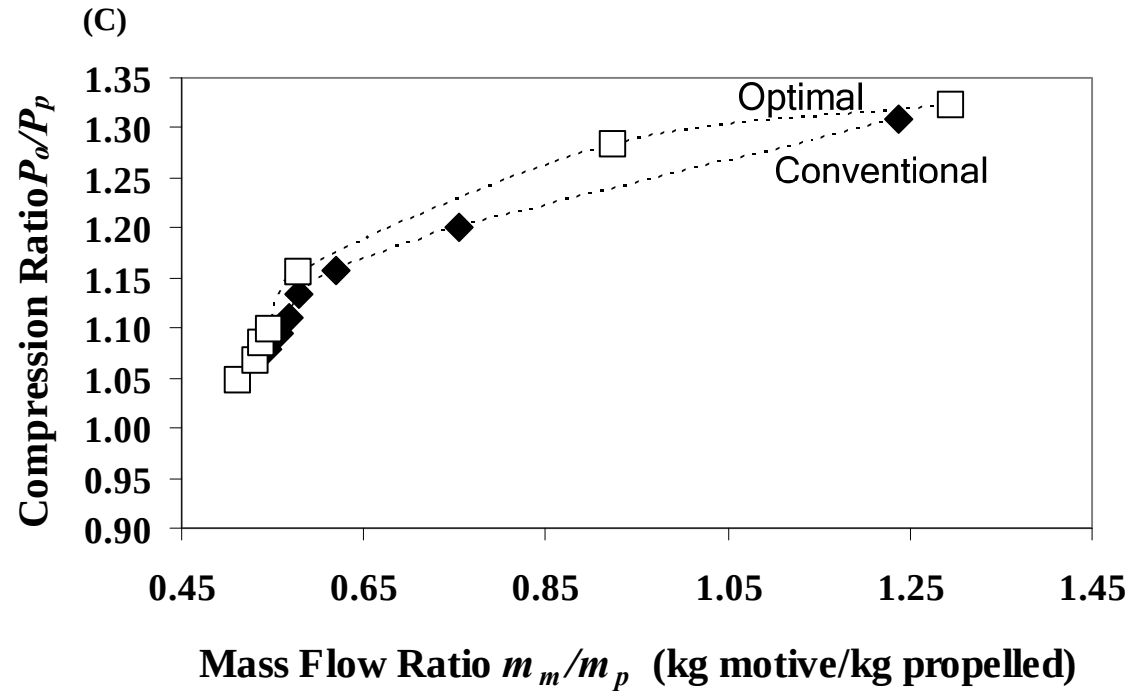

Figure 58. Continued.

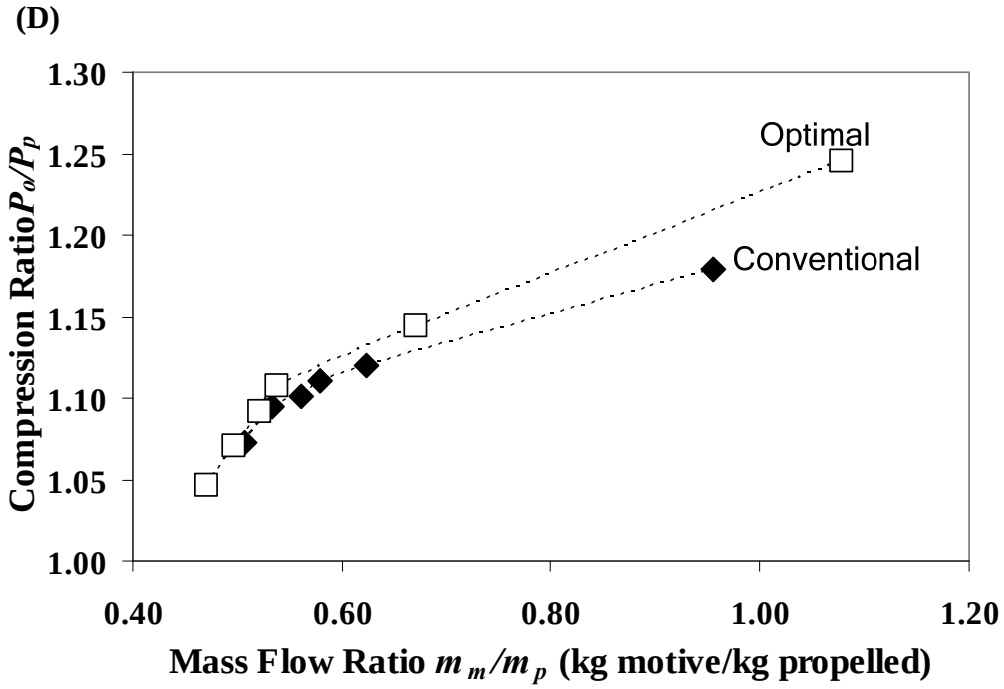

Figure 58. Continued.

.

Another parameter that determines the jet ejector performance is motive-stream usage. The design that uses less motive stream to produce the same compression ratio is the more efficient design; therefore, the reduction in motive-stream usages was also investigated. The results show that the optimal design consumes less motive stream when operating at the same compression ratio.

Table 33 summarizes the mass flow ratios for both designs at various compression ratios. The percentage reduction in motive-stream usage is calculated as follows:

$$\text{Percent reduction} = \left(\frac{\text{Conventional} - \text{Optimal}}{\text{Optimal}} \right) \times 100 \qquad (77)$$

The terms in the equation represent each mass flow ratio. Table 34 summarizes results from Equation 77.

According to Table 34, the percentage reduction in motive-stream usage is best at higher compression ratios and lower motive velocities. A typical reduction of the motive stream is about 8 – 10% compared to the conventional jet ejector, which reduces operating costs by about 8 – 10% as well. The optimal jet ejector consumes less motive stream than the conventional jet ejector up to 24.44% at compression ratio 1.20 and motive velocity 290 m/s.

Table 33. Summary of the mass flow ratios for both designs at various compression ratios.

Compression ratio (P_o/P_p)	Mass flow ratio (m_m/m_p)							
	Motive velocity 390 m/s		Motive velocity 370 m/s		Motive velocity 320 m/s		Motive velocity 298 m/s	
	Optimum	Conven-tional	Optimum	Conven-tional	Optimum	Conven-tional	Optimum	Conven-tional
1.1	0.68	0.70	0.69	0.72	0.54	0.57	0.53	0.56
1.2	0.78	0.82	0.85	0.89	0.70	0.75	0.90	1.12
1.3	0.89	0.97	1.03	1.12	1.08	1.23	1.50	*
1.4	1.02	1.11	1.24	1.42	2.44	*	*	*

* Data are unavailable; Shaded area is the design condition.

Table 34. Reduction in motive stream usage.

Compression ratio (P_o/P_p)	Motive stream reduction (%)			
	Motive velocity 390 m/s	Motive velocity 370 m/s	Motive velocity 320 m/s	Motive velocity 298 m/s
1.1	2.94	4.35	4.65	5.66
1.2	5.13	4.71	7.14	24.44
1.3	8.48	8.74	13.89	*
1.4	8.82	14.52	*	*

*****Data are unavailable; Shaded area is the design condition.

According to Table 34, the percentage reduction in motive-stream usage is best at higher compression ratios and lower motive velocities. A typical reduction of the motive stream is about 8 – 10% compared to the conventional jet ejector, which reduces operating costs by about 8 – 10% as well. The optimal jet ejector consumes less motive stream than the conventional jet ejector up to 24.44% at compression ratio 1.20 and motive velocity 290 m/s.

Robustness Analysis

A robust jet ejector will perform well over a wide range of operating conditions. Figures 59(A) – (D) compare the variation in efficiency over a wide range of motive velocities for both the optimal and conventional jet ejectors for different compression ratios. The efficiency of the optimal design is maintained over a wide range of motive velocities compared to the conventional design. This characteristic is more pronounced at higher compression ratios (1.30 and 1.40).

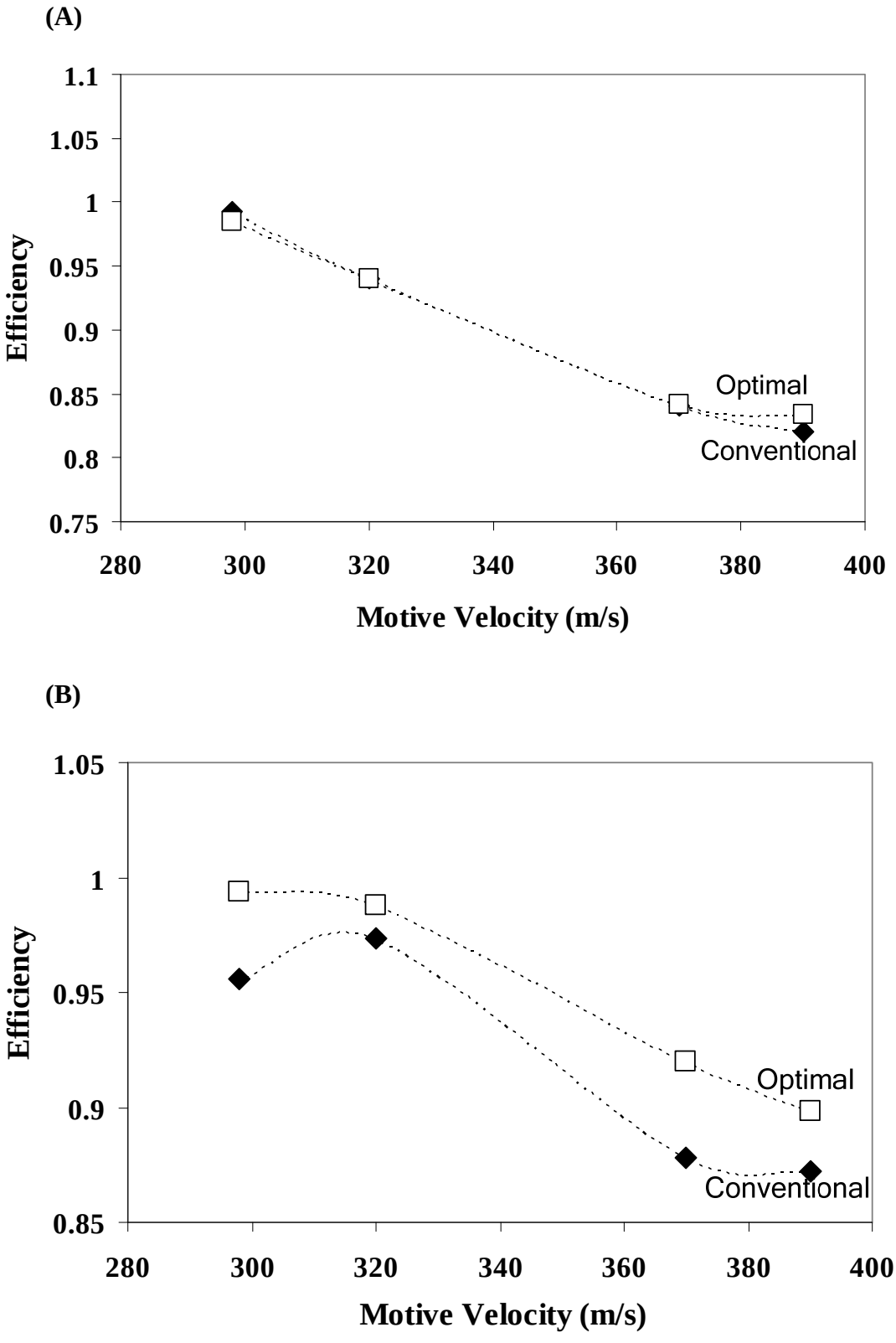

Figure 59. Efficiency for a given motive velocity for optimal and conventional jet ejector at various compression ratios (A) 1.10, (B) 1.20, (C) 1.30, and (D) 1.40.

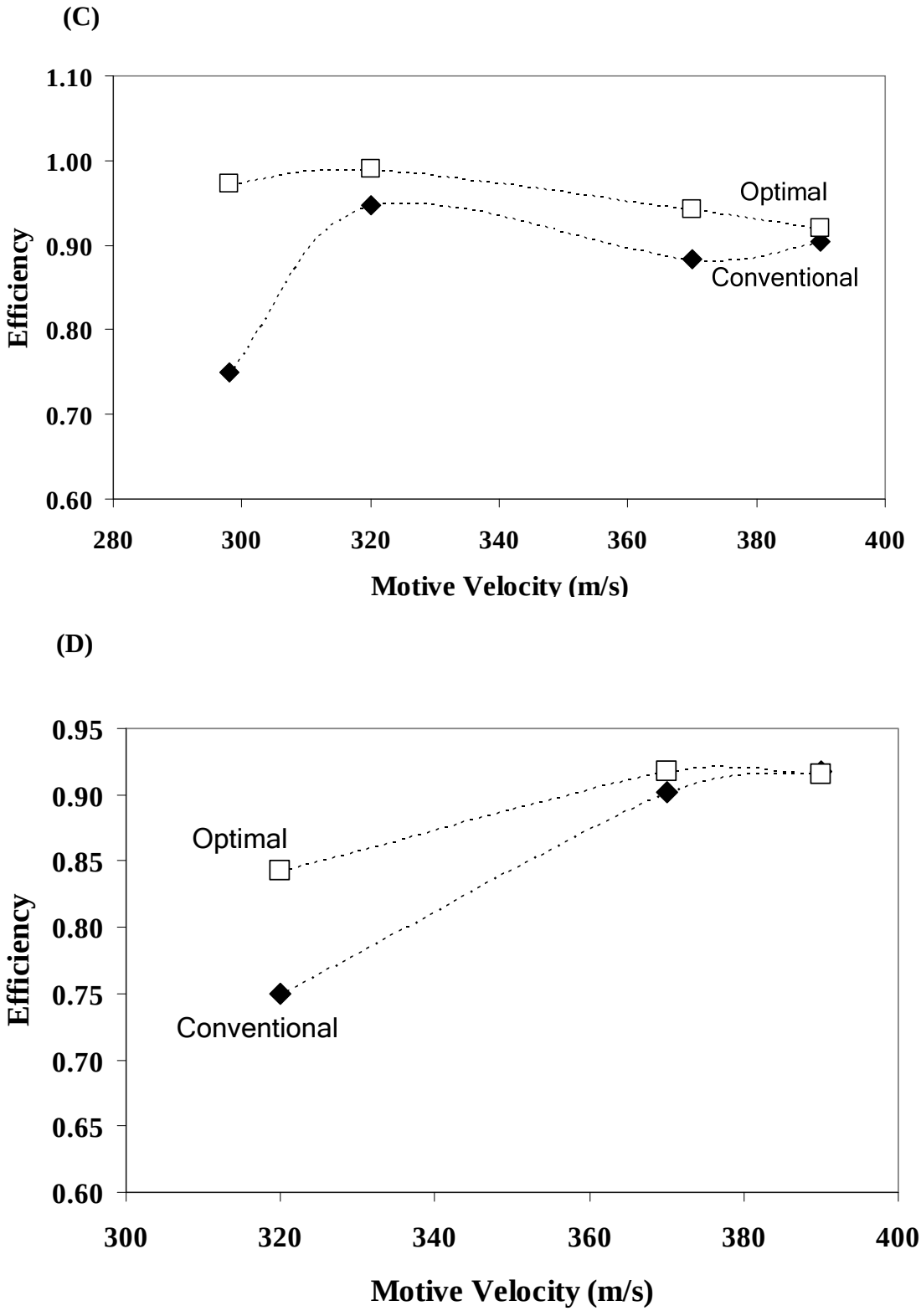

Figure 59. Continued.

CFD Analysis

Table 35 displays the percent deviation between experiment and CFD model on both compression ratio and efficiency at various motive velocities. Figures 60(A) – (D) and 61(A) – (D) show the compression ratios and efficiencies, respectively, for the optimal jet ejector and CFD modeling. CFD modeling over-predicts at low mass flow ratios and under-predicts at high mass flow ratios on both compression ratio and efficiency. This characteristic is similar for all motive velocities. The transition point is about mass flow ratio 1.00 kg motive/kg propelled. The overall deviation between both results is 13.10% and 8.71% on compression ratio and efficiency, respectively.

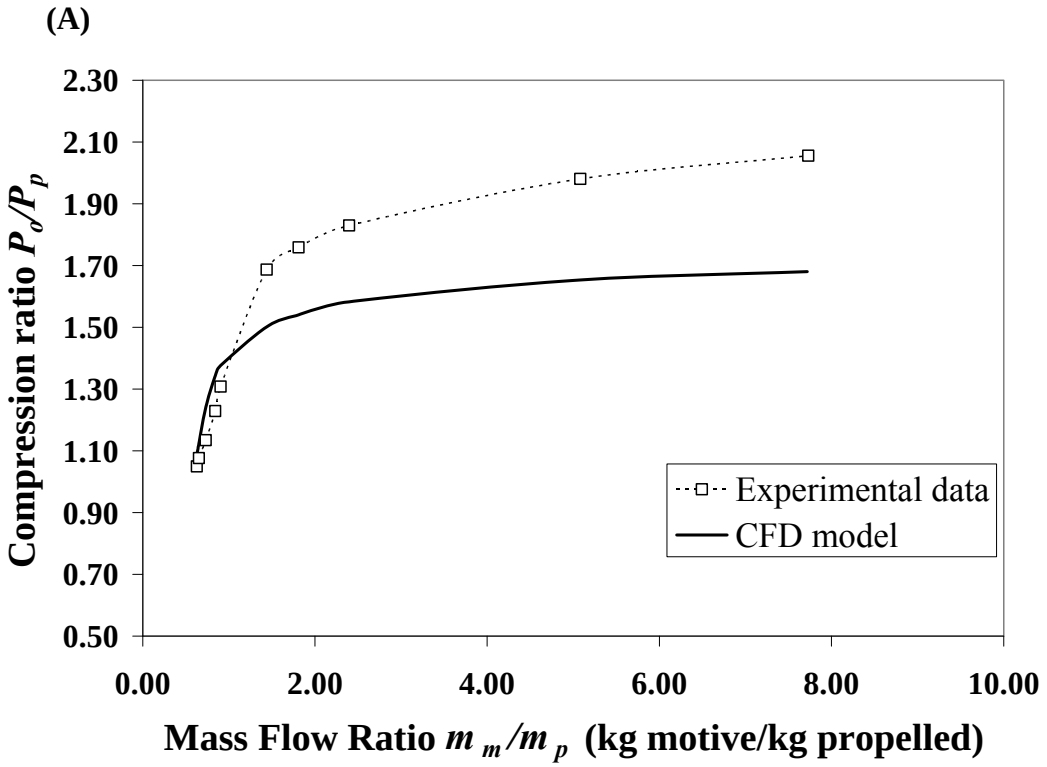

Figure 60. Compression ratio of optimal jet ejector compared to CFD model at motive velocities (A) 390 m/s, (B) 370 m/s, (C) 320 m/s, and (D) 298 m/s.

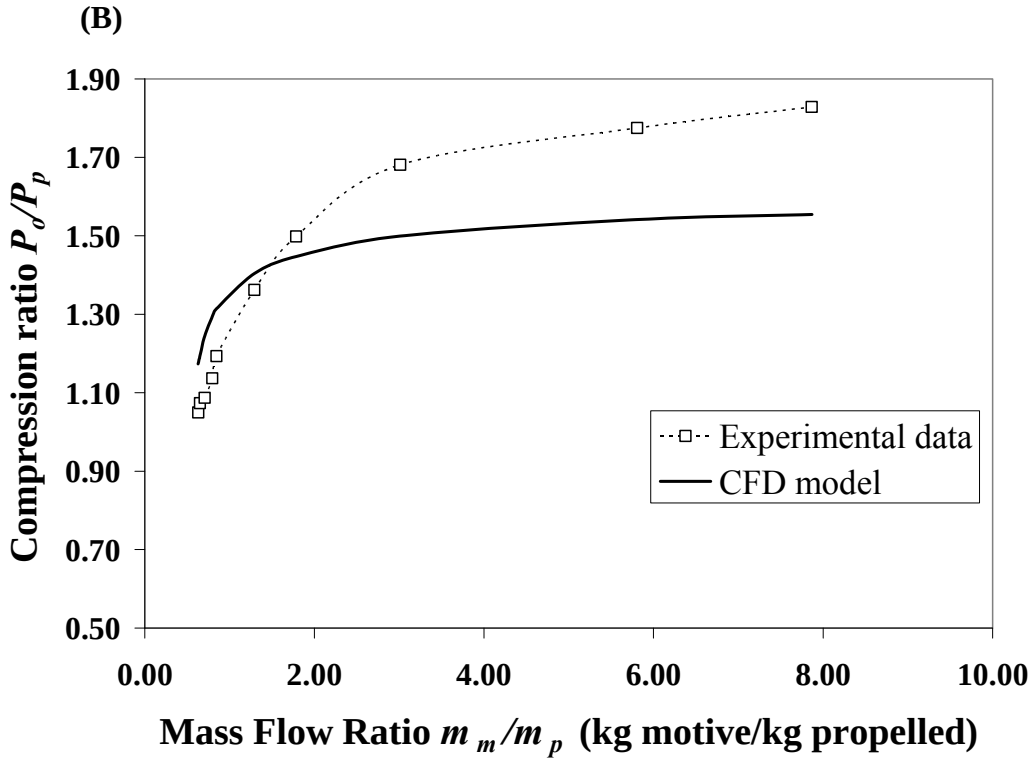

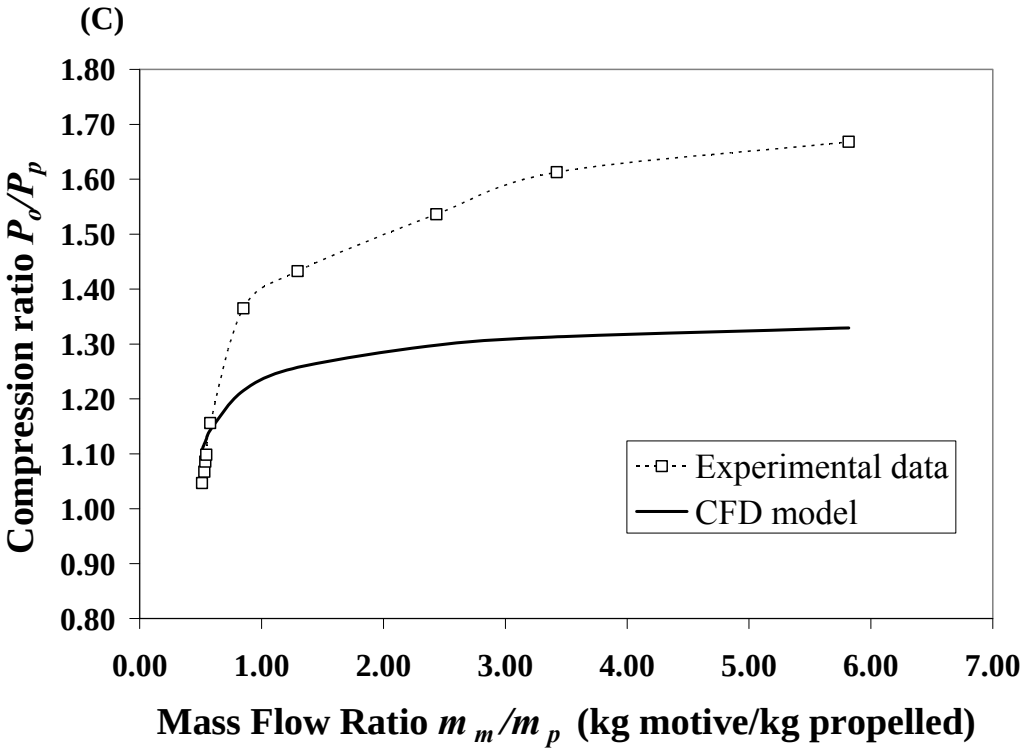

Figure 60. Continued.

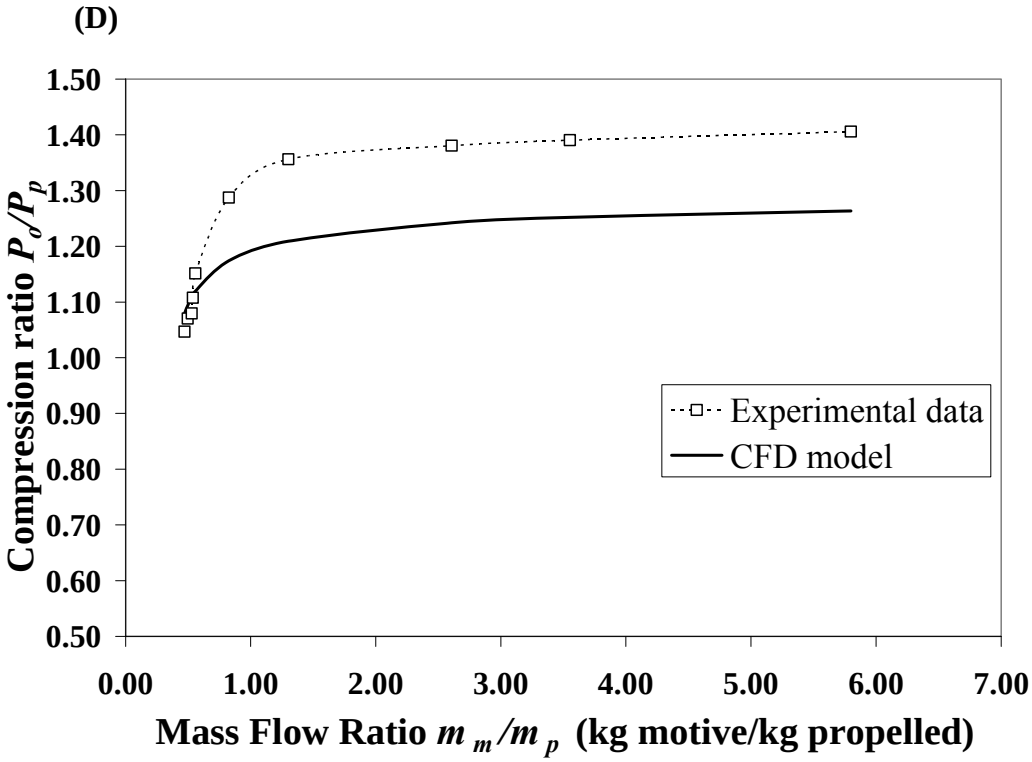

Figure 60. Continued.

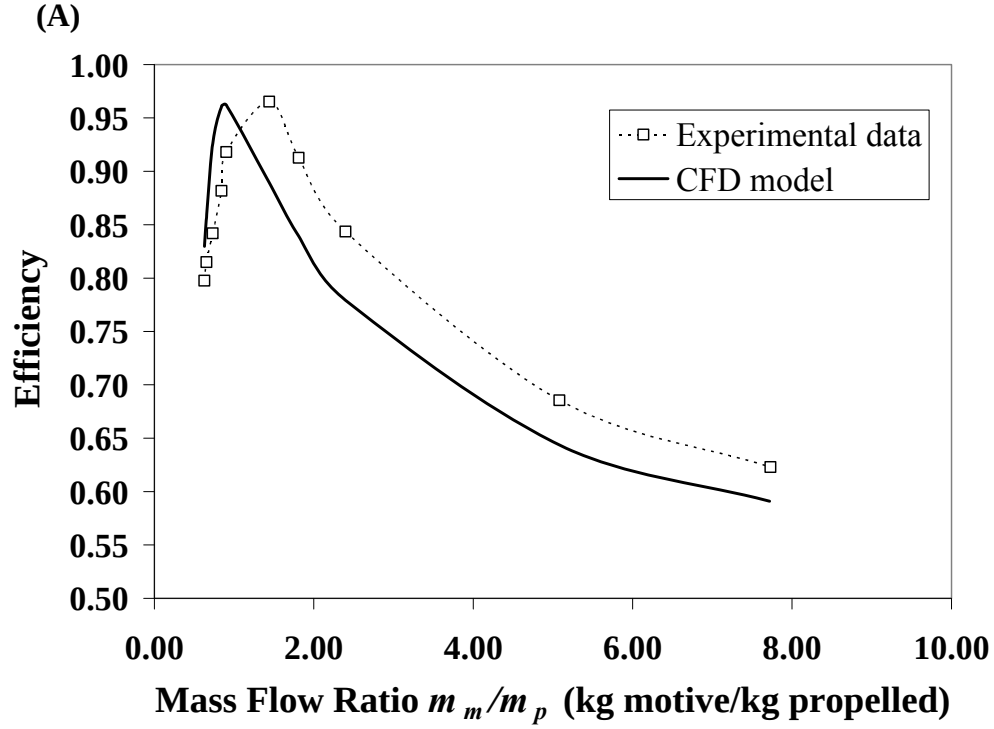

Figure 61. Efficiency of optimal jet ejector compared to CFD model at motive velocities (A) 390 m/s, (B) 370 m/s, (C) 320 m/s, and (D) 298 m/s.

(B)

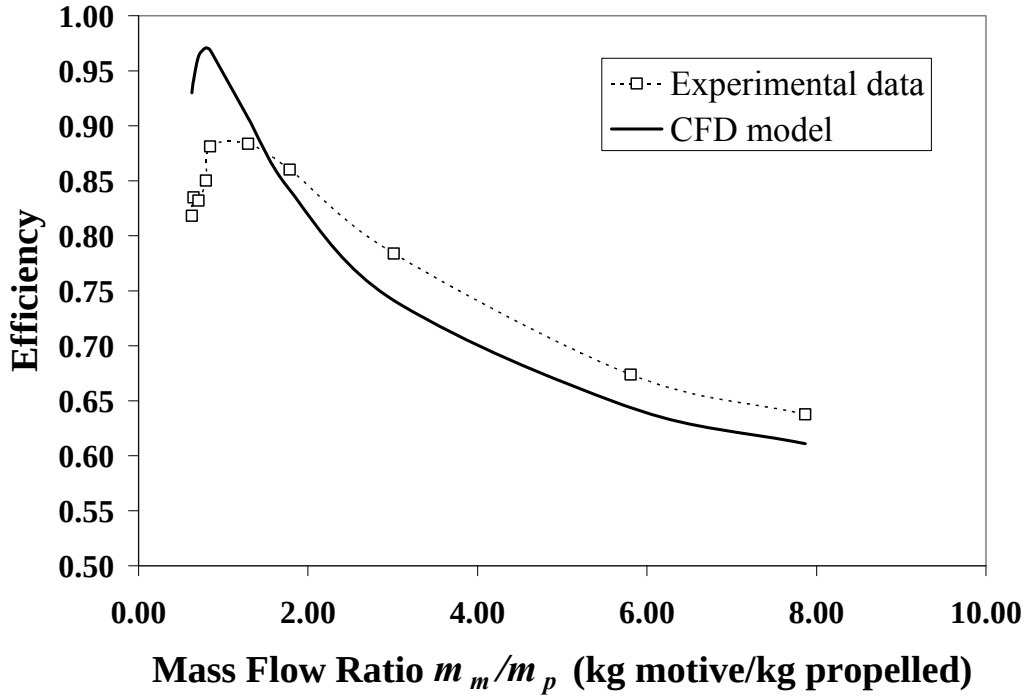

(C)

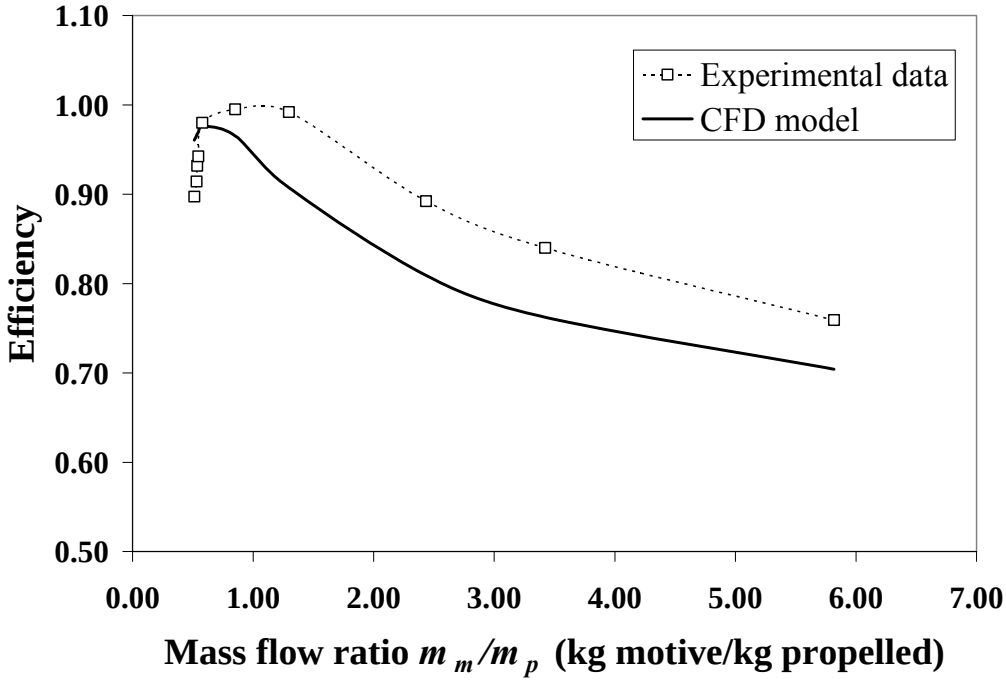

Figure 61. Continued.

(D)

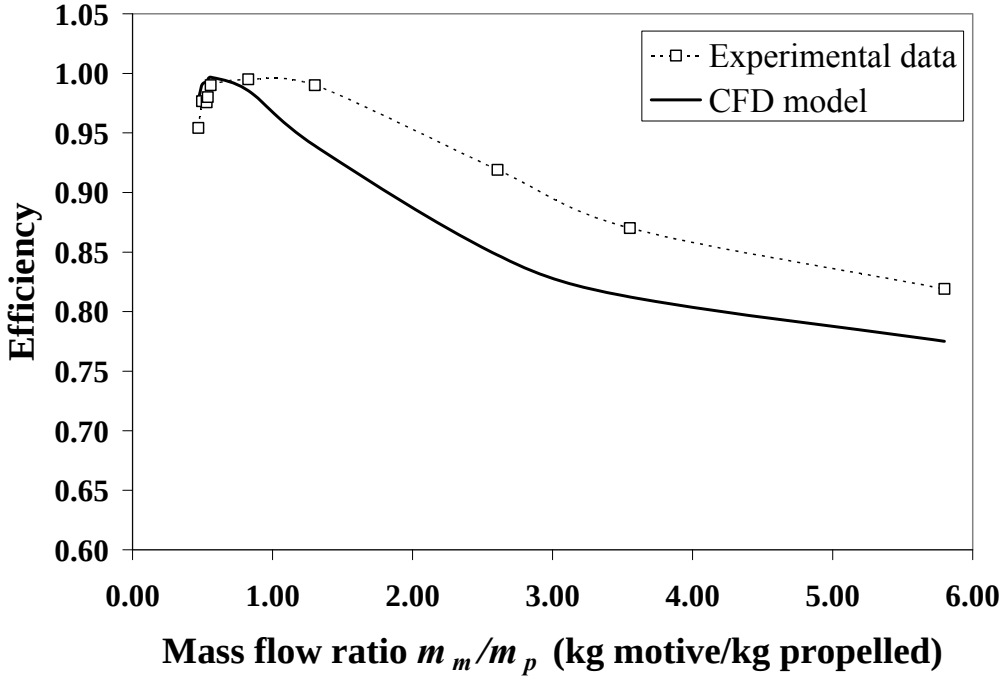

Figure 61. Continued.

Table 35. Results comparing between experimental results and CFD modeling at various motive velocities (A) 390 m/s, (B) 370 m/s, (C) 320 m/s, and (D) 298 m/s.

(A)

Mass flow rate m_m/m_p	Compression ratio P_o/P_p		% Deviation	Efficiency η		% Deviation
	Experiment	Simulation		Experiment	Simulation	
0.63	1.050	1.086	3.49	0.798	0.830	4.04
0.65	1.076	1.125	4.50	0.815	0.857	5.12
0.73	1.134	1.241	9.46	0.842	0.926	9.99
0.84	1.229	1.343	9.31	0.882	0.961	9.00
0.90	1.308	1.376	5.17	0.918	0.962	4.80
1.44	1.687	1.502	10.98	0.965	0.889	7.87
1.81	1.759	1.540	12.42	0.913	0.839	8.04
2.40	1.830	1.583	13.52	0.844	0.779	7.61
5.08	1.981	1.654	16.51	0.686	0.644	6.13
7.73	2.055	1.680	18.25	0.623	0.591	5.15
		Average	**14.80**		**Average**	**9.68**

Table 35. Continued.

(B)

Mass flow rate m_m/m_p	Compression ratio P_o/P_p		% Deviation	Efficiency η		% Deviation
	Experiment	Simulation		Experiment	Simulation	
0.63	1.050	1.173	11.78	0.818	0.930	13.67
0.65	1.073	1.195	11.30	0.835	0.942	12.77
0.71	1.087	1.245	14.55	0.832	0.963	15.77
0.80	1.137	1.295	13.91	0.850	0.971	14.19
0.85	1.193	1.314	10.14	0.881	0.969	9.93
1.29	1.362	1.404	3.08	0.884	0.907	2.64
1.78	1.498	1.447	3.44	0.860	0.842	2.13
3.01	1.681	1.499	10.83	0.784	0.741	5.44
5.81	1.775	1.541	13.16	0.674	0.644	4.41
7.87	1.828	1.554	14.99	0.638	0.611	4.20
		Average	**15.31**		**Average**	**12.16**

(C)

Mass flow rate m_m/m_p	Compression ratio P_o/P_p		% Deviation	Efficiency η		% Deviation
	Experiment	Simulation		Experiment	Simulation	
0.51	1.047	1.108	5.81	0.897	0.961	7.04
0.53	1.067	1.118	4.77	0.914	0.966	5.62
0.54	1.086	1.122	3.35	0.932	0.967	3.83
0.55	1.098	1.127	2.59	0.942	0.970	2.86
0.58	1.156	1.143	1.10	0.980	0.976	0.40
0.85	1.365	1.215	10.96	0.995	0.965	3.00
1.30	1.433	1.257	12.24	0.992	0.908	8.52
2.44	1.536	1.298	15.52	0.892	0.809	9.29
3.42	1.613	1.313	18.59	0.840	0.762	9.25
5.82	1.668	1.329	20.32	0.759	0.704	7.23
		Average	**13.61**		**Average**	**8.15**

Table 35. Continued.

(D)

Mass flow rate m_m/m_p	Compression ratio P_o/P_p		% Deviation	Efficiency η		% Deviation
	Experiment	Simulation		Experiment	Simulation	
0.47	1.047	1.079	3.12	0.954	0.978	2.50
0.50	1.070	1.094	2.19	0.977	0.991	1.44
0.53	1.079	1.109	2.71	0.976	0.993	1.76
0.54	1.108	1.112	0.41	0.980	0.995	1.51
0.56	1.151	1.120	2.74	0.990	0.997	0.69
0.83	1.287	1.174	8.81	0.995	0.986	0.96
1.30	1.356	1.209	10.83	0.990	0.939	5.14
2.61	1.381	1.242	10.03	0.919	0.848	7.78
3.55	1.391	1.252	9.97	0.870	0.812	6.63
5.80	1.406	1.263	10.14	0.819	0.775	5.37
		Average	**8.70**		**Average**	**4.83**

Conclusion

The optimal and conventional jet ejectors had nearly identical geometries (throat diameter, length, inlet diameter, discharge diameter, and nozzle shape). The two major differences between the optimal and conventional jet ejectors were the jet ejector type and nozzle position. A constant-area design was employed for the optimal jet ejector whereas a constant-pressure design was employed for the conventional jet ejector. In the optimal jet ejector, the nozzle outlet was located right at the beginning of the throat section, as suggested in Chapter VI. In the conventional design, the nozzle outlet is located in the mixing chamber a bit upstream of the throat section. These two adjustments make the optimal design perform better and more robustly than the conventional design. Compared to the conventional jet ejector, the optimal jet ejector can reduce the motive-stream consumption by 8% at the design condition, which will reduce operating cost by 8% as well. The experimental results of the optimal jet ejector were compared to the

predictions from CFD modeling. The overall deviation is 13.10% and 8.71% on compression ratio and efficiency, respectively.

CHAPTER X

APPLYING A HIGH-EFFICIENCY JET EJECTOR IN A VAPOR-COMPRESSION DESALINATION SYSTEM

Introduction

Chapter VI summarizes the optimal jet ejector geometry (nozzle diameter ratio, throat diameter ratio, and throat length ratio), compression ratio and efficiency. This chapter shows how to implement the results. This case study will clarify how a jet ejector should operate to achieve a certain compression ratio, how to specify the motive velocity that obtains the best performance (compression ratio and efficiency), and how to determine the mass flow ratio, and what the optimal jet ejector geometry is for a specified operating condition. The mass flow ratio affects the motive steam consumption. Theoretically, if the mass flow ratio (m_m/m_p) is low, the amount of motive steam used in the jet ejector will be small, which lowers the operating cost. On the other hand, if the mass flow ratio is high, the jet ejector will consume a lot of motive steam, which increases the operating cost. According to the optimization results, the compression ratio is greater and the efficiency is lower at high mass flow ratios. Oppositely, the compression ratio is lower and the efficiency is greater at low mass flow ratios.

Methodology

Here, the procedure for implementing the results is explained. In the sample situation, a jet ejector using steam as a working fluid is operated at compression ratio

1.10. A typical application would be in thermocompression distillation. A compression ratio of 1.10 supports a temperature difference of 1°C in a two-stage still.

1. Search the optimization results that fall within the specified compression ratio region from Table 14, as shown in Table 36.

Table 36. Results according to Step 1.

Motive Velocity (m/s)	Mass Flow Ratio	Compression Ratio	Efficiency
170	10	1.0689	0.9810
	50	1.1004	0.9789
	100	1.1114	0.9783
340	0.50	1.0597	0.9447
	1.00	1.1195	0.9303
510	0.10	1.0145	0.9474
	0.50	1.145	0.8686
680	0.10	1.0289	0.9120
	0.50	1.2676	0.7890
850	0.10	1.0590	0.8789
	0.50	1.3922	0.6928
1020	0.10	1.0706	0.8254
	0.50	1.4136	0.5689
1104	0.10	1.0790	0.7943
	0.25	1.2232	0.6390

At a motive velocity of 170 m/s, the mass flow ratio is almost 50 to achieve the 1.10 compression ratio, which means a jet ejector that propels 1 kg/s of steam will consume 50 kg/s of motive steam. This does not make economic sense; even though, the efficiency is very high (97.89%). Higher velocities (340 to 1104 m/s) use less motive steam, but have a lower efficiency.

2. Plot compression ratio versus mass flow ratio for each motive velocity, as shown in Figure 62.

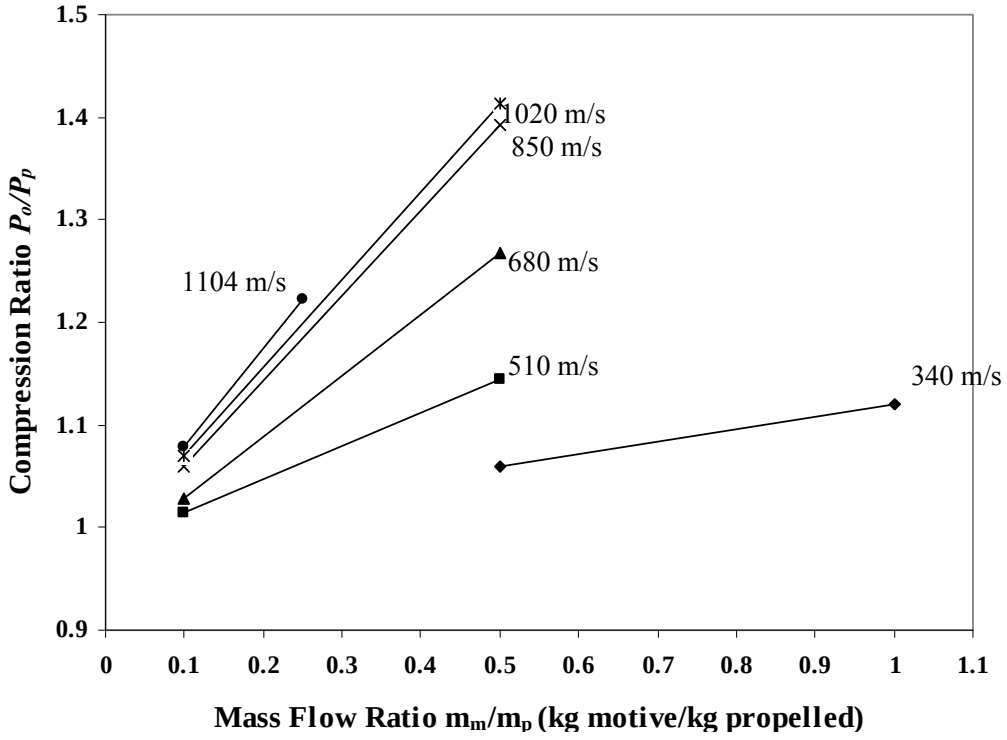

Figure 62. The graph presenting the relationship between compression ratio and mass flow ratio of each motive velocity.

3. Draw a horizontal line through the desired compression ratio (Figure 63). (In the sample case, the compression ratio is 1.10.)

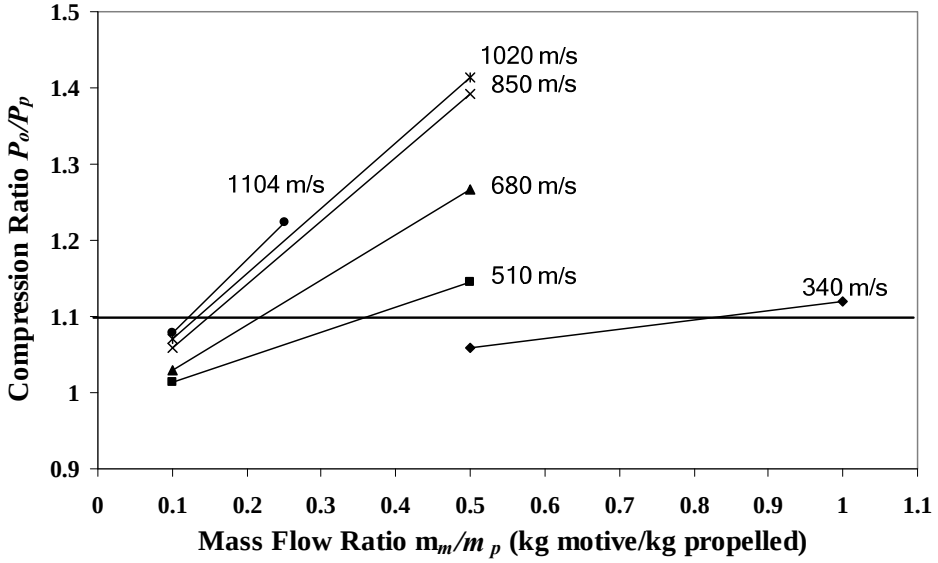

Figure 63. Graph according to Step 3.

The horizontal line intersects each curve. At the intersection point, a vertical line was drawn to the *x*-axis, which indicates the required mass flow ratio for each motive velocity (Figure 64).

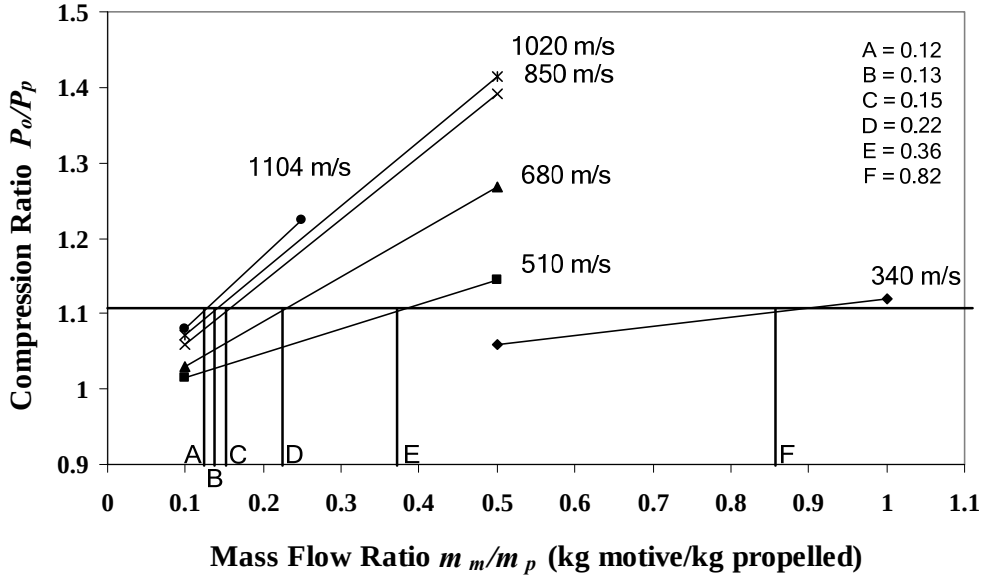

Figure 64. The graph presents the required mass flow ratio of each motive velocity to achieve 1.10 compression ratio.

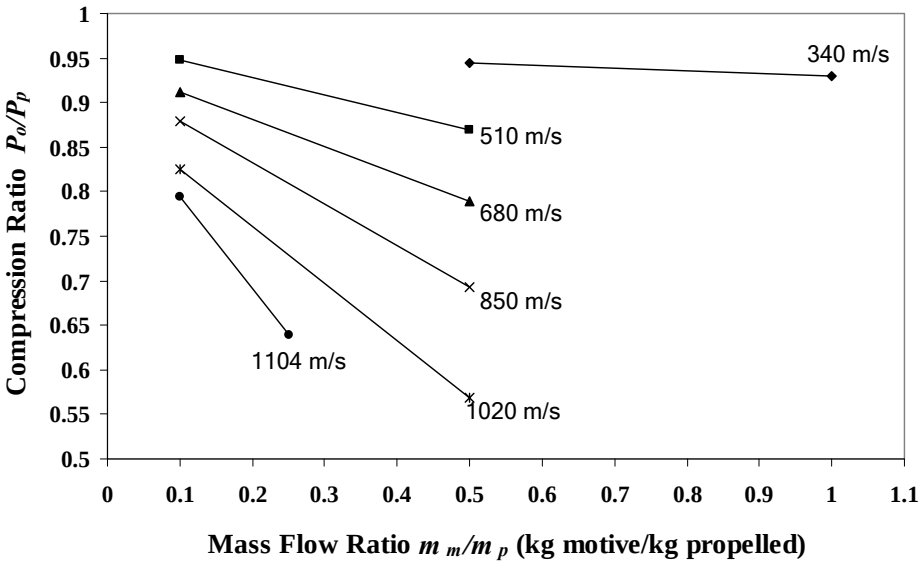

Figure 65. Graph presenting the relationship between efficiency and mass flow ratio of each motive velocity.

4. Plot the efficiency versus mass flow ratio at each motive velocity (Figure 65).

To identify the efficiency, draw a vertical line from the mass flow ratio obtained from Step 3 and then draw a horizontal line to the *y*-axis (Figure 66).

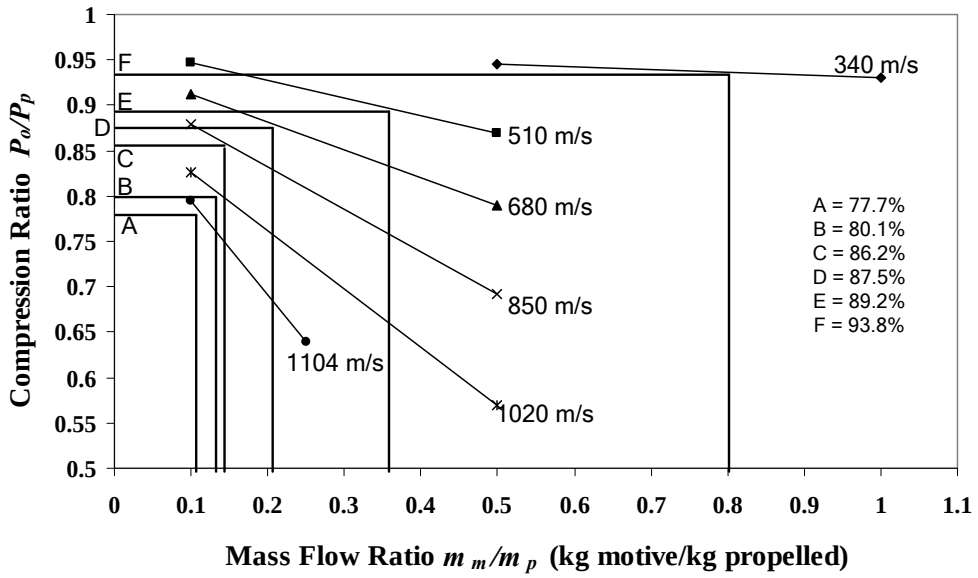

Figure 66. The graph presenting the efficiency of each motive velocity at 1.10 compression ratio.

5. Summarize the compression ratio and efficiency information for each motive velocity (Table 37).

Table 37. Summary of the mass flow ratio and efficiency for each motive velocity at 1.10 compression ratio.

Required Saturated Steam Pressure (Appendix E; atm)	Motive Velocity (m/s)	Mass Flow Ratio	Efficiency
1.69	340	0.82	93.8%
3.22	510	0.36	89.2%
6.21	680	0.22	87.5%
12.78	850	0.15	86.2%
31.42	1020	0.13	80.1%
60.66	1104	0.12	77.7%

The results in Table 37 indicate that, for a 1.10 compression ratio, there are many possible operating conditions. The next step is to select the best motive velocity that consumes the smallest amount of motive steam, but still has a satisfactory efficiency. According to Table 37, the mass flow ratios at motive velocities between 340 and 680 m/s are high, so the operating costs are high. A suitable motive velocity should be between 850 and 1104 m/s. A motive velocity of 1104 m/s requires high-pressure, high-temperature steam. At some point, as the motive velocity increases, the required steam temperature and pressure will be so high as to be uneconomical. At a steam pressure of 12.78 to 31.42 atm, the motive velocity is 850 to 1020 m/s and the mass flow ratio is 0.15

and 0.13 respectively, and the efficiency is 86.2% to 80.1%. The optimal geometry is obtained from either Table 14 or Figures 29A or B in Chapter VI.

Optimum Jet Ejector Implemented in a Vapor-Compression Desalination System

Desalination processes recover water from seawater. Among water treatment technologies, distillation is the most efficient alternative at reducing the widest range of water contaminants. The implementation of an optimum jet ejector in vapor-compression distillation system is discussed in this chapter. Figure 67 shows an optimum jet ejector implemented in a two-stage thermocompression evaporator. A multi-effect evaporator train operates at successively lower pressures and temperatures. Steam from a high-pressure evaporator boils water in an adjacent low-pressure evaporator. The jet ejector pulls vapors from the low-pressure latent heat exchanger, compresses them, and returns them to the high-pressure latent heat exchanger. A single latent heat exchanger including the heat flow is displayed in Figure 68. In a latent heat exchanger, the steam latent heat of condensation is transferred to vaporize water from seawater. Assuming the latent heat exchanger is well insulated, the condensing-steam enthalpy change equals the seawater boiling-side enthalpy change (Lara Ruiz, 2005); therefore, the enthalpy balance equation is defined as

Heat to condense steam in condensor = Heat to evaporate water in evaporator (78)

$$Q_c = Q_e \tag{79}$$

$$M_c\left(H_c^v - H_c^l\right) = M_e\left(H_e^v - H_e^l\right) \tag{80}$$

where

H_c^v = specific enthalpy of condensate vapor $\left(\text{kJ/kg}\right)$

H_c^l = specific enthalpy of condensate liquid $\left(\text{kJ/kg}\right)$

H_e^v = specific enthalpy of evaporate vapor $\left(\text{kJ/kg}\right)$

H_e^l = specific enthalpy of evaporate liquid $\left(\text{kJ/kg}\right)$

M_c = mass of condensate $\left(\text{kg}\right)$

M_e = mass of evaporate $\left(\text{kg}\right)$

Q_c = heat of condensate $\left(\text{kJ}\right)$

Q_e = heat of evaporate $\left(\text{kJ}\right)$

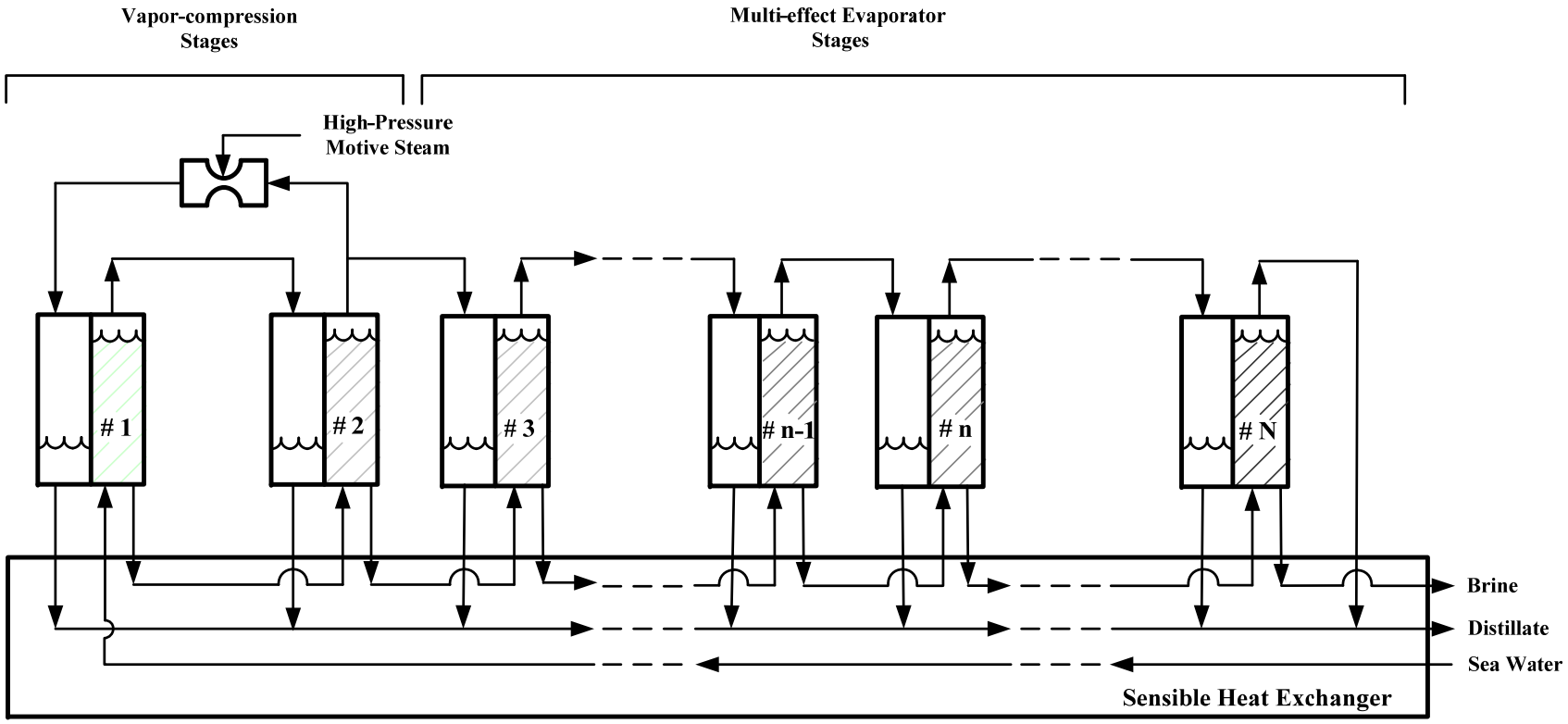

Figure 67. A jet ejector implemented in a two-stage thermocompression still with multi-effect evaporator.

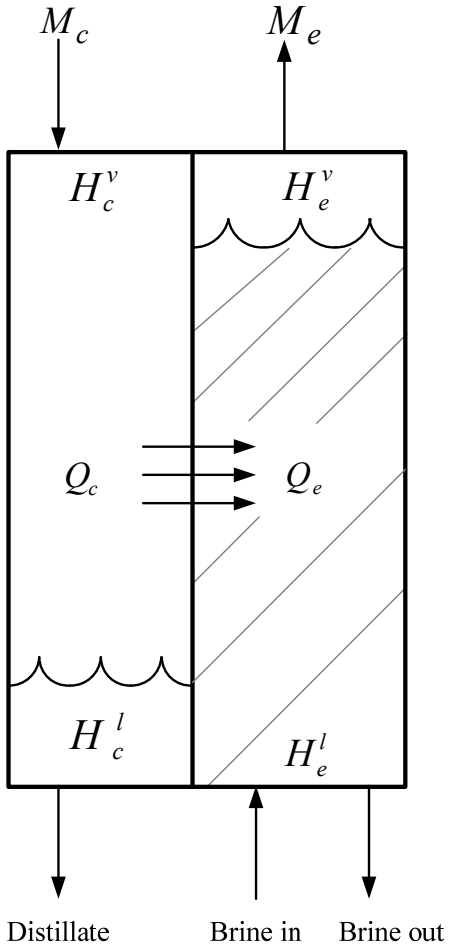

Figure 68. A single latent heat exchanger.

The enthalpy balance equation has the following assumptions:

1. no leakage or entrainment
2. negligible flow of non-condensible gases
3. no heat losses from evaporator
4. small superheat of steam
5. small subcooling of condensate

When water evaporates from the brine stream in the evaporator, the salt concentration (salinity) is changed. The salt concentration is calculated by Equation 6.

$$\text{Salt concentration}(\text{salinity; g/kg water}) = \frac{\text{mass of salt (g)}}{\text{mass of brine in (kg)} - \text{mass of steam evaporated (kg)}} \quad (81)$$

Increasing the salt concentration elevates its boiling temperature and reduces its vapor pressure (Lara Ruiz, 2005). The reduced vapor pressure is calculated by

$$\log_{10}(P/P_o) = hS + jS^2 \quad (82)$$

where

P = vapor pressure of salt water at the same temperature $(10^5$ Pa$)$

P_o = pure-water vapor pressure $(10^5$ Pa$)$

h = -2.1609×10^{-4}

j = -3.5012×10^{-7}

S = salinity (g salt/kg seawater)

The vapor pressure of pure water at a measured temperature (P_o) can be obtained from steam tables.

Next, an example calculation of the vapor-compression distillation system with an optimum jet ejector is presented. Seawater with 3.5% salt concentration at 25ºC is fed in the desalination system. The temperature at the condenser side of the first latent heat exchanger is specified at 121 ºC. The temperature difference between condenser and evaporator of each latent heat exchanger is specified at 1 ºC. The temperature at the

evaporator side of the final heat exchanger is specified no lower than 29 ºC to maintain the heat transfer from the outgoing brine stream and distillate to the incoming seawater (Figure 67). Fluid in the evaporator is saturated, because the case assumes that superheat of steam and subcooling of condensate are small. The calculation of the first few latent heat exchangers is showed below. Figure 69 displays flow diagram of the first few latent heat exchangers implementing an optimum jet ejector.

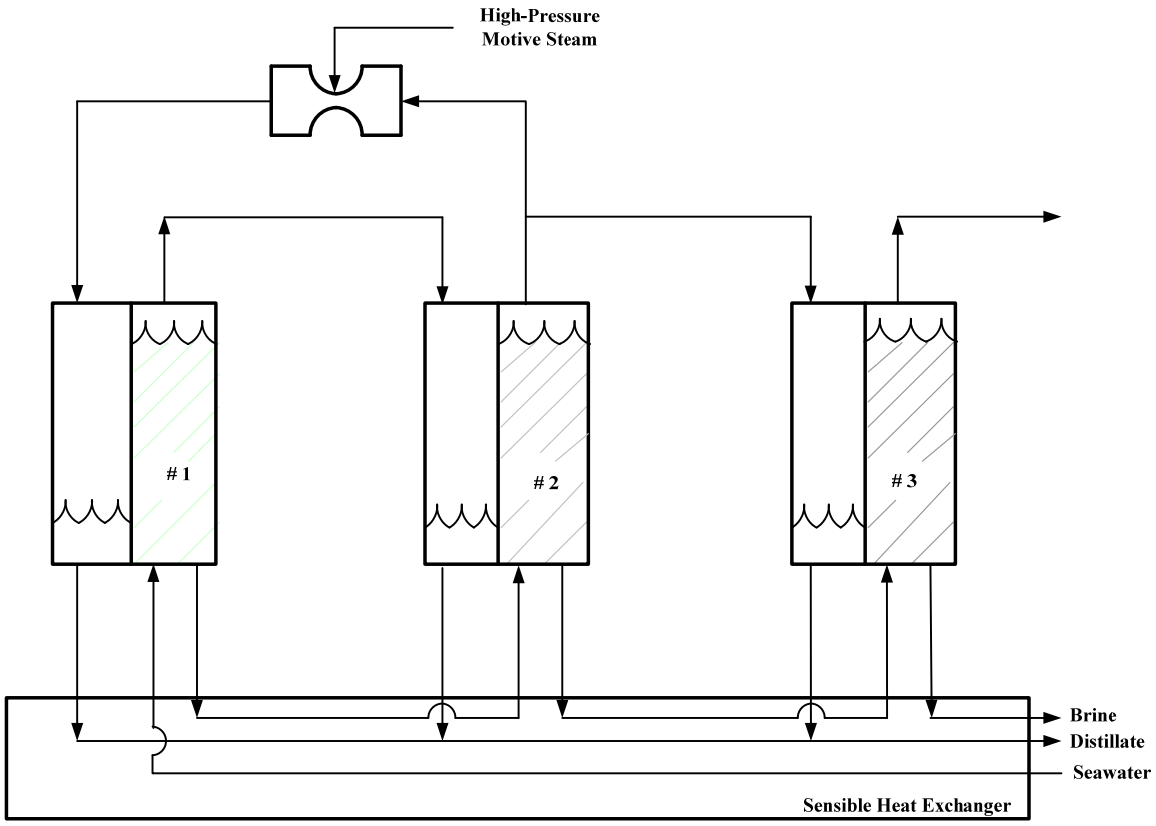

Figure 69. The flow diagram of the first few heat exchangers.

Using a basis of 100 kg of seawater feed (m_s), assume 5 kg of steam evaporates from the first latent heat exchanger to the second latent heat exchanger. From the enthalpy balance, the amount of condensate of the first latent heat exchanger and steam

from the second latent heat exchanger can be calculated. Table 38 summarizes the information using the enthalpy balance. The reduced vapor pressure is considered in the calculation (Equation 82). The vapor pressure of salt water (P) is the pressure of the condenser of the adjacent latent heat exchanger. Then, the temperature of the adjacent latent heat exchanger can be obtained by using steam tables.

Table 38. Information for the enthalpy balance.

Latent heat exchanger #	Condenser				Evaporator				
	T (ºC)	P (atm)	H_c^v (kJ/kg)	H_c^l (kJ/kg)	T (ºC)	P_o (atm)	P (atm)	H_e^v (kJ/kg)	H_e^l (kJ/kg)
1	121.0	2.023	2,709.79	506.65	120.0	1.960	1.924	2,708.10	502.45
2	119.4	1.924	2,707.13	500.02	118.4	1.864	1.828	2,705.45	495.82
3	117.8	1.828	2,704.43	493.28	116.8	1.770	1.734	2,702.75	498.08

The calculation procedure initiates with the temperature of the condenser of the first latent heat exchanger specified at 121 ºC. The vapor pressure and specific enthalpy can be obtained from steam tables. The temperature difference between the condenser and evaporator of each latent heat exchanger is specified at 1 ºC; therefore, the temperature of the latent heat exchanger side of the first evaporator is 120 ºC. Vapor pressure and specific enthalpy of the evaporator side of the first latent heat exchanger are obtained from steam tables. The vapor pressure of salt water is calculated by Equation 82 to define the condenser-side pressure of the adjacent evaporator. Seawater with 3.5% salt concentration is fed in the system; therefore, the seawater salinity at the first latent heat

exchanger is 35 g/kg substituted as *S* in Equation 82. Equation 82 is arranged to compute *P* directly (Equation 83).

$$P = P_o \times 10^{\left(hS + jS^2\right)} \tag{83}$$

$$P = 1.960 \times 10^{\left(-2.1609\times10^{-4}\cdot 35 + -3.50212\times10^{-7}\cdot 35^2\right)}$$

$$P = 1.960 \times 0.981766 = 1.924 \text{ atm}$$

The vapor pressure of the condenser side of the second latent heat exchanger is 1.924 atm. The temperature and specific enthalpy can be obtained from steam tables. Next, the amount of condensate in the first latent heat exchanger and the steam in the second latent heat exchanger (based on 5 kg steam of the first evaporator and 100 kg of seawater feed) are computed by using the enthalpy balance equation (Equation 80).

Calculate the condensate of the first latent heat exchanger:

$$M_c\left(H_c^v - H_c^l\right) = M_e\left(H_e^v - H_e^l\right) \tag{80}$$

$$M_c \times \left(2709.79 - 506.65\right) = 5 \times \left(2708.10 - 502.45\right)$$

$$M_c = \frac{5 \times \left(2708.10 - 502.45\right)}{\left(2709.79 - 506.65\right)} = 5.0057 \text{ kg}$$

Calculate steam of the second latent heat exchanger:

$$M_c\left(H_c^v - H_c^l\right) = M_e\left(H_e^v - H_e^l\right) \tag{80}$$

$$5 \times \left(2707.13 - 500.02\right) = M_e \times \left(2705.45 - 495.82\right)$$

$$M_e = \frac{5 \times \left(2707.12 - 500.02\right)}{\left(2705.45 - 495.82\right)} = 4.994 \text{ kg}$$

Because steam evaporates from the seawater, the salt concentration of the seawater is changed. The new salt concentration in the brine flowing from the first to second latent heat exchanger is calculated by

$$\text{Salt concentration}(\text{salinity; g/kg water}) = \frac{\text{mass of salt (g)}}{\text{mass of brine in (kg)} - \text{mass of steam evaporated (kg)}} \quad (81)$$

$$\text{Salt concentration}(\text{salinity; g/kg water}) = \frac{35}{100-5} = 36.84$$

The salt concentration is used to calculate the vapor pressure (P_o) of the condenser side of the second latent heat exchanger. According to Figure 70, some steam from the second latent heat exchanger is used as propelled steam fed to the jet ejector. The amount of the propelled and high-pressure motive steam is determined by using the mass balance equation (Equations 85 and 86). Figure 70 summarizes the mass flow and vapor pressure of the first two latent heat exchangers.

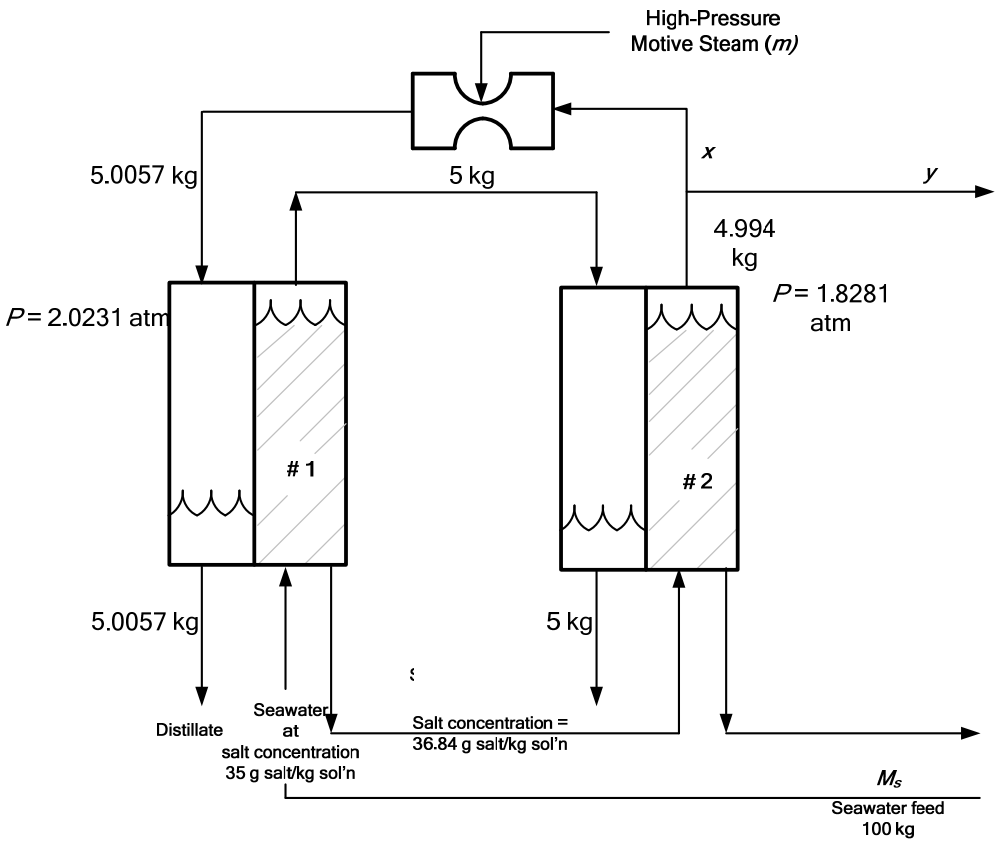

Figure 70. Mass flow and pressure of the first two effects.

From Figure 70, the jet ejector has to compress steam at P = 1.8281 atm to P = 2.0231 atm and feed it to the condenser of the first latent heat exchanger. The required compression ratio of the jet ejector is

$$\text{Compression ratio} = \frac{\text{Outlet pressure}}{\text{Inlet pressure}} = \frac{2.0231}{1.8281} = 1.1067 \qquad (84)$$

According to the optimization result in Chapter VI, an optimum jet ejector with a motive velocity of 1020 m/s (motive steam pressure = 31.42 atm) and compression ratio of 1.1067 operates at 0.142 mass flow ratio (kg motive steam/kg propelled steam). The amount of high-pressure motive steam (m), the propelled stream (x), condensate of the third evaporator (y) is computed by Equations 85 to 87.

Mass balance equations:

$$x + m = 5.0057 \text{ kg} \quad (85)$$

$$x + y = 4.994 \text{ kg} \quad (86)$$

The jet ejector CFD model shows that:

$$\frac{m}{x} = 0.142 \quad (87)$$

Solving the above equations obtains the value of x, y, and m:

$$x = 4.383 \text{ kg}$$

$$y = 0.6111 \text{ kg}$$

$$m = 0.6225 \text{ kg}$$

Then, the calculation procedure is continued by using the enthalpy balance (Equation 81), the salt concentration (Equation 82), and the vapor pressure (P) for seawater (Equation 84) as described above to determine the number of latent heat exchangers in the desalination system. To transfer heat to the incoming seawater (assumed to be 25ºC), the temperature of the liquid leaving the final latent heat exchanger has to be greater than 29ºC.

Results and Discussion

Table 39 summarizes the results: mass flow and temperature in condenser and evaporator of each latent heat exchanger, salt concentration, water component in seawater, and heat from distillate and brine stream.

Table 39. The results of the vapor-compression desalination system implemented an optimum jet ejector.

Latent heat exchanger #	Condenser			Evaporator			Water in brine outlet stream (kg)	Salinity (g salt/kg water)
	Temperature (ºC)	Mass flow of condensate (kg)	$Q_{distillate}$ (kJ)	Temperature (ºC)	Mass flow of evaporated steam (kg)	Q_{brine} (kJ)		
1	121.00	5.006	1,934.21	120.00	5.000	610.77	100	35.00
2	119.42	5.000	1,898.85	118.42	4.994	587.85	95.00	36.84
3	117.82	0.611	227.97	116.82	0.610	592.45	90.01	38.89
4	116.18	0.610	223.52	115.18	0.610	587.89	89.40	39.15
5	114.55	0.610	219.08	114.55	0.609	581.47	88.79	39.42
6	112.92	0.609	214.66	111.92	0.608	576.95	88.18	39.69
7	111.29	0.608	210.25	110.29	0.608	571.87	87.57	39.97
8	109.66	0.608	205.85	108.66	0.607	567.39	86.96	40.25
9	108.03	0.607	201.47	107.03	0.606	562.91	86.35	40.53
10	106.40	0.606	197.10	105.40	0.606	558.45	85.75	40.82
11	104.78	0.606	192.75	103.78	.605	552.36	85.14	41.11

Table 39. Continued.

Latent heat exchanger #	Condenser			Evaporator			Water in brine outlet stream (kg)	Salinity (g salt/kg water)
	Temperature (ºC)	Mass flow of condensate (kg)	$Q_{distillate}$ (kJ)	Temperature (ºC)	Mass flow of evaporated steam (kg)	Q_{brine} (kJ)		
12	103.16	0.605	188.41	102.16	0.604	547.95	84.54	41.40
13	101.53	0.604	184.08	100.53	0.604	543.54	83.93	41.70
14	99.91	0.604	179.77	98.91	0.603	539.15	83.33	42.00
15	98.29	0.603	175.47	97.29	0.602	534.78	82.73	42.31
16	96.68	0.602	171.18	95.68	0.602	530.42	82.12	42.62
17	95.06	0.602	166.91	94.06	0.601	524.63	81.52	42.93
18	93.44	0.601	162.65	92.44	0.600	520.31	80.92	43.25
19	91.83	0.600	158.40	90.83	0.600	516.00	80.32	43.58
20	90.22	0.600	154.16	89.22	0.599	511.71	79.72	43.90
21	88.61	0.599	149.94	87.61	0.598	507.43	79.12	44.24
22	87.00	0.598	145.73	86.00	.598	503.16	78.52	44.57

Table 39. Continued.

Latent heat exchanger #	Condenser			Evaporator			Water in brine outlet stream (kg)	Salinity (g salt/kg water)
	Temperature (ºC)	Mass flow of condensate (kg)	$Q_{distillate}$ (kJ)	Temperature (ºC)	Mass flow of evaporated steam (kg)	Q_{brine} (kJ)		
23	85.39	0.598	141.53	84.39	0.597	497.66	77.93	44.91
24	83.78	0.597	137.35	82.78	0.596	587.89	77.33	45.26
25	82.17	0.596	133.17	81.17	0.596	483.72	76.73	45.61
26	80.57	0.596	129.01	79.57	0.595	479.56	76.14	45.97
27	78.97	0.595	124.87	77.97	0.594	475.42	75.54	46.33
28	77.36	0.594	120.73	76.36	0.594	471.29	74.95	46.70
29	75.76	0.594	116.61	74.76	0.593	467.18	74.35	47.07
30	74.16	0.593	112.50	73.16	0.592	432.02	73.76	47.45
31	72.56	0.592	108.40	71.56	0.592	457.94	73.17	47.83
32	70.97	0.592	104.31	69.97	0.591	453.88	72.58	48.22
33	69.37	0.591	100.23	68.37	0.591	449.82	71.99	48.62

Table 39. Continued.

Latent heat exchanger #	Condenser			Evaporator			Water in brine outlet stream (kg)	Salinity (g salt/kg water)
	Temperature (ºC)	Mass flow of condensate (kg)	$Q_{distillate}$ (kJ)	Temperature (ºC)	Mass flow of evaporated steam (kg)	Q_{brine} (kJ)		
34	67.78	0.591	96.17	66.78	0.590	445.78	71.40	49.02
35	66.18	0.590	92.12	65.18	0.589	441.75	70.81	49.43
36	64.59	0.589	88.08	63.59	0.589	436.74	70.22	49.85
37	63.00	0.589	84.05	62.00	0.588	432.75	69.63	50.27
38	61.41	0.588	80.03	60.41	0.587	428.90	69.04	50.70
39	59.82	0.587	76.02	58.82	0.587	424.97	68.45	51.13
40	58.23	0.587	72.03	57.23	0.586	421.05	67.87	51.57
41	56.64	0.586	68.04	55.64	0.585	417.15	67.28	52.02
42	55.05	0.585	64.06	54.05	0.585	413.26	66.69	52.48
43	53.47	0.585	60.10	52.47	0.584	408.65	66.11	52.94
44	51.88	0.584	56.15	50.88	0.584	404.79	65.53	53.41

Table 39. Continued.

Latent heat exchanger #	Condenser			Evaporator			Water in brine outlet stream (kg)	Salinity (g salt/kg water)
	Temperature (ºC)	Mass flow of condensate (kg)	$Q_{distillate}$ (kJ)	Temperature (ºC)	Mass flow of evaporated steam (kg)	Q_{brine} (kJ)		
45	50.30	0.584	52.20	49.30	0.583	400.94	64.94	53.89
46	48.71	0.583	48.27	47.71	0.582	397.10	64.36	54.38
47	47.13	0.582	44.35	46.13	0.582	393.27	63.78	54.88
48	45.55	0.582	40.44	44.55	0.581	384.90	63.19	55.38
49	43.97	0.581	36.54	42.97	0.581	380.46	62.61	55.90
50	42.39	0.581	32.64	41.39	0.580	376.72	62.03	56.42
51	40.81	0.580	28.76	39.81	0.579	372.99	61.45	56.95
52	39.23	0.579	24.89	38.23	0.579	369.28	60.87	57.50
53	37.65	0.579	21.03	36.65	0.578	365.57	60.29	58.05
54	36.07	0.578	17.18	35.07	0.578	361.88	59.72	58.61
55	34.50	0.578	13.33	33.50	0.577	357.55	59.14	59.18

Table 39. Continued.

Latent heat exchanger #	Condenser			Evaporator			Water in brine outlet stream (kg)	Salinity (g salt/kg water)
	Temperature (ºC)	Mass flow of condensate (kg)	$Q_{distillate}$ (kJ)	Temperature (ºC)	Mass flow of evaporated steam (kg)	Q_{brine} (kJ)		
56	32.92	0.577	9.50	31.92	0.576	353.89	58.56	59.77
57	31.35	0.576	5.68	30.35	0.576	299.40	57.99	60.36

According to Figure 67, heat from the outgoing distillate and brine stream is used to increase the temperature of the incoming seawater from 25 ºC to 120 ºC to feed to the first latent heat exchanger; therefore, the energy balance equation of the heat exchanger will be

$$Q_{\text{seawater}} = Q_{\text{distillate}} + Q_{\text{brine}} \tag{88}$$

$$Q_{\text{seawater}} = M_s \times C_{ps} \times \Delta T \tag{89}$$

$$Q_{\text{distillate}} = \sum_{n=1}^{N} M_d^n \times C_p \times \left(T_c^n - 29\right) + M_e^N \left(H_e^v - H_e^l\right) \tag{90}$$

$$Q_{\text{brine}} = \sum_{n=1}^{N-1} M_b^n \times C_{ps} \times \left(T_e^n - T_e^{n+1}\right) + M_b^N \times C_{ps} \times \left(T_e^N - 29\right) \tag{91}$$

where

Q_{seawater} = the amount of heat for seawater stream (kJ)

$Q_{\text{distillate}}$ = the amount of heat from distillate stream (kJ)

Q_{brine} = the amount of heat from brine stream (kJ)

C_p = specific heat capacity of pure water $\left(\text{kJ}/\left(\text{kg}\cdot^\circ\text{C}\right)\right)$

$= 4.2\ \text{kJ}/\left(\text{kg}\cdot^\circ\text{C}\right)$

C_{ps} = specific heat capacity of salt water $\left(\text{kJ}/\left(\text{kg}\cdot^\circ\text{C}\right)\right)$

M_b^n = mass flow of brine stream of *n* latent heat exchanger (kg)

M_d^n = mass flow of distillate stream of *n* latent heat exchanger (kg)

M_b^N = mass flow of brine stream of the final latent heat exchanger (kg)

M_e^N = mass flow of steam evaporated from the final latent heat exchanger (kg)

M_s = mass flow of seawater stream (kg) = 100 kg

T_c^n = temperature of condenser of *n* latent heat exchanger $\left(^\circ\text{C}\right)$

T_e^n = temperature of evaporator of *n* latent heat exchanger $\left(^\circ\text{C}\right)$

The specific heat capacity of salt water (C_{ps}) varies with temperature and salt concentration. The C_{ps} value is summarized in Table D2. Because C_{ps} is a function of temperature and salt concentration, for accuracy purpose, the calculation of Q_{seawater} is specified at each temperature interval, as shown in Table 40. Heat from the distillate of each latent heat exchanger ($Q_{\text{distillate}}$) and heat of brine stream for each latent heat exchanger (Q_{brine}) are summarized in Table 39. Following Equations 91 and 92, the heat from the distillate ($Q_{\text{distillate}}$) is 11,502.50 kJ and the heat from the brine stream (Q_{brine}) is 26,805.57 kJ, respectively. Q_{seawater}, which is calculated by summing the heat of at each temperature in Table 39, equals to 38,236.5 kJ. The energy balance equation of the heat exchanger is

$$Q_{\text{seawater}} = \text{Q}_{\text{distillate}} + \text{Q}_{\text{brine}} \tag{88}$$

$$38{,}236.5 \approx 11{,}502.50 + 26{,}805.57 = 38{,}308.07$$

The energy balance equation shows that heat from the distillate and brine streams is sufficient to increase the temperature of seawater to 120 ºC before being fed to the first evaporator.

The seawater component, specific heat capacity of seawater, and the detailed data for the case (pressure and specific enthalpy of each effect) are summarized in Appendix D.

Table 40. Q_{seawater} of each temperature interval.

Temperature interval $\left(^{\circ}\text{C}\right)$	C_{ps} $\left(\text{kJ}/\left(\text{kg}\cdot^{\circ}\text{C}\right)\right)$	Q_{seawater} $\left(\text{kJ}\right)$
120 - 115	4.073	2,036.5
115 - 105	4.060	4,060
105 – 95	4.048	4,048
95 – 85	4.036	4,036
85 – 75	4.027	4,027
75 – 65	4.018	4,018
65 – 55	4.011	4,011
55 – 45	4.004	4,004
45 – 35	4.00	4,000
35 - 25	3.996	3,996

From Table 40, the total amount of distillate is:

$$M_d = \sum_{n=1}^{N} M_d^n + M_e^N - m = 42.637 + 0.576 - 0.6225 \qquad (92)$$

$$= 42.59 \text{ kg}$$

where

M_d = mass flow of total distillate $\left(\text{kg}\right)$

The vapor-compression desalination system implemented with an optimum jet ejector with 0.6225 kg high-pressure motive stream can produce 42.59 kg of water, or 1 kg of high-pressure motive steam can produce 68.42 kg of water. At the final step, the amount of steam evaporated from the first latent heat exchanger (Figure 31; 5 kg initial) was optimized. The calculation procedure described above was followed, but the amount of steam evaporated from the first evaporator was adjusted. The results are presented at Table 41.

Table 41. The results of different amounts of steam from the first latent heat exchanger.

	Amount of steam evaporated from the first latent heat exchanger (kg)*				
	4.5	4.8 (Optimum)	5.0	5.5	6.0
$\frac{M_d}{m}$	60.84	69.39	68.42	68.39	67.46
$\frac{M_d}{M_s}$	0.3407	0.4129	0.4259	0.4689	0.5050
$\frac{\text{Conc.}_b}{\text{Conc.}_s}$	1.5168	1.7034	1.7420	1.8830	1.990
Number of stages	58	58	57	57	56

* Basis: 100 kg seawater feed.

Table 41 shows that there is an optimal amount of steam evaporated from the first latent heat exchanger (4.8 kg steam evaporated/100 kg seawater feed). Above this optimum, the salt concentration increases too much, which lowers the vapor pressure.

This has two negative effects: 1) increases the pressure ratio in the vapor compression stages, which increases motive steam requirement, and 2) reduces the number of multi-effect evaporator stages operating beneath the vapor-compression stages. Below this optimum, too little distillate is recovered relative to the fixed energy costs associated with heating the seawater feed up to the evaporator temperature.

Conclusion

At the optimum condition, the brine concentration (Conc.$_b$) is 1.7034 times that of the seawater concentration (Conc.$_s$). The amount of distillate recovered (M_d) per unit of seawater feed (M_s) is 0.4129. The total number of latent heat exchanger stages is 58.

CHAPTER XI

SUMMARY AND CONCLUSIONS

Jet ejectors are widely used in the chemical industrial process because they are highly reliable with low capital and maintenance costs. However, jet ejectors have a low efficiency compared with mechanical compressors. A high-efficiency jet ejector, which was designed and presented in the High Efficiency Jet Ejector invention disclosure of Holtzapple (2001) is an engaging solution to resolve the low efficiency problem. This research was conducted to investigate the optimal geometry and operating conditions for a high-efficiency jet ejector.

CFD software was applied in this research. Many experiments were done to verify the reliability of CFD modeling. The results confirm that CFD modeling can provide high-quality solutions that agree well with experiment data. Therefore, the research results from CFD modeling have high accuracy and reliability.

The dimensionless group analysis indicated that the dimensionless principle could apply together with the research result to make the result valid for any fluid, geometric scale, and operating pressure. For a given momentum ratio and the motive-stream Mach number, the static pressure of the propelled and motive streams is calculated from C_p and C_{pm} in the research results, respectively. The inlet and outlet static pressures calculated from C_p allow the jet ejector efficiency to be calculated, regardless of the fluid type, using newly defined efficiency equation when the density, mass flow rate, pressure, velocity, and temperature of the propelled, motive, and outlet streams are known.

The optimal geometry of a high-efficiency jet ejector was discovered. The research results cover wide range of application. The motive velocity condition covering in the study is between 170 and 1105 m/s, whereas the conventional motive velocity operating in the industries is between 500 to 800 m/s. This confirms that the results cover the industrial application. On the mass flow ratio, the lower bound is 0.02 and the upper bound is 100.0. The results of the optimization study confidently cover all kinds of applications. Furthermore, the dimensionless analysis makes the optimization results valid on any fluid type, geometric scale, and operating condition. The optimum nozzle position is – 0.05 to 0.05 times the inlet diameter in most cases, which is compatible with the ESDU (1986) recommendation. As a consequence, the result was easily obscured with numerical error from CFD modeling. The jet-ejector efficiency after the optimization study is above 90% provided the motive velocity is below Mach 1.2 with all nozzle diameters. This is remarkable improvement from a conventional jet ejector design.

Future Research

This dissertation has been covered all of the significant matter of the jet ejector. There are very few things requiring an investigation. In the author's opinion, it would be best if the experiment in comparing between the high-efficiency jet ejector and a conventional jet ejector could be further explored. Due to the cost of the jet ejectors, it limited the exploration of this experiment stage. However, the results were verified that the simulation results provide highly accuracy and reliability comparing with the results from an actual jet ejector.

LITERATURE CITED

Berkeley, F. D., "Ejectors Give Any Suction Pressure," *Chem Eng. J.*, **64**, 4(1957).

Croft, D. R., and D. G. Lilley, "Jet Pump Design and Performance Analysis," AIAA 14th Aerospace Science Meeting, AIAA Paper 76183, New York (1976).

Croll, W. S., "Keeping Steam Ejectors," *Chem. Eng. J.*, **105**, 4(1998).

Da-Wen, S., and I. W. Eames, "Recent Developments in the Design Theories and Applications of Ejectors," *J.Inst. Energy*, **68** (1995).

Deen, W. M., *Analysis of Transport Phenomena*, Oxford University Press, New York (1998).

DeFrate, L. A., and A. E. Hoerl, "Optimum Design of Ejectors Using Digital Computers," *Chem. Eng. Prog. Symp. Series*, **21** (1959).

Djebedjian, B., S. Abdalla, and M. A. Rayan, "Parametric Investigation of Boost Jet Pump Performance," *Proceedings of FEDSM, ASME Fluids Engineering Summer Conference*, Boston (2000).

El-Dessouky, H., H. Ettouney, I. Alatiqi, and G. Al-Nuwaibit, "Evaluation of Steam Jet Ejectors," *Chem. Eng. Process.*, **41**, 6 (2002).

Engdahl, R. B., and W. C. Holton, "A General Method of Designing Gas and Gas-Liquid Injectors Using Laws of Turbulent Jet Mixing," *J. Appl. Mech. Trans. ASME.*, **65** (1943).

Engineering Sciences Data Unit (ESDU), *Ejector and Jet Pump; Design for Steam Driven Flow,* Item number 86030, ESDU International Ltd., London (1986).

Fletcher, C. A. J., *Computational Techniques for Fluid Dynamics*, Volumes I & II, 2nd ed., Springer-Verlag, Orlando, FL (1991).

Fluent Inc., Fluent User Guides, www.fluent.com, (2001).

Habashi, W. G., *Solution Techniques for Large-Scale CFD Problems*, John Wiley & Sons, New York (1995).

Happle J., and H. Brenner, *Low Reynolds Number Hydrodynamics(Mechanics of Fluids and Transport Processes),* McGraw Hill, New York (1965).

Hedges, K. R., and P. G. Hill, "Compressible Flow Ejectors; Flow Field Measurements and Analysis," *ASME Trans. Fluid Eng.,* **96**, 3 (1974).

Hoggarth, M. L., "The Design and Performance of High-Pressure Injectors as Gas Jet Boosters," *Process Inst. Mech. Eng*., **185** (1970).

Holton, W. C., "Effect of Molecular Weight and Entrained Fluid on the Performance of Steam-Jet Ejectors," *Trans. Am. Soc. Mech. Eng.*, **73** (1951).

Holton, W. C., and E. J. Schulz, "Effect of Temperature of Entrained Fluid on the Performance of Steam-Jet Ejectors," *Trans. Am. Soc. Mec. Eng.*, **73** (1951).

Holtzapple, M. T., "High-Efficiency Jet Ejector," (Invention Disclosure) Department of Chemical Engineering, Texas A&M University, College Station, Texas (2001).

Keenan, J. H., and E. P. Neumann, "A Simple Air Ejector," *ASME J. Appl. Mech*., **9** (1942).

Kim, H. D., T. Setoguchi, S. Yu, and S. Raghunathan, "Navier-Stokes Computations of the Supersonic Ejector-Diffuser System with a Second Throat," *J. Therm. Sci*., **8**, 2 (1999).

Knight, G. B., "Five Ways to Automatically Control Pressure for Ejector Vacuum Systems," *Chem. Eng. J*., **66**, 6 (1959).

Kroll, A. E., "The Design of Jet Pumps," *Chem. Eng. Prog*., **1**, 2 (1947).

Lines, J. R. and Smith, R. T., "Ejector System Trouble Shooting," *Int. J. of Hydro*. *Eng.,* (1997).

Mains, W. D., and R. E. Richenberg, "Steam Jet Ejectors in Pilot and Production Plants," *Chem. Eng. Process.,* **63**, 3 (1967).

Mark, M. and Foster, A. R., *Thermodynamics Principles and Applications*, Allyn and Bacon, Inc., Boston, MA (1979).

Porteous, A, *Desalination Technology – Developments and Practice*, Applied Science Publishers, New York, NY (1983).

Reinke, B., M. Neal, and S. K. Gupta, "Flow Inside A Jet-Ejector Pump for Vacuum Applications," *J. Ind. Inst. Chem. Engrs*., **44**, 3 (2002).

Riffat, S. B., and P. Everitt, "Experimental and CFD Modeling of an Ejector System for Vehicle Air Conditioning*," J. Inst. Ener*gy, **72** (1999).

Riffat, S. B., G. Gam, and S. Smith, "Computational Fluid Dynamics Applied to Ejector Pumps," *Appl. Therm. Eng. J*., **16**, 4 (1996).

Riffat, S. B., and S. A. Omer, "CFD Modelling and Experimental Investigation of an Ejector Refrigeration System Using Methanol as the Working Fluid," *Int. J. Energy Res.*, **25**, 2 (2001).

Schmitt, H., *Diversity of Jet Pump and Ejector Techniques*, The Second Symposium on Jet Pumps & Ejectors and Gas Lift Techniques, BHRA Fluid Engineering, Bedford, UK (1975).

Smith, J. M., and H. C. Van Ness, *Introduction to Chemical Engineering Thermodynamics*, 3rd ed., McGraw-Hill, New York (1975).

Steam Jet Syphons; Design, Construction, and Operation, AMETEK Inc., Cornwells Heights, PA (1979).

Vishwannathappa, D. M., "High-Efficiency Jet Ejector," Department of Chemical Engineering, Texas A&M University, College Station, Texas (2001).

APPENDIX A

MATHEMATICAL DERIVATION OF AN EFFICIENCY EQUATION

An efficiency equation is needed to determine the performance of the jet ejector, and to determine the optimal geometry. Unfortunately, the conventional efficiency equation cannot be applied directly in our research for two reasons, which are explained below; therefore, a new efficiency equation is derived. Before applying this new equation in the optimization study, the accuracy of the equation must be verified first.

The traditional efficiency equation is presented in Equation A1.

$$\eta = \frac{m_p\left(H_o - H_p\right)}{m_m\left(H_m - H_o\right)} \tag{A1}$$

where,

m_p = mass flow rate of the propelled stream $\left(\text{kg/s}\right)$

m_m = mass flow rate of the motive stream $\left(\text{kg/s}\right)$

H_m = specific enthalpy of the motive stream $\left(\text{J/kg}\right)$

H_o = specific enthalpy of the outlet stream $\left(\text{J/kg}\right)$

H_p = specific enthalpy of the propelled stream $\left(\text{J/kg}\right)$

The traditional efficiency equation cannot be applied for the following reasons:

1. The traditional efficiency equation accounts for only the effect of stream enthalpy. The effect of kinetic energy is not included in the equation, which is incorrect.

2. The traditional efficiency equation is inconvenient to interface with CFD, because CFD does not allow us to specify fluid enthalpy directly.

The derivation and verification of the newly defined efficiency equation are presented in the following section.

In the jet ejector, there are three major energy components concerned.

1. Kinetic energy
2. Pressure energy
3. Flow work

Kinetic Energy

Kinetic energy was introduced by Lord Kelvin in 1856. The importance of this quantity was earlier recognized by Thomas Young, an English physicist, who in 1807 called it simply energy, the first recorded instance of the use of this word (Smith et al., 1975). Kinetic energy has the following general formation:

$$E_k = \frac{1}{2} m\left(u_2^2 - u_1^2\right) = \Delta \frac{mu^2}{2} \qquad \text{(A2)}$$

where,

E_k = kinetic energy (J)

m = mass of the object (kg)

u_2 = final velocity $(\mathrm{m/s})$

u_1 = initial velocity $(\mathrm{m/s})$

From Equation A2, the energy need to accelerate an object from initial velocity u_1 to final velocity u_2 is the kinetic energy.

Pressure Energy

The pressure energy is used to compress the fluid from initial pressure P_1 to final pressure P_2. For compressible fluids, the pressure energy equals to

$$E_P = \dot{m}\left(P\hat{V}\right)\frac{\gamma}{\gamma-1}\left(\left(\frac{P_2}{P_1}\right)^{\frac{\gamma-1}{\gamma}}-1\right) \tag{A3}$$

where,

E_P = pressure energy $\left(\text{J}\right)$

$\dot{m}$ = fluid mass flow rate $\left(\text{kg/s}\right)$

P = pressure $\left(\text{Pa}\right)$

$\hat{V}$ = specific volume $\left(\text{m}^3/\text{kg}\right)$

γ = ratio of heat capacities = C_P / C_V

P_1 = initial pressure $\left(\text{Pa}\right)$

P_2 = final pressure $\left(\text{Pa}\right)$

Assume the ideal gas law;

$$PV = nRT = \frac{m}{MW}RT \tag{A4}$$

where,

V = volume $\left(\text{m}^3\right)$

n = number of moles

R = universal gas constant = 8.314 $\frac{\text{J}}{\text{gmol}\cdot\text{K}}$

T = temperature $\left(\text{K}\right)$

MW = molecular weight (g/gmol)

Rearrange Equation A3;

$$\frac{PV}{m} = P\hat{V} = \frac{RT}{MW} \tag{A5}$$

Substituting Equation A5 into Equation A3 gives rise to Equation A6.

$$E_P = \dot{m}\left(\frac{RT}{MW}\right)\frac{\gamma}{\gamma - 1}\left(\left(\frac{P_2}{P_1}\right)^{\frac{\gamma-1}{\gamma}} - 1\right) \tag{A6}$$

Flow Work

Flow energy relates to the mass flowing into or out of the system (Mark et al., 1979). If the mass is flowing into the system, the surroundings provide the energy to the mass; conversely, the system must do work on the surroundings if the mass is flowing out of the system. Figure A1 displays the mechanism of flow work.

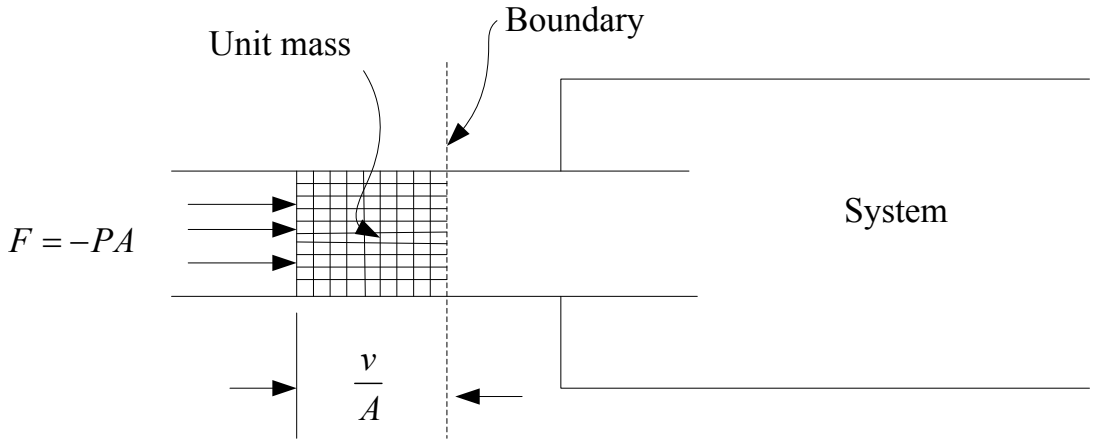

Figure A1. As a unit mass crosses the boundary upon entering the system, the surroundings do an amount of work $-PV$ on the system. This energy necessary to cross the boundary is known as flow energy or flow work (Mark and Foster, 1979).

As shown in Figure A1, if the unit mass is to enter the system, a force is necessary to overcome the pressure at the entry position (Mark et al., 1979). The amount of force to push the unit mass to enter the system equals a factor between pressure and the cross-sectional area which the unit mass moves through. If we multiply the cross-sectional area with the distance which the unit mass has gone through, it will equal the volume of the unit mass; which is called the specific volume of the substance.

$$\hat{V} = A \times \text{Distance} \tag{A7}$$

Consequently,

$$\text{Distance} = \frac{\hat{V}}{A} \tag{A8}$$

To derive the flow work, the work definition is applied first.

$$\text{Flow work} = \text{Force} \times \text{Distance} \tag{A9}$$

which is;

$$\text{Flow work} = PA \times \frac{\hat{V}}{A} = P\hat{V} \tag{A10}$$

Note that P and $\hat{V}$ are both properties that relate to the fluid entering or leaving the system. As such, the flow work will be associated with the mass entering or leaving the system (Mark et al., 1979).

The Efficiency Equation Derivation

As stated above, there are three major energy components associated in the system: kinetic energy, pressure energy, and flow work. Figure A2 displays the relationship of the energy in the system.

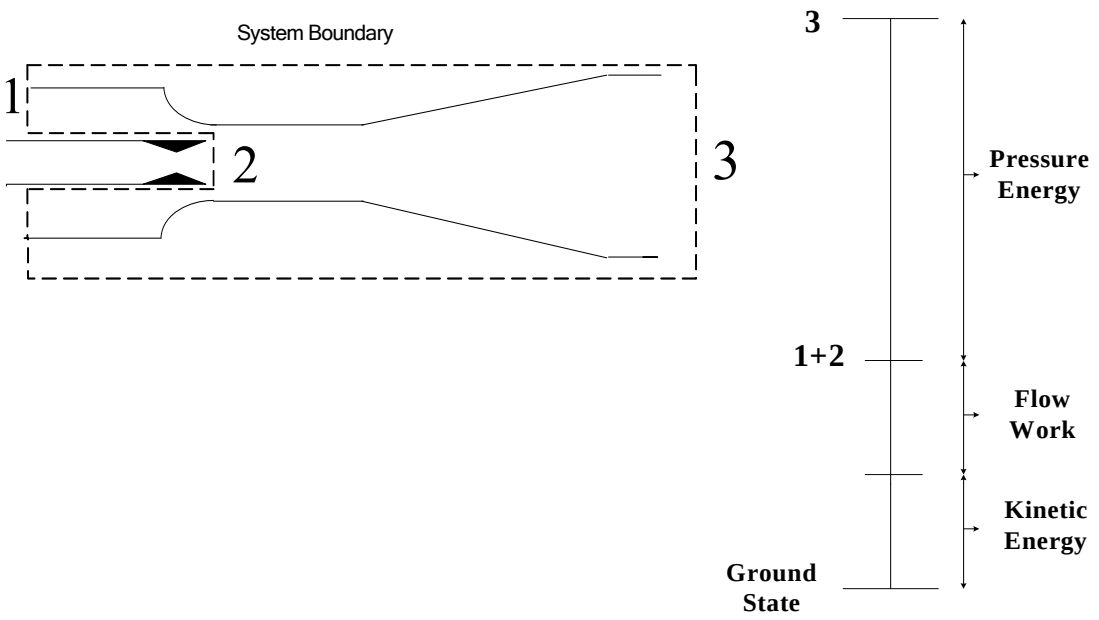

Figure A2. Energy diagram in jet ejector.

The efficiency equation is formulated as follows:

$$\eta = \frac{\text{Total Energy Output}}{\text{Total Energy Input}} \tag{A11}$$

From Figure A2,

$$\text{Total Energy Output} = [\text{Kinetic Energy} + \text{Flow Work} + \text{Pressure Work}]_{\text{output}} \tag{A12}$$

$$\text{Total Energy Input} = [\text{Kinetic Energy} + \text{Flow Work}]_{\text{propelled}} + [\text{Kinetic Energy} + \text{Flow Work}]_{\text{motive}} \tag{A13}$$

which is,

$$\text{Total Energy Output} = \frac{1}{2}\dot{m}_1 v_1^2 + \frac{1}{2}\dot{m}_m v_m^2 + \dot{m}_1 \frac{RT_1}{MW} + \dot{m}_m \frac{RT_m}{MW} + \tag{A14}$$

$$\dot{m}_1\left(\frac{RT_1}{MW}\right)\frac{\gamma}{\gamma-1}\left[\left(\frac{P_2}{P_1}\right)^{\frac{\gamma-1}{\gamma}} - 1\right] + \dot{m}_m\left(\frac{RT_m}{MW}\right)\frac{\gamma}{\gamma-1}\left[\left(\frac{P_2}{P_m}\right)^{\frac{\gamma-1}{\gamma}} - 1\right]$$

$$\text{Total Energy Input} = \frac{1}{2}\dot{m}_1 v_1^2 + \frac{1}{2}\dot{m}_m v_m^2 + \dot{m}_1 \frac{RT_1}{MW} + \dot{m}_m \frac{RT_m}{MW} \tag{A15}$$

where,

P_2 = outlet pressure (Pa)

P_1 = inlet pressure of propelled stream (Pa)

P_m = inlet pressure of motive stream (Pa)

v_2 = outlet velocity (m/s)

v_1 = inlet velocity of propelled stream (m/s)

v_m = inlet velocity of motive stream (m/s)

m_1 = inlet mass flow rate of propelled stream (kg/s)

m_m = inlet mass flow rate of motive stream (kg/s)

T_1 = temperature of propelled stream (K)

T_m = temperature of motive stream (K)

Combining Equations A14 and A15, the newly defined efficiency equation is:

$$\eta = \frac{\frac{1}{2}\left(\dot{m}_m + \dot{m}_1\right)v_2^2 + \dot{m}_1 \frac{RT_1}{MW} + \dot{m}_m \frac{RT_m}{MW} + \dot{m}_1\left(\frac{\gamma}{\gamma-1}\right)\frac{RT_1}{MW}\left[\left(\frac{P_2}{P_1}\right)^{\frac{\gamma-1}{\gamma}} - 1\right] + \dot{m}_m\left(\frac{\gamma}{\gamma-1}\right)\frac{RT_m}{MW}\left[\left(\frac{P_2}{P_m}\right)^{\frac{\gamma-1}{\gamma}} - 1\right]}{\frac{1}{2}\dot{m}_1 v_1^2 + \frac{1}{2}\dot{m}_m v_m^2 + \dot{m}_1 \frac{RT_1}{MW} + \dot{m}_m \frac{RT_m}{MW}} \tag{A16}$$

Next, the validation of the efficiency equation is described. The model to verify the equation is presented in Figure A3. It is assumed that every device operates at 100%

efficiency. Given this assumption, if the efficiency equation is defined properly, the outlet conditions should equal the inlet conditions.

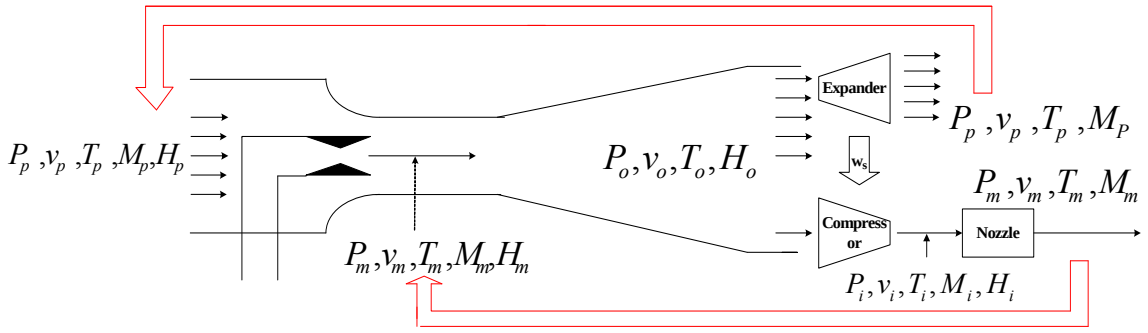

Figure A3. Ejector including the turbine-compressor cycle.

Restated, by going through reversible processes (jet ejector, expander, compressor and nozzle) the outlet conditions will be identical to the initial conditions, provided the newly defined efficiency equation is correct. The verification procedure is presented as follows:

1. The propelled and motive stream conditions (e.g., mass flow rate, static pressure, density, velocity, temperature) are defined at the inlet.
2. The static pressure of outlet stream is calculated from the newly defined efficiency equation by assuming that jet ejector operates at 100% efficiency (i.e., the efficiency term on the left hand side of Equation A17 equals 1.0).
3. The outlet stream is separated to two parts. The mass of the first part equals the propelled stream, whereas the second part equals the motive stream.

4. The first part is injected to an isentropic expander. To get back to the initial specified propelled stream, shaft energy is extracted from the outlet stream by the expander.
5. The second part is injected to an isentropic compressor. Energy from the isentropic expander is injected into the isentropic compressor to compress the stream to an intermediate stage before feeding through the isentropic nozzle. The intermediate condition is obtained from this step.
6. The intermediate stream goes through the isentropic nozzle. The stream exiting the nozzle must equal the initial specified motive-stream velocity.

Next, the calculation procedure is explained with a step-by-step instruction.

Step 1: An arbitrary jet ejector is chosen for an analysis. The fluid properties of the propelled and motive streams are specified and displayed in Table A1. Each equipment performs isentropically (frictionless, adiabatic, and 100% efficiency). The static pressure of the outlet stream is calculated from the newly defined efficiency equation.

Table A1. The specified valued of fluid properties.

	Fluid Properties		
	Propelled	Motive	Outlet
Static Pressure (Pa)	101,325	101,325	**Be evaluated**
Temperature (K)	373	373	373
Mass Flow Rate (kg/s)	0.67	0.5	1.17
Velocity (m/s)	10	300	10

Step 2: Assuming that the jet ejector operates at 100% efficiency, the value of the efficiency term of the left-hand side equals 1.0. The denominator of Equation A16 moves to the left hand side (Equation A17).

$$\begin{aligned}&\frac{1}{2}\dot{m}_1 v_1^2+\frac{1}{2}\dot{m}v_m^2+\dot{m}_1\frac{RT_1}{MW}+\dot{m}_m\frac{RT_m}{MW}\\&=\frac{1}{2}\left(\dot{m}_1+\dot{m}_m\right)v_2^2+\dot{m}_1\frac{RT_1}{MW}+\dot{m}_m\frac{RT_m}{MW}+\dot{m}_1\left(\frac{\gamma}{\gamma-1}\right)\frac{RT_1}{MW}\left[\left(\frac{P_2}{P_1}\right)^{\frac{\gamma-1}{\gamma}}-1\right]\\&+\dot{m}_n\left(\frac{\gamma}{\gamma-1}\right)\frac{RT_m}{MW}\left[\left(\frac{P_2}{P_m}\right)^{\frac{\gamma-1}{\gamma}}-1\right]\end{aligned} \tag{A17}$$

To extract the outlet-stream pressure, Equation A17 gives Equation A18.

$$P_2=\left\{\left[\frac{1}{2}\dot{m}_m\left(v_m^2-v_2^2\right)\left(\frac{\gamma-1}{\gamma}\right)\frac{MW}{R}+T_m\dot{m}_m+T_1\dot{m}_1\right]\times\left[\frac{\left(P_1+P_m\right)^{\frac{\gamma-1}{\gamma}}}{\left(T_m\dot{m}_m P_1^{\frac{\gamma-1}{\gamma}}+T_1\dot{m}_1 P_m^{\frac{\gamma-1}{\gamma}}\right)}\right]\right\}^{\frac{\gamma}{\gamma-1}} \tag{A18}$$

All parameters in Equation A18 are substituted by the values providing in Table A1. The static pressure of the outlet stream is

$$P_2=113{,}117.20 \quad \text{Pa}$$

The answer can be checked by back substituting P_2 in Equation A16. If the answer is correct, the value of the efficiency term will equal to unity.

Step 3: A following energy balance equation is applied to calculate the temperature of the outlet stream.

$$\Delta E_K + \Delta E_P + \Delta(H + PV) = W + Q \tag{A19}$$

where,

ΔE_K = kinetic energy change (J)

ΔE_P = potential energy change (J)

H = enthalpy (J)

PV = flow work (J)

W = shaft work (J)

Q = heat exchanging between the system and surrounding (J)

The flow work and potential energy difference are zero, so only the shaft work and enthalpy term appear in the system. Equation 19 is reduced to Equation A20.

$$\Delta KE = -\Delta H \tag{A20}$$

which is:

$$\Delta KE = \frac{1}{2}\dot{m}_m\left(v_2^2 - v_m^2\right) + \frac{1}{2}\dot{m}_1\left(v_2^2 - v_1^2\right) \tag{A21}$$

$$\Delta H = \dot{m}_1 C_P\left(T_2 - T_1\right) + \dot{m}_m C_P\left(T_2 - T_m\right) \tag{A22}$$

where,

C_P = heat capacity at constant pressure $(\mathrm{J/(mol \cdot K)})$

An ideal gas law is applied to evaluate C_P

$$C_P = \frac{\gamma}{\gamma - 1}R = \frac{1.3}{0.3}R = 4.333R \tag{A23}$$

Equations (A20), (A21), (A22) are substituted into Equation A19. Equation A19 is rearranged to compute the temperature of the outlet stream, which is

$$T_2 = \frac{1}{2}\left(\frac{MW}{C_P}\right)\frac{\dot{m}_m}{\left(\dot{m}_m + \dot{m}_1\right)}\left(v_m^2 - v_2^2\right) + \frac{\left(\dot{m}_1 T_1 + \dot{m}_m T_m\right)}{\left(\dot{m}_1 + \dot{m}_m\right)} \tag{A24}$$

$$T_2 = 382.60 \text{ K}$$

Step 4: The shaft work from the turbine is evaluated by

$$W_S = \dot{m}_1\left(\frac{\gamma}{\gamma - 1}\right)\left(\frac{RT_2}{MW}\right)\left[1 - \left(\frac{P_1}{P_2}\right)^{\frac{\gamma-1}{\gamma}}\right] \tag{A25}$$

where,

$W_S =$ shaft work (J)

$$W_S = 12{,}870.70 \text{ J}$$

Step 5: The shaft work powers the compressor, which compresses the second part of the outlet stream. An intermediate condition before going though the nozzle is expected after this stage. The pressure can be computed by the following Equation A26.

$$W_S = \dot{m}_m\left(\frac{\gamma}{\gamma - 1}\right)\left(\frac{RT_2}{MW}\right)\left[\left(\frac{P_3}{P_2}\right)^{\frac{\gamma-1}{\gamma}} - 1\right] \tag{A26}$$

To extract P_3, Equation A26 is rearranged and gives rise to Equation A27.

$$P_3 = P_2 \times \left[\left(\frac{\gamma - 1}{\gamma}\right)\frac{MW \cdot W_S}{RT_2 \cdot \dot{m}_m} + 1\right]^{\frac{\gamma}{\gamma-1}} \tag{A27}$$

$$P_3 = 130{,}541.89 \text{ Pa}$$

Step 6: The temperature of the intermediate stream is calculated by the ideal gas law for a compressible gas, which is

$$\frac{T_3}{T_2} = \left(\frac{P_3}{P_2}\right)^{\frac{\gamma-1}{\gamma}} \tag{A28}$$

where,

P_3 = static pressure at the intermediate stage (Pa)

T_3 = temperature at the intermediate stage (K)

$$T_3 = T_2 \times \left(\frac{P_3}{P_2}\right)^{\frac{\gamma-1}{\gamma}} = 395.46 \text{ K} \tag{A29}$$

Step 7: The intermediate stream is fed through the nozzle. The velocity at the nozzle exit is calculated by Equation A30.

$$\frac{1}{2}\left(v_m^2 - v_3^2\right) = \left(\frac{\gamma}{\gamma-1}\right)\left(\frac{RT_3}{MW}\right)\left[1 - \left(\frac{P_m}{P_3}\right)^{\frac{\gamma-1}{\gamma}}\right] \tag{A30}$$

where,

v_3 = fluid velocity at the intermediate stage (m/s)

$$v_m = \sqrt{v_3^2 + \frac{2 \cdot RT_3}{MW}\left(\frac{\gamma}{\gamma-1}\right)\left[1 - \left(\frac{P_m}{P_3}\right)^{\frac{\gamma-1}{\gamma}}\right]} \tag{A31}$$

$v_m = 300.005$ m/s

Step 8: Finally, the analysis is extended by adjusting propelled and motive stream mass flow rate with a wide range from 0.1 to 1.0 kg/s. The calculation result of both cases is displayed in Table A2 and A3 respectively.

Table A2. Calculation result from adjusting propelled-stream mass flow rate.

Stream Properties of Each Stage	M_p (kg/s)					
	0.1	0.3	0.5	0.7	0.9	1.0
P_2 (Pa)	125,270.6	118,914.6	115,222.0	112,809.7	111,110.6	110,436.5
T_2 (K)	391.7	387.0	384.2	382.4	381.0	380.5
W_s (J/s)	3781.8	8612.0	11566.6	13560.4	14996.5	15573.8
P_3 (Pa)	130,540.8	130,540.8	130,540.8	130,540.8	130,540.8	130,540.8
T_3 (K)	395.5	395.5	395.5	395.5	395.5	395.5
V_m (m/s)	**300.00**	**300.00**	**300.00**	**300.00**	**300.00**	**300.00**

Table A3. Calculation result from adjusting motive-stream mass flow rate.

Stream Properties of Each Stage	M_m (kg/s)					
	0.1	0.3	0.5	0.7	0.9	1.0
P_2 (Pa)	104,803.30	109,758.61	113,116.81	115,541.89	117,374.97	118,133.30
T_2 (K)	375.92	379.95	382.60	384.48	385.87	386.45
W_s (J/s)	4,114.78	9,695.20	13,303.66	15,828.46	17,694.01	18,455.32
P_3 (Pa)	130,540.82	130,540.82	130,540.82	130,540.82	130,540.82	130,540.82
T_3 (K)	395.46	395.46	395.46	395.46	395.46	395.46
V_m (m/s)	**300.00**	**300.00**	**300.00**	**300.00**	**300.00**	**300.00**

Conclusion, the condition of the outlet stream is identical to the initial specified condition over a wide range of propelled and motive stream mass flow rates. This validates the newly defined efficiency equation.

APPENDIX B

RESULTS OF MODEL ACCURACY EXPERIMENT

In the model accuracy experiment, the simulation results are compared to experimental results obtained from Manohar Vishwanathappa, a graduate chemical engineering student at Texas A&M University. Both of the simulation and experimental results are summarized in this section. The experimental results are shown in Table B1, whereas the simulation results are shown in Table B2.

Table B1. Experimental data.

v_m (m/s)	Pinch 0		Pinch 1		Pinch 2		Pinch 3	
	m_p (kg/s)	ΔP (Pa)	m_p (kg/s)	ΔP (Pa)	m_p (kg/s)	ΔP (Pa)	m_p (kg/s)	ΔP (Pa)
562.86	0.65	684.96	0.61	856.82	0.57	1,153.22	0.37	2,179.41
527.86	0.61	637.63	0.57	732.28	0.54	1,028.68	0.36	1,853.12
490.03	0.55	468.26	0.53	607.75	0.5	841.87	0.34	1,556.72
448.95	0.5	358.67	0.47	468.26	0.48	622.69	0.33	1,120.84
411.19	0.44	234.13	0.42	326.28	0.41	435.88	0.32	794.55

The pinch valve is located at the downstream of jet ejector to produce back pressure. The number behind the pinch indicates the diameter of the pinch valve. Pinch 0

(see Figure B1-A) indicates that the diameter is largest (perfectly open). Pinch 3 (see Figure B1-D) indicates that the diameter is smallest. The geometry of the jet ejector is detailed in Appendix F.

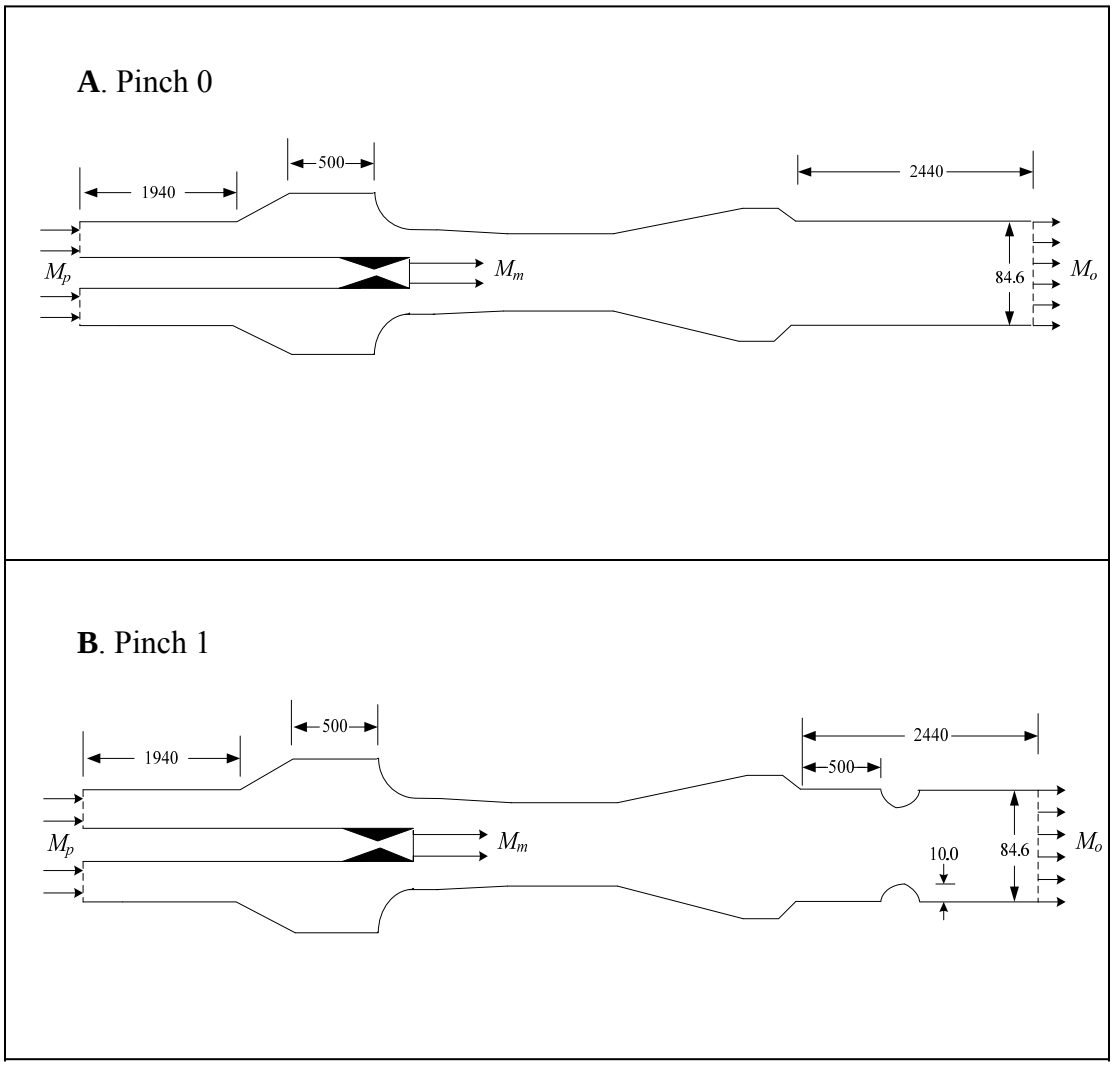

Figure B1. Location and dimension of pinch valve in an experimental set A) pinch 0, B) pinch 1, C) pinch 2, D) pinch 3 (unit: millimeter).

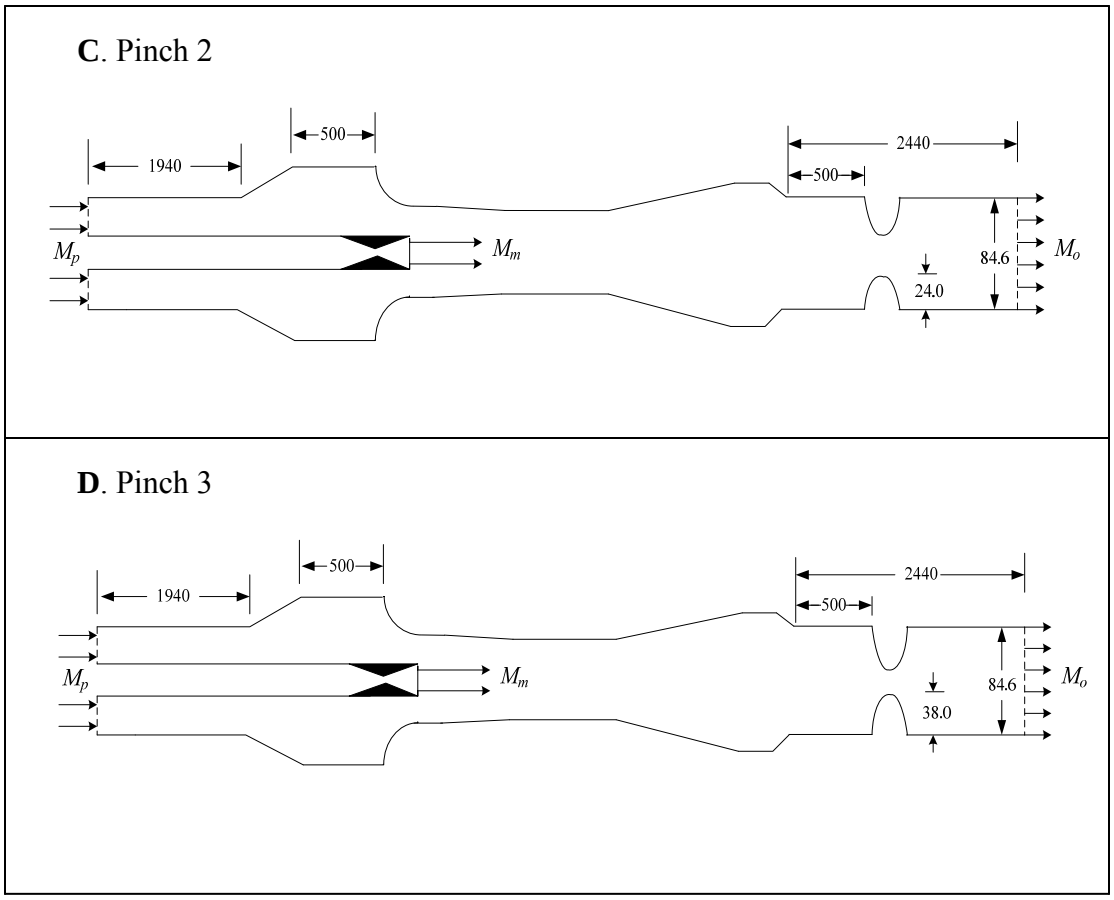

Figure B1. (Continued)

Because the pinch valve itself is not included in the simulation model, the propelled-stream mass flow rate is adjusted to match the back pressure produced by the pinch valve. This removes the complexity of trying to simulate the flow through the pinch valve. In the simulation experiment, the propelled mass flow rate is adjusted over a wide range to cover the experimental region. All the simulation results according to the motive stream velocity are summarized as follows:

Table B2. Simulation data A) motive stream velocity at 563 m/s, B) at 528 kg/s, C) at 490 m/s, D) at 449 m/s, E) at 411 m/s.

A. Motive stream velocity = 563 m/s

v_m (m/s)	m_p (kg/s)	Pressure (Pa)		
		Inlet	Outlet	Difference
563	0.67	100,990	101,320	330
	0.65	100,535	101,321	786
	0.61	100,106	101,321	1,215
	0.58	99,851	101,322	1,471
	0.55	99,617	101,322	1,705
	0.52	99,400	101,322	1,922
	0.49	99,195	101,322	2,127
	0.46	99,002	101,322	2,320
	0.43	98,822	101,322	2,500
	0.4	98,649	101,322	2,673
	0.37	98,484	101,322	2,838

Table B2. (Continued).

B. Motive stream velocity = 528 m/s

v_m (m/s)	m_p (kg/s)	Pressure (Pa)		
		Inlet	Outlet	Difference
528	0.61	100,906	101,321.3	415.3
	0.58	100,654.5	101,321.5	667
	0.55	100,423.4	101,321.6	898.2
	0.52	100,209.3	101,321.8	1,112.5
	0.49	100,009.8	101,322	1,312.2
	0.46	99,821.4	101,322.1	1,500.7
	0.43	99,649	101,322.3	1,673.3
	0.40	99,484.7	101,322.4	1,837.7
	0.37	99,446	101,322.5	1,876.5
	0.34	99,144	101,322.8	2,178.8

C. Motive stream velocity = 490 m/s

v_m (m/s)	m_p (kg/s)	Pressure (Pa)		
		Inlet	Outlet	Difference
490	0.55	101,062	101,321.7	259.7
	0.52	100,649.4	101,321.9	472.5
	0.49	100,651.5	101,322	670.5
	0.46	100,467	101,322.2	855.2
	0.43	100,300	101,322.4	1,022.4
	0.40	100,139	101,322	1,183
	0.37	99,969.5	101,322.6	1,333.1
	0.28	99,705	101,323	1,618

Table B2. (Continued).

D. Motive stream velocity = 449 m/s

v_m (m/s)	m_p (kg/s)	Pressure (Pa)		
		Inlet	Outlet	Difference
449	0.49	101,176	101,322	146
	0.46	100,993	101,322	329
	0.43	100,823	101,322	499
	0.40	100,670	101,323	653
	0.37	100,531	101,323	792
	0.34	100,399	101,323	924
	0.31	100,266	101,323	1,057
	0.28	100,139	101,323	1,184

E. Motive stream velocity = 411 m/s

v_m (m/s)	m_p (kg/s)	Pressure (Pa)		
		Inlet	Outlet	Difference
411	0.43	101,194	101,322	128
	0.40	101,038	101,323	285
	0.37	100,896	101,323	427
	0.31	100,651	101,323	672
	0.28	100,535	101,323	788
	0.25	100,427	101,323	896

APPENDIX C

FLUID PROPERTIES OF OPTIMIZATION CASES

The fluid properties (e.g., fluid static pressure, mass flow rate, velocity, and density) are summarized in this section. They are reported separately for each motive velocity (170 to 1104 m/s). The optimum nozzle diameter ratio; D_N/D_P, of each motive velocity is also included.

Table C1. Static pressure and compression ratio.

Motive velocity	Mass flow ratio	Static pressure (Pa)		
		Motive stream	Propelled stream	Outlet stream
170 m/s (D_N/D_P = 0.05)	0.03	101,379.2	101,258.6	101,324.1
	0.05	101,321.6	101,264.1	101,324.8
	0.10	100,952.3	101,177.9	101,325.6
	0.50	99,275.6	100,197.6	101,325.2
	1.00	98,353.9	99,109.2	101,325.2
	5.00	95,590.9	95,963.8	101,325.1
	10.00	94,833.8	94,797.5	101,325.1
	50.00	94,441.8	92,083.1	101,325.2
	100.00	94,328.3	91,166.8	101,325.1
340 m/s (D_N/D_P = 0.046)	0.03	102,075.9	101,066.6	101,322.1
	0.05	101,348.5	101,066.8	101,327.2
	0.10	99,346.7	100,667.6	101,327.1
	0.50	91,801.4	95,613.9	101,325.6
	1.00	86,212.1	90,513.3	101,325.5

340 m/s (D_N/D_P = 0.046)	5.00	74210.6	70,512.1	101325.3
	10.00	79203.0	56,863.3	101324.6
	50.00	74863.1	44,600.2	101325.3
	100.00	74134.6	38,711.0	101325.3
510 m/s (D_N/D_P = 0.044)	0.03	102,118.9	100,741.9	101319.2
	0.05	101,320.8	100,717.2	101329.4
	0.10	101,279.0	99,877.9	101328.8
	0.50	100,368.3	88,495.4	101326.4
	1.00	99,797.1	76,529.6	101325.7
	5.00	99,637.9	44,389.3	101325.5
	10.00	99,333.3	35,598.2	101325.4
	50.00	98,779.8	23,711.9	101325.4
	100.00	98,789.3	21,857.2	101325.4
640 m/s (D_N/D_P = 0.044)	0.03	102,535	100,160.5	101304.1
	0.05	101,510.3	100,157.5	101329.7
	0.10	101,686.0	98,482.1	101332.1
	0.50	100,694.2	79,938.4	101328.8
	1.00	100,420.4	65,197.5	101326.7
	5.00	100,309.4	32,933.0	101325.7
	10.00	100,247.5	24,538.2	101325.6
	50.00	100,082.5	12,960.6	101325.7
	100.00	100,057.3	10,400.8	101325.7
850 m/s (D_N/D_P = 0.044)	0.05	101,332.3	99,052.9	101299.6
	0.09	101,301.5	96,630.2	101309.0
	0.10	101,330.9	95,661.6	101306.1
	0.50	101,249.9	72,783.6	101331.4
	1.00	101,022.0	59,653.8	101328.5
	5.00	100,639.8	24,536.2	101326.5
	10.00	100,862.0	16,676.8	101327.2
	50.00	100,517.4	6,832.3	101326.3
	100.00	100,492.3	4,659.2	101326.4
1020 m/s	0.03	101,463.0	98,220.6	101,282.7
	0.05	101,498.5	97,897.2	101,300.9

1020 m/s (D_N/D_P = 0.03)	0.09	101,454.6	95,735.7	101,321.6
	0.10	101,352.4	94,648.7	101,327.3
	0.50	101,173.2	71,681.5	101,330.4
	1.00	101,050.2	52,772.2	101,327.7
	5.00	100,784.8	19,359.3	101,304.5
	10.00	100,694.6	11,900.9	101,327.2
	50.00	100,735.0	3,065.7	101,326.1
	100.00	100,724.6	1,733.6	101,326.0
1104 m/s (D_N/D_P = 0.03)	0.05	101,502.6	96,018.9	101,325.5
	0.075	101,562.4	95,045.3	101,263.4
	0.10	101,595.1	93,872.6	101,290.0
	0.25	101,491.8	82,840.6	101,332.7
	0.50	101,232.4	70,393.5	101,336.0
	1.00	101,166.0	56,990.5	101,331.8
	5.00	101,080.7	16,122.2	101,295.2
	10.00	101,081.6	9,243.9	101,368.1

Table C2. Density and velocity.

Motive velocity	Mass flow ratio	Density (kg/m^3)			Velocity (m/s)	
		Motive stream	Propelled stream	Outlet stream	Propelled stream	Outlet stream
170 m/s (D_N/D_P = 0.05)	0.03	0.6004	0.5883	0.5886	13.831	5.929
	0.05	0.6001	0.5883	0.5886	8.299	5.157
	0.10	0.5980	0.5878	0.5886	4.157	5.067
	0.50	0.5885	0.5821	0.5886	0.840	2.344
	1.00	0.5832	0.5757	0.5886	0.423	1.700
	5.00	0.5675	0.5575	0.5886	0.101	1.128
	10.00	0.5632	0.5507	0.5886	0.050	1.046
	50.00	0.5640	0.5509	0.5886	0.027	0.950
	100.00	0.5603	0.5296	0.5886	0.028	0.989
340 m/s	0.03	0.6412	0.5875	0.5887	24.714	10.580

340 m/s (D_N/D_P = 0.046)	0.05	0.6373	0.5872	0.5887	14.836	9.960
	0.10	0.6268	0.5849	0.5887	7.449	9.518
	0.50	0.5863	0.5554	0.5886	1.554	4.308
	1.00	0.5558	0.5259	0.5886	0.827	3.123
	5.00	0.4922	0.4120	0.5886	0.213	2.074
	10.00	0.4968	0.3342	0.5886	0.145	1.862
	50.00	0.4925	0.2591	0.5887	0.034	1.771
	100.00	0.4887	0.2249	0.5887	0.020	1.767
510 m/s (D_N/D_P = 0.044)	0.03	0.7163	0.5858	0.5887	37.821	16.148
	0.05	0.7104	0.5853	0.5887	22.710	15.199
	0.10	0.7101	0.5802	0.5887	11.457	12.501
	0.50	0.7035	0.5141	0.5886	2.587	6.473
	1.00	0.7008	0.4450	0.5885	1.493	4.673
	5.00	0.6977	0.2579	0.5887	0.515	2.988
	10.00	0.6955	0.2068	0.5887	0.320	2.764
	50.00	0.6914	0.1377	0.5887	0.098	2.594
	100.00	0.6910	0.1270	0.5887	0.053	2.569
680 m/s (D_N/D_P = 0.044)	0.03	0.8331	0.5786	0.5889	61.08	25.75
	0.05	0.8495	0.5823	0.5888	36.414	20.779
	0.10	0.8514	0.5722	0.5881	18.533	19.857
	0.50	0.8421	0.4644	0.5887	4.562	9.795
	1.00	0.8442	0.3787	0.5886	2.801	7.018
	5.00	0.8390	0.1919	0.5886	1.104	4.432
	10.00	0.8370	0.1426	0.5886	0.744	4.122
	50.00	0.8359	0.0753	0.5887	0.281	3.900
	100.00	0.8356	0.0604	0.5887	0.176	3.861
850 m/s (D_N/D_P = 0.044)	0.05	1.1296	0.5769	0.5889	61.263	26.255
	0.09	1.1258	0.5622	0.5890	34.919	30.197
	0.10	1.1270	0.5561	0.5889	31.778	26.461
	0.50	1.1284	0.4295	0.5887	8.232	14.558
	1.00	1.1227	0.3465	0.5887	5.103	10.636
	5.00	1.1190	0.1425	0.5886	2.480	6.741
	10.00	1.1237	0.0969	0.5888	1.776	5.326

850 m/s	50.00	1.1190	0.0397	0.5886	0.877	5.996
	100.00	1.1187	0.0271	0.5886	0.643	5.905
1020 m/s (D_N/D_P = 0.03)	0.03	1.8973	0.5740	0.5892	93.913	39.302
	0.05	1.8978	0.5757	0.5888	56.180	24.053
	0.09	1.8939	0.5565	0.5890	32.276	30.951
	0.10	1.8901	0.5501	0.5890	29.401	30.429
	0.50	1.8940	0.4164	0.5887	7.773	13.753
	1.00	1.8950	0.3066	0.5887	5.279	9.875
	5.00	1.8741	0.1125	0.5878	2.808	6.289
	10.00	1.8733	0.0691	0.5885	2.337	5.804
	50.00	1.8832	0.0178	0.5886	1.810	5.397
	100.00	1.8830	0.0101	0.5886	1.606	5.351
1104 m/s (D_N/D_P = 0.03)	0.05	3.0825	0.5654	0.5893	100.711	42.321
	0.075	3.0855	0.5412	0.5889	70.141	30.874
	0.10	3.0860	0.5463	0.5889	52.117	23.687
	0.25	3.0693	0.5112	0.5890	22.284	30.081
	0.50	3.0857	0.4587	0.5889	12.420	21.515
	1.00	3.0629	0.3311	0.5887	8.605	15.772
	5.00	3.0638	0.0930	0.5891	6.118	10.313
	10.00	3.0633	0.0537	0.5880	5.307	11.826

The total pressure is

$$P_{total} = P_{static} + P_{dynamic} \tag{C1}$$

and, the dynamic pressure is

$$P_{dynamic} = \frac{1}{2} \times \rho \times v^2 \tag{C2}$$

APPENDIX D

SALT WATER PROPERTIES AND

THE DETAIL DATA OF THE DESALINATION CASE STUDY

Table D1. Composition of seawater

Ion	Concentration in seawater (g/kg)
Chloride	19.344
Sodium	10.773
Sulfate	2.712
Magnesium	1.294
Calcium	0.412
Potassium	0.399
Bicarbonate	1.142
Bromide	0.067
Strontium	0.008
Boron	0.004
Fluoride	0.0013
Total	35.00

Table D2. Specific heat capacity of seawater (C_{ps}).

	Salinity (g/kg)															
t (°C)	0[a]	10	20	30	40	50	60	70	80	90	100	110	120	130	140	150
0	4.209	4.143	4.081	4.021	3.964	3.910	3.858	3.809	3.763	3.720	3.679	3.641	3.606	3.573	3.543	3.516
10	4.198	4.136	4.077	4.020	3.965	3.913	3.863	3.815	3.770	3.727	3.686	3.648	3.612	3.579	3.547	3.518
20	4.189	4.131	4.074	4.020	3.967	3.917	3.868	3.822	3.777	3.735	3.649	3.656	3.619	3.584	3.552	3.521
30	4.184	4.128	4.074	4.021	3.971	3.922	3.874	3.829	3.785	3.743	3.702	3.663	3.626	3.591	3.557	3.525
40	4.180	4.127	4.075	4.024	3.975	3.927	3.881	3.836	3.793	3.751	3.710	3.671	3.633	3.597	3.562	3.529
50	4.180	4.128	4.078	4.029	3.981	3.934	3.888	3.844	3.801	3.759	3.719	3.679	3.641	3.604	3.568	3.533
60	4.181	4.131	4.082	4.034	3.987	3.941	3.896	3.853	3.810	3.768	3.727	3.687	3.649	3.611	3.574	3.538
70	4.186	4.137	4.088	4.041	3.995	3.950	3.905	3.861	3.819	3.777	3.736	3.696	3.657	3.618	3.581	3.544
80	4.192	4.144	4.096	4.050	4.004	3.959	3.914	3.871	3.828	3.786	3.745	3.704	3.665	3.626	3.588	3.551
90	4.202	4.154	4.106	4.059	4.014	3.968	3.924	3.880	3.837	3.795	3.754	3.713	3.673	3.634	3.595	3.558
100	4.213	4.165	4.118	4.071	4.025	3.979	3.934	3.891	3.847	3.805	3.763	3.722	3.82	3.642	3.603	3.565
110	4.228	4.179	4.131	4.083	4.037	3.991	3.946	3.901	3.857	3.815	3.772	3.731	3.690	3.651	3.612	3.573
120	4.245	4.195	4.146	4.097	4.050	4.003	3.957	3.912	3.868	3.825	3.782	3.740	3.700	3.659	3.620	3.582
130	4.264	4.213	4.162	4.113	4.064	4.016	3.970	3.924	3.879	3.835	3.792	3.750	3.709	3.669	3.629	3.591
140	4.286	4.233	4.181	4.129	4.079	4.030	3.982	3.936	3.890	3.845	3.802	3.760	3.718	3.678	3.639	3.601
150	4.311	4.255	4.201	4.148	4.096	4.045	3.996	3.948	3.902	3.856	3.812	3.769	3.728	3.688	3.649	3.611
160	4.338	4.279	4.222	4.167	4.113	4.061	4.010	3.961	3.913	3.867	3.823	3.780	3.738	3.698	3.659	3.622
170	4.367	4.306	4.246	4.188	4.132	4.078	4.025	3.974	3.926	3.878	3.833	3.790	3.748	3.708	3.670	3.634
180	4.399	4.334	4.271	4.210	4.152	4.095	4.041	3.988	3.938	3.890	3.844	3.800	3.758	3.719	3.681	3.646

[a] While these values for pure water are within the claimed accuracy, more accurate values are available in the appropriate ESDU Date Item

Table D2. Continued.

	Salinity (g/kg)										
t (°C)	30	31	32	33	34	35	36	37	38	39	40
0	4.021	4.015	4.010	4.004	3.998	3.992	3.987	3.981	3.975	3.970	3.964
10	4.020	4.014	4.009	4.003	3.998	3.992	3.987	3.981	3.976	3.971	3.965
20	4.020	4.015	4.009	4.004	3.999	3.993	3.988	3.983	3.978	3.973	3.967
30	4.021	4.016	4.011	4.006	4.001	3.996	3.991	3.986	3.981	3.976	3.971
40	4.024	4.019	4.014	4.009	4.004	4.000	3.995	3.990	3.985	3.980	3.975
50	4.029	4.024	4.019	4.014	4.009	4.004	4.000	3.995	3.990	3.985	3.981
60	4.034	4.029	4.025	4.020	4.015	4.011	4.006	4.001	3.997	3.992	3.987
70	4.041	4.037	4.032	4.027	4.023	4.018	4.013	4.009	4.004	4.000	3.995
80	4.050	4.045	4.040	4.036	4.031	4.027	4.022	4.017	4.013	4.008	4.004
90	4.059	4.055	4.050	4.046	4.041	4.036	4.032	4.027	4.023	4.018	4.014
100	4.071	4.066	4.061	4.057	4.052	4.048	4.043	4.038	4.034	4.029	4.025
110	4.083	4.079	4.074	4.069	4.065	4.060	4.055	4.051	4.046	4.041	4.037
120	4.097	4.092	4.088	4.083	4.078	4.073	4.069	4.064	4.059	4.054	4.050
130	4.113	4.108	4.103	4.098	4.093	4.088	4.083	4.078	4.074	4.069	4.064
140	4.129	4.124	4.119	4.114	4.109	4.104	4.099	4.094	4.089	4.084	4.079
150	4.148	4.142	4.137	4.132	4.127	4.121	4.116	4.111	4.106	4.101	4.096
160	4.167	4.162	4.156	4.151	4.145	4.140	4.135	4.129	4.124	4.119	4.113
170	4.188	4.182	4.177	4.171	4.165	4.160	4.154	4.149	4.143	4.137	4.132
180	4.120	4.204	4.198	4.192	4.187	4.181	4.175	4.169	4.163	4.157	4.152

Table D3. The detail data of the desalination case study.

Latent heat exchanger #	Condenser			Evaporator		
	P (atm)	H_c^v (kJ)	H_c^l (kJ)	P_o (atm)	H_e^v (kJ)	H_e^l (kJ)
1	2.0231	2,709.79	502.45	1.9602	2,708.10	502.45
2	1.9245	2,707.13	500.02	1.8640	2,705.45	495.82
3	1.8282	2,704.43	493.28	1.7702	2,702.72	489.08
4	1.7342	2,701.68	486.42	1.6787	2,700.00	482.22
5	1.6444	2,698.94	479.56	1.5913	2,697.25	475.36
6	1.5584	2,696.19	472.71	1.5076	2,694.51	468.51
7	1.4763	2,693.45	465.86	1.4277	2,691.77	461.67
8	1.3978	2,690.71	459.02	1.3514	2,689.03	454.83
9	1.3229	2,687.97	452.19	1.2785	2,686.29	447.99
10	1.2514	2,685.24	445.36	1.2090	2,683.56	441.17
11	1.1831	2,682.51	438.54	1.1427	2,680.82	434.34
12	1.1180	2,679.78	431.73	1.0794	2,678.09	427.53

Table D3. Continued.

Latent heat exchanger #	Condenser			Evaporator		
	P (atm)	H_c^v (kJ)	H_c^l (kJ)	P_o (atm)	H_e^v (kJ)	H_e^l (kJ)
13	1.0560	2,677.05	424.92	1.0192	2,675.37	420.72
14	0.9969	2,674.32	418.11	0.9618	2,672.64	413.92
15	0.9406	2,671.60	411.32	0.9071	2,669.92	407.12
16	0.8870	2,668.88	404.52	0.8551	2,667.20	400.33
17	0.8360	2,666.16	397.74	0.8057	2,664.48	393.54
18	0.7875	2,663.44	390.96	0.7587	2,661.76	386.76
19	0.7414	2,660.73	384.18	0.7140	2,659.05	379.98
20	0.6977	2,658.02	377.41	0.6716	2,656.34	373.21
21	0.6561	2,655.31	370.65	0.6313	2,653.63	366.45
22	0.6166	2,652.60	363.89	0.5932	2,650.92	359.69
23	0.5792	2,649.90	357.14	0.5569	2,648.22	352.94
24	0.5438	2,647.19	350.39	0.5226	2,645.51	346.19

Table D3. Continued.

Latent heat exchanger #	Condenser			Evaporator		
	P (atm)	H_c^v (kJ)	H_c^l (kJ)	P_o (atm)	H_e^v (kJ)	H_e^l (kJ)
25	0.5102	2,644.49	343.65	0.4901	2,642.81	339.45
26	0.4783	2,641.79	336.91	0.4594	2,640.11	332.71
27	0.4482	2,639.10	330.18	0.4303	2,637.42	325.98
28	0.4197	2,636.40	323.45	0.4027	2,634.72	319.25
29	0.3928	2,633.71	316.73	0.3767	2,632.03	312.53
30	0.3674	2,631.02	310.01	0.3522	2,629.34	305.81
31	0.3434	2,628.33	303.30	0.3290	2,626.65	299.10
32	0.3207	2,625.65	296.59	0.3072	2,623.96	292.40
33	0.2993	2,622.96	289.89	0.2866	2,621.28	285.69
34	0.2792	2,620.28	283.20	0.2671	2,618.60	279.00
35	0.2602	2,617.60	276.50	0.2489	2,615.92	272.31
36	0.2424	2,614.92	269.82	0.2317	2,613.24	265.62

Table D3. Continued.

Latent heat exchanger #	Condenser			Evaporator		
	P (atm)	H_c^v (kJ)	H_c^l (kJ)	P_o (atm)	H_e^v (kJ)	H_e^l (kJ)
37	0.2256	2,612.24	262.13	0.2155	2,610.56	258.94
38	0.2098	2,609.57	256.46	0.2004	2,607.89	252.26
39	0.1950	2,606.90	249.78	0.1861	2,605.21	245.58
40	0.1811	2,604.22	243.11	0.1727	2,602.54	238.91
41	0.1680	2,601.55	236.45	0.1602	2,599.87	232.25
42	0.1558	2,598.88	229.78	0.1485	2,597.20	225.58
43	0.1443	2,596.22	223.12	0.1375	2,594.53	218.92
44	0.1336	2,593.55	216.47	0.1272	2,591.87	212.27
45	0.1236	2,590.89	209.82	0.1176	2,589.20	205.62
46	0.1142	2,588.22	203.17	0.1086	2,586.54	198.97
47	0.1054	2,585.56	196.52	0.1002	2,583.88	192.32
48	0.0973	2,582.90	189.88	0.0924	2,581.22	185.68

Table D3. Continued.

Latent heat exchanger #	Condenser			Evaporator		
	P (atm)	H_c^v (kJ)	H_c^l (kJ)	P_o (atm)	H_e^v (kJ)	H_e^l (kJ)
49	0.0897	2,580.24	183.24	0.0851	2,578.56	179.05
50	0.0826	2,577.58	176.61	0.0784	2,575.90	172.41
51	0.0760	2,574.93	169.98	0.0721	2,573.25	165.78
52	0.0699	2,572.27	163.35	0.0662	2,570.59	159.15
53	0.0642	2,569.62	156.72	0.0608	2,567.94	152.53
54	0.0589	2,566.97	150.10	0.0557	2,565.28	145.90
55	0.0540	2,564.31	143.48	0.0511	2,562.63	139.28
56	0.0494	2,561.66	136.87	0.0467	2,559.98	132.67
57	0.0452	2,559.01	130.25	0.0427	2,557.33	126.05

APPENDIX E

THE PROCEDURE TO CALCULATE

THE INLET MOTIVE-STREAM PRESSURE

Identifying the inlet pressure of motive stream is one of the critical steps, because the inlet pressure indicates how much energy required to propelling a steam in order to achieve a particular motive velocity. The calculation procedure of identifying the inlet motive-stream pressure will be exemplified in this section. An isentropic flow condition is assumed in the calculation. The procedure is initialized with an equation of computing the fluid flow through nozzle; Equation E1.

$$u_2^2 = \frac{2\eta g_c \gamma \ P_2}{(\gamma - 1) \ \rho_2}\left[1 - \left(\frac{P_2}{P_1}\right)^{(\gamma-1)/\gamma}\right] \qquad \text{(E1)}$$

where,

u_2 = motive velocity at nozzle outlet (m/s)

η = nozzle efficiency = 0.95 (typical value)

$g_c = 1 \ \left((\text{kg} \cdot \text{m})/(\text{N} \cdot \text{s}^2)\right)$

γ = ratio of heat capacities = C_P / C_V =1.3 for steam

ρ = fluid density (kg/m^3)

P_2 = total pressure of the motive stream at nozzle outlet (Pa)

P_1 = total pressure of the motive stream at nozzle inlet (Pa)

The total pressure of the motive stream at nozzle inlet (P_1) is the calculating parameter. Therefore, Equation E1 turns to Equation E2 to compute P_1.

$$P_1 = \frac{P_2}{\left[1 - \frac{u_2^2(\gamma - 1)\ \rho_2}{2\eta\ \gamma\ g_c P_2}\right]^{\gamma/(\gamma-1)}} \qquad \text{(E2)}$$

Then, all the parameter values are substitutes into Equation E2 to calculate P_1; as shown below.

u_2 = 1020 m/s

P_2 = 1,083,340 Pa (The value is obtained from the CFD software.)

ρ_2 = 1.8882 kg/m^3 (The value is obtained from the CFD software.)

After substituting all the parameter values, Equation E2 turns to Equation E3.

$$P_1 = \frac{1{,}083{,}340}{\left[1 - \frac{1020^2 \times (1.3 - 1) \times 1.8882}{2 \times 0.95 \times 1.3 \times 1 \times 1{,}083{,}340}\right]^{1.3/(1.3-1)}} \qquad \text{(E3)}$$

$$= 3{,}183{,}818 \text{ Pa (31.42 atm)}$$

The inlet pressure of the motive stream (P_1) for each motive velocity is summarized in Table E1.

Table E1. Summarized the fluid properties of various motive velocities.

Motive velocity	Total pressure at nozzle outlet		Fluid density	Total pressure at nozzle inlet	
	(Obtained from the CFD software)			(Obtained from calculation)	
(m/s)	(Pa)	(atm)	(kg/m^3)	(Pa)	(atm)
170	106,394	1.05	0.5809	115,700	1.14
340	123,536	1.22	0.6373	171,118	1.69
510	191,442	1.89	0.7019	326,366	3.22
680	295,324	2.91	0.8418	628,946	6.21
850	507,113	5.00	1.1241	1,294,788	12.78
1020	1,083,340	10.69	1.8882	3,183,818	31.42
1104	1,975,270	19.49	3.0750	6,146,188	60.66

APPENDIX F

RESULTS OF EXTRA STUDY IN CONVERGENT NOZZLE

This study is conducted to understand a convergent nozzle, which is applied to the cascade analysis. (Note: a convergent nozzle can produce an exit velocity less than, or equal to, Mach 1.0) The goal of this study is to understand inlet and outlet velocity for a given nozzle shape. Various mass flow rates are injected through various nozzle shapes. The outlet velocity corresponding to each mass flow rate and shape of convergent nozzle is reported. The efficiency of each case is also evaluated. Steam is used as fluid, and the pressure in the exit space is maintained constant at 101.3 kPa. The simulation model is demonstrated in Figure F1. The simulation result is summarized in Table F1.

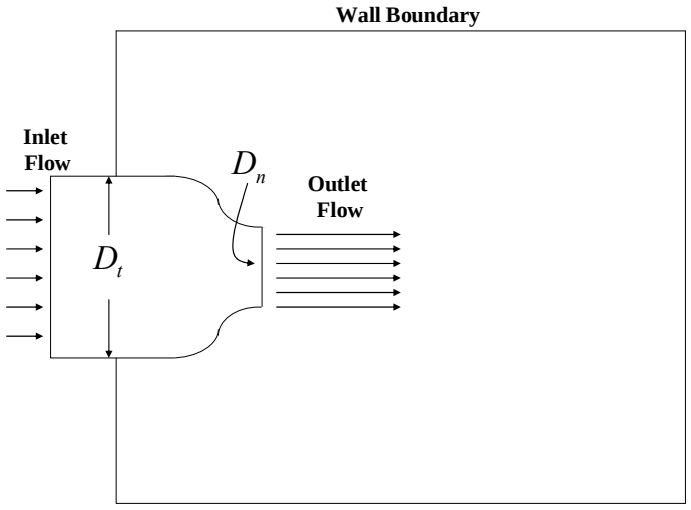

Figure F1. Simulation model of the convergent nozzle study.

Table F1. Simulation result of various nozzle diameter ratio.

$\frac{D_n}{D_t}$	Mass flow rate (kg/s)		Velocity (m/s)		Mach number		Efficiency
	Inlet	Outlet	Inlet	Outlet	Inlet	Outlet	
0.45	0.14	0.14	29.94	110.87	0.06	0.23	0.9983
	0.19	0.19	34.33	144.12	0.07	0.30	0.9980
	0.23	0.23	41.05	176.65	0.09	0.37	0.9971
	0.28	0.28	47.02	208.32	0.10	0.44	0.9960
	0.32	0.32	52.20	238.99	0.11	0.51	0.9949
	0.34	0.34	54.47	253.88	0.12	0.54	0.9944
0.40	0.14	0.14	25.44	171.45	0.05	0.36	0.9959
	0.19	0.19	31.21	220.76	0.07	0.47	0.9935
	0.23	0.23	35.70	267.28	0.08	0.57	0.9909
	0.28	0.28	38.94	310.39	0.08	0.66	0.9888
	0.32	0.32	41.08	348.95	0.09	0.74	0.9899
	0.34	0.34	41.82	365.92	0.09	0.77	0.9880
0.35	0.14	0.14	20.95	287.62	0.04	0.61	0.9849
	0.19	0.19	23.19	354.65	0.05	0.75	0.9817
	0.23	0.23	24.14	401.45	0.05	0.85	0.9844
	0.28	0.28	24.53	429.27	0.05	0.90	0.9899
	0.32	0.32	24.72	445.40	0.05	0.94	0.9943
	0.34	0.34	24.80	450.94	0.05	0.95	0.9957
0.30	0.14	0.14	10.95	448.60	0.02	0.94	0.9775
	0.19	0.19	11.13	469.51	0.02	0.97	0.9901
	0.23	0.23	11.18	478.86	0.02	0.99	0.9930
	0.28	0.28	11.21	483.99	0.02	1.00	0.9943
	0.32	0.32	11.18	487.98	0.02	1.00	0.9983
	0.34	0.34	11.19	489.32	0.02	1.01	0.9991

From the simulation result, the highest outlet velocity of convergent nozzle is about Mach 1.0 with a 0.3 diameter ratio. In the cascade, the motive velocity is Mach 0.95 and 0.99. Mach 0.95 is obtainable with 0.35 nozzle diameter ratio and inlet velocity at 24.80 m/s. The efficiency is 99.57%. Mach 0.99 is obtained with a nozzle diameter ratio equal to 0.3 and inlet velocity at 11.18 m/s. The efficiency is 99.30%. From this experiment, we conclude that if the motive velocity is maintained below Mach 1.0, the shock wave is avoided and the simple convergent nozzle can be applied. Generally, the convergent nozzle has a greater efficiency than a convergent-divergent nozzle; therefore, the overall efficiency of the cascade system with the convergent nozzle will be more than the system with the convergent-divergent nozzle.

APPENDIX G

ADDITIONAL RESULTS ON EXPERIMENT COMPARISON BETWEEN OPTIMUM AND CONVENTIONAL JET EJECTOR

This section is an extension part from Chapter IX (Experiment comparison between optimum and conventional jet ejector). In Chapter IX, nozzle used in the jet ejector performs best at 90 psig motive pressure, but in this appendix nozzle performs best at 60 psig. Therefore, both nozzle geometries are slightly different. The nozzle geometry is summarized in Table G1.

Table G1. Summarizing nozzle geometries used in the experiment.

Nozzle section	Length of nozzle cross-sectional diameter			
	Perform best at 90 psig		Perform best at 60 psig	
	inch	mm	inch	mm
Inlet	0.995	25.273	0.995	25.273
Center	0.454	11.532	0.546	13.868
Outlet	0.700	17.780	0.845	21.463

Figures G1(A) – (D) and Figures G2(A) – (D) show the compression ratios and efficiencies, respectively, for the optimal and conventional jet ejectors. Both jet ejectors are designed to provide maximum efficiency at compression ratio 1.30 and motive velocity 60 psig (312 m/s).

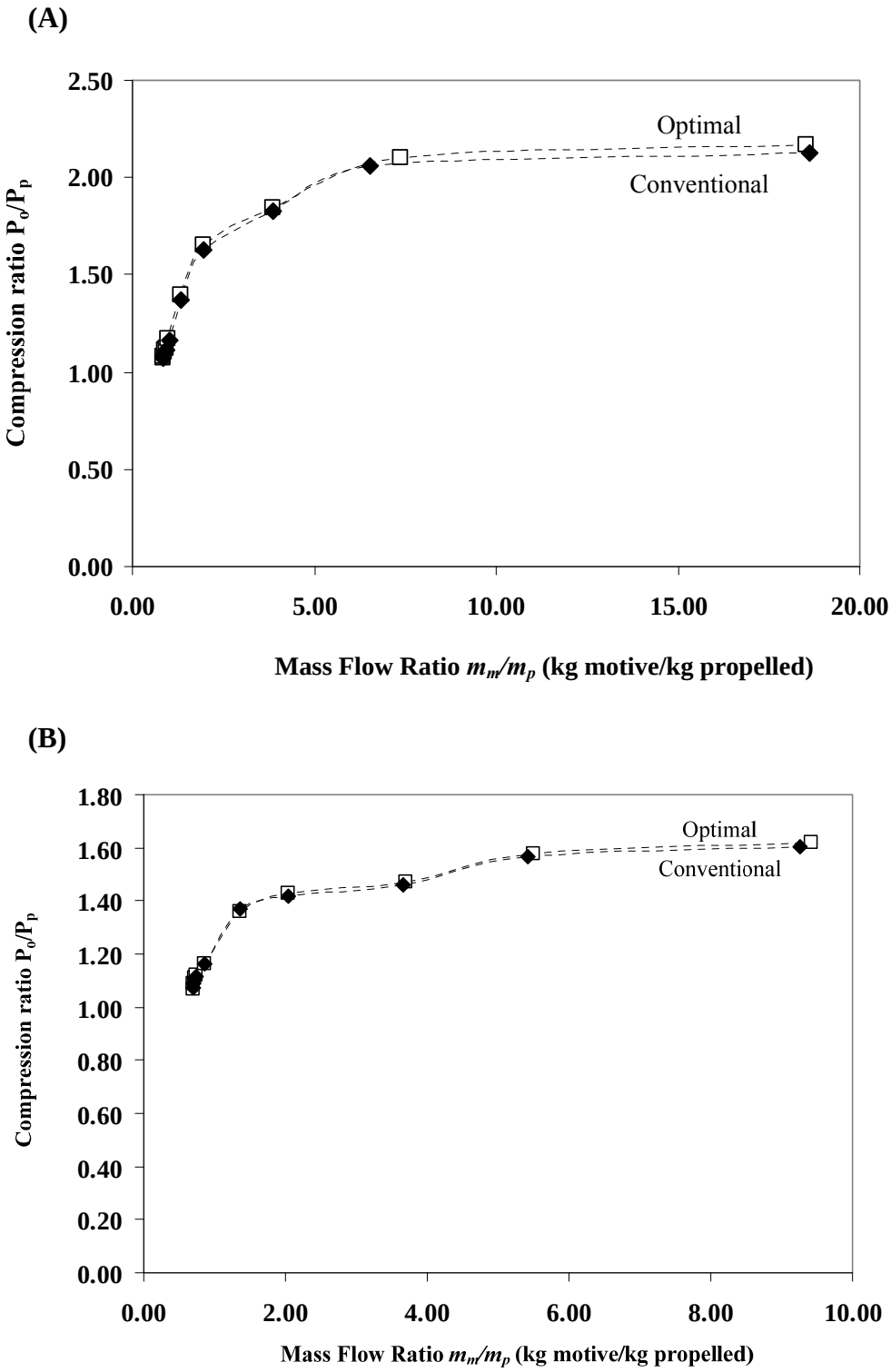

Figure G1. Compression ratio for a given mass flow ratio for optimal and conventional jet ejector at motive velocities (A) 345 m/s (70 psig), (B) 312 m/s (60 psig), (C) 309 m/s (50 psig), and (D) 296 m/s (50 psig).

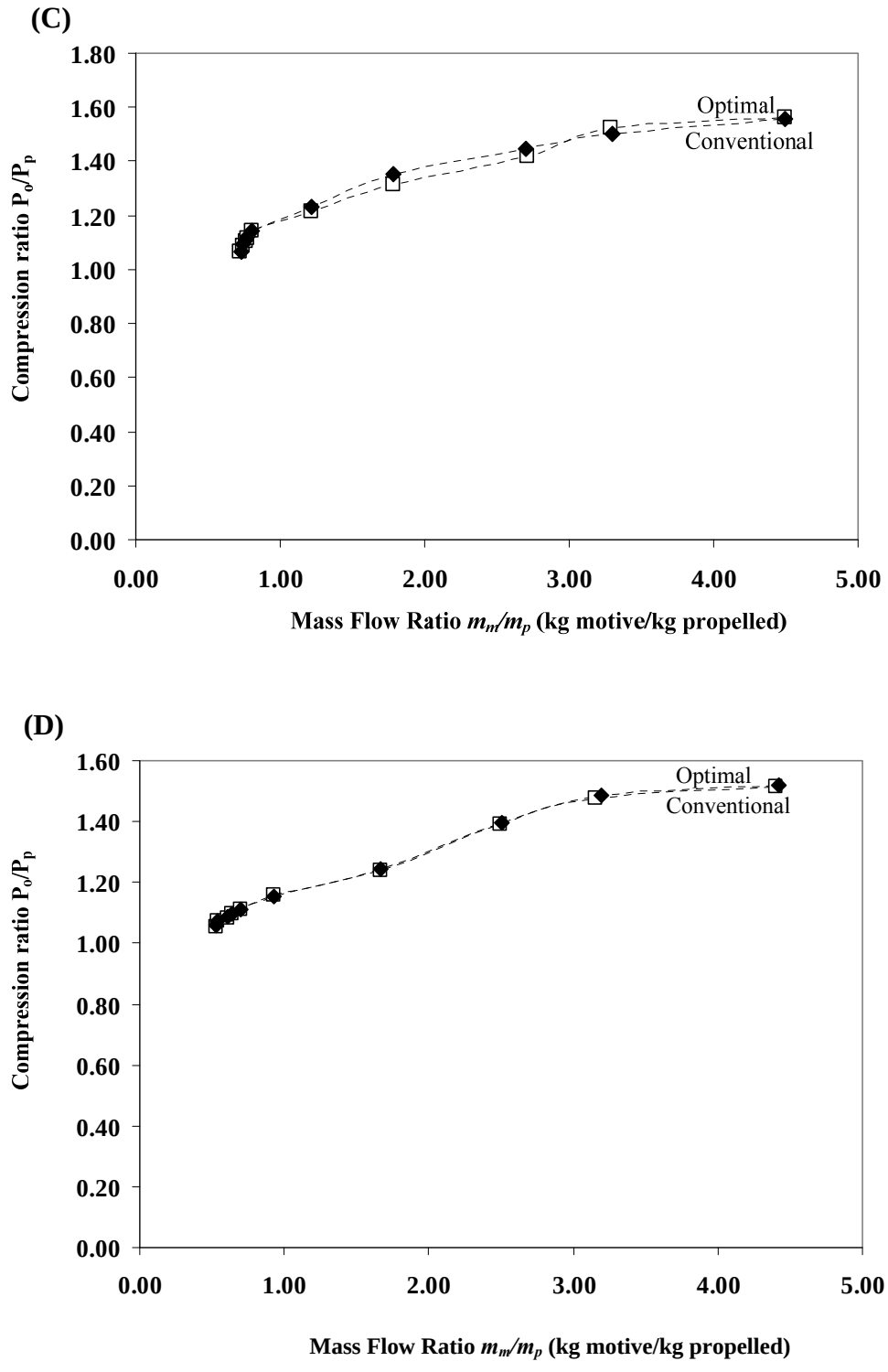

Figure G1. Continued.

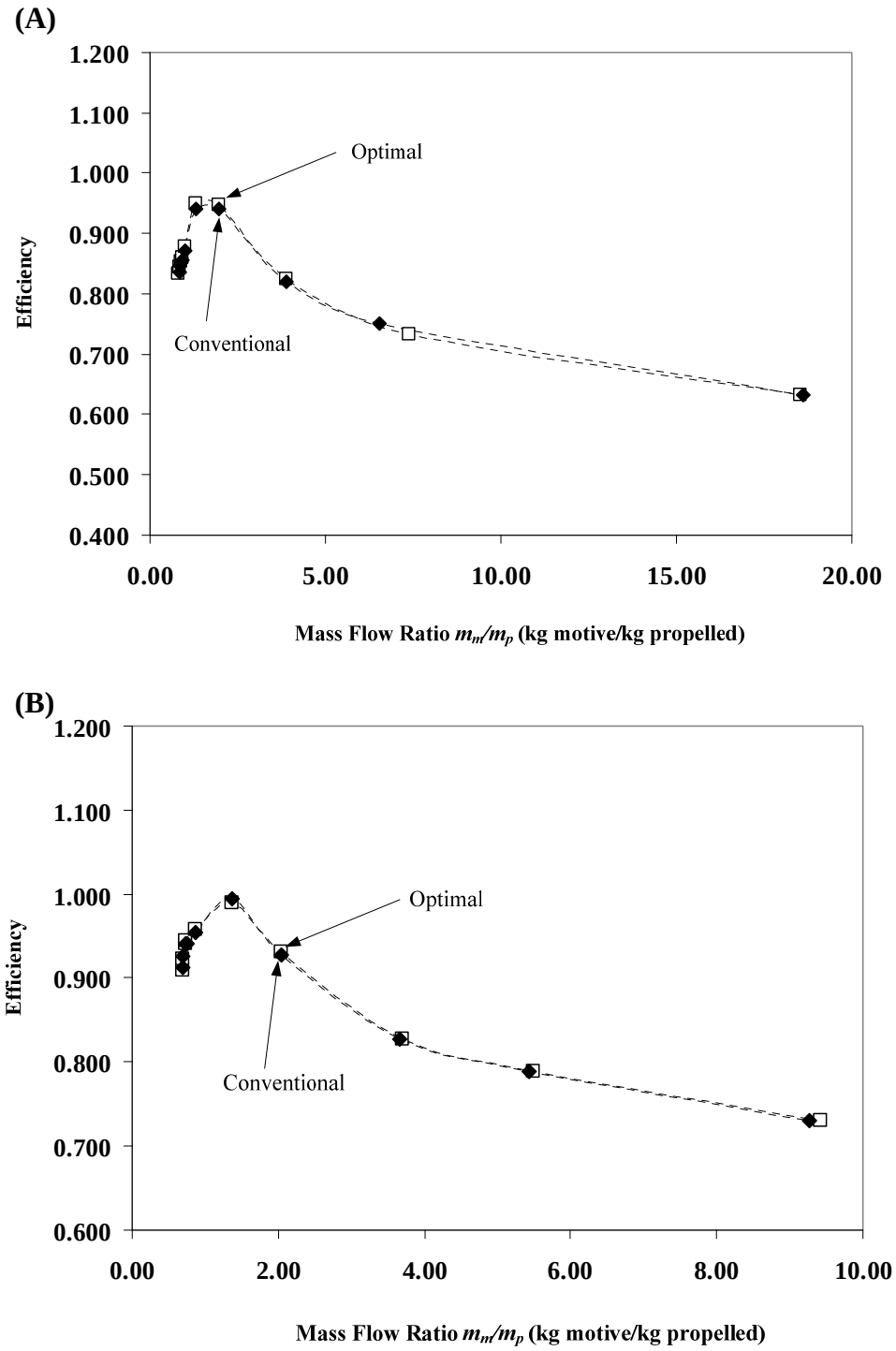

Figure G2. Efficiency for a given mass flow ratio for optimal and conventional jet ejector at motive velocities (A) 345 m/s (70 psig), (B) 312 m/s (60 psig), (C) 309 m/s (50 psig), and (D) 296 m/s (50 psig).

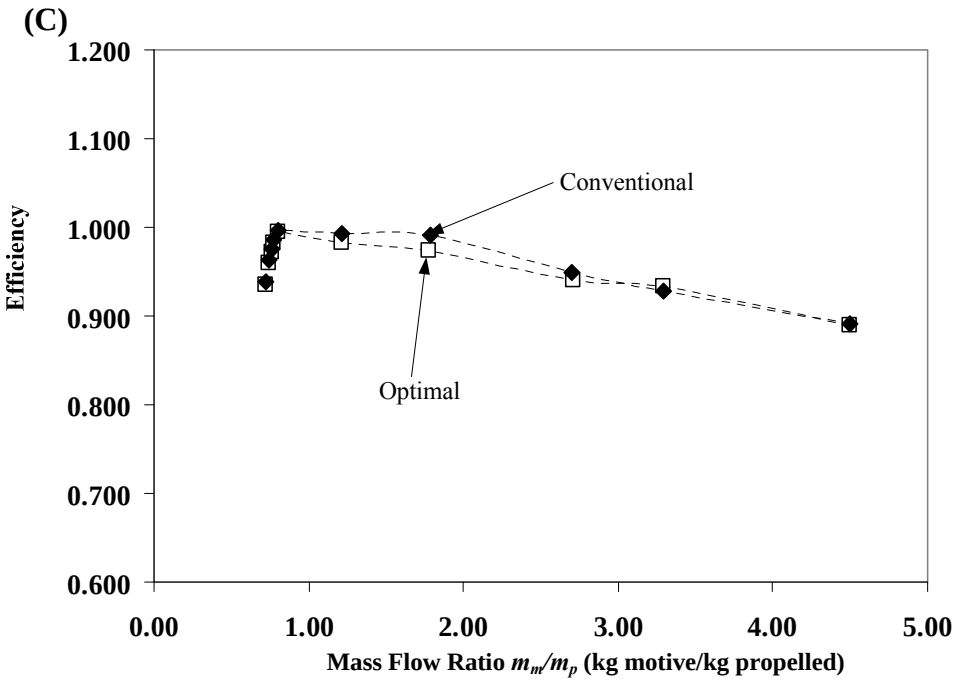

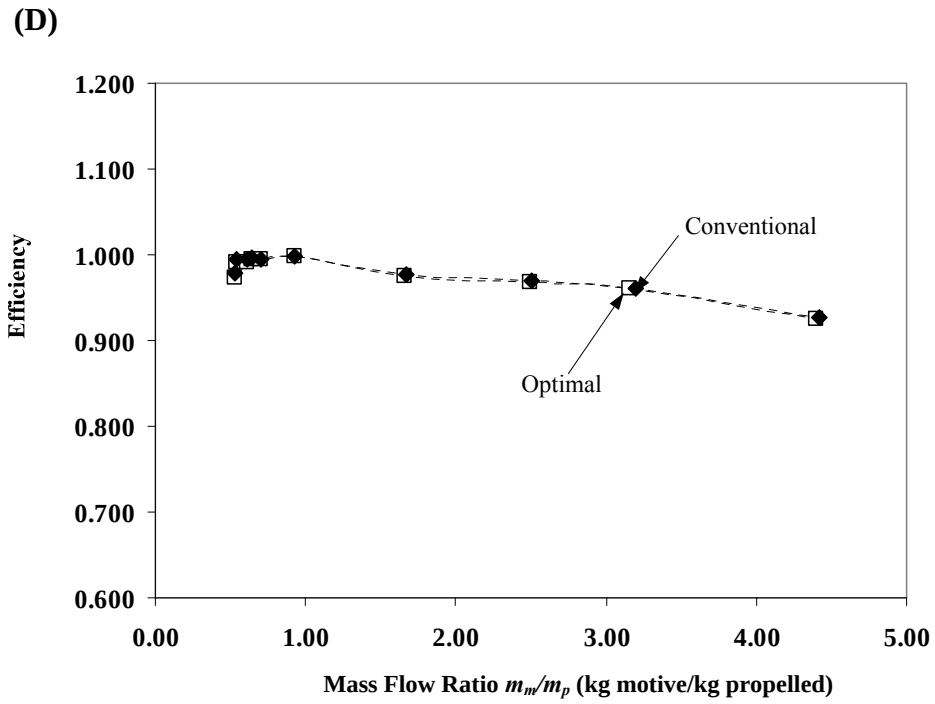

Figure G2. Continued.

The optimal design is built according to the optimization results presented in Chapter VI. The jet ejector provided by Graham Corp. is commonly used in industry. The same nozzle was used in both jet ejectors; therefore, the effect of nozzle selection on jet ejector performance was eliminated. As shown in Figures G1(A) – (D), the compression ratio rapidly increases at low mass flow ratios and then gradually increases above mass flow ratios of 1.50 kg motive/kg propelled. The efficiency increases rapidly at low mass flow ratios, reaches the maximum, and then drops after the peak. As shown in Figures G1 – G2, the optimal and conventional jet ejectors perform evenly on both compression ratio and efficiency for the entire operating condition.

CFD Analysis

Figures G3(A) – (D) and G4(A) – (D) show the compression ratios and efficiencies, respectively, for the optimal jet ejector and CFD modeling. CFD modeling over-predicts at low mass flow ratios and under-predicts at high mass flow ratios on both compression ratio and efficiency. This characteristic is similar for all motive velocities. The transition point is about mass flow ratio 1.00 kg motive/kg propelled.

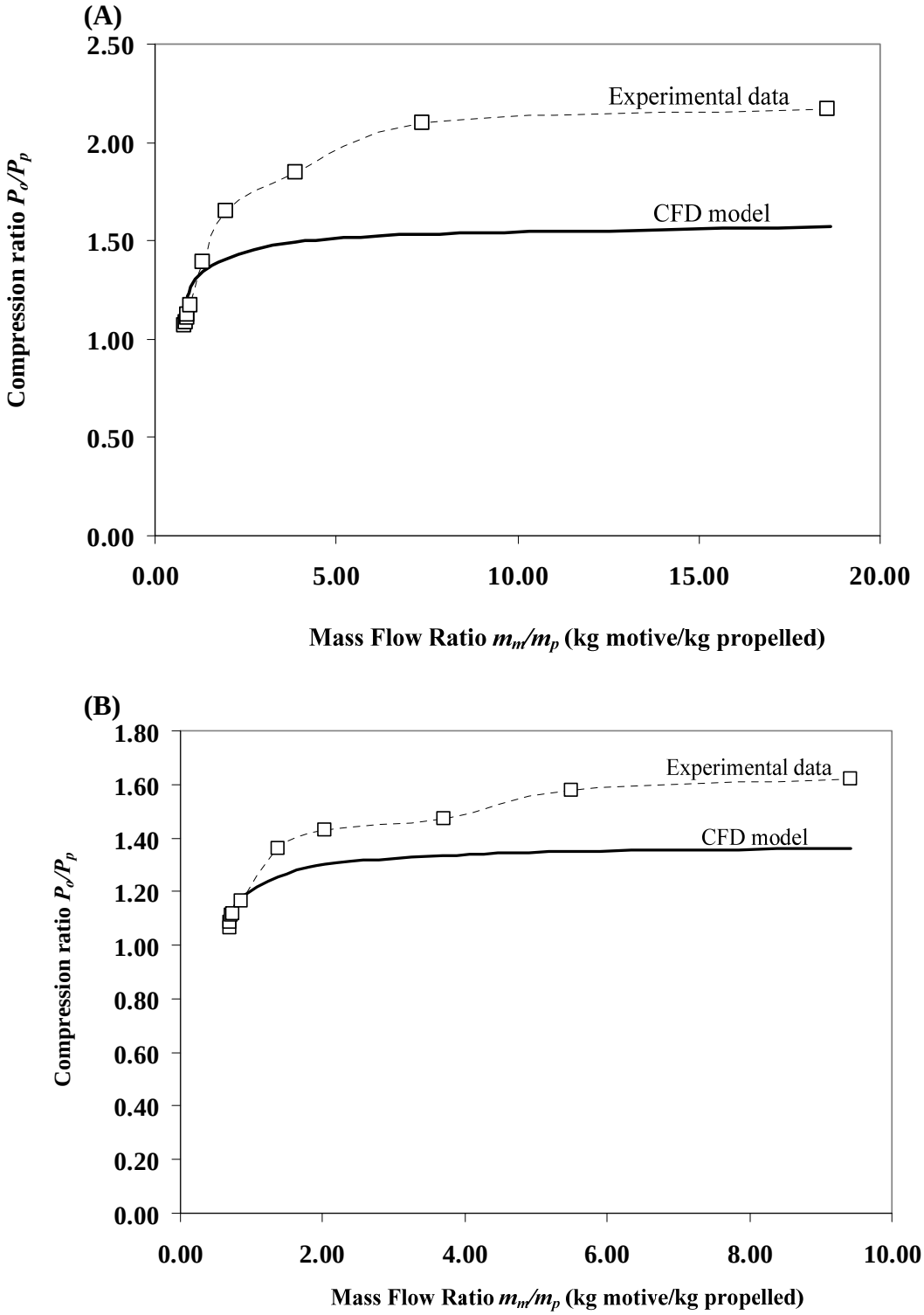

Figure G3. Compression ratio of optimal jet ejector compared to CFD model at motive velocities (A) 345 m/s (70 psig), (B) 312 m/s (60 psig), (C) 309 m/s (50 psig), and (D) 296 m/s (50 psig).

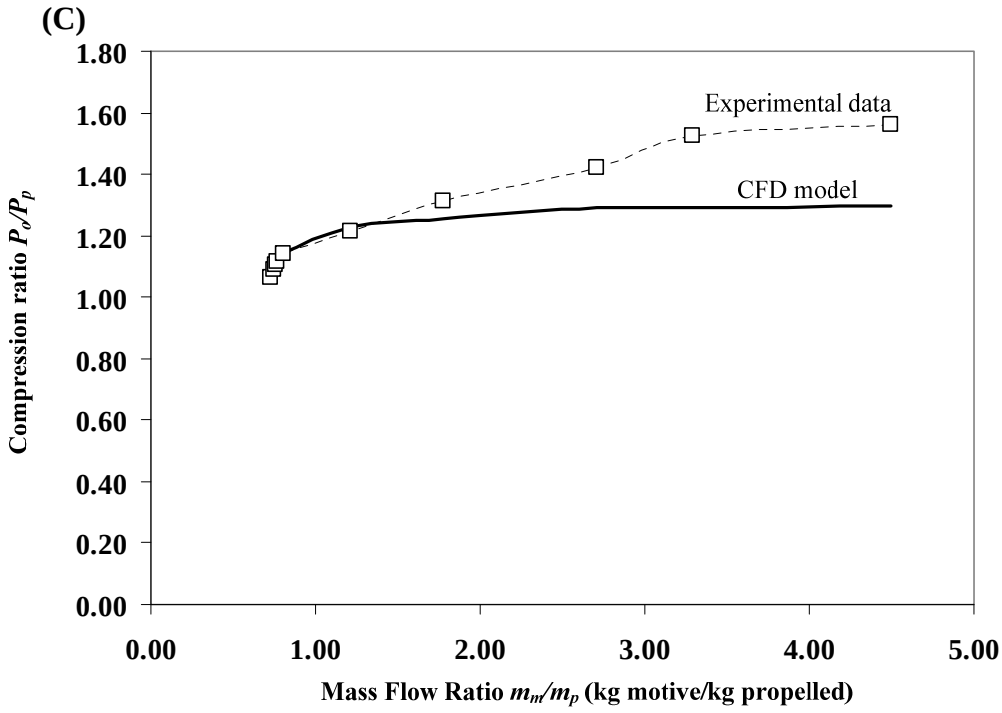

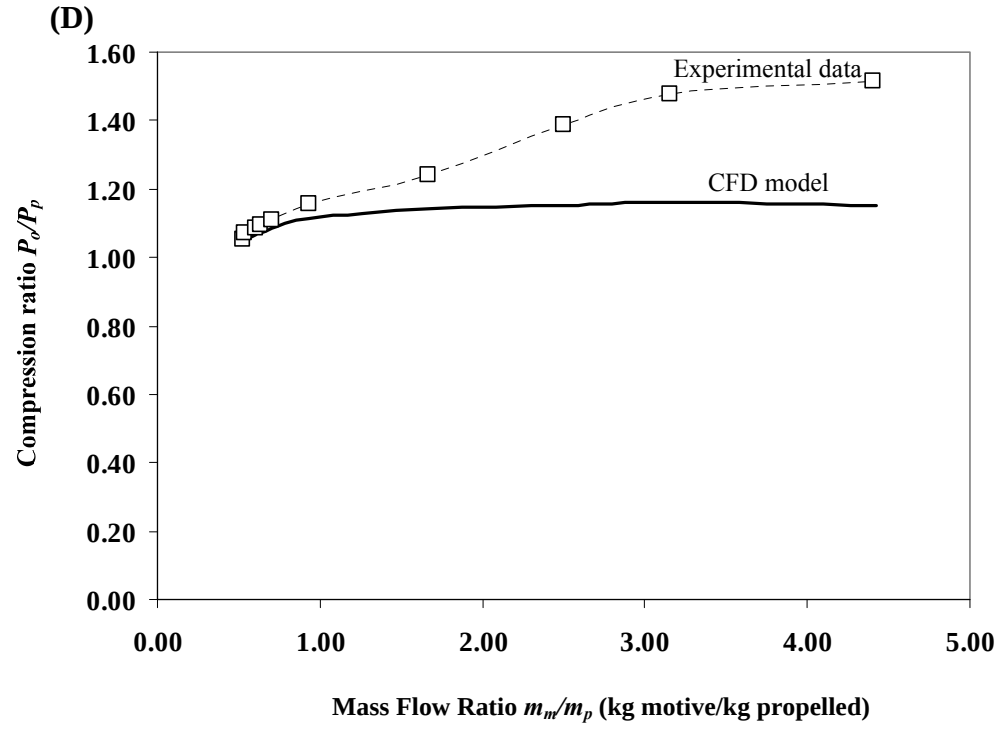

Figure G3. Continued.

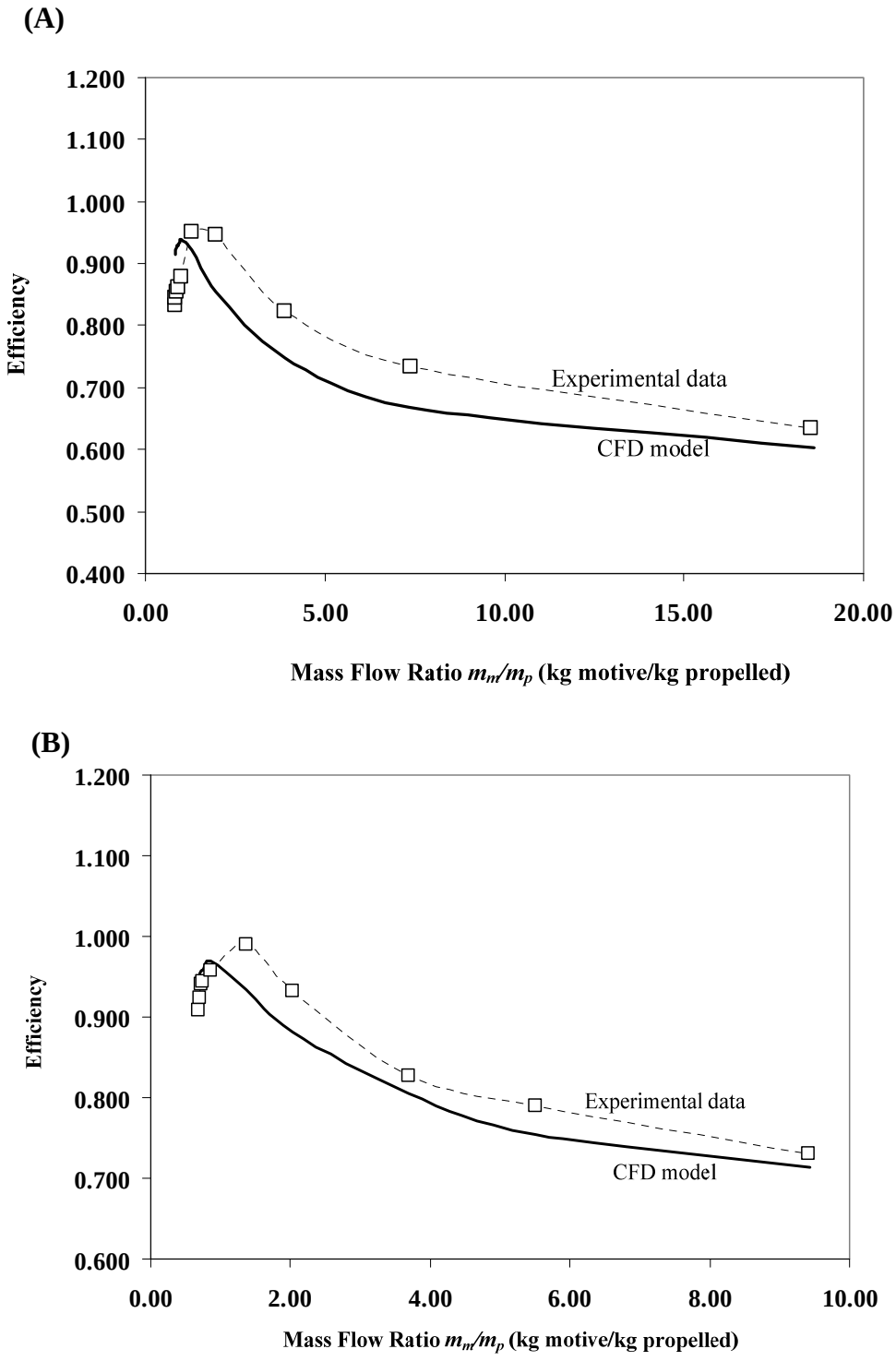

Figure G4. Efficiency of optimal jet ejector compared to CFD model at motive velocities (A) 345 m/s (70 psig), (B) 312 m/s (60 psig), (C) 309 m/s (50 psig), and (D) 296 m/s (50 psig).

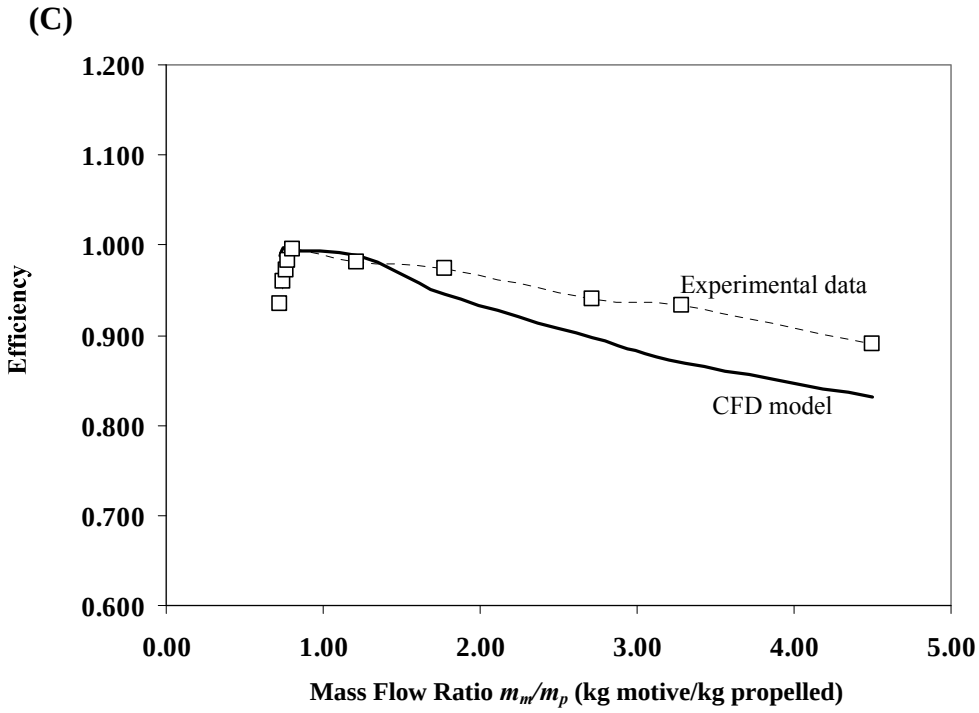

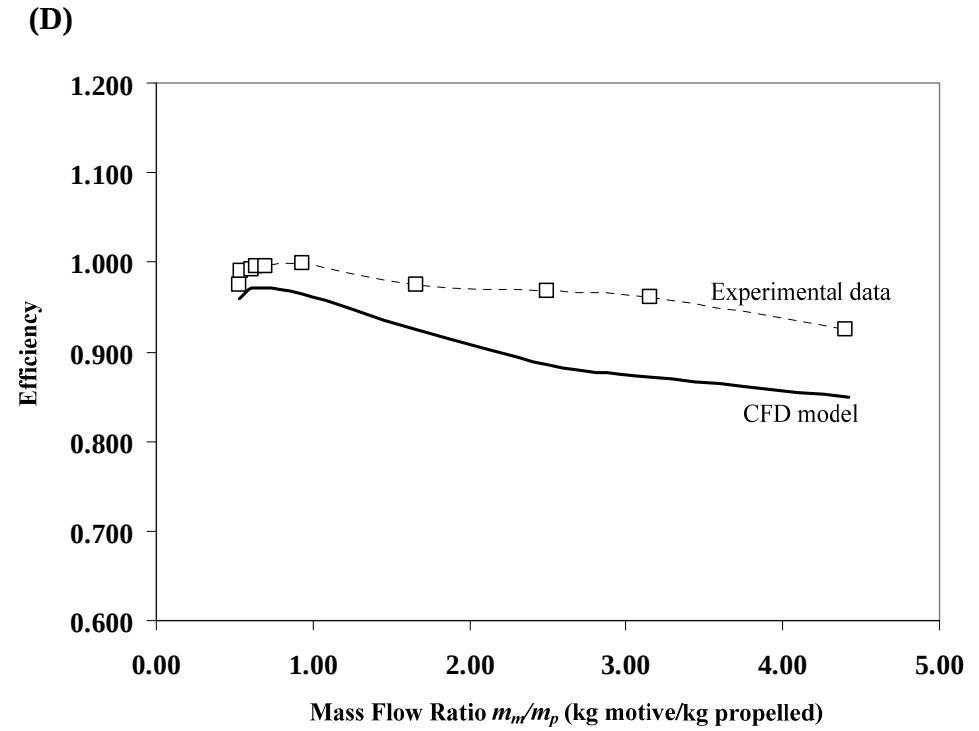

Figure G4. Continued.

VITA

The permanent address for Somsak Watanawanavet is 18 Chalermket 4 Rd, Promprab, Bangkok, Thailand, 10100. His current address is 401 Stasney St., apt#220, College Station, Texas, 77840. Somsak grew up in Bangkok, Thailand. He entered Chulalongkorn University (CU) for his undergraduate study in Bangkok in May 1998. In March 2002, Somsak graduated from the Department of Chemical Engineering with the degree of Bachelor of Engineering and then started his graduate study in the Department of Chemical Engineering at Texas A&M University in College Station, Texas. Somsak completed his Master of Science degree in May 2005 and graduate with his Ph.D. in May 2008.